THE UNIVERSITY *of* EDINBURGH

Understanding Metallophilic Interactions

Qingshu Zheng

Doctor of Philosophy

The University of Edinburgh

2018

Declaration

I declare that this thesis was composed by myself, that the work contained herein is my own except where explicitly stated otherwise in the text, and that this work has not been submitted for any other degree or processional qualification except as specified.

Signature:

Date: 14/09/2018

Contents

Contents i

Acknowledgements iv

Abstract v

Lay summary vi

Abbreviations vii

Chapter 1: Understanding Metallophilic Interactions 1

1.1 Metal–metal bonding and interactions 2

1.2 Applications of metallophilic interactions 5

1.3 Characteristics of metallophilic interactions 11

1.4 Identifying metallophilic interactions 15

1.5 The strength of metallophilic interactions 34

1.6 Summary and outlook 47

1.7 References 48

Chapter 2: Understanding Aurophilic Interactions 54

2.1 Introduction 55

2.2 System design and synthesis 55

2.3 Solid state investigation 58

2.4 Solubility and stability 61

2.5 Estimation of aurophilic interactions by supramolecular aggregation 62

2.6 Estimation of aurophilic interactions by ligand-exchange 69

2.7 Computational studies 75

2.8 Other literature examples 85

2.9 Conclusions 89

2.10 Experimental 90

2.11 References 100

Chapter 3: Understanding Metallophilic Interactions in Group 10 Metal-Complexes 104

3.1 Introduction 105

3.2 Project aim and design 106

3.3 Synthesis, solubility and stability 108

3.4 Crystallography 110

3.5 Experimental estimation of binding energy in solution 112

3.6 Computational estimation of binding energy 119

3.7 Conclusions 133

3.8 Experimental 134

3.9 References 171

Chapter 4: Solvent- and Temperature-Induced Colour Change of a Pt^{II}-Complex 174

4.1 Introduction 175

4.2 Project aims 175

4.3 Results and discussion 176

4.4 Conclusions 191

4.5 References 192

Chapter 5: Overall conclusions 194

Appendix A (Chapter 2) 197

A.1 Crystallography 197

A.2 Correlation between experimental $\Delta\Delta G$ and solvent parameters 204

A.3 EDA results of literature examples 204

Appendix B (Chapter 3) 205

B.1 Crystallography 205

B.2 EDA-NOCV results 221

Acknowledgements

I would like to thank Dr Scott Cockroft for giving me this opportunity to work in the group, for being a fantastic supervisor, for all the help and support. His infinite ideas and knowledge has impressed me a lot and inspired me throughout my PhD.

I am grateful to all the members in the Cockroft group for not only the scientific discussion but also support in daily life. Particularly, I thank Stefan Borsley for the fruitful discussion and the revision with my thesis and papers, for the games of trumps, badminton, and squash. I thank the Official Trumps League, including Big D, Lord Trumpington, Shuffles, Minus 3, and Chucky, for accompanying me over the boring moments.

I thank Dr Fernanda Duarte for her kind help in the computation part of my projects.

Thanks to all the helpful technical staff, especially Dr Lorna Murray and Mr. Juraj Bella for NMR support, and Dr Gary Nicol for crystallography measurement.

I thank University of Edinburgh, China Scholarship Council and European Research Council for funding.

Thanks to my flatmate Dr Xuemao Zhou for your discussion on my projects in the view of a physicist, and for the daily "miserable" competition of who suffers a more miserable PhD life.

Finally, thanks to my parents for your support and understanding.

Abstract

Metallophilic (metal–metal) interactions are weak interactions between closed-shell (d^{10}, s^2) or pseudo-closed-shell (d^8) metal cations. This type of interaction is generally believed to be responsible for various intriguing structures, luminescence, catalysis and magnetism. To gain a better understanding of metallophilic interactions, both experimental and computational investigations have been carried out in this thesis.

Chapter 1 gave an up-to-date literature review on the definition, significance, and methods of estimating metallophilic interactions. The disputed nature and strength of metallophilic interactions encouraged us to further understand them.

Chapter 2 focused on aurophilic interactions between Au^I cations. Aurophilic interactions were observed in the solid state, but not well expressed in solution. Further experimental and computational results suggested that the strength of aurophilic interactions were weaker than electrostatic interactions. The nature of aurophilic interactions arose from orbital interactions rather than dispersion.

Chapter 3 presented the study of metallophilic interactions between group 10 metal centres, including Pt^{II}–Pt^{II}, Pd^{II}–Pd^{II} and Ni^{II}–Ni^{II}. A series of cyclometalated square-planar metal complexes with different metals or substituents were prepared. Pt^{II}–Pt^{II} interactions were found to be stronger than Pd^{II}–Pd^{II} and Ni^{II}–Ni^{II} interactions. The dimerization constants of the Pt-containing complexes increased in line with increasing electron-withdrawing ability.

Chapter 4 investigated the solvent-induced and thermally dependent colour changes of the Pt-containing complexes synthesised in chapter 3. Metallophilic interactions were proposed to be important in influencing the luminescence properties.

Lay summary

Beside the conventional strong metallic bonds in bulk metals, there are also very weak interactions between metal atoms (ions) in compounds. This type of weak interactions is termed as metallophilic (M–M) interactions. The presence of metallophilic interactions has been observed in various structures in the solid state. However, the nature and strength of metallophilic interactions are still disputed. To gain better understanding of metallophilic interactions, both experimental and computational investigations have been carried out in this thesis.

The first chapter briefly introduced what metallophilic interactions are, why and how to study them. Previous studies of the strength and nature of metallophilic interactions were also reviewed.

The second chapter studied aurophilic (gold–gold) interactions. Aurophilic interactions were found to be weak and were not well preserved in solution. Instead electrostatic interactions played a more important role.

The third chapter compared the intensities of platinum–platinum, palladium–palladium and nickel–nickel interactions. Platinum–platinum interactions turned out to be stronger than the latter two. The intensities of metallophilic interactions could also be affected by different functional groups. Computational results suggested these metallophilic interactions were also originated from the mixing of the electron clouds surrounding the metals.

The fourth chapter investigated the colour change of Pt-containing complexes synthesised in the above chapter. Their colours were affected by solvent and temperature. Metallophilic interactions were proposed to be important in influencing their luminescence properties.

Abbreviations

3D	Three dimensional
AO	Atomic orbital
ADF	Amsterdam density functional
BBIMB	1,2-bis(benzimidazol-1-ylmethyl)-benzene
BIMB	1,2-bis(imidazol-1-ylmethyl)-benzene
B3LYP	Becke, three-parameter, Lee-Yang-Parr
BSSE	Basis set superposition error
CCDC	Cambridge crystallographic data centre
CCSD(T)	Coupled-Cluster with single and double and perturbative triple excitations
C_6F_5	Pentafluorobenzene group
CH_2Cl_2	Dichloromethane
$CHCl_3$	Chloroform
COSY	Correlation spectroscopy
d	Doublet (NMR analysis)
DCM	Dichloromethane
DFT	Density functional theory
DMF	Dimethylformamide
DMSO	Dimethyl sulfoxide
ECP	Effective core potentials
EDA	Energy Decomposition Analysis
EDG	Electron donating group

ESI	Electrospray ionization
ESP	Electrostatic potential
Et_2O	Diethyl ether
EtOAc	Ethyl acetate
ETS	Extended transition state
EWG	Electron-withdrawing Group
EXAFS	Extended X-ray absorption fine structure
GD3BJ	Grimme's D3 dispersion with Becke-Johnson damping
HF	Hartree-Fock
HMBC	Heteronuclear Multiple Bond Correlation
HOMO	Highest Occupied Molecular Orbital
HSQC	Heteronuclear Single-Quantum Correlation
IR	Infrared
IUPAC	International Union of Pure and Applied Chemistry
LMP2	Local Møller-Plesset perturbation theory
LUMO	Lowest Unoccupied Molecular Orbital
m	Multiplet (NMR analysis)
m	*meta*
MBI	1-Methylbenzimidazole
m.p.	Melting point
Me	Methyl
MeOH	Methanol
MI	Methyl imidazole

MLCT	Metal-to-ligand charge transfer
MMLCT	Metal-metal-to-ligand charge transfer
M06	Minnesota 2006
MO	Molecular Orbital
MP2	Møller-Plesset perturbation theory
MS	Mass spectroscopy
NBO	Natural Bond Orbital
NCI	Non-covalent interactions
NMR	Nuclear magnetic resonance
NOCV	Natural Orbitals for Chemical Valence
o	*ortho*
p	*para*
PBE	Perdew–Burke-Ernzerhof
s	Singlet (NMR analysis)
SAPT	Symmetry Adapted Perturbation Theory
t	Triplet (NMR analysis)
THF	Tetrahydrofuran
TPSS	Tao-Perdew-Staroverov-Scuseria
SAXS	Small-angle X-ray scattering
SMD	Solvation model based on density
TEM	Transmission electron microscopy
UV-Vis	Ultraviolet–visible
XAFS	X-ray absorption fine-structure

Chapter 1: Understanding Metallophilic Interactions

Abstract

This chapter presents an overview of the literature on metallophilic interactions. Firstly, the concept of metallophilic interactions and the criteria for distinguishing such interactions from metal–metal covalent and dative bonds are introduced. Several computational and experimental methods for identifying and estimating the strength of metallophilic interactions are highlighted. These studies reveal that the origin and strength of metallophilic interactions are still debatable. Metallophilic interactions are found to be significant in molecular construction, luminescence, catalysis, and so on. However, the contribution of metallophilic interactions to molecular assembly is not clear yet. The unclear understanding of metallophilic interactions suggest that it is of great significance to gain further insight into metallophilic interactions.

1.1 Metal–metal bonding and interactions

Bonding and interactions between metal atoms can be categorised into four different classes: metallic bonding, metal–metal covalent bonding, coordination (dative) bonding, and metallophilic interactions (**Figure 1.1**).[1]

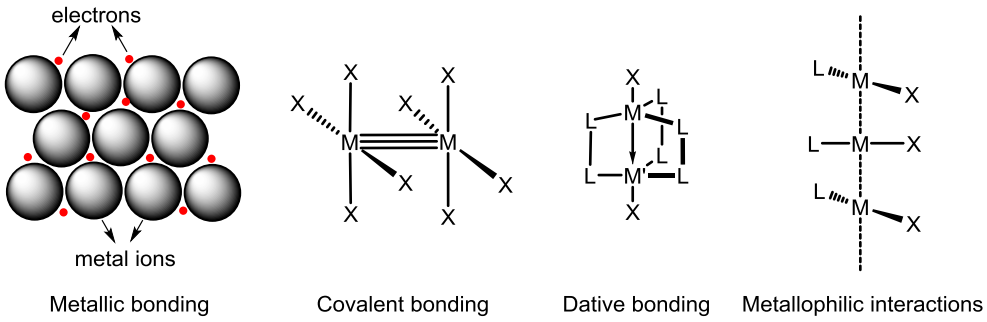

Figure 1.1 Bonding types between metal centres.[1]

1.1.1 Metallic bonding

Metallic bonding is generally observed in bulk metals. It involves the electrostatic attraction between positive metal ions and a 'sea' of delocalised electrons. This type of bonding is so strong that most metals have high melting points and boiling points.

1.1.2 Metal–metal covalent bonding

Metal–metal covalent bonds have been widely found among transition metals, main-group metals and even *f*-block metals. Some selected examples[2–5] with metal–metal bonds are shown in **Figure 1.2**. The nature of metal–metal bonds is understood to be covalent with electron sharing between metal centres. The metal–metal distances are relatively short (1.7 – 2.8 Å). Their bond orders are larger than 1 and could be up to 5. The presence of metal–metal bonds enables these complexes to be applied in metal-organic frameworks,[6] catalysis,[7,8] magnetism,[9,10] and molecular-scale conductors.[11]

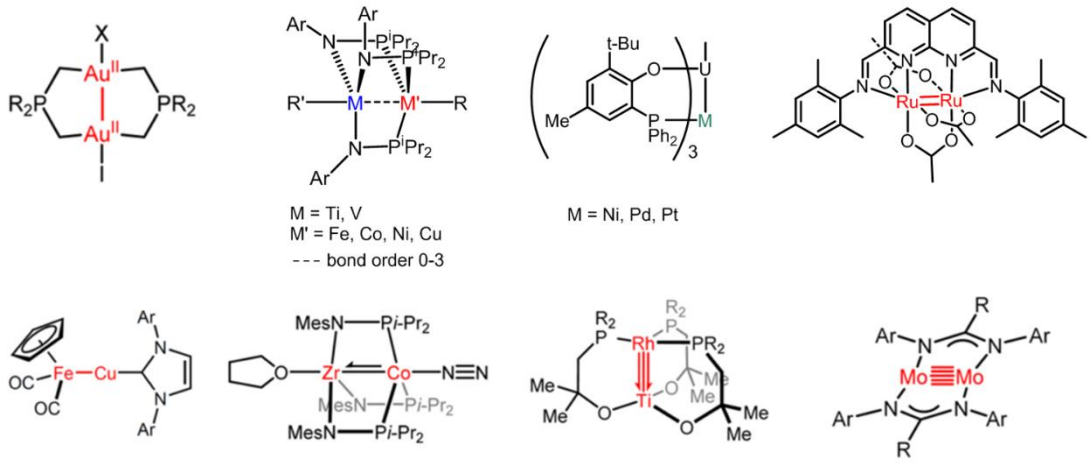

Figure 1.2 Selected complexes with metal–metal covalent bonds.[2–5]

1.1.3 Coordination bonds

Like covalent bonds, coordination metal–metal bonds (also known as dative bonds) are bonding interactions in which a common electron pair is shared between two atoms, with the difference that the origin of the electron pair is from only one metal atom (Lewis donor). Thus, a metal–metal dative bond requires a basic donor metal and an acidic acceptor metal. Pt^{II} has been reported as an excellent donor, whereas Cu^{I}, Ag^{I}, Au^{I}, Hg^{II} and other metals can be good acceptors.[12–14] Several selected complexes with the presence of dative bonding are shown in **Figure 1.3**.

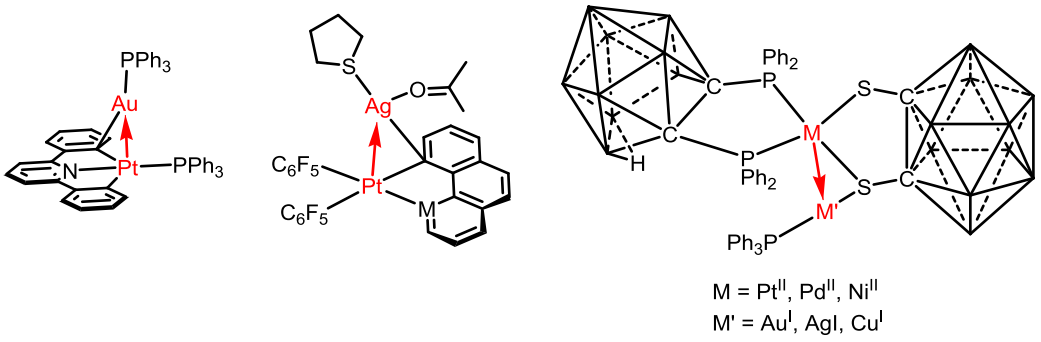

Figure 1.3 Selected examples showing metal–metal dative bonds.[12–14]

Other transition-metal complexes with dative bonding between metal-only Lewis pairs have been reviewed by Braunschweig and co-workers.[15] The M–M distances were measured and compared. These coordination bonds were only very slightly shorter (ca. 2%) than those considered to be "covalent" and were thus practically indistinct.

Therefore, more computational and experimental effort should be paid to gain better understanding of whether the nature of metal–metal coordination bonds really differs from covalent metal–metal bonds, beyond the "origin" of the contributing electrons.

1.1.4 Metallophilic interactions

In contrast to the open-shell metal bonding interactions described above, metallophilic interactions are weak interactions that occur between metal centres with closed shell (d^{10}, s^2) or pseudo-closed shell (d^8) electron configurations. Metallophilic interactions have been observed experimentally and studied theoretically for many elements (**Figure 1.4**), such as elements with an electron configuration of d^{10} (Hg^{II}, Au^{I}, Ag^{I}, Cu^{I}, Pt^{0}, Pd^{0}), d^8 (Au^{III}, Pd^{II}, Pt^{II}, Ir^{I}, Rh^{I}, Ru^{0}), and s^2 (Hg^{0}, Tl^{I}, Pb^{II}, Bi^{III}). The short-lived Rg^{1I} has been predicted to be a metallophilic species, but this behaviour has yet to be observed.

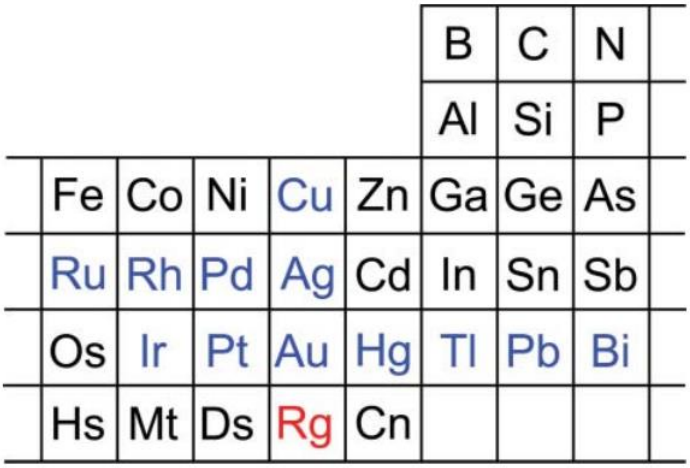

Figure 1.4 Elements that show metallophilic interactions with experimental evidence (blue). Metallophilic interactions in Rg (red) only have theoretical support. Reproduced from ref 16.

The term "metallophilicity" is derived from the term "aurophilicity", which was first introduced in gold chemistry to describe the Au^{I}–Au^{I} interaction.[17–19] Au^{I} has a $5d^{10}$ closed-shell electronic configuration, and it was expected that only weak van der Waals forces would be observed and that the positive charges of the gold cations should obviously generate a significant Coulombic repulsion at short distances. However, a large amount of experimental and computational evidence revealed the

existence of aurophilic interactions.[20–23] The term "aurophilicity" was thus widely accepted. Since then, similar interactions involving other metal centres were also observed, thus terminologies "platinophilic interactions" (Pt–Pt), "argentophilic interactions" (Ag–Ag), "mercurophilic interactions" (Hg–Hg) and others,[24,25] have been used. Considering there were also many examples of interactions between different metal cations, like Au^{I}–Ag^{I}, Au^{I}–Au^{III}, Au^{III}–Pt^{II}, Pt^{II}–Pd^{II} and so on, the extended and more general terms "metallophilic interactions" and "metallophilicity" were therefore adopted.

Before detailing the current state of knowledge surrounding the underlying physical origin and quantitative aspects of metallophilic interactions, it is pertinent to provide an overview of applications in which the qualitative influence of metallophilic interactions have been implicated.

1.2 Applications of metallophilic interactions

Metallophilic interactions have attracted extensive attention in the recent decades due to their potential roles in structure construction, nanomaterials, luminescence, catalysis, molecular sensing, and beyond. However, it should be cautioned that the putative roles of metallophilic interactions in many chemical systems are rarely rigorously verified beyond qualitative suggestions, particularly in larger supramolecular assemblies or materials.

1.2.1 Structure construction

Just like other non-covalent interactions, such as hydrogen bonding and π–π interactions, metallophilic interactions can be used for constructing various structures[26] ranging from clusters to three-dimensional networks. As the strength of metallophilic interactions is weak, the assembly behaviour of the complexes can be easily affected by external stimuli, such as concentration, solvent, temperature, and mechanical grinding.[27–29] Consequently, a material can display different crystal structures and morphologies in response to such environmental changes. For instance, Yam *et al.*[30] reported an alkynylplatinum(II) terpyridine complex functionalised with polyhedral oligomeric silsesquioxanes (POSS) moieties (**Figure 1.5**). The complex

self-assembled into distinct nanorings and rod-like nanostructures in different solvent mixture. The self-association process was governed by Pt−Pt and π−π stacking interactions as well as the hydrophobic interactions provided by the POSS moieties, which could be systematically controlled by the variation of solvent composition. Spectroscopic changes including UV−vis absorption, emission studies, and the electronic micrographs were observed along with the morphological transformation.

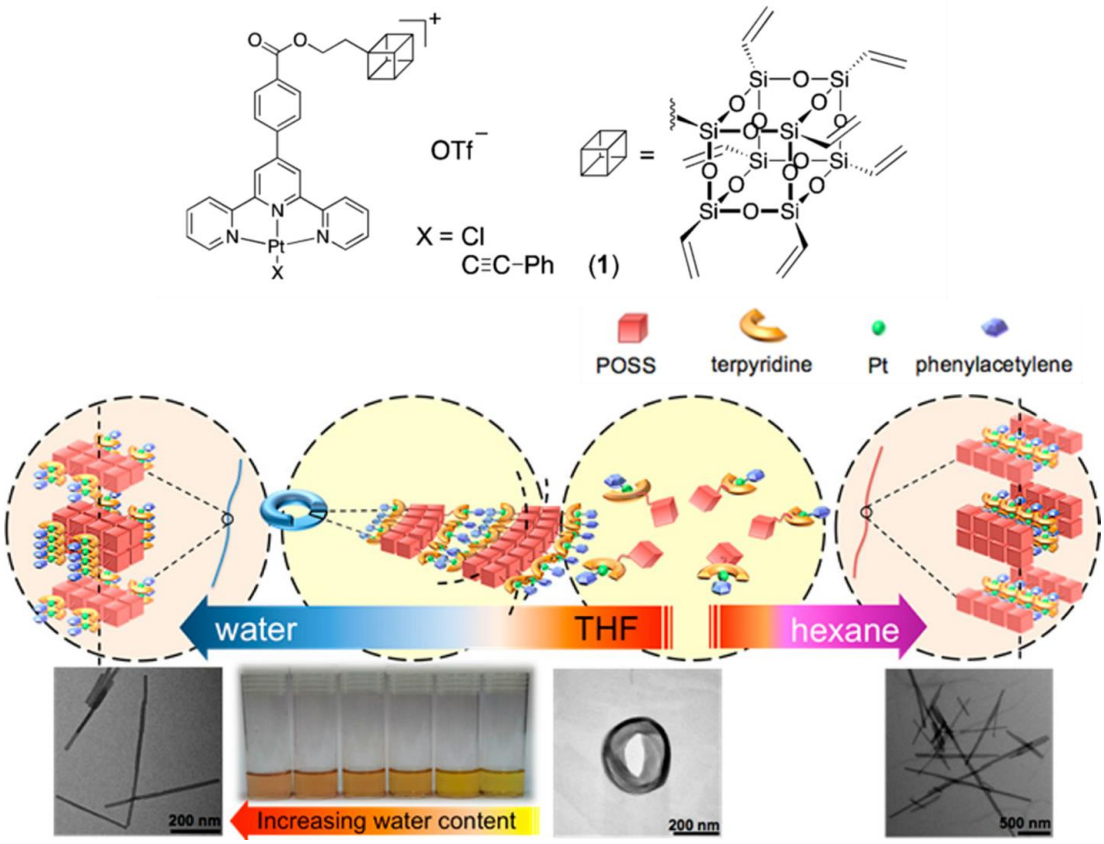

Figure 1.5 Alkynylplatinum(II) terpyridine complex showing morphology transformation triggered by solvent composition. Reproduced from ref 30.

1.2.2 Nanomaterials

Yam *et al.*[31] demonstrated that metal–metal interactions and π–π interactions could direct the end-to-end aggregation of gold nanorods. A water-soluble thioacetate-containing Pt^{II} complexes was firstly synthesised. Then the complex was selectively attached to the ends of nanorods by *in situ* deprotection of the thioacetate group in the presence of basic pyrrolidine. The anisotropic functionalisation was due to the presence of the protective CTAB layer on the sides of the GNRs. The end-to-end

assembly was directly observed by TEM images. The extent of the assembly was concentration dependent with longer aggregated GNR chains forming at higher concentrations of the Pt-complex. Red shifts in concentration-dependent UV-vis spectra confirmed that higher concentration-induced increase of low energy absorption band and higher extent of aggregation. Therefore, the aggregation of the nanorods was believed to be driven by supramolecular assembly of the Pt-complexes induced by Pt–Pt interactions and π–π interactions.

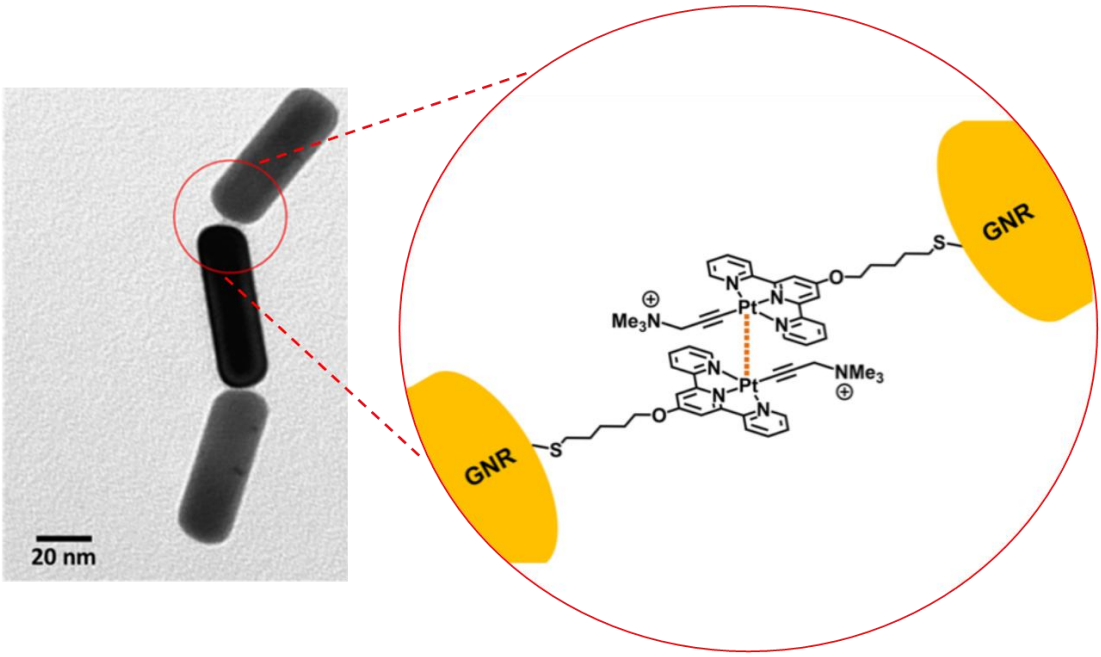

Figure 1.6 TEM images (left) and schematic diagram (right) of the proposed end-to-end assembly of GNRs induced by Pt···Pt and π−π stacking interactions. Reproduced from ref 31.

1.2.3 Luminescence

Complexes containing metals, especially gold and platinum, have attracted increasing attention owing to their intriguing luminescence properties. The presence of metallophilic interactions make these complexes more unique and show more interesting luminescence behaviours. Yam has given several reviews on gold and platinum complexes which show fascinating luminescence properties.[27,32,33] Li *et al.*[34] reported a cluster [{Au(**L**)}$_3$] (**L**=3-(2-thienyl)pyrazolate) with two crystal forms. As depicted in **Figure 1.7**, form *a* and form *b* exhibited orange–red and white emissions, respectively. The introduction of the thiophene group induced the uncommon high-

energy blue–green emission. Together with the low-energy orange–red band, which originates from the monomer–excimer equilibrium and exhibits aurophilic phosphorescence, the compound is able to give off white light in both solution and solid states.

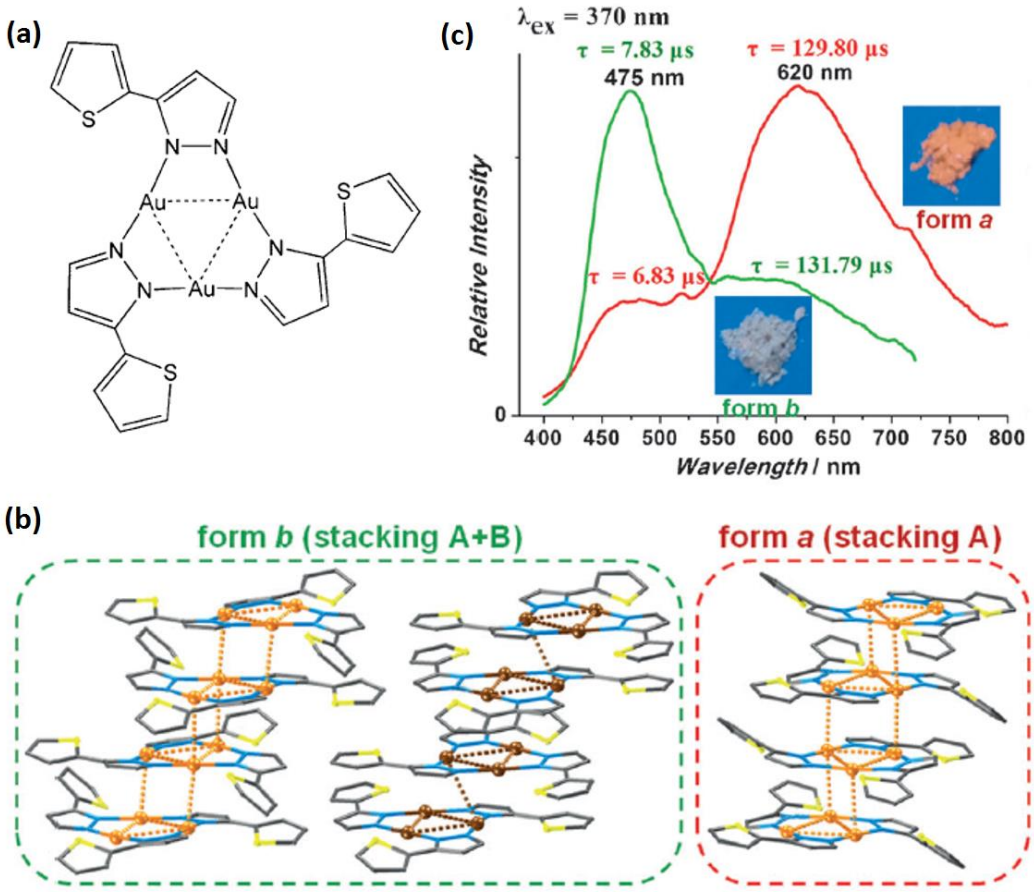

Figure 1.7 (a) Structural formula of the [{Au(L)}$_3$]. (b) The two crystal forms *a* and *b* with different sacking mode. (c) Their emission spectra exited at 370 nm. Reproduced from ref 34.

1.2.4 Catalysis

The first experimental support for the presence of aurophilic interactions in Au^{I} catalysis was found by Gagné.[35] Other gold-based catalysts containing aurophilic interactions have been found since then.[35–37] In 2015, Weber and Gagné[38] discussed whether aurophilicity in gold catalysis was good or bad for catalytic performance. Two examples showing the potential drawbacks and benefits of aurophilic interactions are outlined below.

An extensive experimental study of the mechanism of Au^{I}-catalysed hydroalkoxylation of alkynes were conducted by Zhdanko and Maier[39] using NMR spectroscopy. Based on experimental results, a mechanism for gold-catalysed hydroalkoxylation was proposed (**Figure 1.8**). Firstly, it was proposed that the gold catalyst $LAu(Sol)^{+}$ coordinated to the alkyne substrate to form π complex **A**. The π complex **A** was then attacked by a nucleophilic alcohol forming the vinyl-gold complex **BH**. A proton was released to generate the vinyl gold species **B**, which could competitively undergo protonolysis or auration to give π complex **E** or diaurated species **D**, respectively. The enol ether gold complex **E** would quickly exchange ligand with substrate or the solvent molecule to finally yield enol ether product **C** and complete the catalytic cycle. In contrast, the diaurated complex **D** was unable to undergo direct protodeauration and its formation was strongly thermodynamically favoured. Therefore, the complex **D** with the presence of aurophilic interactions disrupted the catalysis. Hence it was proposed that catalysis performance would be better without the presence of aurophilic interactions.

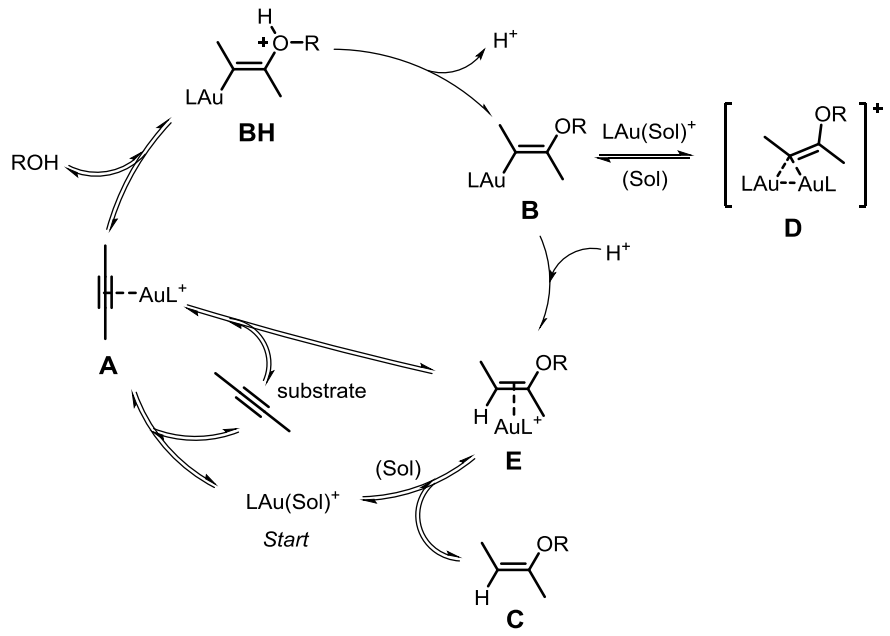

Figure 1.8 The mechanism of the gold-catalysed hydroalkoxylation of alkynes.[39]

Smirnova and Echavarren[40] prepared a robust hexanuclear Au^{I}-cluster **2**. This gold cluster was catalytically active in a variety of gold-catalysed reactions. For instance, catalyst **2** can catalyse [4+2] cycloaddition of 1,6-enyne bearing a disubstituted alkyne

with a *o*-tolyl substituent. Although catalyst **1** was found to be more active, the good catalysis performance of catalyst **2** suggested aurophilicity could contribute to access new reactivity.

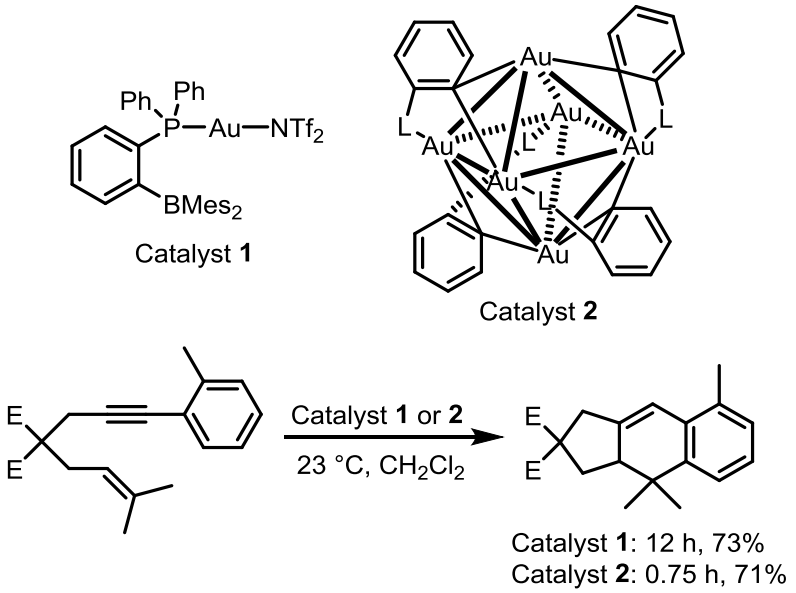

Figure 1.9 Catalyst **1** without aurophilic interactions and catalyst **2** with aurophilic interactions used for [4+2] cycloaddition.[40]

From the above examples, catalytic activity was hindered by aurophilic interactions in most cases as aggregates were less active than monomeric $[LAu]^+$, but some catalysts with aurophilicity also behaved good catalytic activity.[38,41] Further investigation on the role of metallophilic interactions for catalysis are worthy to be exploited.

1.2.5 Molecular/ion sensing

Metallophilic interactions can be utilised for metal cation sensing. For instance, Ying[42] developed a simple method to selectively detect Hg^{II} cations using fluorescent Au NCs (nanoclusters) in aqueous solution. The fluorescence of the Au NCs solution was quenched by adding Hg^{II} (**Figure 1.10**) due to the proposed formation of metallophilic interactions. More importantly, only Hg^{II} cations could quench the fluorescence while other metal cations could not, even for Ag^{I} or Pd^{II} which could also form potential metallophilic interactions with the Au NCs. Because of the high selectivity and low

detection concentration (0.5 nM) for Hg^{II} over other metal ions, the detecting process could thus be developed as a promising simple test strip for Hg^{II} cations.

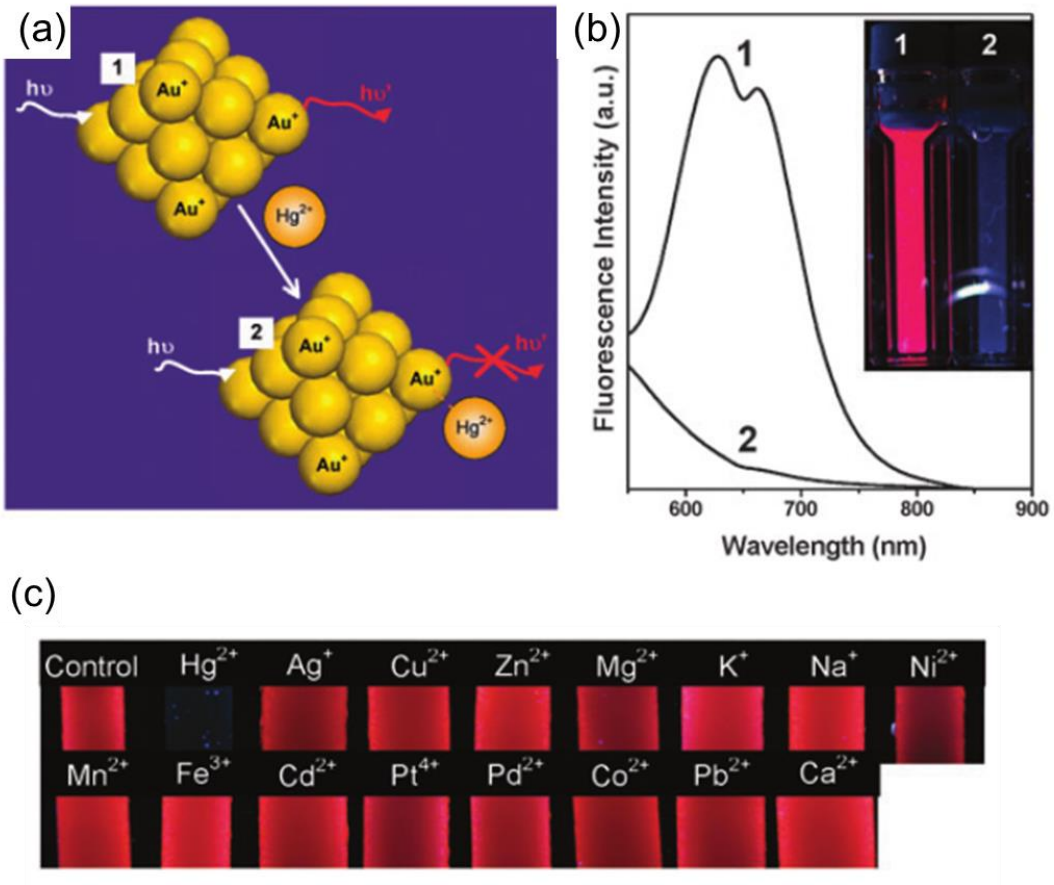

Figure 1.10 (a) Scheme showing Hg^{II} detection through Au^{I}–Hg^{II} metallophilic interactions/bonds, causing the fluorescence quenching of Au NCs. (b) Emission spectra and images under UV light of Au NCs (1) without and (2) with Hg^{II} ions. (c) Photographs of the test strips with Au NCs under UV light, which were dipped in solutions of various metal ions. Reproduced from ref 42.

1.3 Characteristics of metallophilic interactions

Metal–metal covalent bonds, dative bonds and metallophilic interactions are among the various terms used to describe bonding and interactions between metal centres in organometallic complexes. However, these bonding and interactions are sometimes confusing and difficult to distinguish. For instance, it is difficult to identify the bonding type of a Pt^{II}–Au^{I} contact with a distance of ~2.7 Å without detailed analysis. The disputed nature (dispersion or orbital hybridisation) of metallophilic interactions

further increases the confusion. Consequently, "metal–metal bonds",[5,11,43–46] "metal–metal interactions",[27,32,47] "metallophilic bonding",[48] and "metallophilic interactions"[19,24,25,49–51] all appear in the literature. Are they used correctly? Are they the same? To answer these questions and distinguish metallophilic interactions, metal–metal covalent bonds, and metal–metal dative bonds, we need to discuss several criteria shown below.

I) The electron configuration / oxidation state

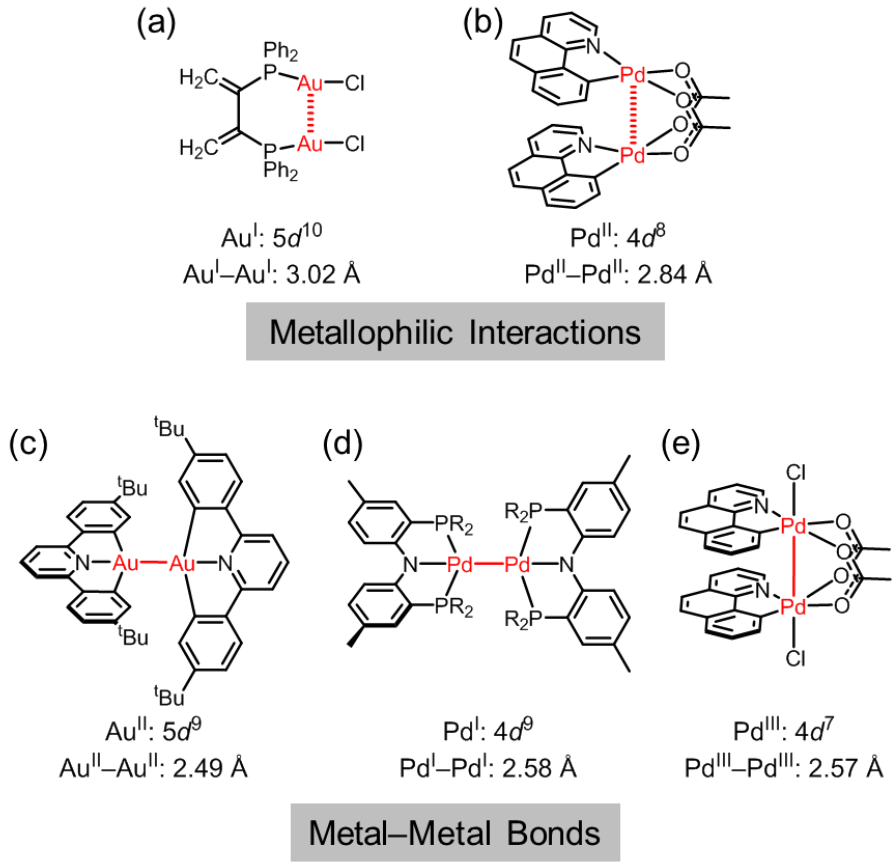

Figure 1.11 Complexes containing gold and palladium cations with different electron configurations. Closed-shell Au^{I} and pseudo-closed shell Pd^{II} can form metallophilic interactions, while open shell Au^{II}, Pd^{I} and Pd^{III} result in metal–metal bonds.[20,52–54]

As mentioned above, one of the requirements for metallophilic interactions is that the valence electron configuration should be closed shell (d^{10}, s^{2}) or pseudo-closed shell (d^{8}). While for metal–metal bonding, the metal centres have open-shell electron configurations. For example, Au^{I} has a 5d^{10} closed-shell electron configuration while

Au^{II} adopts a $5d^9$ open-shell configuration. Consequently, aurophilic interactions can be formed between Au^{I} cations, while covalent bonds are generated between Au^{II} cations (**Figure 1.11**). Similarly, pseudo-closed shell Pd^{II} with an electron configuration of $4d^8$ can participate in metallophilic interactions, whereas open-shell Pd^{II} ($4d^9$) and Pd^{III} ($4d^7$) can form metal–metal bonds.

II) Metal–metal distance

Another general criterion for distinguishing metallophilic interactions and metal–metal bonding is the metal–metal distance. Numerous crystal structures of metal complexes have been reported, from which the metal–metal distance can be measured. Generally, metallophilic interactions have been implicated as occurring when the distance between two metals is shorter than the sum of their van der Waals radii. Meanwhile, covalent metal–metal bonds are identified as being shorter (< 2.6 Å, **Figure 1.12**) than the interatomic distances associated with metallophilic interactions (2.5–3.5 Å). However, it should be noted that these distance ranges are just arbitrarily defined from empirical observations, and distinct ranges of distances for metallophilic interactions and metal–metal bonding have not been identified or defined. Therefore, metal–metal distance merely provides an indicator of potential interactions and bonding modes.

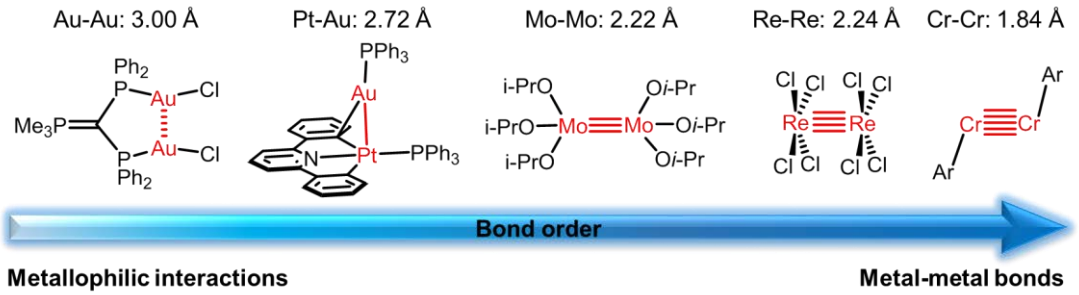

Figure 1.12 Selected complexes showing the difference between metallophilic interactions and metal–metal bonds.[20,55–58]

III) Bond order

The bond order (BO) of a chemical bond (called also multiplicity of the bond) in diatomics is defined as half the difference between the number of bonding electrons (n_b) and the number of antibonding electrons (n_a): $BO = (n_b - n_a) / 2$. As shown in

Figure 1.12, if the bond order is smaller than 1, yet attractive forces are observed between the centres, then metallophilic interactions are thus present. The metal−metal bond must be a covalent bond if the bond order is larger than 1. If the bond order is equal to 1, the bond may be a covalent or dative bond. Several theories for accessing bond order have been developed, like Wiberg bond order (WBO),[59] Mayer Bond Order (MBO),[60,61] Natural Localized Molecular Orbital Bond Order (NLMOBO),[62] and Laplacian Bond Order (LBO)[63]. Detailed introduction of these theories is beyond the scope of this thesis and will therefore not be discussed here. Interested readers are instead directed to the comprehensive review by Tsipis, which discusses the potential and challenges of using these methods for the computational study of metallophilic interactions.[50]

Combining the above-mentioned electron configuration, distance and bond order characteristics together, metallophilic interactions can hence be distinguished from metal−metal bonds.

IV) Relativistic effects

Relativistic effects play significant roles in heavy elements.[64] Hence, metallophilicity can be influenced by relativistic effects significantly. Electrons increase their average velocity and approach the speed of light ***c*** (137 a.u., a.u. = atomic units) with increasing atomic nuclear charge (Z). The mass of the electrons must increase due to relativity. Consequently, the *s* electrons (and to a lesser extent, *p* electrons) are more strongly bound, occupy smaller orbitals, and shield the nuclear charge from *d* and *f* electrons (**Figure 1.13**). The *d* and *f* electrons are therefore less bound and occupy larger orbitals. Due to relativistic effects, elements around gold (Ir, Pt, Au, Hg and Tl) in the periodic table exhibit distinct orbital contractions, with the greatest effect being seen on gold itself.

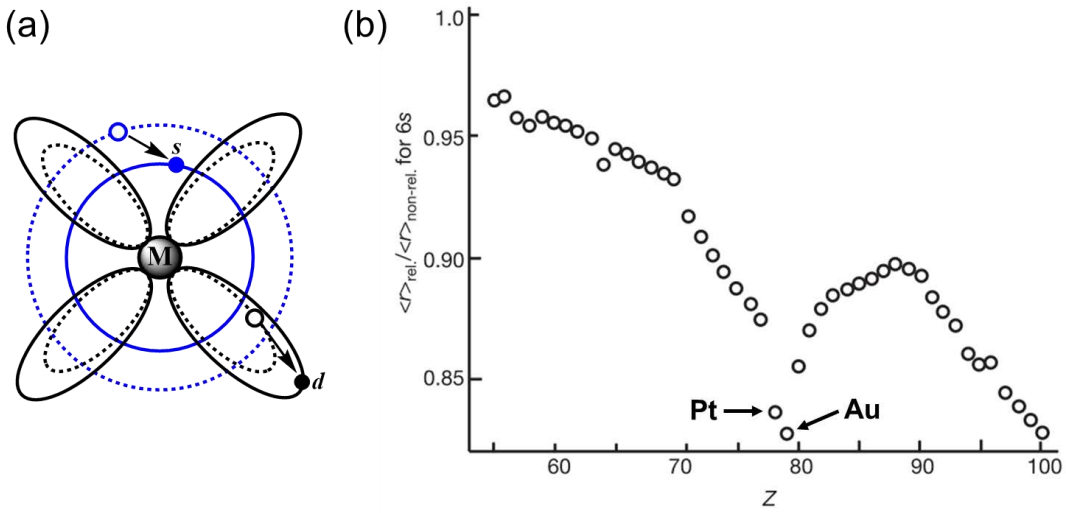

Figure 1.13 (a) *s* orbital contraction and *d* orbital expansion due to relativistic effects. (b) Calculated relativistic contraction of 6*s* orbitals. *Z* is atomic number, $\langle r \rangle_{rel.}$ and $\langle r \rangle_{non\text{-}rel.}$ are calculated radii of the elements considering and not considering relativistic effect. Reproduced from ref 64,65.

1.4 Identifying metallophilic interactions

Although metallophilic interactions have been widely observed in the solid state,[18,19,66] and have been implicated in a wide range of applications as outlined in section 1.2, very few studies have provided convincing measurement of such interactions occurring in solution.[67–69] Furthermore, the major contributors to such interactions is still a matter of debate, with hybridisation of molecular orbitals[70] or dispersion interactions[18,19,22] (in other words, van der Waals interactions) being suggested as being the most important to date.

1.4.1 Computational methods

1.4.1.1 Computational theory

Computational methods reported for metallophilic interactions are mainly based around *ab initio* and density functional theory (DFT) approaches.

Ab initio

Ab initio methods derive directly from quantum theory. The term "*Ab initio*" means "from first principles" or "from the beginning", implying that the input parameters it uses are physical constants. Post Hartree-Fock (HF) methods, like Møller-Plesset perturbation theory (MP2, MP3…), and couple cluster theory (CCSD, CCSD(T)), are often employed to compute complexes including late transition metals. MP2 is capable of describing dispersion, but it is also well-known for overestimating van der Waals attractions, which would therefore be likely to overstate the significance of metallophilic interactions. CCSD(T) is generally very accurate and often regarded as a benchmark calculation, but is also very computationally expensive.

Early work by Hoffman and co-workers ascribed short metal–metal (Au^{I}–Au^{I} and Pt^{0}–Pt^{0}) bonding to orbital hybridisation based on extended Hückel calculations.[70,71] This orbital hybridisation hypothesis was also supported by Calhorda.[72] However, Pyykkö and co-workers[22] suggested that aurophilic interactions are attributed to correlation effects with a further strengthening by relativistic effects.[64] They calculated the interaction energies for a $[(ClAuPH_3)_2]$ model dimer in parallel, perpendicular and anti-parallel configurations at the Hartree-Fock (HF), the second-order Møller-Plesset (MP2) and the third-order Møller-Plesset (MP3) levels (**Figure 1.14**). The MP2 calculations, which took correlation effects (interaction between electrons in the electronic structure of a quantum system) into account, corresponded well with the experimental observation, while the Hartree-Fock (HF) method, which did not consider correlation effects, did not correlate well with experimental results. As the dispersion energy (the attractive component of van der Waals interactions) is often a major energy component arising from electron correlation energy, aurophilic interactions were thus regarded as having a dispersion origin.

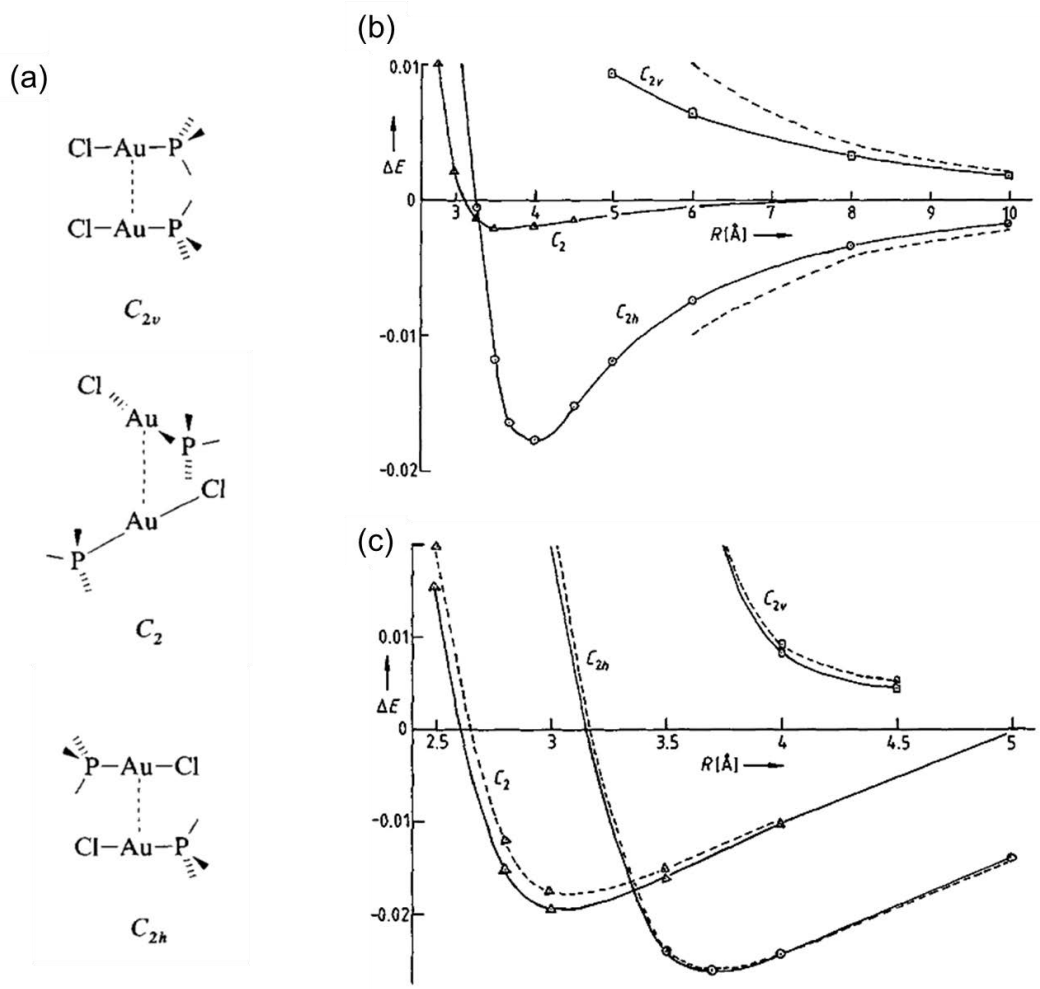

Figure 1.14 (a) Three different configurations (C_{2v}, C_2, and C_{2h}) of $(ClAuPH_3)_2$ used for calculations. Corresponding interaction energies ΔE computed at the (b) HF (solid line), and (c) MP2 (solid line) and MP3 (dashed line) levels. Reproduced from ref 22.

Density Functional Theory

Density Functional Theory (DFT) is a powerful quantum mechanical modelling method. The name density functional theory comes from the use of functionals to describe the electron density. Owing to the popularity of DFT in chemistry and physics, the Nobel Prize for chemistry in 1998 was awarded to Walter Kohn (for developing DFT) and to John Pople (for developing computational methods in quantum chemistry in general). The Density Functionals (DFs) in DFT can be categorised into the following groups: local density approximation (LDA), generalised gradient approximation (GGA), meta-GGA, hybrid DFs, double-hybrid DFs, and fully non-local range-separated DFs. These categorisations have been discussed in another

review from Tsipis.[73] Perdew and co-workers[74] framed such methods in analogy to Jacob's ladder (**Figure 1.15**), offering a general prescription for the design and selection of density functional approximations.

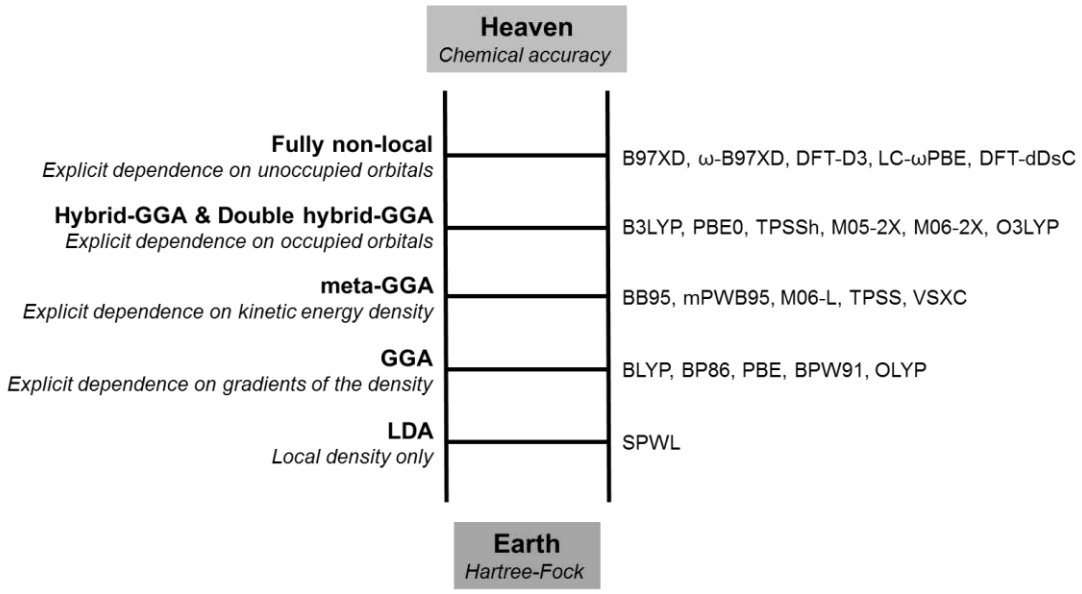

Figure 1.15 Jacob's ladder depiction of the hierarchy of DFT functionals from least accurate (HF) to the heaven of chemical accuracy. Common DFT functionals are listed at the right-hand side.[74]

DFT has been used extensively to calculate metal-containing complexes due to its low computational cost and high accuracy. An exhaustive review of DFT and its recent application to transition metal chemistry has been given by Cramer and Truhlar,[75] while Maslowsky Jr.,[76] Neese,[77] and Tsipis[50] reviewed some recent successful applications of DFT to metal–metal bonding.

Otero-de-la-Roza and co-workers[78] found that relativistic effects helped to strengthen aurophilic interactions, not by stabilising the Au–Au attraction, but by hindering the formation of ionic Au–X (X = halogen anion) attraction. They employed dispersion-corrected density-functional theory, LC-ωPBE-XDM, to study metallophilic interactions for unsupported dimers $[MX(PH_3)]_2$ (M = Cu, Ag, Au, X = H, F, Cl, Br, I) shown in **Figure 1.16**. Three packing geometries, *ortho*, *para*, and η^2 (involving anionic bridges between the metals), were examined. They found that relativistic effects could increase the electron affinity of metal centres and gold was much more influenced than silver. The increased electron affinity reduced the electron-donating

ability of a metal centre to the bonded anion, destabilising geometry η^2. Consequently, Au-complex was more likely to aggregate in *ortho* and *para* geometries. In contrast, Ag and Cu, which were less affected by relativistic effects, preferred η^2 ligand coordination mode.

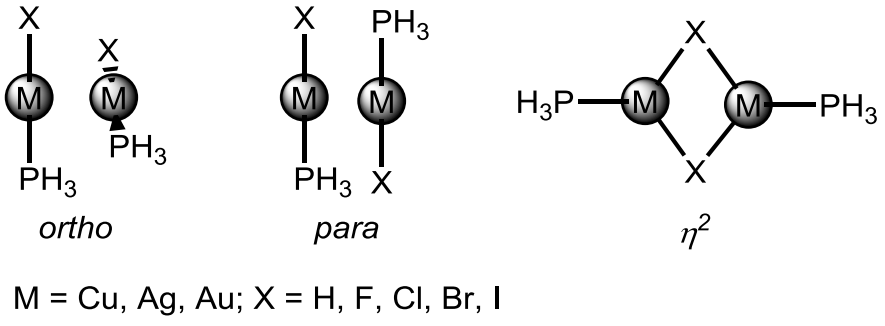

Figure 1.16 The *ortho*, *para*, and η^2 geometries of unsupported dimers $[MXPH_3]_2$ (M = Cu, Ag, Au; X = H, F, Cl, Br, I).[78]

Based on both *ab initio* and DFT, various computational methods have been developed to qualitatively and quantitatively study metallophilic interactions. Qualitative methods will be discussed first, and the quantitative studies will be reviewed in section 1.5.1. Reported methods for identifying metallophilic interactions include atoms in molecules (AIM)[79,80] and non-covalent interaction (NCI) analysis.[81]

1.4.1.2 Atoms in molecules (AIM)

Atoms in Molecules (AIM) is a theoretical tool developed by Bader for analysing the electronic structure of a molecule based on the topology of the electron density distribution.[80] The theory analyses the topology of the electron density distribution ρ, its gradient field $\nabla\rho$, and its Laplacian $\nabla^2\rho$, which provide information about the interactions in a molecule or complex. The points where gradient norm $\nabla\rho$ is zero (except at infinity) are called critical points (CPs). When electron density distribution ρ is high and Laplacian $\nabla^2\rho$ is negative at a bond critical point (BCP), the interaction is covalent. Metallophilic interactions have been identified as having a small ρ and a positive $\nabla^2\rho$. More recently, the ratio of the local electron potential energy density (V_c) to the kinetic energy density (G_c), $|V_c|/G_c$, was found to be a better descriptor or bonding.[82–84] When $|V_c|/G_c < 1$, the interactions between atoms are closed-shell

metallophilic interactions; when $|V_c|/G_c > 2$, they are covalent interactions; and when $1 < |V_c|/G_c < 2$, they can be categorised as being intermediate interactions.

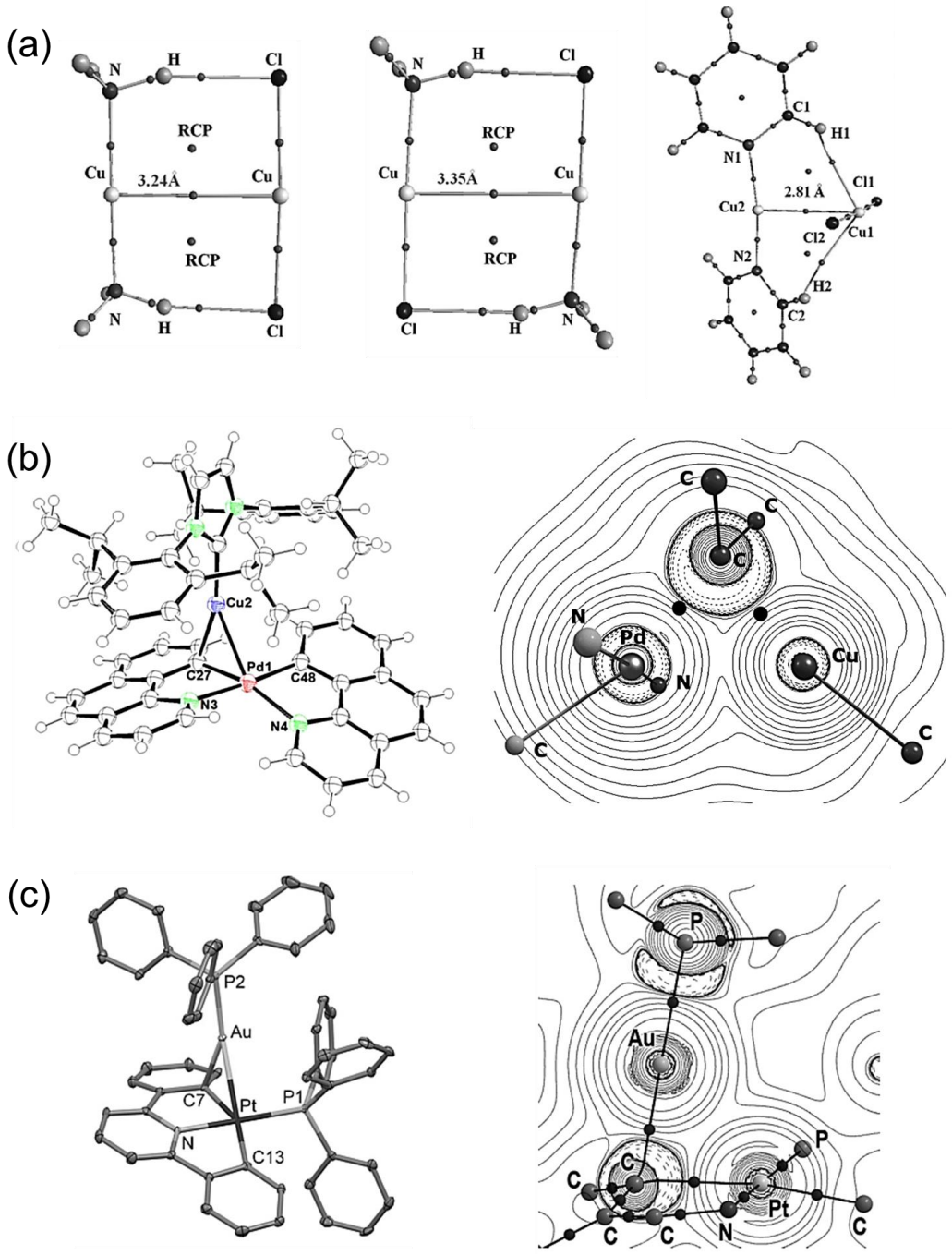

Figure 1.17 Complexes analysed by AIM. Bond critical points (black dots) have been found between Cu^{I} centres (a) but not observed in Pd^{II}–Cu^{I} (b) and Au^{I}–Pt^{II} (c). Reproduced from ref 43,58,85.

AIM has been used to study weak interactions such as hydrogen bonds,[86–88] metal–olefin complexes,[89] π–π interactions.[90] Metal–metal interactions have also been examined by AIM. For instance, Dinda and Samuelson[85] employed AIM to study Cu^{I}–Cu^{I} bonding in several dinuclear copper^{I} complexes (**Figure 1.17**). Their analysis showed that a bond critical point (BCP) between two Cu atoms was present in most cases. By examining the ratio, $|V_c|/G_c$, at the critical point suggested that these interactions had both ionic and covalent nature. However, the authors noted that bond critical points were not observed in some of the dinuclear copper^{I} complexes, indicating that AIM did not always work for studying metal–metal interactions. Similarly, no bond path and no BCP were found in complexes containing Pd^{II}–Cu^{I} and Pt^{II}–Au^{I} reported by other researchers.[43,58] These failed cases suggest further development of AIM-based methods is required for reliable analysis of metal–metal interactions.

1.4.1.3 Non-covalent interactions (NCI) analysis

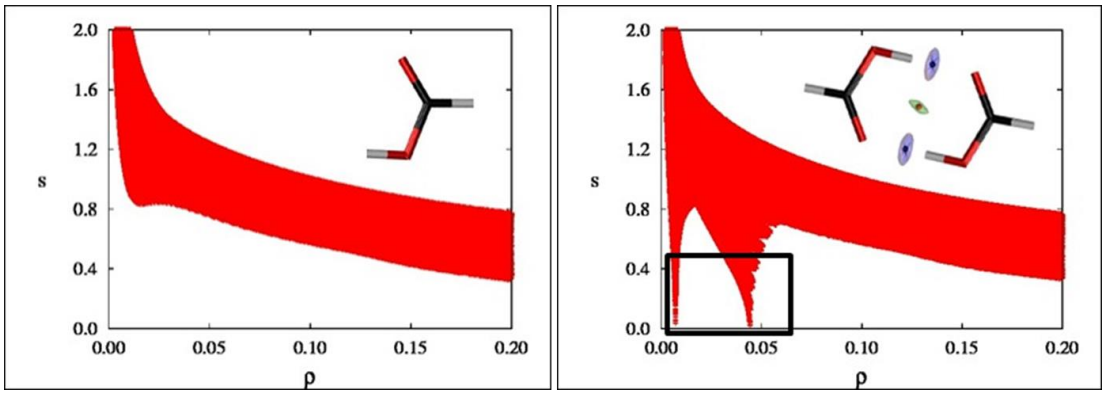

Figure 1.18 Plots of the reduced density gradients *s* versus the electron density *ρ* for the monomer (left) and dimer (right) of formic acid. Reproduced from ref 91.

Based on the electron density and its derivatives, Yang and co-workers developed the non-covalent interactions (NCI) analysis and program NCIPLOT to identify and visualise non-covalent interactions, such as van der Waals interactions, hydrogen bonds, and steric repulsion.[81,91] The NCI method is based on the relationship between the reduced density gradient *s* and the electron density *ρ*. Spikes in the low-density and low-gradient region appear in the plots of *s* versus *ρ*, which indicate the presence of

weak noncovalent interactions. For example, the main difference between the monomer and dimer of formic acid is the appearance of two such spikes in the plots of s versus ρ (**Figure 1.18**). These new peaks correspond to the non-covalent regions between two formic acid molecules.

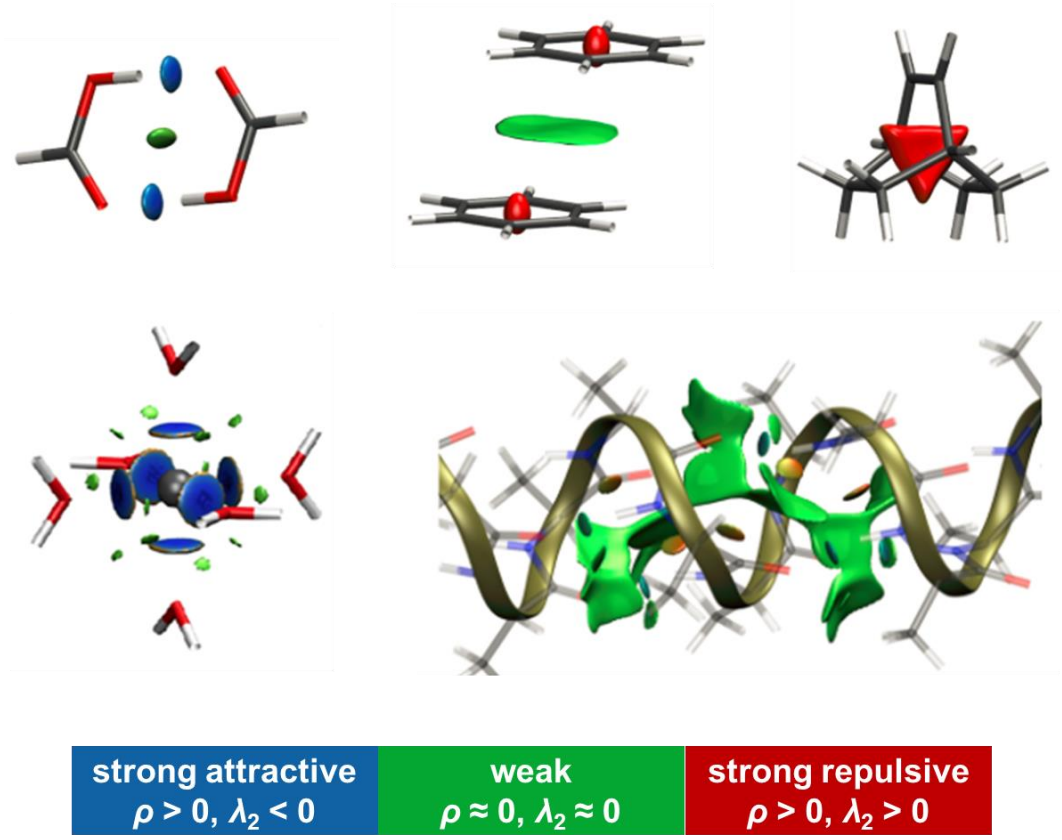

Figure 1.19 Selected examples analysed by NCI showing the presence of non-covalent interactions. Reproduced from ref 91.

However, the plots of s versus ρ cannot identify whether the weak interactions are attractive (e.g. hydrogen bonding) or repulsive (e.g. steric repulsion). To distinguish different interaction types, the second density Hessian eigenvalue λ_2 is introduced. The sign of λ_2 can be used to differentiate the bonded ($\lambda_2 < 0$) and non-bonded ($\lambda_2 > 0$) interactions. Hence, combining ρ and the sign of λ_2 together (sign(λ_2) ρ) gives both information of interaction type and strength. Some examples are listed in **Figure 1.19**. Blue areas represent strong attraction, red means strong repulsion, and weak interactions are denoted in green colour. NCI is computationally efficient, which

enable NCI plots to be employed not only in organic molecules, inorganic complexes and solids, but also in large biological systems (proteins or DNA).

NCI was first used to examine metallophilic interactions by Pinter, De Proft and co-workers.[92] The NCI analysis (**Figure 1.20**) clearly indicated the existence of metallophilic interactions between two metals in complexes [{(NHC)MCl}$_2$] (M = Cu, Ag, Au), which increased in strength from Cu to Ag to Au.

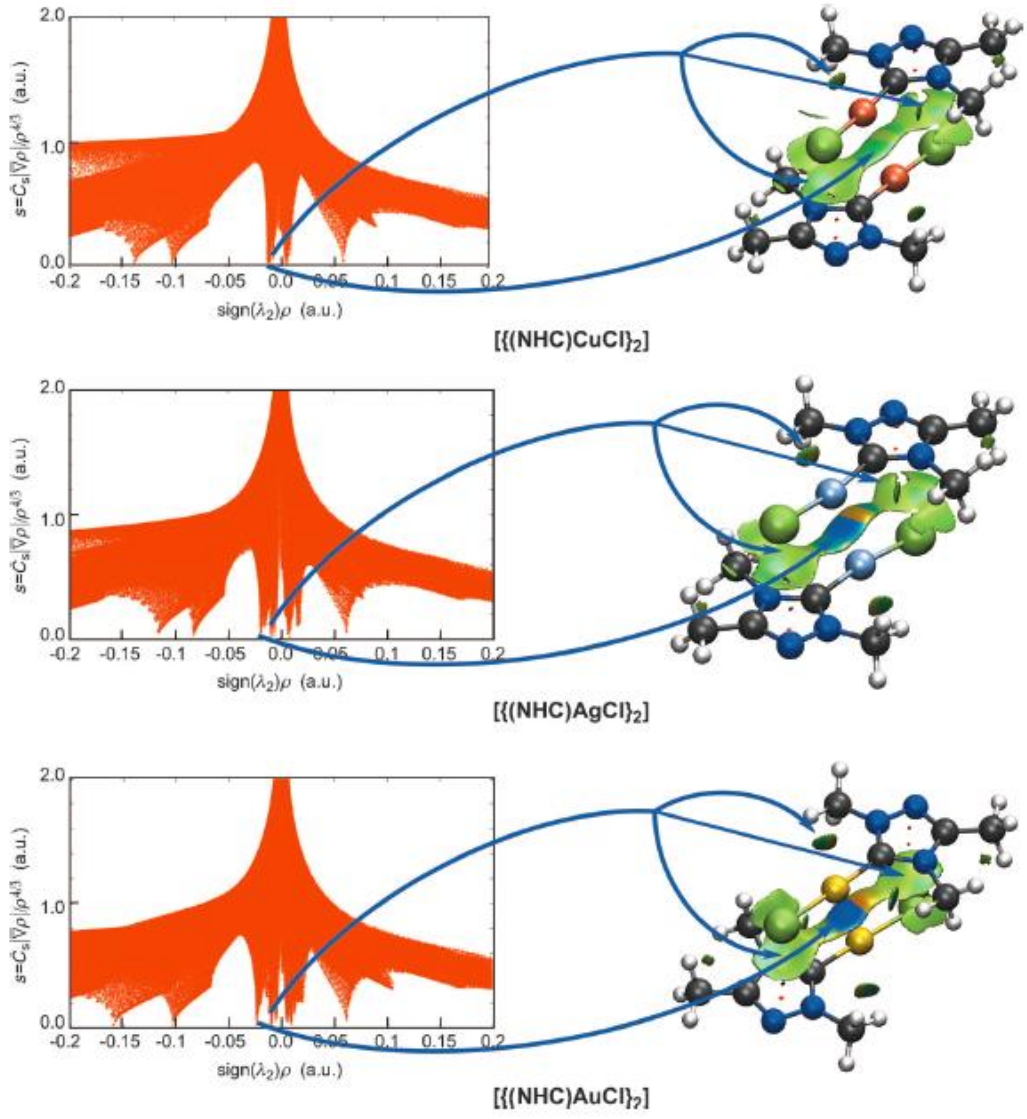

Figure 1.20 Plots of the reduced density gradient *s* versus the electron density *ρ* multiplied by the sign of the second Hessian eigenvalue λ_2 (left) and gradient isosurfaces with s = 0.5 a.u. (right) for [{(NHC)MCl}$_2$] (M= Cu, Ag, Au). Reproduced from ref 92.

1.4.2 Experimental methods

Many characterisation tools can be employed to identify the presence of metallophilic interactions in the solid state and in solution, including single-crystal X-ray diffraction, NMR spectroscopy, UV-vis spectroscopy, photoluminescence, mass spectrometry, Raman spectroscopy, extended X-ray absorption fine structure (EXAFS), small-angle X-ray scattering (SAXS) and so on.

1.4.2.1 Single-crystal X-ray diffraction

The presence of metallophilic interactions in the solid state has been judged mainly on the basis of short metal–metal distances (shorter than the sum of van der Waals radii). Single-crystal X-ray diffraction is thus a powerful and widely used method to assess metallophilic interactions. Thousands or more structures showing short metal–metal contacts can be found in the Cambridge Structural Database (CSD). There are also several reviews from Schmidbaur,[18,19,24,25] Yam,[32,33] Che,[97] and other groups[26] illustrating various crystal structures with metallophilic interactions. **Figure 1.21** provides some selected crystal structures ranging from single molecules to 3D assemblies, showing the presence of short Au–Au contacts.

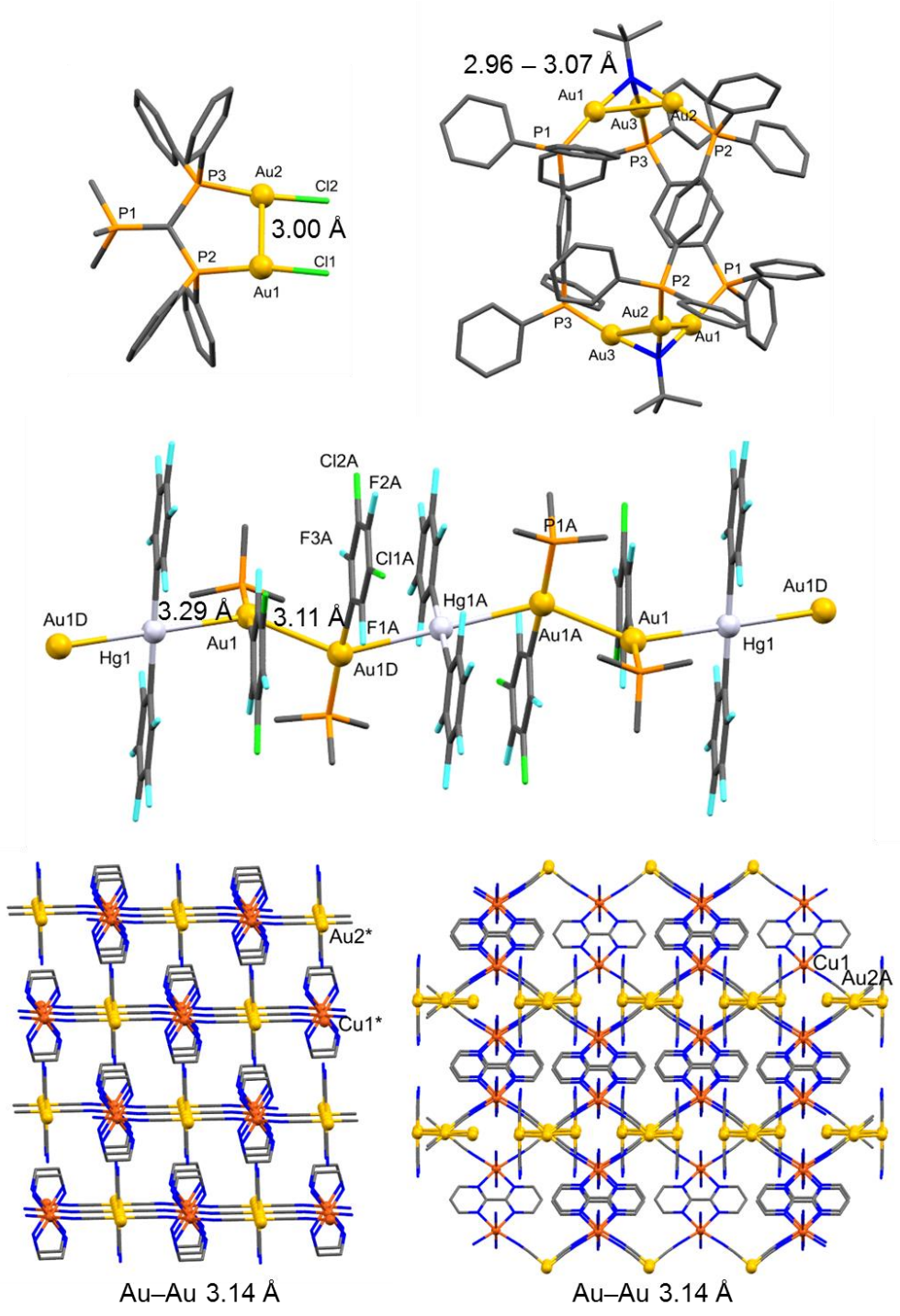

Figure 1.21 Selected literature structures constructed by metallophilic interactions ranging from single molecule to 3D network.[20,93–96]

1.4.2.2 UV-vis and photoluminescence spectroscopy

Several excellent reviews on the role of metallophilic interactions in the photophysical properties of metal complexes have been reported.[27,32,98] To understand why UV-vis and photoluminescence spectroscopy can be used for distinguishing metallophilic interactions, some basic knowledge of the photophysics of metal complexes should be introduced first.

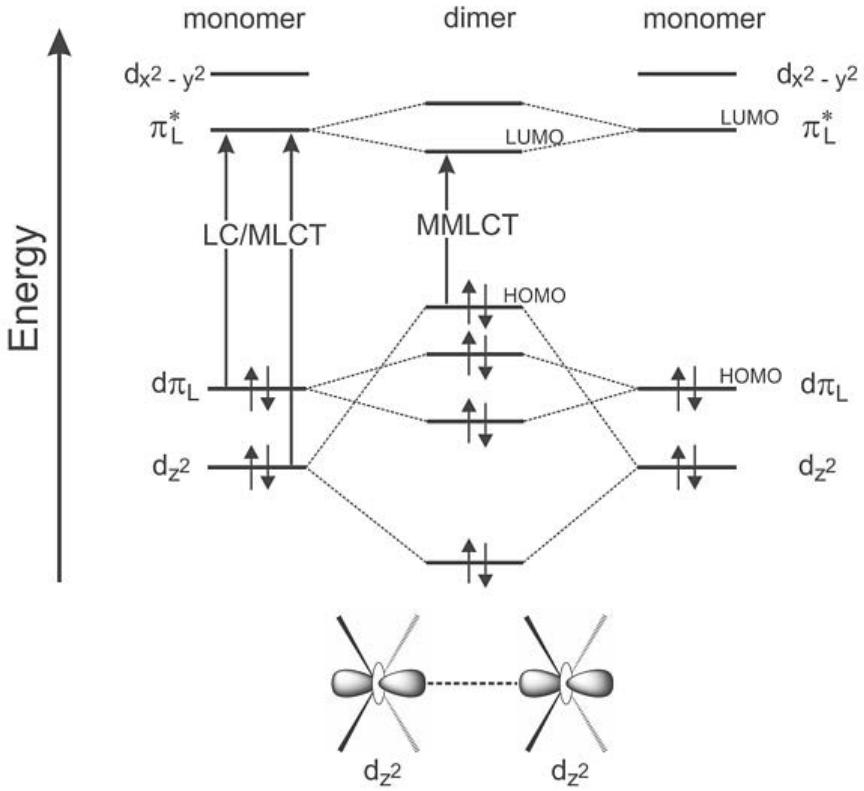

Figure 1.22 Simplified molecular orbital (MO) diagram of two interacting Pt^{II}-complexes and related LC, MLCT, and MMLCT transitions. Reproduced from ref 99.

The presence of metal centres in a complex induces orbital mixing between metal *nd* orbitals and ligand π orbitals. The electronic transitions between filled and empty orbitals yield ligand-centred (LC), metal-centred (MC), metal-to-ligand (MLCT), ligand-to-metal (LMCT), and ligand-to-ligand (LLCT) charge transfer (**Figure 1.22**). When two monomers are put into close contact (3.0-3.5 Å), which typically involves metal–metal (d_{z2}–d_{z2}) interactions and π–π stacking, orbitals from monomers can further hybridize with each other. The establishment of the metallophilic interactions (d_{z2}–d_{z2}) induces the possible metal–metal-to-ligand charge transfer (MMLCT). This

MMLCT is generally of lower energy, thus a long wave absorption or emission can be observed in UV-vis or photoluminescence spectra respectively.

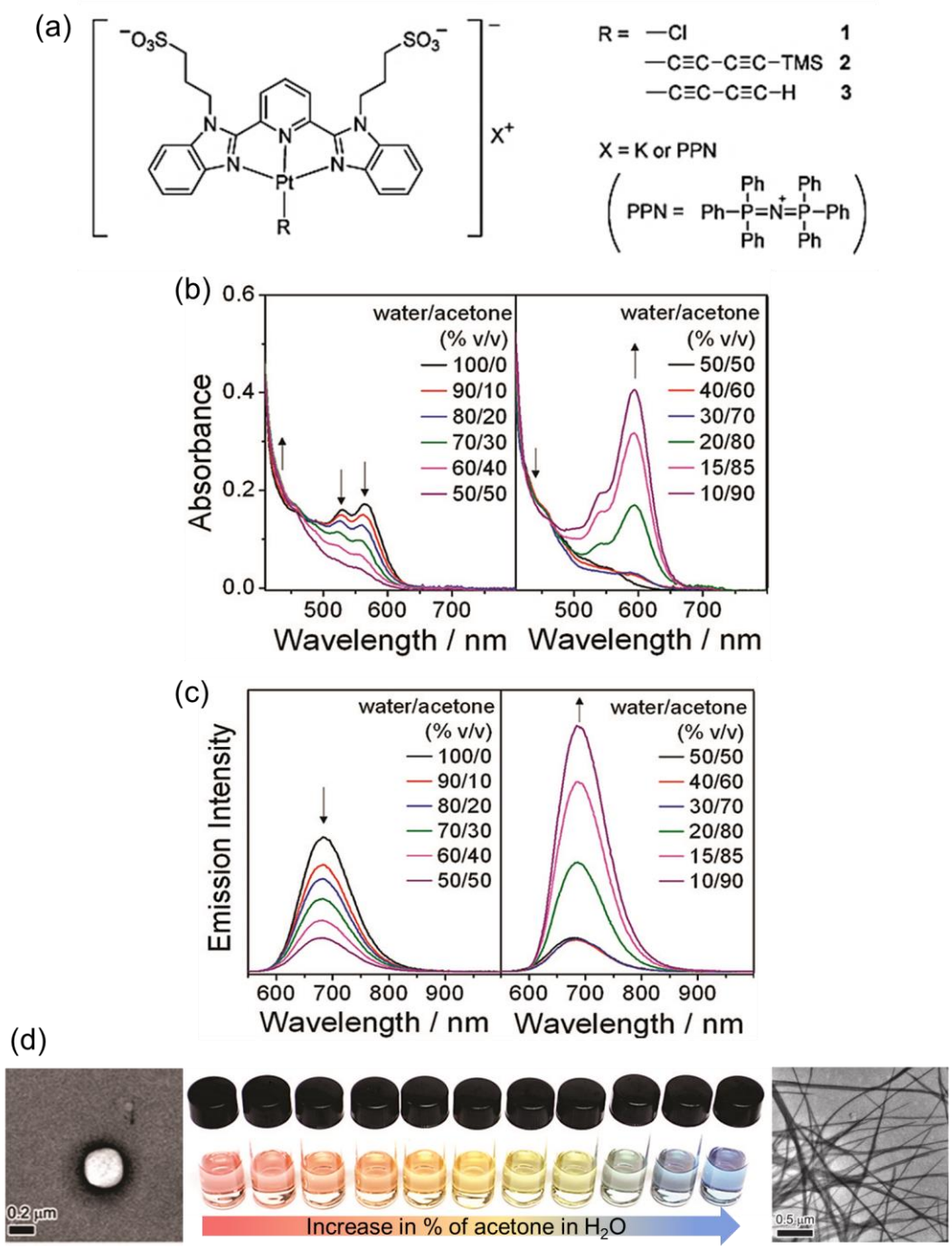

Figure 1.23 (a) Amphiphilic anionic Pt^{II}-complexes, and (b) UV-vis absorption spectra, (c) photoluminescence emission spectra, (d) visible colour change and morphology transformation of complex **1** in different acetone/water mixture. Reproduced from ref 28.

Yam *et al.*[28] prepared a series of amphiphilic anionic Pt^{II}-complexes (**Figure 1.23**) that could aggregate in water through Pt–Pt and π–π stacking interactions. These complexes showed intriguing solvatochromic changes and morphology transformation. For instance, the solution of complex **1**·K changed from red (100% water) to yellow (50% acetone/water) to blue (90% acetone/water). The MMLCT absorption bands at 532 and 564 nm in the UV-vis absorption decreased upon increasing the acetone content from 0% to 50%. Then from 50% to 90%, new absorption bands at 542 and 594 nm appeared and became stronger. The photoluminescence emission spectra gave consistent results. The emission band at 683 nm, which corresponded to ^{3}MMLCT, decreased in intensity upon increasing the percentage of acetone in water and a new band with slightly lower energy appeared. These results, combined with microscopy observations indicated that increasing the content of acetone in water resulted in these amphiphilic anionic Pt^{II} complexes undergoing initial aggregation into vesicles, followed by partial-disaggregation and reaggregation into nanofibers (**Figure 1.23**d).

1.4.2.3 NMR spectroscopy

As a basic and widely used characterisation method in chemistry, NMR spectroscopy provides a powerful tool for examining the presence of metallophilic interactions in solution. NMR spectroscopy can identify species in different chemical environments or with different sizes (by 2D DOSY). Hence, if the presence of metallophilic interactions induces a change in the chemical environment or size of the species, then NMR spectroscopy is potentially helpful.

There has been a reasonable number of reports of using NMR spectroscopy to prove the presence, or estimate the strength of metallophilic interactions.[20,21,69,100–102] For example, Finze *et al.*[100] prepared binuclear complexes $[(R_3PAu)_2CRCB_{11}H_{11}]$ (R = Me (**4**), Et (**5**)) shown in **Figure 1.24**. The complexes were dimers in the solid state with four intermolecular Au–Au contacts in the range 3.04–3.16 Å. The intramolecular Au–Au distances were 3.41 Å for **4** and 3.58 Å for **5**. ^{1}H DOSY NMR spectroscopy was employed to examine whether these complexes dissociated in DMSO-d_6, acetone-d_6, and CD_2Cl_2-d_2. The tetranuclear Au^I cluster $\mathbf{4_2}$ remained dimeric in solution while complex **5** kept a balance with its dimer $\mathbf{5_2}$. Upon increasing the temperature from 25 °C to 75 °C, $\mathbf{5_2}$ completely dissociated into monomer **5** while $\mathbf{4_2}$ were still dimeric.

In the variable-temperature ^{31}P NMR spectra of complex **4** at 80–100 °C, only one single peak corresponding to $\mathbf{4_2}$ was detected. For the VT-^{31}P NMR spectra of complex **5**, two signals were observed at low temperature. The peak at δ = 23.6 ppm was attributed to $\mathbf{5_2}$, whereas the signal at δ = 32.9 ppm was **5**. At higher temperature, the peaks became broader and merged into one peak at above 30 °C. Van't Hoff analysis using the intensities of the signals of **5** and $\mathbf{5_2}$ in the range of –50 to +30 °C were performed, yielding an association enthalpy of –37 ± 5 kJ mol^{-1} and a free energy of –12 ± 5 kJ mol^{-1} at 25 °C.

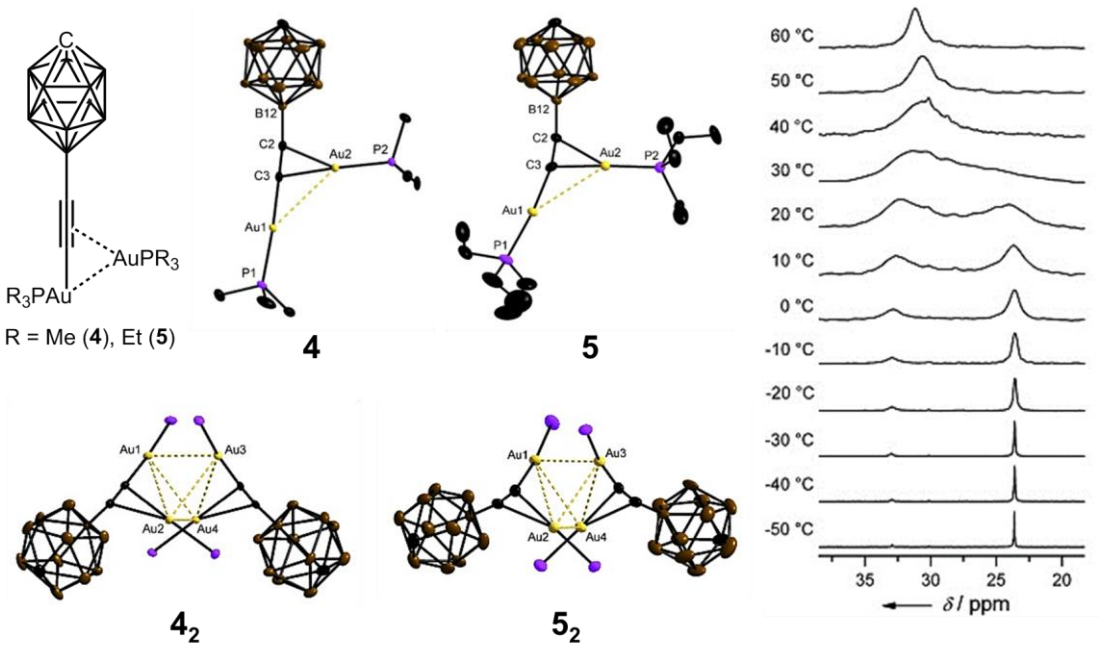

Figure 1.24 Structures of monomeric and dimeric complexes $[(R_3PAu)_2CRCB_{11}H_{11}]$ (R = Me (**4**), Et (**5**)), and temperature-dependent ^{31}P NMR spectra of complex **5** in THF-d_8. Reproduced from ref 100.

1.4.2.4 Mass spectrometry (MS)

Mass spectrometry (MS) is a simple and efficient method for characterising the mass and the states of complexes in solution. Low energy ionisation methods, such as ESI (Electrospray ionization) and FAB (Fast atom bombardment) are suggested to help maintain weak metallophilic interactions during the analysis. Diversi *et al.*[103] prepared a series of complexes $[Au_2(StBu)(L_2)][BF_4]$ (L = PMe_3, PEt_3, $PtBu_3$, PPh_3, dppm, dppe). These complexes adopted tetranuclear structures in the solid state, with four gold centres bound together by aurophilic interactions and bridging groups. MS (ESI)

was employed to study whether these complexes remained as tetranuclear structures or disassembled in solution (**Figure 1.25**). The results suggested that some of the complexes maintained tetranuclear structures in solution, which was confirmed by diffusion-ordered NMR spectroscopy (DOSY).

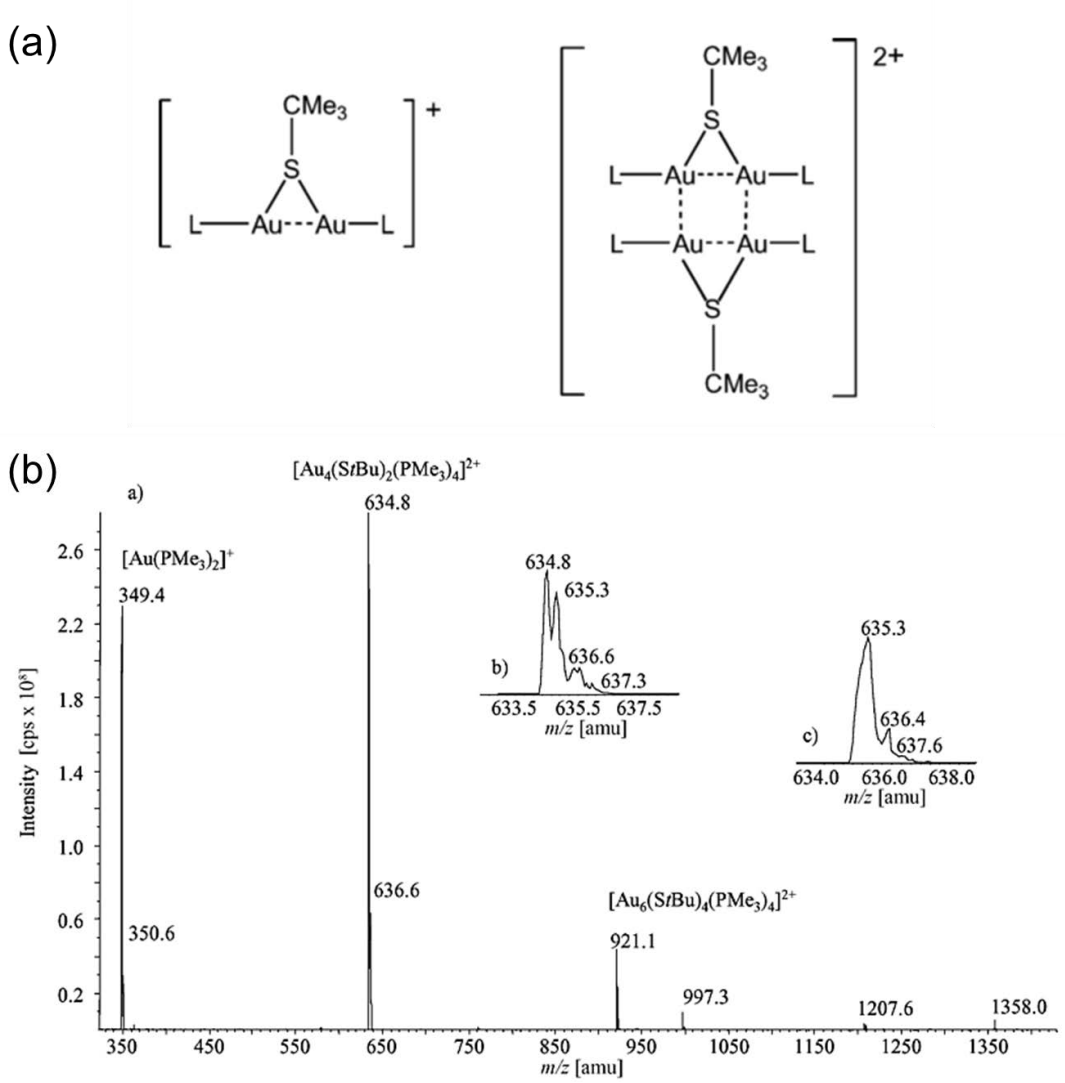

Figure 1.25 (a) Two proposed states for $Au_2(StBu)(L_2)][BF_4]$ in solution. (b) Mass spectrum for $Au_2(StBu)(PMe_3)_2][BF_4]$. Reproduced from ref 103.

1.4.2.5 Raman spectroscopy

Raman spectroscopy can also be used for charactering metallophilic interactions.[104,105] For instance, Che and co-workers[105] investigated Raman spectra of complex $[Au_2(dcpm)_2](ClO_4)_2$ (dcpm = bis-(dicyclohexylphosphine)methane). The obtained resonance Raman spectrum after intensity corrections and subtractions of the Rayleigh

line, glass bands, and solvent bands is shown in **Figure 1.26**. The band at 88 cm^{-1} was assigned to Au–Au stretch, which suggested the presence of aurophilic interactions. Other bands at –88, ± 176, 265, 350 cm^{-1} were attributed to Au–Au stretch overtones, which were reverse transition and transitions occurring over more than one vibrational level.

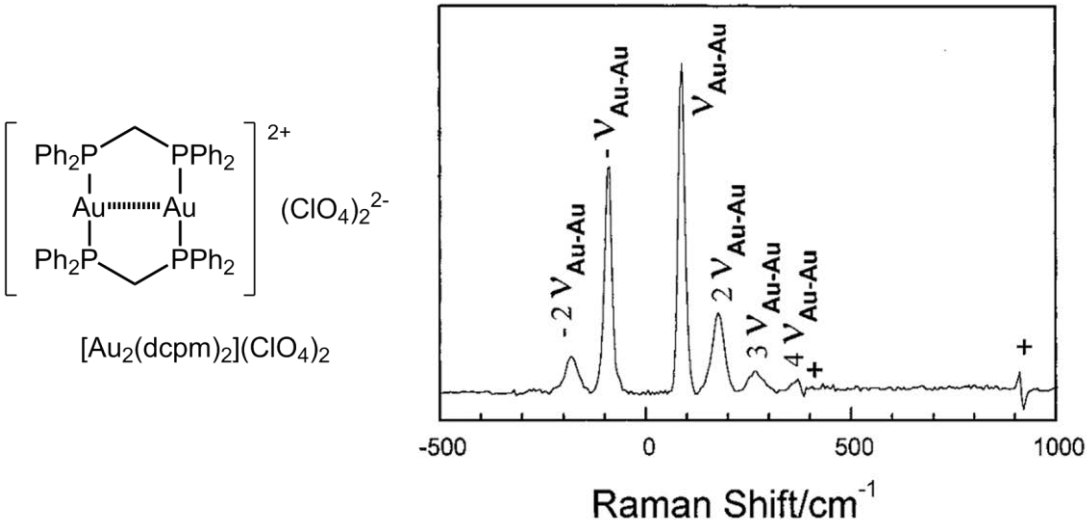

Figure 1.26 Complex $[Au_2(dcpm)_2](ClO_4)_2$ and corresponding resonance Raman spectrum excited at 282.4 nm in acetonitrile. Reproduced from ref 105.

1.4.2.6 Small-angle X-ray scattering (SAXS)

Small-angle X-ray scattering (SAXS) can supply information of the size, shape, and interactions of nanoparticles,[106] biomolecules,[107] clusters,[108] and so on in solution. This technique is capable of detecting nanoscale materials in the range of 1–150 nm in size. The strong scattering of heavy metal centres in metal complexes make SAXS a promising technique to detect metallophilic interactions, though it is very challenging to interpret data from small molecular species. Sanz Miguel, Nyman and other co-workers[109] supplied evidence of metallophilic interactions in solution by SAXS (**Figure 1.27**). The complexes $[Ag_2(bisMeOEtIm)_2](NO_3)_2$ and $[Ag_2(bisBuIm)_2](NO_3)_2$ adopted two switchable conformations *U* and *Z*. Conformer *U* readily aggregated in the presence of Ag–Ag interactions, which were supported by single-crystal structures. Whereas conformer Z was difficult to assemble due to the hinderance of the side arms. When decreasing concentration of the complex or adding $AgNO_3$, experimental SAXS data showed larger scattering attributed to larger sized

species. This was attributed to association of *U* conformers into dimers at lower concentration. Therefore, the presence of argentophilic interactions in solution was observed by SAXS at the molecular level.

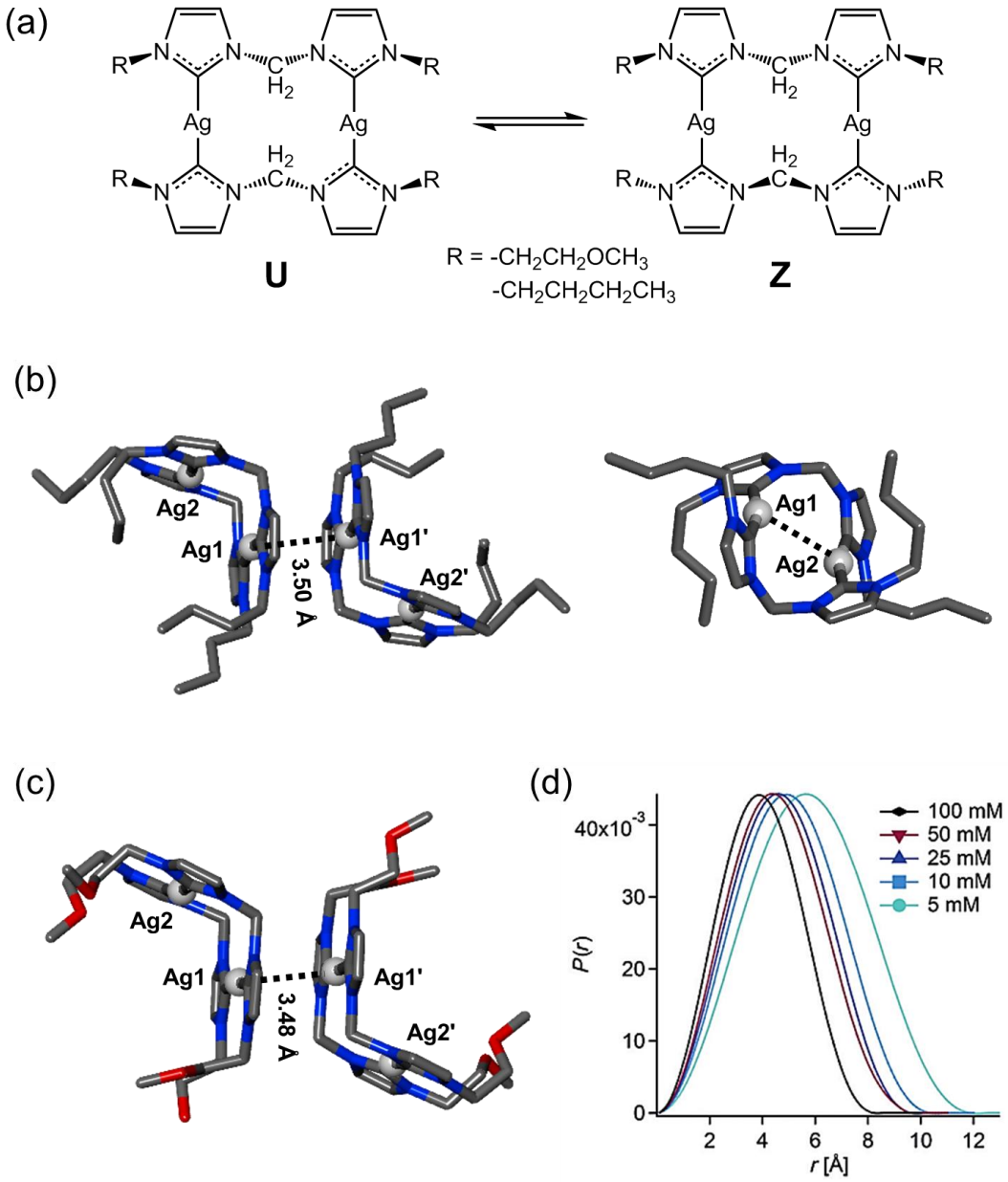

Figure 1.27 Equilibrium between the conformer U and conformer Z (a), corresponding crystal structures (b, c) of complexes $[Ag_2(bisMeOEtIm)_2](NO_3)_2$ and $[Ag_2(bisBuIm)_2](NO_3)_2$.[109] Intensity-normalized pair distance distribution functions (PDDF) showing the size of species in solution of $[Ag_2(bisMeOEtIm)_2](NO_3)_2$ in acetonitrile at different concentrations.

1.4.2.7 Extended X-ray absorption fine structure (EXAFS)

X-ray absorption fine-structure (XAFS)[110,111] arises from the modulation of the X-ray absorption coefficient at energies near and above an X-ray absorption edge. Unlike X-ray diffraction, XAFS can analyse non-crystalline materials, including liquid and frozen solutions. XAFS is typically divided into two regimes: X-ray absorption near-edge spectroscopy (XANES) and extended X-ray absorption fine-structure spectroscopy (EXAFS). XANES is strongly sensitive to formal oxidation state and coordination chemistry (e.g., octahedral, tetrahedral coordination) of the absorbing atom, while the EXAFS is used to determine the distances, coordination number, and species of the neighbours of the absorbing atom. Therefore, EXAFS can be utilised to measure metal–metal distances, and thus examine the presence, or not, of metallophilic interactions in solution.

Several papers have employed EXAFS to investigate metallophilic interactions.[68,112,113] Lagunas *et al.*[68] collected EXAFS spectra for fully-supported, semi-supported and unsupported complexes (**Figure 1.28**) in the solid state and in solution. For fully-supported complexes $[Au_2(dppm)_2Cl_2]$, $[Au_2(dppm)_2][BF_4]_2$ and semi-supported complex $[\{Au(SC_6H_4Me\text{-}3)\}_2](\mu\text{-dpephos})]$, the Au–Au contacts both in the solid state and in solution were successfully extracted from EXAFS spectra and showed good agreement with the crystallographic data. Hence, EXAFS was a promising method for determining metallophilic interactions in solution. However, EXAFS also had its limitations. For instance, Au–Au distances in solution for a semi-supported complex $[(AuCl)_2(\mu\text{-xantphos})]$ and unsupported complex $[Au_2(SPh)_2(PPh_3)_2]$ could not be modelled with confidence. In addition, some metal complexes might not be very stable under X-ray irradiation in solution.

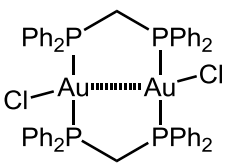

$[Au_2(dppm)_2Cl_2]$

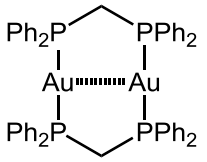

$[Au_2(dppm)_2][BF_4]_2$

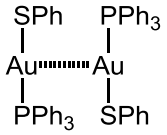

$[Au_2(SPh)_2(PPh_3)_2]$

Solid:	2.93	2.90	3.08
Solution:	3.08	2.97	-
Crystallography:	2.99	2.93	3.15

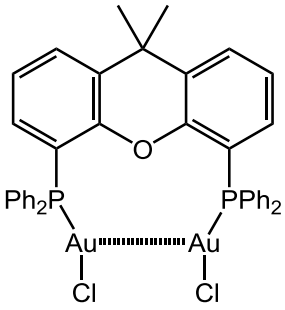

$[(AuCl)_2(\mu\text{-xantphos})]$

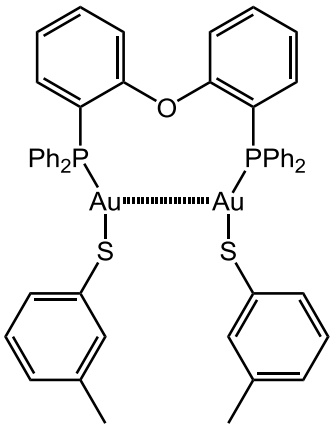

$[\{Au(SC_6H_4Me\text{-}3)\}_2](\mu\text{-dpephos})]$

Solid:	2.99	3.01
Solution:	-	2.89
Crystallography:	2.99	3.01

Figure 1.28 Complexes used for EXAFS study, Au−Au distances extracted from EXAFS in the solid state and in solution, and Au−Au distances (in Å) obtained from crystal structures.[68]

1.5 The strength of metallophilic interactions

1.5.1 Computational estimation of metallophilic interactions

A considerable number of computational methods, including dissociation energy calculation, LMP2 partitioning,[23,114] and energy decomposition analysis (EDA),[115,116] have been reported to quantitively determine the strength of metallophilic interactions.

1.5.1.1 Dissociation energy

Early estimations of the strength of metallophilic interactions approximated the strength as being equal to the sum-total of the intermolecular interactions between two complexes. Some selected examples employed for assessing the strength of

metallophilic interactions are given in **Figure 1.29**. Pinter and De Proft[92] assessed the strength of aurophilic interactions in anti-parallel $[(NHC)AuCl]_2$ dimer to be 18.4 kJ mol^{-1} by MP2 computations. The same dimer was estimated by Ghosh[117] using DFT and gave a strength of 36.0 kJ mol^{-1}. Omary *et al.*[118] evaluated the aurophilicity to be 41.8 kJ mol^{-1} by MP2 in anti-parallel dimer $[ClAu(CO)]_2$.

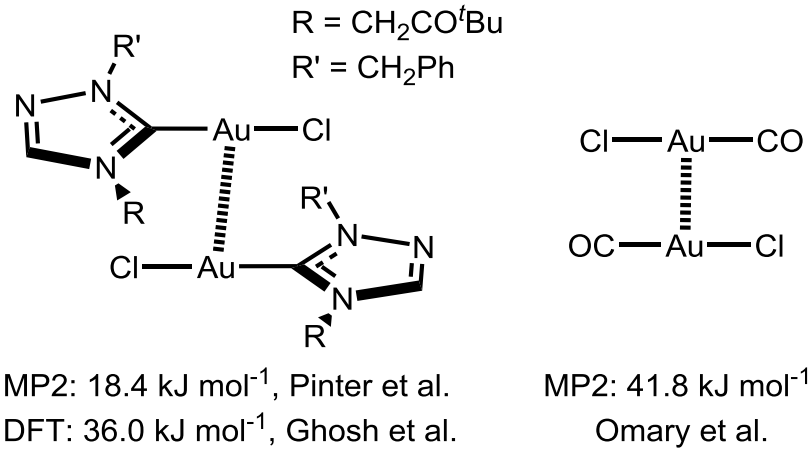

Figure 1.29 Dimeric complexes employed for investigating the strength of metallophilic interactions by MP2 or DFT.[92,117,118]

1.5.1.2 Local correlation method

Werner and co-workers have developed an energy partitioning method to study metallophilic interactions by local second-order Møller-Plesset perturbation theory (LMP2).[23,119] Compared to the traditional MP2 approach, LMP2 is less computationally expensive, and its basis set superposition error (BSSE; a potentially very significant problem in theoretical studies of metallophilicity) is much reduced.

A comparison study of metallophilic attraction in $(X–M–PH_3)_2$ (M = Cu, Ag, Au; X = H, Cl) dimers has been performed by Werner, Stoll and co-workers using local MP2 calculations (LMP2).[120] As illustrated in **Figure 1.30**, attractions between $X–M–PH_3$ (X = H, Cl) monomers decreased from M = Au *via* Ag to Cu, with the reductions of 10–20% and 25–35%, respectively. Energy partitioning analysis of the intermolecular interaction showed dispersive and non-dispersive components were of similar importance. The contribution of M–M interactions significantly decreased from Au (43%) to Ag (30%) and Cu (18%). The authors acknowledged that MP2 was known

for overestimating van der Waals interactions, which made their results for the interaction energies too large by between 0 and 25%.

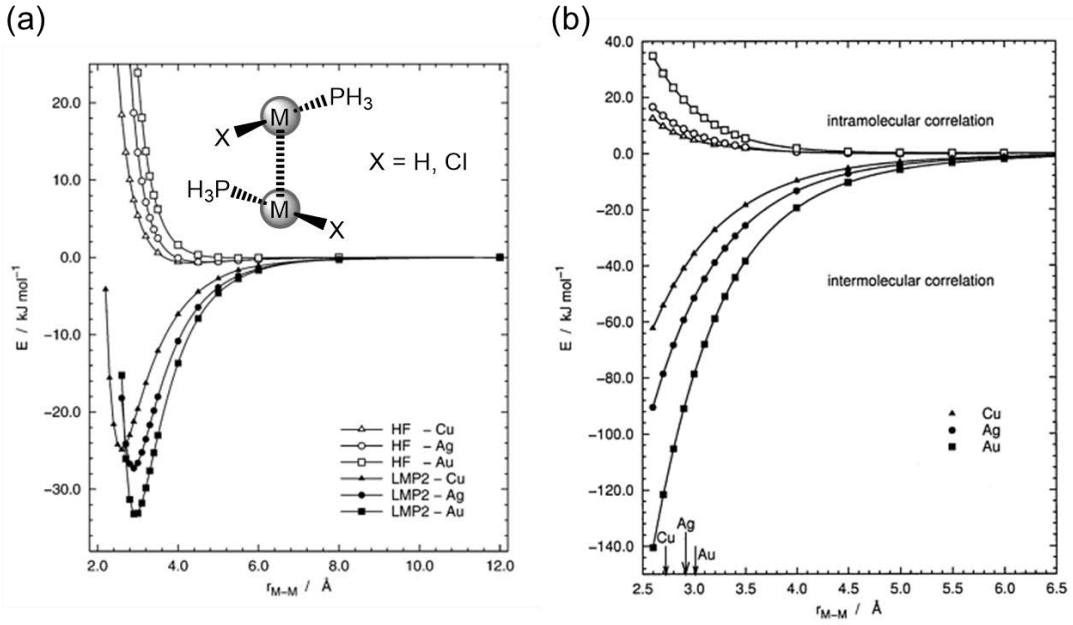

Figure 1.30 SCF and LMP2 intermolecular interaction energies (a) and inter- and intramolecular correlation contributions to the LMP2 interaction energy (b) of the H–M–PH_3 dimer. Reproduced from ref 120.

1.5.1.3 Energy decomposition analysis (EDA)

The energy decomposition analysis (EDA) developed by Morokuma[121] and by Ziegler and Rauk[122,123] is a powerful tool to estimate the bonding energy between two fragments A and B in a molecule A–B. Useful introductions to the EDA method have been written by Frenking and collaborators.[115,124] The EDA considers the formation of a molecule A–B with the corresponding wavefunction Ψ_{AB} and energy E_{AB} as the result of the interactions between fragments A and B with energies E_A and E_B.

The overall bond dissociation energy is calculated from:

$$\Delta E = \Delta E_{\text{prep}} + \Delta E_{\text{int}}$$

where ΔE is the bond dissociation energy to form the bond, ΔE_{prep} is the energy needed to make the relaxed free fragments change their geometries to the states in the bonded molecule. ΔE_{int} is the interaction energy between the fragments.

The interaction energy ΔE_{int} can be further decomposed into 4 terms:

$$\Delta E_{int} = \Delta E_{elstat} + \Delta E_{Pauli} + \Delta E_{orb} + \Delta E_{disp}$$

where ΔE_{elstat} is electrostatic attraction, ΔE_{Pauli} is Pauli repulsion which is the origin of steric effects, ΔE_{disp} is dispersion interactions. ΔE_{orb} is orbital interactions which describes charge transfer (donor–acceptor interactions between occupied orbitals on one moiety with unoccupied orbitals of the other, including the HOMO–LUMO interactions) and polarization (empty/occupied orbital mixing on one fragment due to the presence of another fragment). EDA combined with the natural orbitals for chemical valence (EDA-NOCV) can further decompose ΔE_{orb} into contributions of orbitals with different symmetry, which makes it possible to distinguish between σ, π, and δ bonding. The number of significant contributions from pairwise orbitals is usually small (< 5) so that specific interactions can easily be identified.

Pinter and De Proft[92] also utilised EDA-NOCV to qualitatively and quantitatively study the nature of metallophilic interactions. The electrostatic attraction was found to be the dominant contribution (61–62%), though contributions from orbital interactions (22%) and dispersion interactions (16–17%) were also important. Among the NOCV orbitals, two most significant NOCV orbitals were found. The first dominant NOCV−1 orbital revealed depletion of the electron density between the monomers and accumulation on the exterior side of the dimer. The second NOCV orbital (NOCV−2) clearly showed an accumulation of electron density between two metal centres, supporting the formation of metallophilic interactions. Moreover, the metallophilic interactions in the [{(NHC)AgX}$_2$] (X=F, Cl, Br, I) were found to become stronger along the sequence F < Cl < Br < I, suggesting metallophilic interactions could be modulated by varying the halogen connected to the metal.

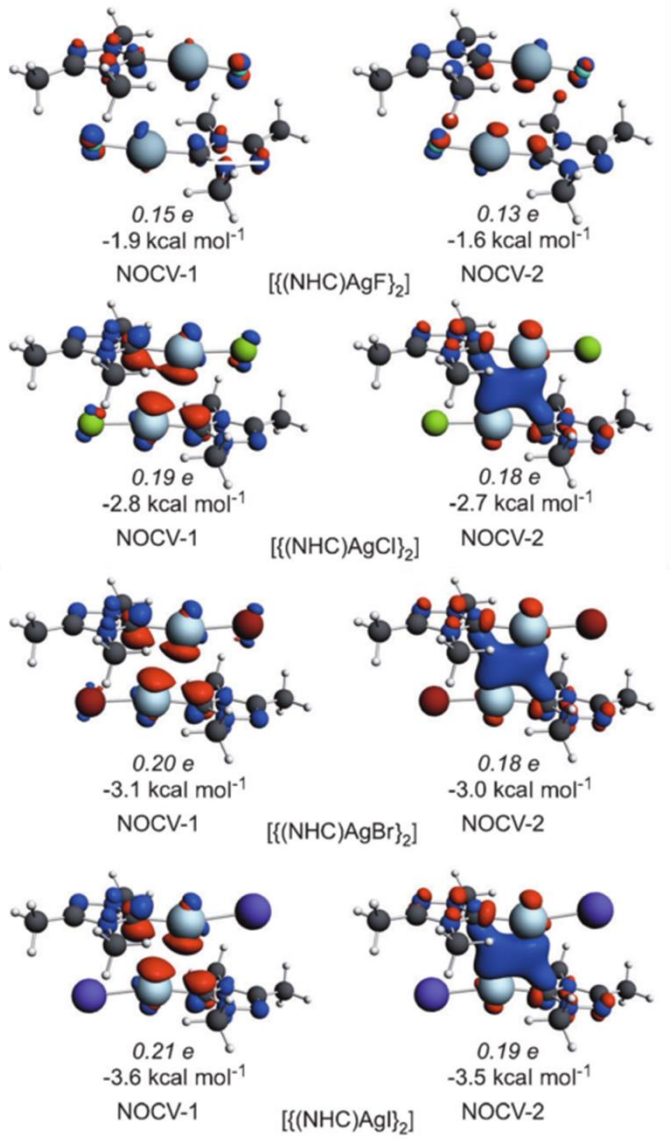

Figure 1.31 NOCV orbitals with the corresponding density change and associated energies for [{(NHC)AgX}$_2$](X=F, Cl, Br, I). Reproduced from ref 92.

Recently, Chen *et al.*[48] reported a computational study of the metallophilic interactions in series of Pd^{II}–Cu^{I} and Pd^{II}–Zn^{II} heterometallic complexes. Taking the Pd^{II}–Zn^{II} series as an example (**Figure 1.32**), EDA results demonstrated that dispersion contributed less than electrostatic and orbital interactions. ETS-NOCV analysis further illustrated that the orbital interactions between metal atoms played a significant or dominant role to the overall interactions.

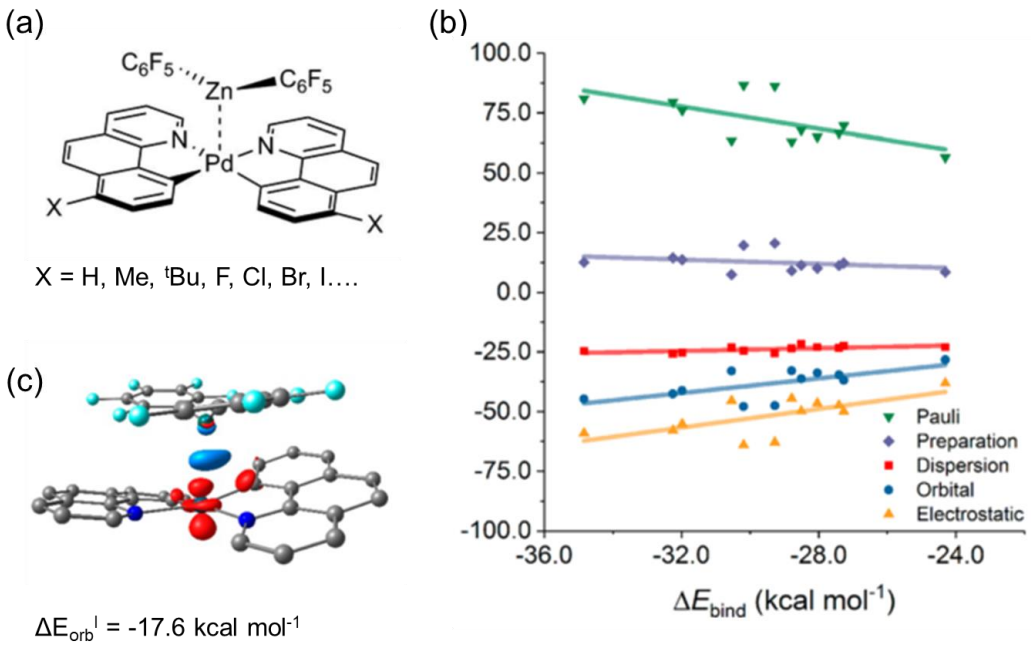

Figure 1.32 Pd^{II}–Zn^{II} heterometallic complexes (a), plots of the respective contributions to the total binding energy generated from EDA (b), and deformation densities for an example compound (c). Red: areas of charge depletion, blue: areas of charge accumulation. Reproduced from ref 48.

Other energy decomposition methods, such as symmetry-adapted perturbation theory (SAPT),[125] charge decomposition analysis (CDA),[126] the energy partitioning scheme of Ram and Hoffmann,[127,128] also provide powerful tools for dissecting non-covalent interactions. However, their application to metallophilic interactions has yet to be reported, which may be due to the challenge of dealing with heavy metal centres. However, with the development of the computational theories, these methods are promising tools for future estimation of metallophilic interactions.

1.5.2 Experimental measurement of metallophilic interactions

Experimentally derived estimations of the strength of metallophilic interactions are very limited. Even for the most widely studied aurophilic (Au–Au) interactions, only a few studies have been reported. Evaluating the strength of metallophilic interactions is apparently of great importance. By knowing how strong the interactions are, we can use metallophilic interactions to design and construct various intriguing structures, to explain their role in photoluminescence, catalysis etc. Several methods have been

reported on how to estimate the strength of metallophilic interactions. These methods include using molecular balances, supramolecular aggregation, ligand-exchange and so on.

1.5.2.1 Molecular balances / conformational equilibria

Some flexible complexes exhibit equilibria between two (or more) conformational states due to the possibility of rotation about a single bond. These complexes are commonly referred as molecular torsion balances. A tutorial review presenting the usage of molecular torsion balances for estimating non-covalent interactions has been given by Cockroft and Mati.[129] As a type of non-covalent interaction, metallophilic interactions have also been estimated by molecular torsion balances utilising conformational equilibria.

Schmidbaur[20,21] synthesised doubly phosphino-substituted ylides (**Figure 1.33**), which changed their ground state *syn/anti* orientation to a symmetrical *syn/syn* conformation upon double complexation with -AuCl. The short Au−Au distance of only around 3.0 Å, bending of Au in P-Au-Cl axis towards to another Au, and the smaller P-C-P angle in the crystal structure of the gold complexes, strongly suggest the existence of attractive aurophilic interactions. Variable temperature ^{31}P NMR spectroscopy showed two PPh_2 groups are equivalent, which suggested the complex only adopted a folded structure in solution. Therefore, this complex could not be used as a molecular balance to estimate aurophilic interactions. However, as the rotation energy barrier of pure ligands ($\Delta G_{barrier}$ = 40 kJ mol^{-1}) was known, the authors simply took an approximated value of 29 – 33 kJ mol^{-1} as the strength of aurophilic interactions. The energy of this interaction was also assessed to be in the order of 29 kJ mol^{-1} in their follow-up report,[20] based on changes in the conformation of the butadiene skeleton. This estimation, however, is incorrect. As can be seen in from **Figure 1.33**c and **Figure 1.33**d, the rotation energy barrier of the ligand is a separate energetic process compared to the strength of aurophilic interactions.

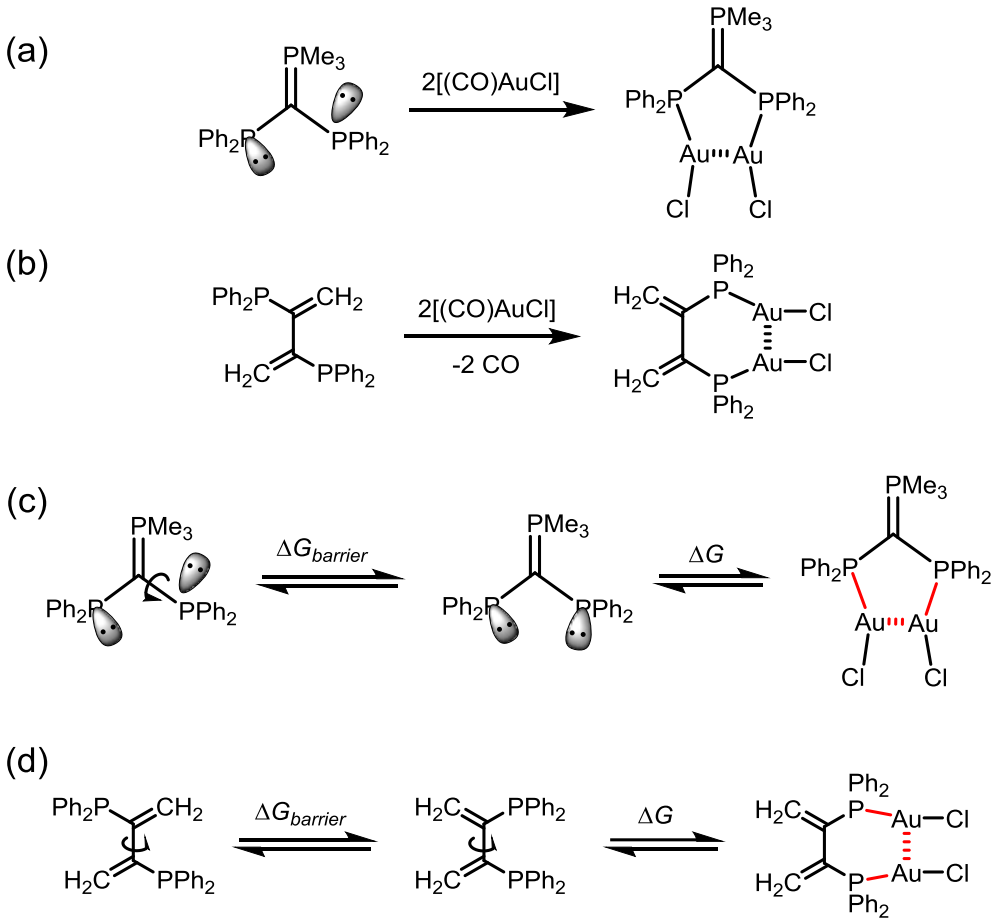

Figure 1.33 Schmidbaur's Au^{I}-complexes yielded from phosphino-substituted ylides (a) and butadiene (b), showing the presence of attractive aurophilic interactions.[20,21] Equilibria between ligands and the corresponding Au^{I} complexes (c,d), illustrating the rotation energy barrier $\Delta G_{barrier}$ is very different from the strength of Au–Au interactions. The red solid and dash lines represent new bonding formed after complexation of Au^{I}.

Similarly, Hawthorne *et al.*[102] synthesised an auracarborane 1,1′-$(AuPPh_3)_2$-[2-(1′,2′-$C_2B_{10}H_{10}$)-1,2-$C_2B_{10}H_{10}$], which had *syn* and *anti*-conformers. Crystallography showed a short Au−Au distance of 3.119(2) Å, which indicated the existence of aurophilic interactions. Variable-temperature ^{31}P NMR spectra demonstrated two peaks below 280 K, suggesting a dynamic equilibrium between the *syn* and *anti*-conformers of the complex. The authors believed it was justified to overlook the electrostatic interactions and steric effects associated with the two bulky PPh_3 groups and regarded the energy barrier of *syn* form to transition state (46 kJ mol^{-1}) as the strength of aurophilic interactions.

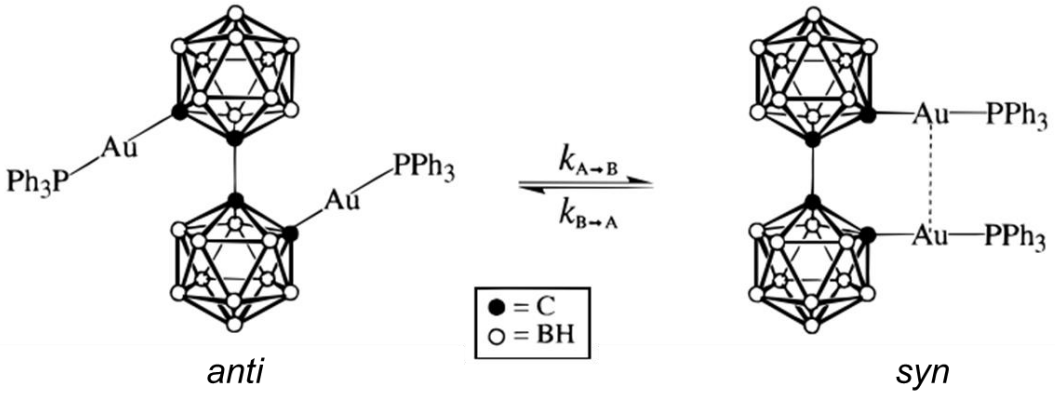

Figure 1.34 Auracarborane molecular balance used by Hawthorne *et al.* to estimate the strength of aurophilic interactions.[102]

1.5.2.2 Supramolecular aggregation

Lima *et al.*[69] studied the aggregation of two complexes [Au(4-pyridylethynyl)(phosph)] (phosph = 1,3,5-triaza-7-phosphaadamantane (**6**) and 3,7-diacetyl-1,3,7-triaza-5-phosphabicyclo[3.3.1]nonane (**7**)) through absorption spectra and ^{1}H NMR spectroscopy (**Figure 1.35**). The appearance of new absorption bands at around 375 nm for complex **6** and 340 nm for complex **7** suggested the presence of aggregates. These bands could be attributed to the presence of aurophilic interactions ($\sigma^{*}_{Au-Au} - \pi^{*}$ transition). Variable-temperature and variable-concentration ^{1}H NMR spectra indicated complex **7** aggregated faster than complex **6**. The aggregation constants were retrieved using an isodesmic model. The aggregation energies were thus calculated to be around –20 kJ mol^{-1}. Relativistic density functional theory computations were carried out to find out the possible aggregation mode. The computed Gibbs free energies were in the order of the experimental values. Moreover, the calculated free energy of complex **7** was smaller than that of complex **6**, which was also consistent with the experimental result.

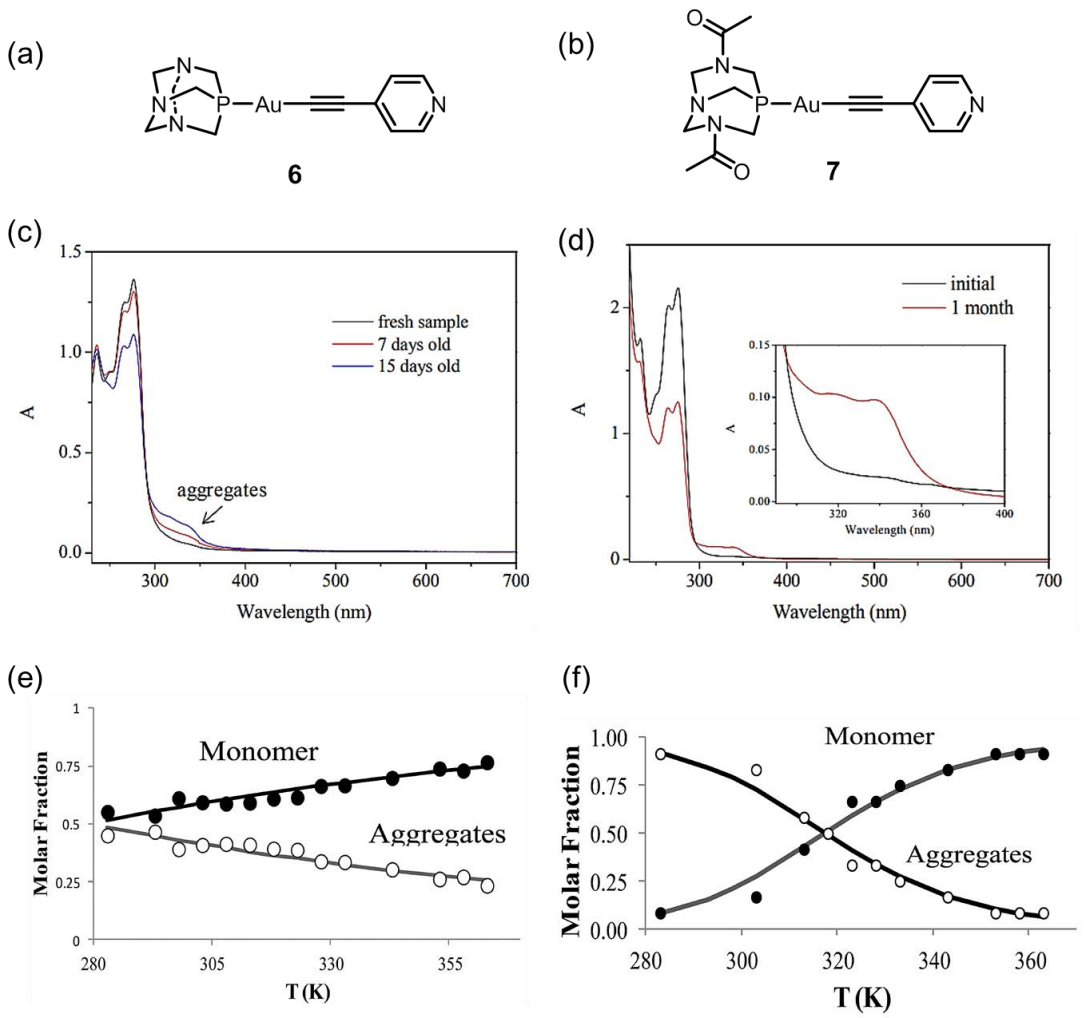

Figure 1.35 Complexes **6** (a), **7** (b), corresponding UV-vis spectra (c, d), and aggregation change obtained from variable-temperature ^{1}H NMR spectra (e, f). Closed circles − molar fractions of the monomer; open circles − molar fraction of aggregates; solid lines − fitting of the molar fractions with isodesmic model. Reproduced from ref 69.

1.5.2.3 Collision induced dissociation

Collision-induced dissociation (CID) is a mass spectrometry technique to induce fragmentation of molecular ions in the gas phase. This method has been used by Chen to study transmetalation reactions involving metal–metal bonds/interactions.[43–46] For example, a bimetallic Pd/Cu complex $[(bhq)_2Pd^{II}{\cdot}Cu^{I}(IPr)]^{+}$ (**Figure 1.36**a) with a short Pd–Cu distance of 2.55 Å was prepared. The identity of the complex was confirmed by the *m*/*z* ratio and its isotope pattern in mass spectrum (**Figure 1.36**b). Upon CID measurement, a single product $[IPr]Cu^{+}$ was generated. In an energy-resolved CID cross section experiment, reactant and product ion intensities were

recorded at different CID gas (Xe) pressures (20 to 110 μTorr) as a function of the collision offset, extrapolated to zero pressure, and subsequently fit with the L-CID program[130] (**Figure 1.36**c). The activation energy was determined to be 213 kJ mol^{-1}. As a comparison, an activation energy of 176 kJ mol^{-1} from the control complex (**Figure 1.36**d) was also obtained. The energy difference of 38 kJ mol^{-1} was approximately the strength of Pd^{II}–Cu^{I} bonding.

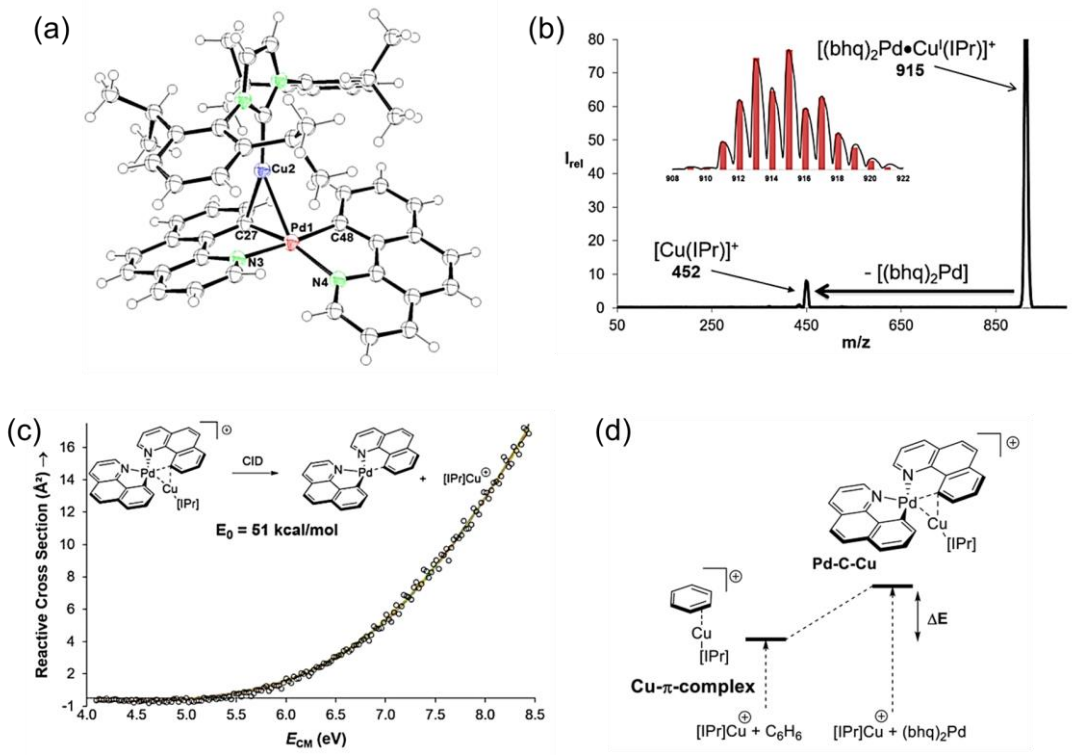

Figure 1.36 Single crystal structure (a), mass spectrum unpon CID (b), and zero-pressure-extrapolated cross sections (circles) with L-CID-fitted curves (lines) of complex $[(bhq)_2Pd^{II}\cdot Cu^{I}(IPr)]^+$ (c). Model system with control complex Cu-π-complex to single the energy difference caused by Pd–Cu interactions (d). Reproduced from ref 43.

Rulí ek, Roithova and other co-operators[131] have recently examined the strength of aurophilic interactions by combing experimental CID measurements and computational studies together. They firstly measured the binding energies of a series of cationic dimers $[(LH)AuCl]^+$...[(L')AuCl] (**Figure 1.37**) by CID experiments. The experimental binding energies were determined and used as benchmarks for correlated quantum chemical calculations (CCSD(T)-calibrated SCS-MP2/CBS method). The overall attractive interactions were 100−165 kJ mol^{-1} in the charged dimers and

70−105 kJ mol^{-1} in the corresponding neutral dimers [(LH)AuCl]...[(L')AuCl]. The strength of aurophilic interactions was singled out to be 20−30 kJ mol^{-1}, accounting for 30% of the overall interaction energy in the neutral dimers. The energy of the aurophilic interactions is thus comparable or even larger than that of strong hydrogen bonds.

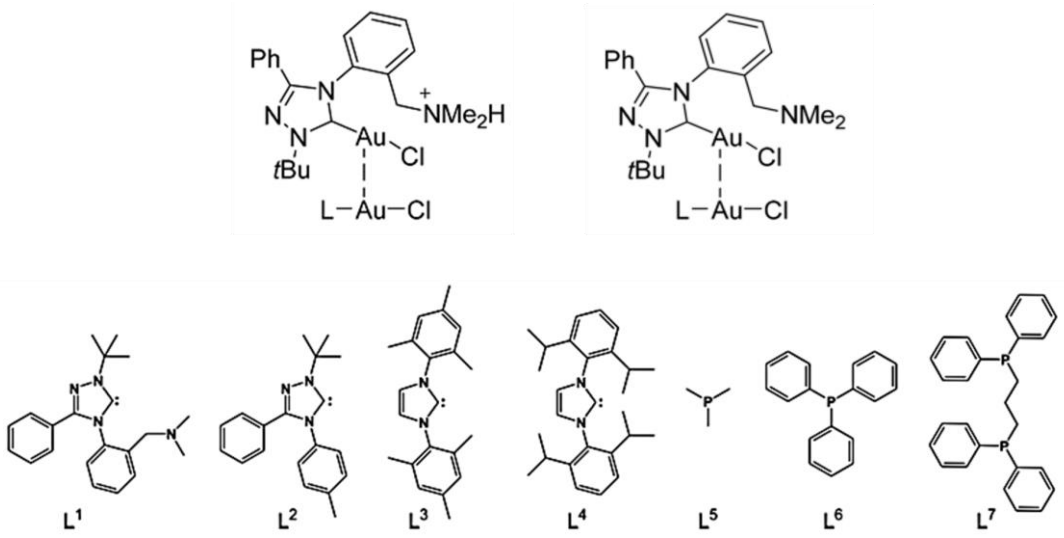

Figure 1.37 Complexes used for calibration of the strength of aurophilic interactions. Reproduced from ref 131.

1.5.2.4 Ligand-exchange

Ligand-exchange is widely employed in supramolecular chemistry to prepare interesting structures and adjust material properties.[132] By proper design, this strategy can also be employed to estimate non-covalent interactions.

Gschwind[133] reported the first method for quantifying noncovalent ligand–ligand interactions in transition-metal complexes (**Figure 1.38**). Chiral ligands A, A* (enantiomer of A) and B could form complexes ML_2X_n (M = transition metal, L= chiral ligand A/A*, X= achiral ligand). Two equilibria of generating heterocomplexes ($MABX_n$ and MA^*BX_n) from two homocomplexes (MA_2X_n / $MA^*_2X_n$, MB_2X_n) could be formed. The free energy $\Delta G°$ of each equilibrium could be determined from the complex integrals using equation $\Delta G° = -RT\ln K$. As homocomplexes MA_2X_n and $MA^*_2X_n$ were enantiomeric, their energies were the same. The energy difference between the systems was thus caused by the energy difference between the two

heterocomplexes $MABX_n$ and MA^*BX_n. The supramolecular noncovalent interactions could then be worked out.

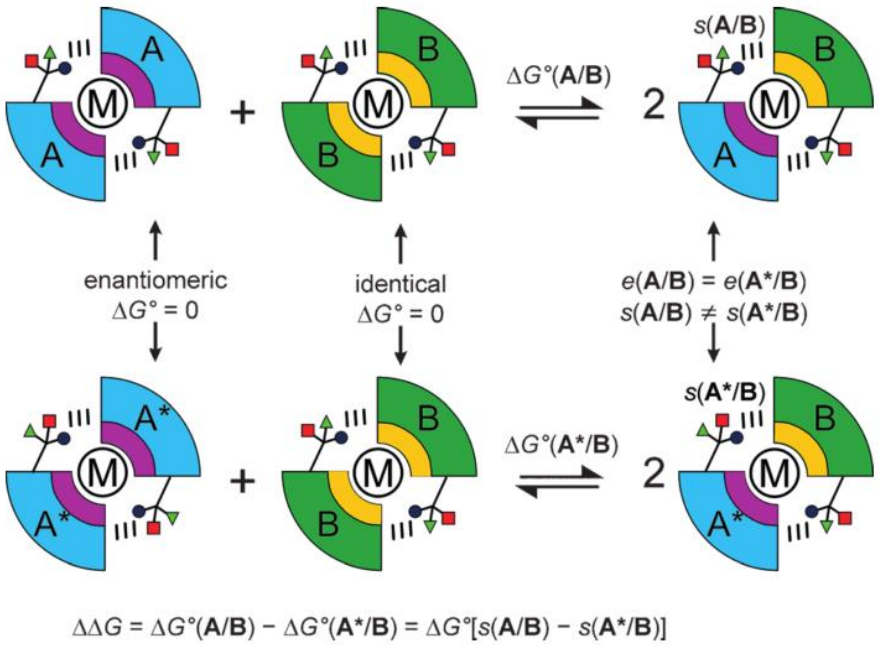

Figure 1.38 Two equilibria employed by Gschwind to quantify noncovalent ligand–ligand interactions (dashed lines).[133] A, A* (blue) and B (green) are chiral ligands. Purple and yellow sectors represent different stereoelectronic and electrostatic properties. When the heterocomplexes have same stereoelectronic and electrostatic properties (*e*(A/B) = *e*(A*/B)), the noncovalent interactions are different (*s*(A/B) ≠ *s*(A*/B)). The energy difference $\Delta\Delta G$ equals to the difference in noncovalent interactions.

1.6 Summary and outlook

A brief introduction of metallophilic interactions has been given in this chapter. Metallophilic interactions can be distinguished from the metal–metal covalent bonding and dative bonding by comparing their electron configuration, bond distance and bond order. The presence of metallophilic interactions in the solid state and in solution can be identified by several computational and experimental approaches. The nature of metallophilic interactions are still a matter of debate, with either dispersion or orbital interactions both being proposed as major contributors. Although a considerable number of computational assessments of the strength of metallophilic interactions have been published, experimental investigations have rarely been reported. Moreover, experimental evaluation of the contribution from metallophilic interactions to molecular assembly is not clear either. This thesis therefore aims to understand the nature, strength and contribution of metallophilic interactions through a combined experimental and computational approach.

1.7 References

1 L. H. Doerrer, *Comments Inorg. Chem.*, 2008, **29**, 93–127.

2 J. A. Hlina, J. R. Pankhurst, N. Kaltsoyannis and P. L. Arnold, *J. Am. Chem. Soc.*, 2016, **138**, 3333–3345.

3 I. Dutta, A. Sarbajna, P. Pandey, S. M. W. Rahaman, K. Singh and J. K. Bera, *Organometallics*, 2016, **35**, 1505–1513.

4 B. Wu, M. J. T. Wilding, S. Kuppuswamy, M. W. Bezpalko, B. M. Foxman and C. M. Thomas, *Inorg. Chem.*, 2016, **55**, 12137–12148.

5 I. G. Powers and C. Uyeda, *ACS Catal.*, 2017, **7**, 936–958.

6 C. Huang, X. Han, Z. Shao, K. Gao, M. Liu, Y. Wang, J. Wu, H. Hou and L. Mi, *Inorg. Chem.*, 2017, **56**, 4874–4884.

7 C. Werlé, R. Goddard, P. Philipps, C. Farès and A. Fürstner, *J. Am. Chem. Soc.*, 2016, **138**, 3797–3805.

8 T. J. Steiman and C. Uyeda, *J. Am. Chem. Soc.*, 2015, **137**, 6104–6110.

9 S. Vaddypally, D. J. Jovinelli, I. G. McKendry and M. J. Zdilla, *Inorg. Chem.*, 2017, **56**, 3733–3737.

10 N. Lichtenberger, R. J. Wilson, A. R. Eulenstein, W. Massa, R. Clérac, F. Weigend and S. Dehnen, *J. Am. Chem. Soc.*, 2016, **138**, 9033–9036.

11 J. F. Berry and C. C. Lu, *Inorg. Chem.*, 2017, **56**, 7577–7581.

12 O. Crespo, M. C. Gimeno, A. Laguna, O. Lehtonen, I. Ospino, P. Pyykkö and M. D. Villacampa, *Chem. Eur. J.*, 2014, **20**, 3120–3127.

13 J. Forniés, V. Sicilia, J. M. Casas, A. Martín, J. A. López, C. Larraz, P. Borja and C. Ovejero, *Dalton Trans.*, 2011, **40**, 2898.

14 J. Forniés, S. Ibáñez, E. Lalinde, A. Martín, M. T. Moreno and A. C. Tsipis, *Dalton Trans.*, 2012, **41**, 3439.

15 J. Bauer, H. Braunschweig and R. D. Dewhurst, *Chem. Rev.*, 2012, **112**, 4329–4346.

16 L. H. Doerrer, *Dalton Trans.*, 2010, **39**, 3543.

17 F. Scherbaum, A. Grohmann, B. Huber, C. Krüger and H. Schmidbaur, *Angew. Chem. Int. Ed. Engl.*, 1988, **27**, 1544–1546.

18 H. Schmidbaur and A. Schier, *Chem. Soc. Rev.*, 2008, **37**, 1931.

19 H. Schmidbaur and A. Schier, *Chem. Soc. Rev.*, 2012, **41**, 370–412.

20 H. Schmidbaur, K. Dziwok, A. Grohmann and G. Müller, *Chem. Ber.*, 1989, **122**, 893–895.

21 H. Schmidbaur, W. Graf and G. Müller, *Angew. Chem. Int. Ed. Engl.*, 1988, **27**,

417–419.

22 P. Pyykkö and Y. Zhao, *Angew. Chem. Int. Ed. Engl.*, 1991, **30**, 604–605.

23 N. Runeberg, M. Schütz and H.-J. J. Werner, *J. Chem. Phys.*, 1999, **110**, 7210–7215.

24 H. Schmidbaur and A. Schier, *Organometallics*, 2015, 34, 2048–2066.

25 H. Schmidbaur and A. Schier, *Angew. Chem. Int. Ed.*, 2015, 54, 746–784.

26 M. J. Katz, K. Sakai and D. B. Leznoff, *Chem. Soc. Rev.*, 2008, **37**, 1884–1895.

27 K. M.-C. Wong and V. W.-W. Yam, *Acc. Chem. Res.*, 2011, **44**, 424–434.

28 C. Po, A. Y. Tam, K. M. Wong and V. W. Yam, *J. Am. Chem. Soc.*, 2011, **133**, 12136–12143.

29 H. Ito, T. Saito, N. Oshima, N. Kitamura, S. Ishizaka, Y. Hinatsu, M. Wakeshima, M. Kato, K. Tsuge and M. Sawamura, *J. Am. Chem. Soc.*, 2008, **130**, 10044–10045.

30 H. L. Au-Yeung, S. Y. L. Leung, A. Y. Y. Tam and V. W. W. Yam, *J. Am. Chem. Soc.*, 2014, **136**, 17910–17913.

31 F. C. M. Leung, S. Y. L. Leung, C. Y. S. Chung and V. W. W. Yam, *J. Am. Chem. Soc.*, 2016, **138**, 2989–2992.

32 V. W.-W. Yam and E. C.-C. Cheng, *Chem. Soc. Rev.*, 2008, **37**, 1806.

33 V. W.-W. Yam, V. K.-M. Au and S. Y.-L. Leung, *Chem. Rev.*, 2015, **115**, 7589–7728.

34 W.-X. Ni, M. Li, J. Zheng, S.-Z. Zhan, Y.-M. Qiu, S. W. Ng and D. Li, *Angew. Chem. Int. Ed.*, 2013, **52**, 13472–13476.

35 D. Weber, M. A. Tarselli and M. R. Gagné, *Angew. Chem. Int. Ed.*, 2009, **48**, 5733–5736.

36 J. E. Heckler, M. Zeller, A. D. Hunter and T. G. Gray, *Angew. Chem. Int. Ed.*, 2012, **51**, 5924–5928.

37 D. Weber, T. D. Jones, L. L. Adduci and M. R. Gagné, *Angew. Chem. Int. Ed.*, 2012, **51**, 2452–2456.

38 D. Weber and M. R. Gagné, in *Homogeneous Gold Catalysis*, ed. L. M. Slaughter, Springer International Publishing, Cham, 2015, pp. 167–211.

39 A. Zhdanko and M. E. Maier, *Chem. Eur. J.*, 2014, **20**, 1918–1930.

40 E. S. S. Smirnova and A. M. Echavarren, *Angew. Chem. Int. Ed.*, 2013, **52**, 9023–9026.

41 T. J. Brown, D. Weber, M. R. Gagné and R. A. Widenhoefer, *J. Am. Chem. Soc.*, 2012, **134**, 9134–9137.

42 J. Xie, Y. Zheng and J. Y. Ying, *Chem. Commun.*, 2010, **46**, 961–963.

43 R. J. Oeschger and P. Chen, *J. Am. Chem. Soc.*, 2017, **139**, 1069–1072.

44 D. Serra, M. E. Moret and P. Chen, *J. Am. Chem. Soc.*, 2011, **133**, 8914–8926.

45 M. E. Moret, D. Serra, A. Bach and P. Chen, *Angew. Chem. Int. Ed.*, 2010, **49**, 2873–2877.

46 R. J. Oeschger, D. H. Ringger and P. Chen, *Organometallics*, 2015, **34**, 3888–3892.

47 Y. Kajitani, K. Tsuge, Y. Sasaki and M. Kato, *Chem. Eur. J.*, 2012, **18**, 11196–11200.

48 E. Paenurk, R. Gershoni-Poranne and P. Chen, *Organometallics*, 2017, **36**, 4854–4863.

49 H. Schmidbaur and A. Schier, *Chem. Soc. Rev.*, 2008, **37**, 1931–1951.

50 A. C. Tsipis, *Coord. Chem. Rev.*, 2017, **345**, 229–262.

51 E. R. T. Tiekink, *Coord. Chem. Rev.*, 2014, **275**, 130–153.

52 C. M. Fafard, D. Adhikari, B. M. Foxman, D. J. Mindiola and O. V. Ozerov, *J. Am. Chem. Soc.*, 2007, **129**, 10318–10319.

53 D. C. Powers and T. Ritter, *Nat. Chem.*, 2009, **1**, 302–309.

54 D. Roşca, D. A. Smith, D. L. Hughes and M. Bochmann, *Angew. Chem. Int. Ed.*, 2012, **51**, 10643–10646.

55 M. H. Chisholm, *Polyhedron*, 1986, **5**, 25–30.

56 F. A. Cotton, N. F. Curtis, C. B. Harris, B. F. G. Johnson, S. J. Lippard, J. T. Mague, W. R. Robinson and J. S. Wood, *Science*, 1964, **145**, 1305–1307.

57 T. Nguyen, A. D. Sutton, M. Brynda, J. C. Fettinger, G. J. Long and P. P. Power, *Science*, 2005, **310**, 844–847.

58 M. Baya, Ú. Belío, I. Fernández, S. Fuertes and A. Martín, *Angew. Chem. Int. Ed.*, 2016, **55**, 6978–6982.

59 K. B. Wiberg, *Tetrahedron*, 1968, **24**, 1083–1096.

60 M. I., *Int. J. Quantum Chem.*, 1986, **29**, 73–84.

61 I. Mayer, *Chem. Phys. Lett.*, 1983, **97**, 270–274.

62 A. E. Reed and P. v. R. Schleyer, *J. Am. Chem. Soc.*, 1990, **112**, 1434–1445.

63 T. Lu and F. Chen, *J. Phys. Chem. A*, 2013, **117**, 3100–3108.

64 P. Pyykko and J. P. Desclaux, *Acc. Chem. Res.*, 1979, **12**, 276–281.

65 K. Sun, M. Kohyama, S. Tanaka and S. Takeda, *J. Energy Chem.*, 2015, **24**, 485–489.

66 S. Sculfort and P. Braunstein, *Chem. Soc. Rev.*, 2011, **40**, 2741.

67 U. E. I. Horvath, J. M. McKenzie, S. Cronje, H. G. Raubenheimer and L. J. Barbour, *Chem. Commun.*, 2009, 6598.

68 H. de la Riva, A. Pintado-Alba, M. Nieuwenhuyzen, C. Hardacre and M. C. Lagunas, *Chem. Commun.*, 2005, 4970.

69 R. Gavara, E. Aguiló, C. F. Guerra, L. Rodríguez and J. C. Lima, *Inorg. Chem.*, 2015, **54**, 5195–5203.

70 Y. Jiang, S. Alvarez and R. Hoffmann, *Inorg. Chem.*, 1985, **24**, 749–757.

71 A. Dedieu and R. Hoffmann, *J. Am. Chem. Soc.*, 1978, **100**, 2074–2079.

72 L. F. Veiros and M. J. Calhorda, *J. Organomet. Chem.*, 1996, **510**, 71–81.

73 A. C. Tsipis, *Coord. Chem. Rev.*, 2014, **272**, 1–29.

74 J. P. Perdew, A. Ruzsinszky, J. Tao, V. N. Staroverov, G. E. Scuseria and G. I. Csonka, *J. Chem. Phys.*, , DOI:10.1063/1.1904565.

75 C. J. Cramer and D. G. Truhlar, *Phys. Chem. Chem. Phys.*, 2009, **11**, 10757–10816.

76 E. Maslowsky, *Coord. Chem. Rev.*, 2011, **255**, 2746–2763.

77 F. Neese, *Coord. Chem. Rev.*, 2009, **253**, 526–563.

78 A. Otero-De-La-Roza, J. D. Mallory and E. R. Johnson, *J. Chem. Phys.*, , DOI:10.1063/1.4862896.

79 R. F. W. Bader, *J. Phys. Chem. A*, 1998, **102**, 7314–7323.

80 R. F. W. Bader, *Acc. Chem. Res.*, 1985, **18**, 9–15.

81 E. R. Johnson, S. Keinan, P. Mori Sánchez, J. Contreras García, A. J. Cohen and W. Yang, *J. Am. Chem. Soc.*, 2010, **132**, 6498–6506.

82 E. Espinosa, I. Alkorta, J. Elguero and E. Molins, *J. Chem. Phys.*, 2002, **117**, 5529–5542.

83 S. Jenkins and I. Morrison, *Chem. Phys. Lett.*, 2000, **317**, 97–102.

84 P. R. Varadwaj and H. M. Marques, *Phys. Chem. Chem. Phys.*, 2010, **12**, 2126.

85 S. Dinda and A. G. Samuelson, *Chem. Eur. J.*, 2012, **18**, 3032–3042.

86 B. Raghavendra, P. K. Mandal and E. Arunan, *Phys. Chem. Chem. Phys.*, 2006, **8**, 5276–5286.

87 B. G. de Oliveira, *Phys. Chem. Chem. Phys.*, 2013, **15**, 37–79.

88 M. Rozenberg, *RSC Adv.*, 2014, **4**, 26928–26931.

89 A. Reisinger, N. Trapp, C. Knapp, D. Himmel, F. Breher, H. RÃ¼egger and I. Krossing, *Chem. Eur. J.*, 2009, **15**, 9505–9520.

90 C. Biswas, M. G. B. Drew, D. Escudero, A. Frontera and A. Ghosh, *Eur. J. Inorg. Chem.*, 2009, 2238–2246.

91 J. Contreras-García, E. R. Johnson, S. Keinan, R. Chaudret, J. P. Piquemal, D. N. Beratan and W. Yang, *J. Chem. Theory Comput.*, 2011, **7**, 625–632.

92 B. Pinter, L. Broeckaert, J. Turek, A. Růžička and F. De Proft, *Chem. Eur. J.*, 2014, **20**, 734–744.

93 J. R. Shakirova, E. V. Grachova, A. J. Karttunen, V. V. Gurzhiy, S. P. Tunik and I. O. Koshevoy, *Dalton Trans.*, 2014, **43**, 6236–6243.

94 T. Lasanta, J. M. Lõpez-De-Luzuriaga, M. Monge, M. E. Olmos and D. Pascual, *Chem. Eur. J.*, 2013, **19**, 4754–4766.

95 D. B. Leznoff, B.-Y. Xue, R. J. Batchelor, F. W. B. Einstein and B. O. Patrick, *Inorg. Chem.*, 2001, **40**, 6026–6034.

96 J. Suárez-Varela, H. Sakiyama, J. Cano and E. Colacio, *J. Chem. Soc. Dalt. Trans.*, 2006, 249–256.

97 C. M. Che and S. W. Lai, *Coord. Chem. Rev.*, 2005, **249**, 1296–1309.

98 J. Kalinowski, V. Fattori, M. Cocchi and J. A. G. Williams, *Coord. Chem. Rev.*, 2011, **255**, 2401–2425.

99 A. Aliprandi, D. Genovese, M. Mauro and L. De Cola, *Chem. Lett.*, 2015, **44**, 1152–1169.

100 A. Himmelspach, M. Finze and S. Raub, *Angew. Chem. Int. Ed.*, 2011, **50**, 2628–2631.

101 A. Deák, T. Megyes, G. Tárkányi, P. Király, L. Biczók, G. Pálinkás and P. J. Stang, *J. Am. Chem. Soc.*, 2006, **128**, 12668–12670.

102 D. E. Harwell, M. D. Mortimer, C. B. Knobler, F. A. L. L. Anet and M. F. Hawthorne, *J. Am. Chem. Soc.*, 1996, **118**, 2679–2685.

103 F. Balzano, A. Cuzzola, P. Diversi, F. Ghiotto and G. Uccello-Barretta, *Eur. J. Inorg. Chem.*, 2007, **2007**, 5556–5562.

104 B.-H. Xia, H.-X. Zhang, C.-M. Che, K.-H. Leung, D. L. Phillips, N. Zhu and Z.-Y. Zhou, *J. Am. Chem. Soc.*, 2003, **125**, 10362–10374.

105 K. H. Leung, D. L. Phillips, M.-C. Tse, C.-M. Che and V. M. Miskowski, *J. Am. Chem. Soc.*, 1999, **121**, 4799–4803.

106 T. Li, A. J. Senesi and B. Lee, *Chem. Rev.*, 2016, **116**, 11128–11180.

107 C. E. Blanchet and D. I. Svergun, *Annu. Rev. Phys. Chem.*, 2013, **64**, 37–54.

108 M. Nyman, *Coord. Chem. Rev.*, 2017, **352**, 461–472.

109 A. Cebollada, A. Vellé, M. Iglesias, L. B. Fullmer, S. Goberna-Ferrõn, M. Nyman and P. J. Sanz Miguel, *Angew. Chem. Int. Ed.*, 2015, **54**, 12762–12766.

110 M. Newville, *Rev. Mineral. Geochemistry*, 2014, **78**, 33–74.

111 S. Calvin, in *XAFS for Everyone*, 2013, pp. 3–29.

112 N. Carr, J. G. Crossley, A. J. Dent, J. R. Gouge, G. N. Greaves, P. S. Jarrett and A. G. Orpen, *J. Chem. Soc., Chem. Commun.*, 1990, 1369–1371.

113 D. Ellis, L. J. Farrugia, P. Wiegeleben, J. G. Crossley, A. G. Orpen and P. N. Waller, *Organometallics*, 1995, **14**, 481–488.

114 M. Andrejić and R. A. Mata, *Phys. Chem. Chem. Phys.*, 2013, **15**, 18115–18122.

115 G. Frenking and F. Matthias Bickelhaupt, in *The Chemical Bond: Fundamental Aspects of Chemical Bonding*, 2014, pp. 121–157.

116 M. Mitoraj and A. Michalak, *J. Mol. Model.*, 2007, **13**, 347–355.

117 L. Ray, M. M. Shaikh and P. Ghosh, *Inorg. Chem.*, 2008, **47**, 230–240.

118 O. Elbjeirami, S. Yockel, C. F. Campana, A. K. Wilson and M. A. Omary, *Organometallics*, 2007, **26**, 2550–2560.

119 M. Schütz, G. Rauhut and H.-J. Werner, *J. Phys. Chem. A*, 1998, **102**, 5997–6003.

120 L. Magnko, M. Schweizer, G. Rauhut, M. Schutz, H. Stoll and H.-J. Werner, *Phys. Chem. Chem. Phys.*, 2002, **4**, 1006–1013.

121 K. Morokuma, *J. Chem. Phys.*, 1971, **55**, 1236–1244.

122 T. Ziegler and A. Rauk, *Inorg. Chem.*, 1979, **18**, 1558–1565.

123 T. Ziegler and a Rauk, *Theor. Chim. Acta*, 1977, **46**, 1–10.

124 M. von Hopffgarten and G. Frenking, *Wiley Interdiscip. Rev. Comput. Mol. Sci.*, 2012, **2**, 43–62.

125 E. G. Hohenstein and C. D. Sherrill, *Wiley Interdiscip. Rev. Comput. Mol. Sci.*, 2012, **2**, 304–326.

126 S. Dapprich and G. Frenking, *J. Phys. Chem.*, 1995, **99**, 9352–9362.

127 M. Rahm and R. Hoffmann, *J. Am. Chem. Soc.*, 2016, **138**, 3731–3744.

128 M. Rahm and R. Hoffmann, *J. Am. Chem. Soc.*, 2015, **137**, 10282–10291.

129 I. K. Mati and S. L. Cockroft, *Chem. Soc. Rev.*, 2010, **39**, 4195–4205.

130 S. Narancic, A. Bach and P. Chen, *J. Phys. Chem. A*, 2007, **111**, 7006–7013.

131 E. Andris, P. C. Andrikopoulos, J. Schulz, J. Turek, A. Růžička, J. Roithová and L. Rulí ek, *J. Am. Chem. Soc.*, 2018, **140**, 2316–2325.

132 K. Davis, B. Cole, M. Ghelardini, B. A. Powell and O. T. Mefford, *Langmuir*, 2016, **32**, 13716–13727.

133 E. Hartmann and R. M. Gschwind, *Angew. Chem. Int. Ed.*, 2013, **52**, 2350–2354.

Chapter 2: Understanding Aurophilic Interactions

Abstract

Aurophilic interactions are weak interactions between gold cations. This type of interaction is believed to play an important role in structure construction, luminescence, and catalysis. However, the contribution of aurophilic interactions to molecular assembly is not clear, due to the difficulty of separating metallophilic interactions from other weak interactions. Here, single-crystal X-ray diffraction, NMR spectroscopy, UV-vis spectroscopy, electrostatic potential (ESP) maps, non-covalent interactions (NCI) index and energy decomposition analysis (EDA) have been employed to experimentally and computationally estimate aurophilic interactions in a series of complexes. Single-crystal structures illustrate the presence of aurophilic interactions in the solid state. NMR ligand-exchange experiments reveal that aurophilic interactions are very weak and are not strong enough to be preserved in solution. Electrostatic potential (ESP) maps computed by DFT suggest that electrostatic attraction plays a more important role than aurophilic interactions. NCI and EDA confirm the dominant role of electrostatic attraction and the weak strength of aurophilic interactions. EDA-NOCV calculations also suggest that minor favourable contributions from aurophilic interactions result from orbital delocalisation between two gold centres. Caution should be applied in future studies of organometallic complexes to avoid potential overestimation of the energetic significance of aurophilic interactions.

2.1 Introduction

Since the observation of the first short Au–Au contact in the solid state by Schmidbaur,[1] the past several decades have seen a growing interest in aurophilic interactions in gold chemistry, supramolecular chemistry and material chemistry.[2–6] Aurophilic interactions have mostly been observed in the solid state in a range of crystal structures.[7,8] Additionally, a number of solution-phase systems have purportedly used aurophilic interactions, with some examples providing spectroscopic evidence of the interaction.[1,9–14] Aurophilic interactions are also believed to play significant role in constructing the structure of molecules,[7,8,15] luminescence properties,[16,17] and catalysis.[18] However, the nature and strength of aurophilic interactions is subject to significant dispute. As discussed in chapter 1, aurophilic interactions are proposed to originate from either orbital hybridisation or dispersion interactions.[3,19,20] Numerous computations and limited experiments have been performed and they variously estimate the energies to be in the range of 20 to 50 kJ mol^{-1}.[3,8–10,21–25] In particular, the experimental studies are limited due to the assumptions that overlooked important secondary electronic and steric factors,[9,10,24] putting the quality of these prior measurements in doubt.

The obscure origin of aurophilic interactions, and inconclusive evaluation of the interaction energy encourage us to examine aurophilic interactions further, seeking to answer the questions: How important are aurophilic interactions in solution? How much do they contribute to molecular assembly?

2.2 System design and synthesis

To experimentally investigate aurophilic interactions, two potential approaches were employed (**Figure 2.1**). One approach is supramolecular aggregation, in which the complexes assemble together to form dimers and chains with the presence of aurophilic interactions. The equilibrium constants (K_1, K_2, ⋯, and K_n) can be calculated by UV-vis and NMR dilution experiments. Then the binding energies (ΔG), which contain the contributions of aurophilic interactions and aromatic stacking, are calculated as $\Delta G = -RT\ln K$. The other approach is ligand-exchange that replacing a

ligand with a folded bi-connected ligand, forming intramolecular aurophilic interactions. The equilibrium constants K and energies ΔG can be worked out as well. In these approaches, the influence from other secondary interactions, such as electrostatic and steric forces, should be either minimised, or controlled. The desired system must satisfy a number of ideal criteria: i) neutral, to exclude ionic forces, ii) Au^{I} complexes with linear structure, to simplify the study, iii) small, planar complexes, to minimise steric effects, iv) stable and soluble in solution, to enable the study of their solution-phase behaviour.

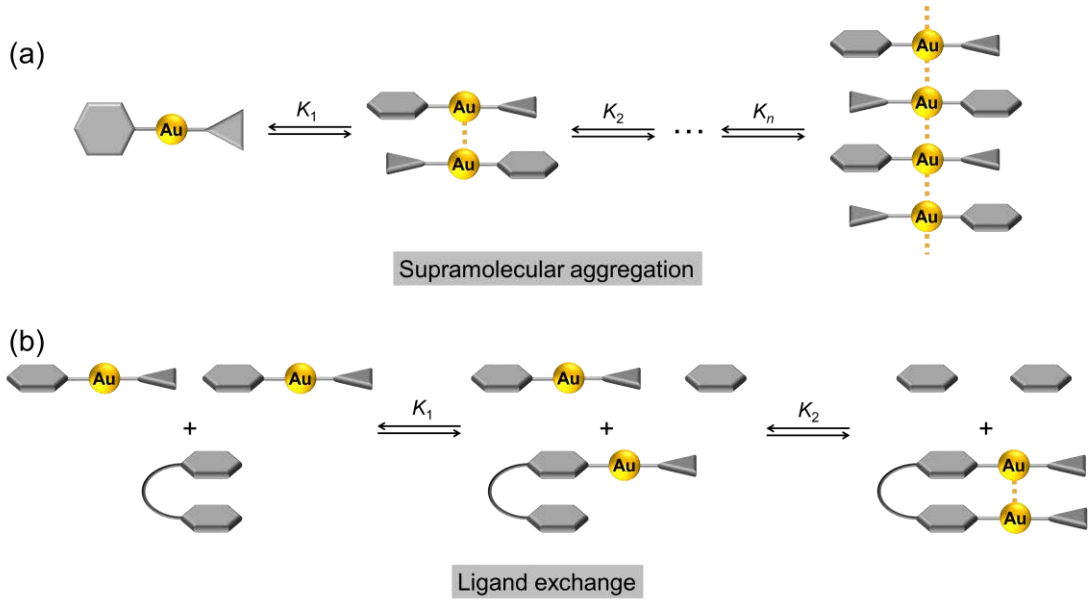

Figure 2.1 Approaches of supramolecular aggregation (a) and ligand-exchange (b) for estimating aurophilic interactions.

Based on these considerations and by searching the Cambridge Structural Database (CSD version 5.38, Feb. 2017), the complexes shown in **Figure 2.2** were designed and synthesised, which satisfied all the ideal criteria. The electron-withdrawing pentafluorobenzyl group was chosen to help stabilise the Au^{I} complexes due to the stronger carbon-gold bond.[26]

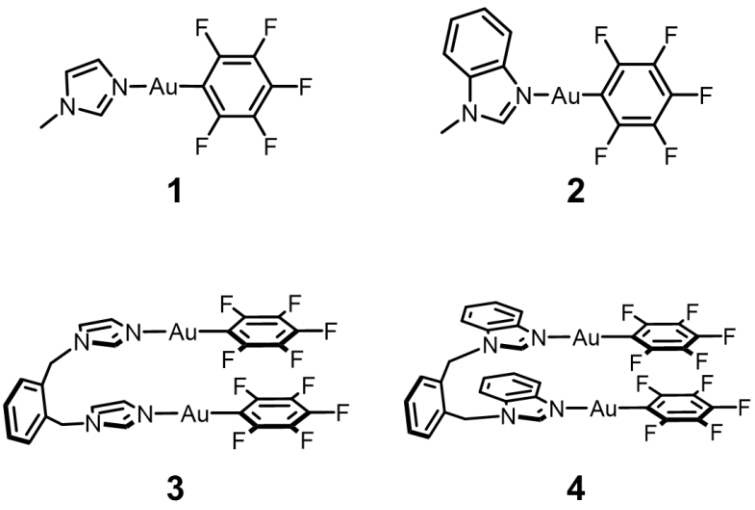

Figure 2.2 Complexes for the study of aurophilic interactions.

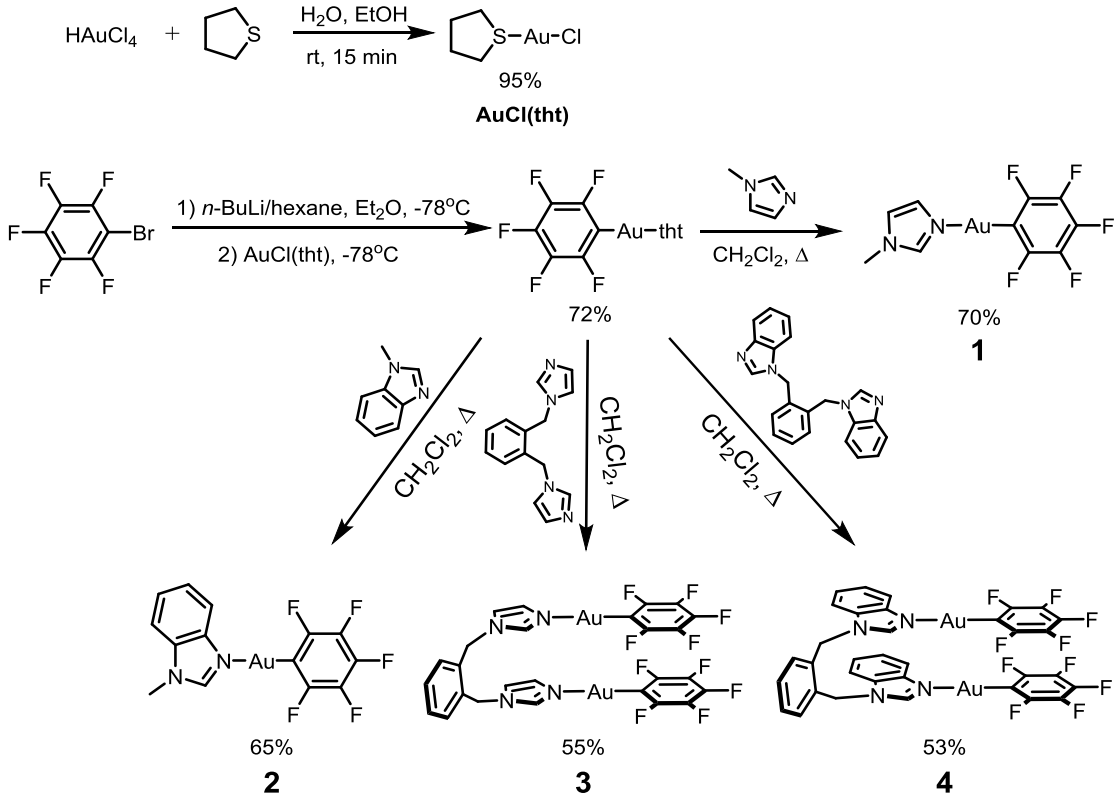

Figure 2.3 Synthetic routes for preparing complexes **1**–**4**.

Complexes **1**–**4** were prepared according to modified literature[27] procedures using the synthetic routes shown in **Figure 2.3**. The complexes AuCl(tht) (tht =

tetrahydrothiophene), $(C_6F_5)Au(tht)$ (C_6F_5 = pentafluorobenzene) and ligands 1,2-bis(imidazol-1-ylmethyl)-benzene, 1,2-bis(benzimidazol-1-ylmethyl)-benzene were synthesised according to the literature.[28–30] Synthetic details are provided in the Experimental section. The identities and purities of the complexes were confirmed by ^{1}H, ^{19}F and ^{13}C NMR, mass spectrometry (ESI-MS) and single-crystal X-ray diffraction.

2.3 Solid state investigation

While the compounds were designed to study aurophilic interactions in solution, solid-state crystal structures were expected to be instructive in confirming that Au–Au contacts were present in the assembled complexes (**Figure 2.1**). Single crystals of complexes **1**–**4** were grown by solvent layering (CH_2Cl_2 / Et_2O). Crystallographic data of complexes **1** and **2** were the same as structures previously reported in literature,[27] their crystallographic data were hence utilised directly without any further refinement. Crystallographic data of complexes **3** and **4** were listed in Appendix A.1.

The Au^{I} in complex **1** is linearly connected to a C_6F_5 group and a methyl imidazole (MI) ligand (**Figure 2.4**). The geometry is not planar with a dihedral angle of ~52°. The Au–Au distance is ~5.30 Å in the unit cell, which is out of the range of aurophilic interactions (2.5–3.5 Å). This indicates the absence of aurophilic interactions in the solid state. Unlike complex **1**, the linear complex **2** adopts a planar geometry. Two adjacent molecules pack with each other in an anti-parallel (head-to-tail) mode. The short Au–Au distance of 3.29 Å demonstrates the possibility of aurophilic interactions. The dimers further packed together forming the herringbone-type structure shown in the **Figure 2.4**.

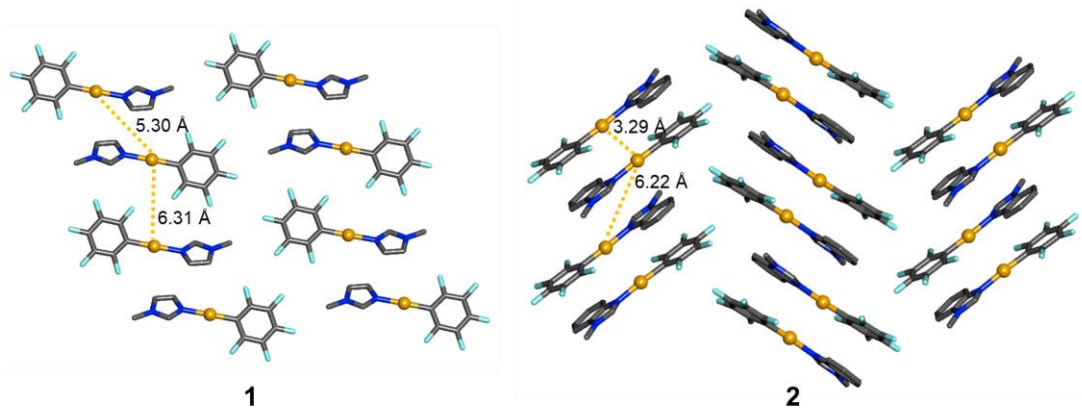

Figure 2.4 Crystal structures of complexes **1–2** with intra- and inter-molecular Au–Au distances. Colour codes: yellow Au, blue N, cyan F, grey C. Hydrogens are omitted for clarity.

Complex **3** contains two Au^{I} cations (**Figure 2.5**). One end of each cation is bonded to a C_6F_5 fragment. Two moieties are linked to two nitrogen atoms in a folded ligand (BIMB) forming a U-shape. Depending on the geometry of the BIMB ligand, two forms of single-crystals (Form I and II) have been observed. The intramolecular Au–Au distances in crystal form I and II are 3.41 Å and 3.45 Å respectively. Both of the distances are shorter than 3.50 Å, suggesting the presence of aurophilic interactions in the solid state. In terms of intermolecular aurophilic interactions, Au–Au distances of 7.47 Å and 3.45 Å are observed in form I and II respectively. Therefore, intermolecular aurophilic interactions are present in form II but not in form I.

The structure of complex **4** is similar to form I of complex **3**, but its unit cell contains two different molecules. The intramolecular Au–Au distances for two molecules are 3.39 Å and 3.45 Å respectively, suggesting the presence of aurophilic interactions. While the intermolecular Au–Au distance is 4.79 Å, which is too long to form intermolecular aurophilic interactions. It should be noted that the two "arms" in complex **4** stacked with each other in a parallel (head-to-head) mode, which is on the contrary to the anti-parallel mode in complex **2**. The reverse mode enables further study of the influence of electrostatic interactions, as discussed in section 2.7.3.

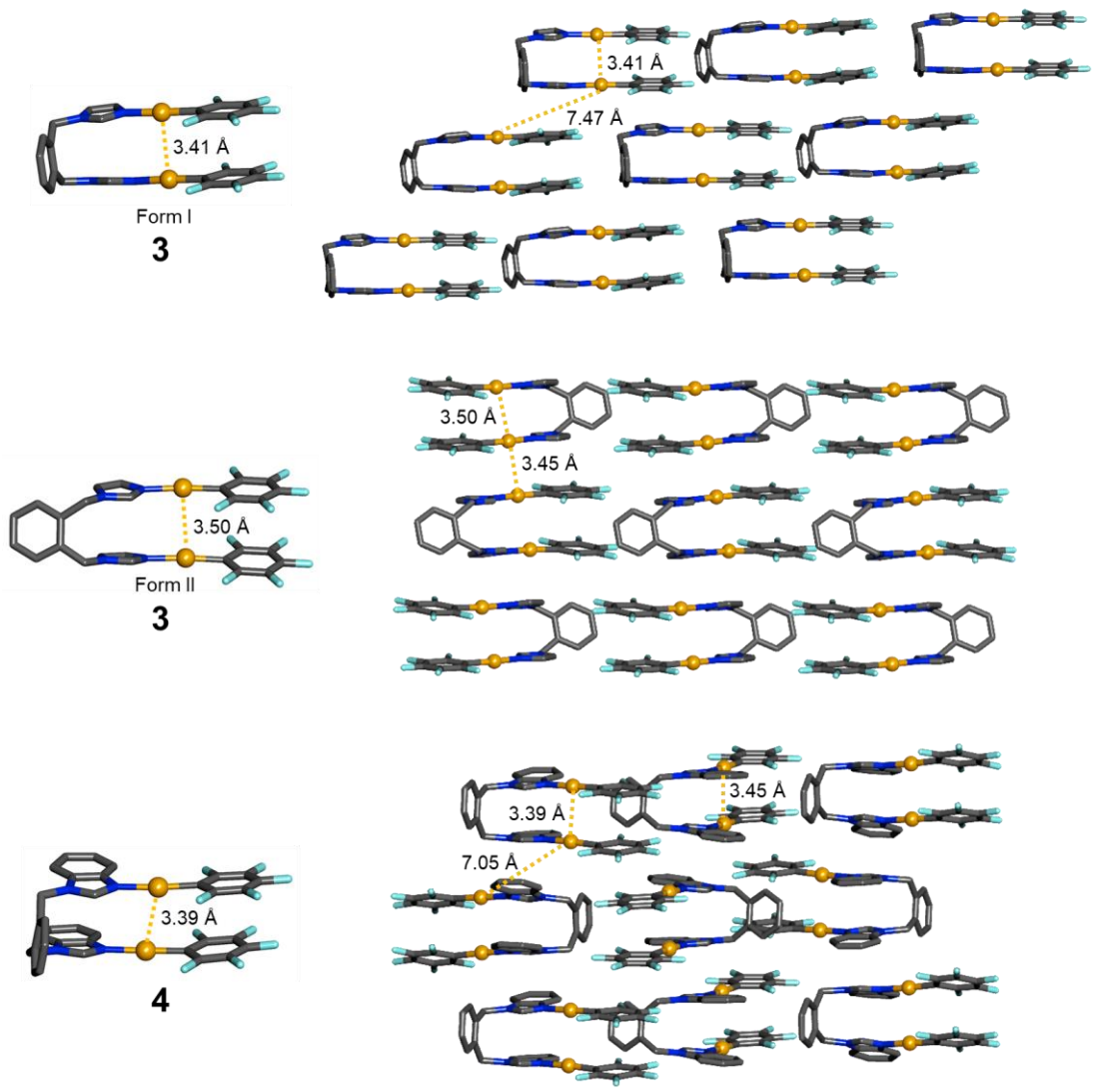

Figure 2.5 Crystal structures of two forms of complex **3** and complex **4** with intra- and inter-molecular Au–Au distances. Colour codes: yellow Au, blue N, cyan F, grey C. Hydrogens are omitted for clarity.

The presence of aurophilic interactions in complexes **2**–**4** in the solid state makes these complexes potential platforms for studying aurophilic interactions. It is also noteworthy that the linear Au^{I} "arms" in complexes **3** and **4** packed with each other in a parallel mode, by contrast with the anti-parallel packing mode in the complex **2**. In this way, the influence of aromatic stacking can also be investigated.

2.4 Solubility and stability

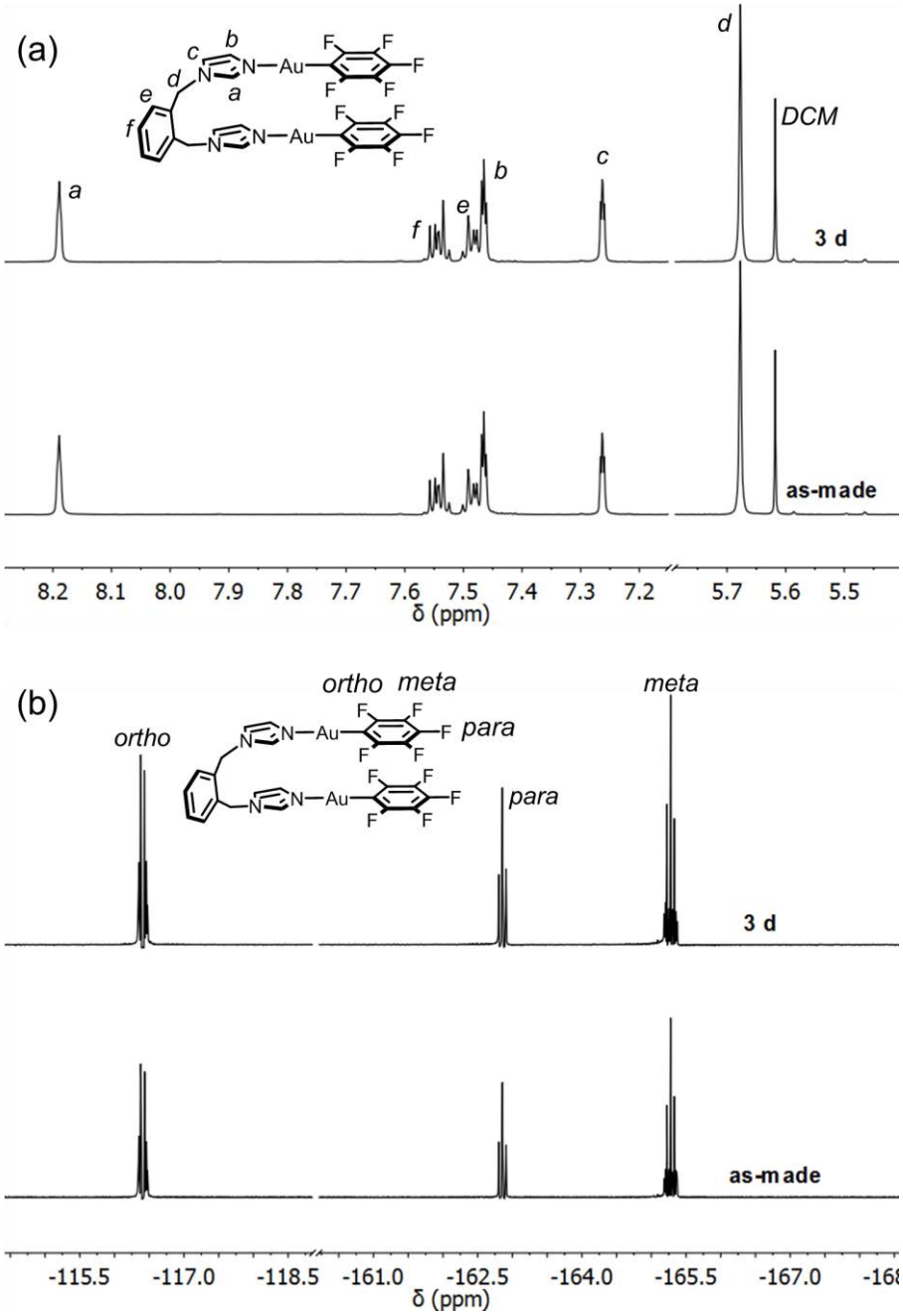

Figure 2.6 ^{1}H NMR (a) and ^{19}F NMR (b) spectra of complex **3** in acetone-d_6. The spectra keep the same after 3 days.

Before studying these complexes in solution, their solubility and stability in solvents have been examined. Complexes **1**–**4** are soluble in acetone, DMSO, EtOAc, THF, DMF, nitrobenzene, but are not/poorly soluble in $CHCl_3$, CH_2Cl_2, acetonitrile,

methanol, and toluene. The saturation concentrations of complexes **2** and **4** are significantly lower than those of complexes **1** and **3**, due to the presence of extra benzene rings in **2** and **4**. For instance, the saturation concentrations of complexes **1**, **2**, **3**, and **4** in acetone are around 800 mM, 25 mM, 450 mM, and 5 mM, respectively. Solutions of these complexes in different solvents are reasonably stable. For example, the acetone solution of complex **3** remained largely unchanged for 3 days as supported by NMR spectra (**Figure 2.6**), but beyond this, the complex was seen to gradually decompose with the solution color changing from colorless to red.

2.5 Estimation of aurophilic interactions by supramolecular aggregation

Since the imidazole (MI) fragment is not in the plane of the [Au(C_6F_5)] moiety in complex **1**, and aurophilic interactions are not observed in the crystal structure, it was uncertain whether aurophilic interactions would be observed in solution. Complexes **2–4**, however, demonstrate planar [imidazole-Au(C_6F_5)] fragments and the presence of aurophilic interactions in the solid state, providing an encouraging starting point for the investigation of solution-phase aurophilic interactions. Therefore, stacking of the molecules into dimers or even polymers may occur at a certain range of concentrations. Taking the assembly of complex **2** as an example (**Figure 2.7**), equilibria between monomers, dimers and oligomers might be present. These equilibrium steps are considered the same (isodesmic model) that all the equilibrium constants K_n (n = 1, 2, 3…) are the same, $K_1 = K_2 = \ldots = K_n$.[31] The equilibrium constant can be calculated by UV-vis and NMR dilution experiments, in which UV-vis absorbance and NMR chemical shifts would change upon varying concentration. By plotting absorbance or chemical shifts against concentration, the equilibrium constant can be obtained. Then the binding energy is thus calculated as $\Delta G = -RT\ln K$.

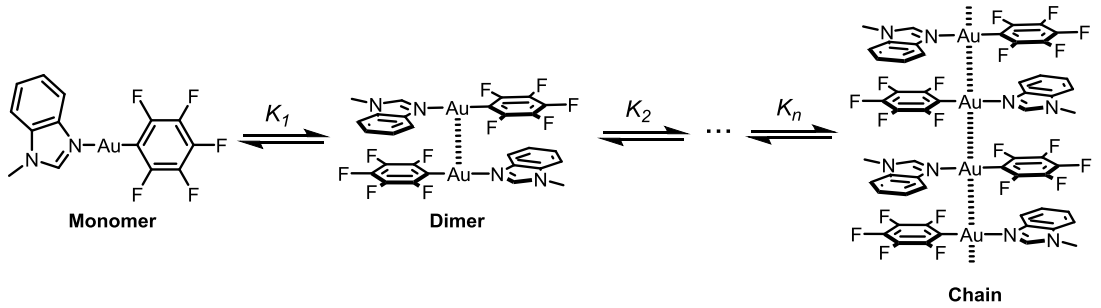

Figure 2.7 Proposed equilibria of complex **2** in solution.

2.5.1 Dilution UV-vis spectroscopy

To examine whether aurophilic interactions are present or not in solution of complexes **2–4**, UV-vis spectroscopy has been performed first. Dichloromethane (DCM) was chosen as the solvent for these initial investigations because it is non-polar and therefore solvation may not interfere with aggregation too much. Although the solubility of complexes **2–4** is not high in DCM (< 5 mM), such concentrations are certainly high enough for performing UV-vis spectroscopy.

The dilution UV-vis absorption spectra of complex **2** at concentrations from 0.001 mM to 2.0 mM in CH_2Cl_2 are shown in **Figure 2.8**. The broad absorption band at 325 nm is assigned to metal-to-ligand charge transfer (MLCT). The absorbance is linearly correlated to concentration, which obeys Beer's law, indicating that no aggregation occurs in that concentration range. The absence of a new absorption band at longer wavelength, e.g. a peak at > 400 nm, due to metal-to-metal ligand charge transfer (MMLCT), implies that aurophilic interactions are not observed by UV-vis spectroscopy. Similarly, the dilution UV-vis absorption spectra of complex **3** also showed a band at 325 nm (**Figure 2.8c**), which again displayed a linear correlation between absorbance and concentration. Therefore, aurophilic interactions were not observed in the solution of complex **3** either.

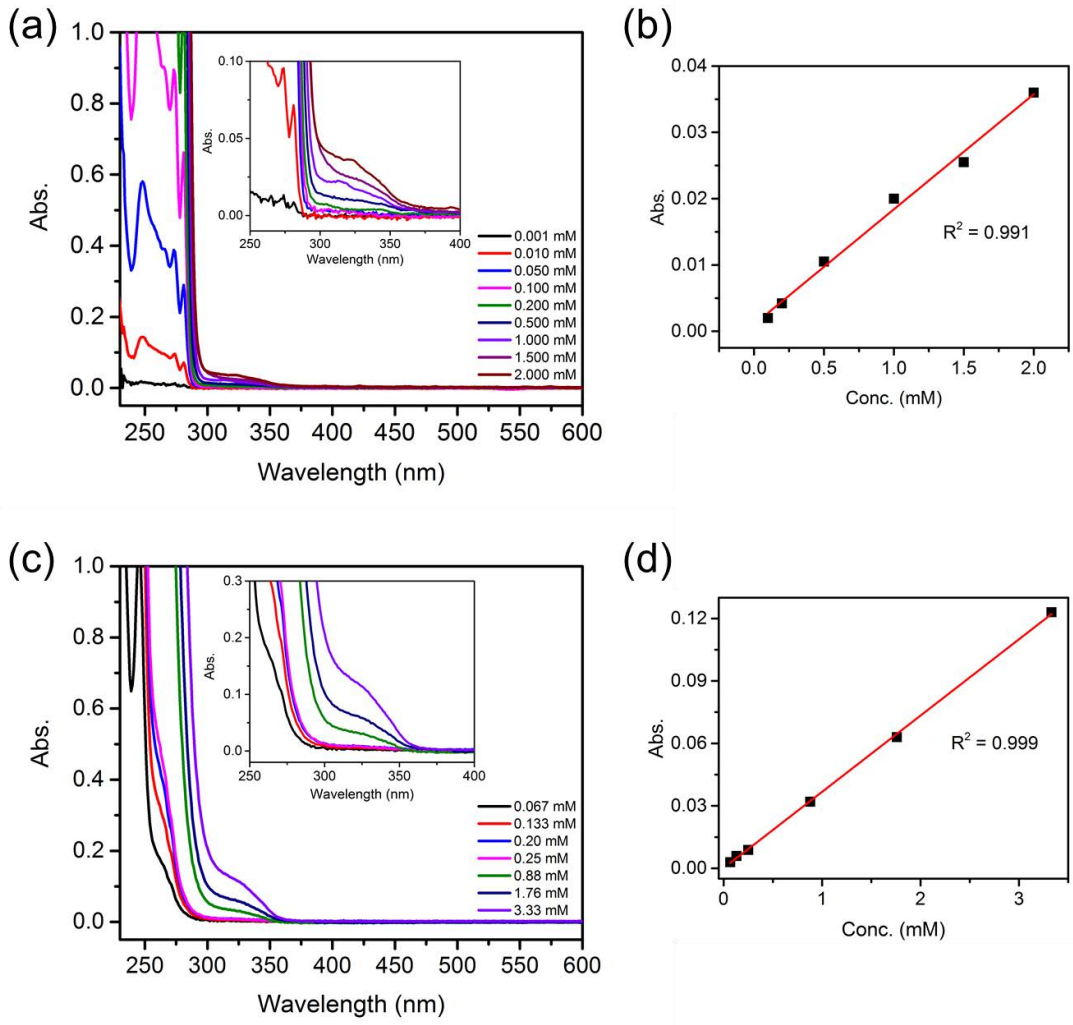

Figure 2.8 Dilution UV-vis absorption spectra (CH_2Cl_2, 298 K) of complex **2** (a), and the linear correlation between concentration and absorbance at 325 nm (b). Dilution UV-vis spectra (CH_2Cl_2, 298 K) of complex **3** (c), and the linear correlation between concentration and absorbance at 325 nm (d). Insets are zoomed in pictures of the absorption bands at 250–400 nm.

The UV-vis spectra of complexes **2** and **3** revealed that self-assembly was not observed in solution. In addition, the absence of MMLCT suggested both inter- and intra-molecular aurophilic interactions were not preserved in solution at the concentrations examined. However, the absence of aggregation is probably due to the low concentration. Therefore, NMR spectroscopy at higher concentrations was then performed.

2.5.2 Dilution NMR spectroscopy

For NMR experiments, the low solubility solvent DCM used in UV-vis spectroscopy was replaced by acetone-d_6, which gave much higher solubility for all of the complexes. Since the ^{19}F NMR spectra of complexes **2–4** are much simpler and cleaner than the corresponding ^{1}H NMR spectra, NMR dilution experiments were monitored mainly using ^{19}F NMR spectroscopy. ^{1}H NMR spectra were still used in some cases as complementary proof.

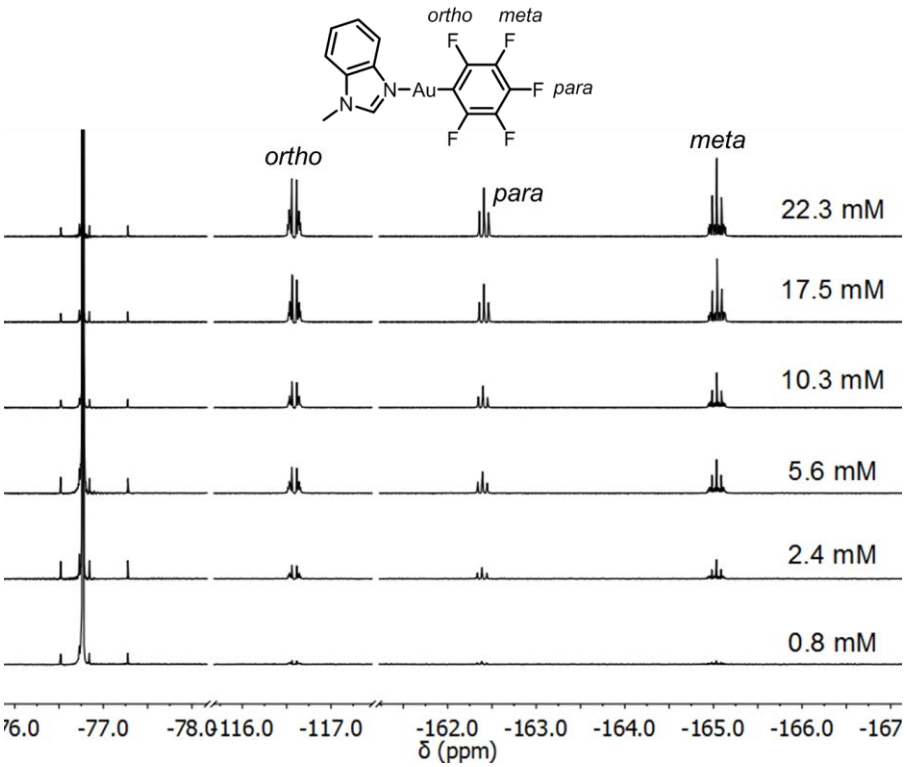

Figure 2.9 Partial ^{19}F NMR spectra (acetone-d_6, 376.5 MHz, 298 K) of complex **2** from concentration of 0.8 mM to 22.3 mM (almost saturated) referenced to CF_3COOH in a capillary as an external standard (–76.8 ppm).

The ^{19}F NMR spectrum of complex **2** in acetone-d_6 contained a multiplet at −116.6 ppm, a triplet at −162.4 ppm, and a multiplet at −165.1 ppm, which correspond to the *ortho*-, *para*-, and *meta*-fluoro-substituents of the C_6F_5 moiety, respectively (**Figure 2.9**). The chemical shifts remained unchanged upon increasing concentration from 0.8 mM to 22.3 mM (almost saturated). Therefore, complex **2** does not aggregate in acetone, indicating intermolecular interactions between monomers were too weak to

induce significant aggregation, setting an upper limit of an association constant of $<10^2$ M^{-1}.

For complex **3**, the ^{19}F NMR spectrum shows a multiplet at −116.3 ppm, a triplet at −162.8 ppm, and a multiplet at −165.2 ppm, which correspond to the *ortho*-, *para*-, and *meta*-F of the C_6F_5 moiety, respectively (**Figure 2.10**). These peaks barely changed when increasing concentration from 2 mM to 444 mM, indicating that complex **3** does not aggregate in acetone under these conditions, and setting an upper limit of an association constant of <10 M^{-1}. Intermolecular aurophilic interactions are thus essentially absent in solution in this concentration range.

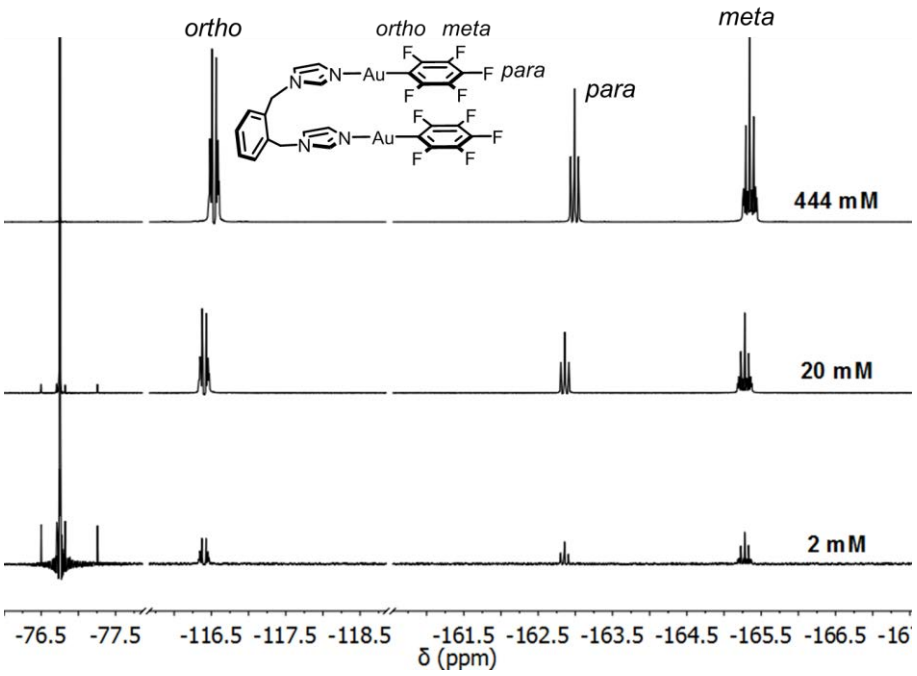

Figure 2.10 Partial ^{19}F NMR spectra (Acetone-d_6, 298 K) of complex **3** at 2 mM, 20 mM and 444 mM. CF_3COOH in a capillary was used as an external standard (–76.8 ppm).

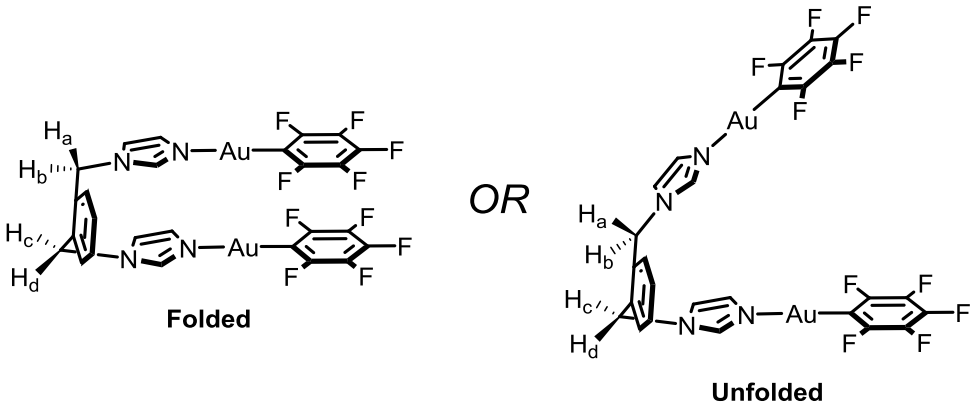

Figure 2.11 Possible folded and unfolded geometries of complex **3** in solution.

^{1}H NMR spectra of complex **3** were performed to examine whether the it adopted a "folded" geometry or an "unfolded" geometry (**Figure 2.11**). If the complex **3** adopts the folded structure, aurophilic interactions are expected to be present due to the short Au–Au contact. The two methylene protons pointing to inside of the complex (H_b, H_c) might be more shielded than the outer two protons (H_a, H_d). As a result, two peaks might be observed if the rotation of Ph-CH_2 is slow on the NMR time scale. Unfortunately, only a single methylene peak was observed at 5.68 ppm in the ^{1}H NMR spectrum at 298 K (**Figure 2.12**). When decreasing the temperature to 213 K (–60 °C), the peak at 5.68 ppm became broadened. The broadening of the peaks suggests 213 K is close to the coalescence temperature, at which the conformational exchange rate is slow enough for one peak to split into two. 298 K is thus much higher than the coalescence temperature. These NMR data therefore suggest that complex **3** is in fast conformational exchange at room temperature, which makes the protons H_a–H_d indistinguishable in NMR spectra.

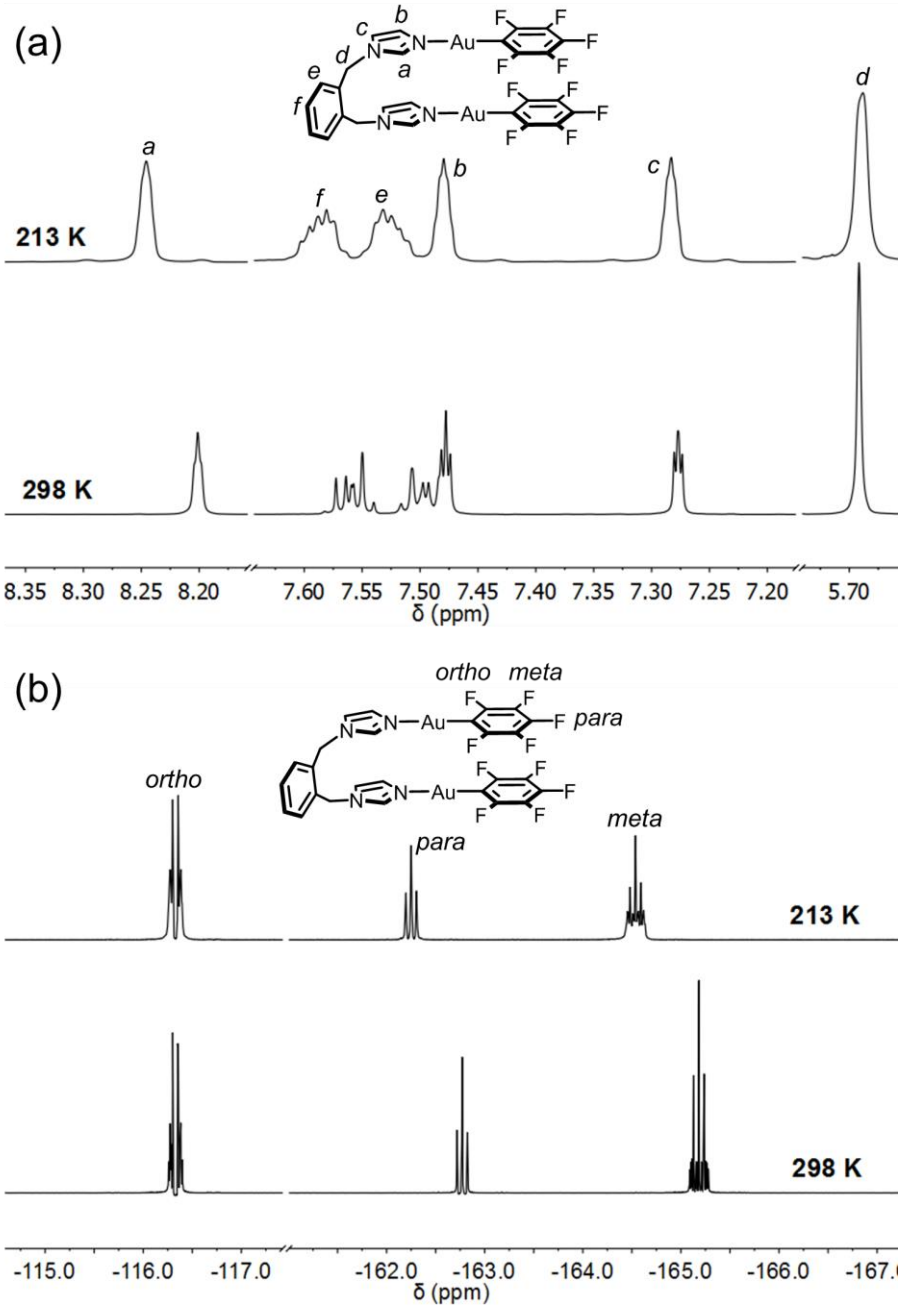

Figure 2.12 ^{1}H NMR (a) and ^{19}F NMR (b) spectra of complex **3** in acetone-d_6 at 298 K and 213 K.

The ^{1}H NMR spectrum of complex **4** also contains a single CH_2 peak, suggesting it is also in fast conformational exchange at room temperature (**Figure 2.32**). Unfortunately, meaningful dilution experiments for complex **4** could not be performed due to its low solubility in acetone (< 5 mM).

The NMR dilution experiments of complexes **2–3** show relatively unchanged spectra, suggesting these complexes do not aggregate significantly in solution at the concentration range examined. Otherwise, obvious changes in chemical shifts should be observed. Hence, intermolecular attraction between these complexes are too weak to drive assembly in solution. In other words, intermolecular aurophilic interactions are weak for this system.

2.6 Estimation of aurophilic interactions by ligand-exchange

2.6.1 Ligand-exchange approach

Ligand-exchange approaches have been previously used to estimate weak non-covalent interactions. For instance, as mentioned in Chapter 1, Gschwind[32] estimated the strength of non-covalent ligand–ligand interactions in transition metal complexes. This method was applied on linear complex **1** and U-shaped complex **3** to investigate aurophilic interactions (**Figure 2.13**). The Au-N bond in these complexes is labile and formed under thermodynamic control. Ligand **MI** and **BIMB** are structurally very similar, the formation of an Au-N bond between the [AuC_6F_5] fragment with either ligand is expected to be energetically equivalent. Furthermore, the formation of a second Au-N bond on the second half of ligand **BIMB** is also expected to be energetically equivalent. In the absence of any interaction between the two [C_6F_5] moieties in complex **3**, its formation is expected to be described by a 2:1 binding model where both equilibrium constants are identical. Therefore, if a difference in the binding constants is experimentally observed, this implies an interaction of the second ligand with the first one. Such an effect may produce either a higher or lower second binding constant, indicating positive and negative cooperativity respectively.

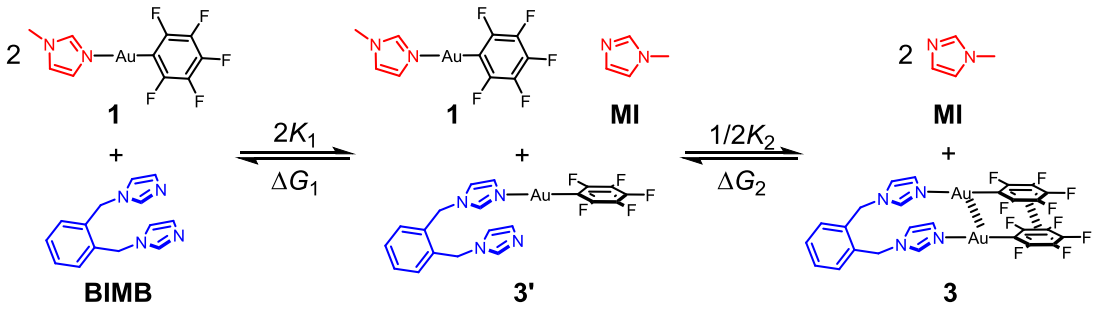

Figure 2.13 Ligand-exchange experiments of mixing complex **1** with ligand BIMB in acetone-d_6 at room temperature.

In a typical experiment, complex **1** and **BIMB** were mixed in a 2:1 ratio. At equilibrium the product distributions are governed by equilibria K_1 and K_2. As the system equilibrates, ligand **MI** in complex **1** is replaced by ligand **BIMB** generating complex **3'** and a free ligand **MI**. The energy change ΔG_1 includes breakage of an (MI)N–Au bond and formation of (BIMB)N–Au bond. In the second step, complex **1** reacts with complex **3'** to form complex **3**. The energy change ΔG_2 not only includes breakage of a (MI)N–Au bond and formation of (BIMB)N–Au bond, but also contains formation of aurophilic interactions and aromatic stacking (C_6F_5–C_6F_5). Therefore, the strength of aurophilic interactions and aromatic stacking can be calculated by using ΔG_2 to subtract ΔG_1. In other words, step 1 serves as a control step for step 2.

Complexes **1**, **3'**, and **3** showed separate / partially overlapping *para*-F peaks in ^{19}F NMR spectra (**Figure 2.14**). The peaks were assigned by comparison against the ^{19}F NMR spectra of pure complex **1** and **3**. The ratios between the integrals of complexes **1**, **3'**, and **3** in the ^{19}F NMR spectra remained constant over time (**Figure 2.15**), suggesting the equilibria are reached in less than 5 minutes.

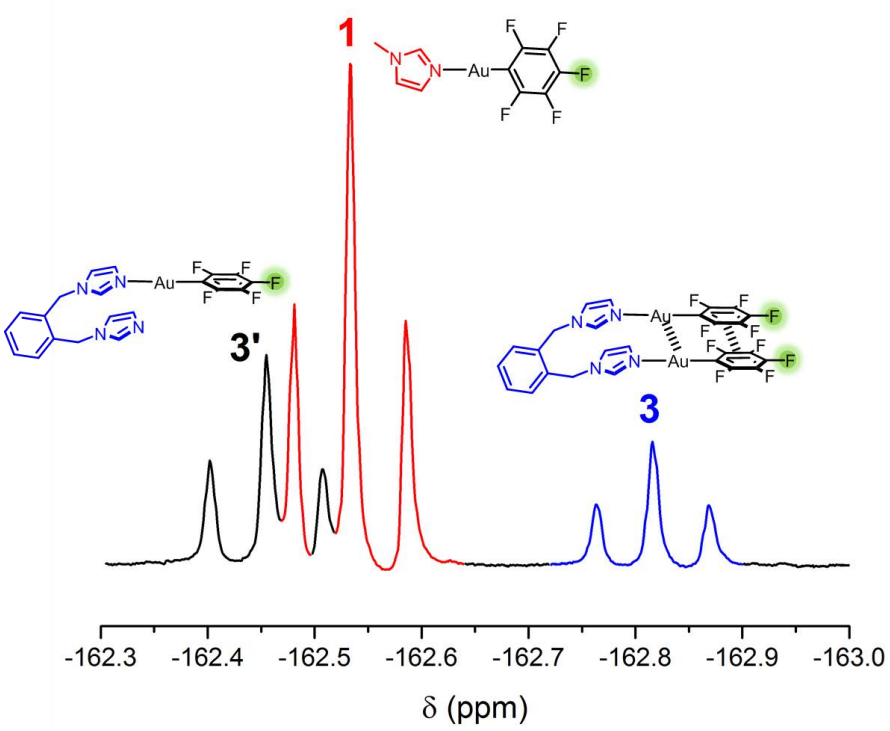

Figure 2.14 Partial ^{19}F NMR spectrum (Acetone-d_6, 376.5 MHz, 298 K) of *para*-F (highlighted in the structures) in complexes **1** (red), **3** (blue), and **3'** (black) for ligand-exchange experiments.

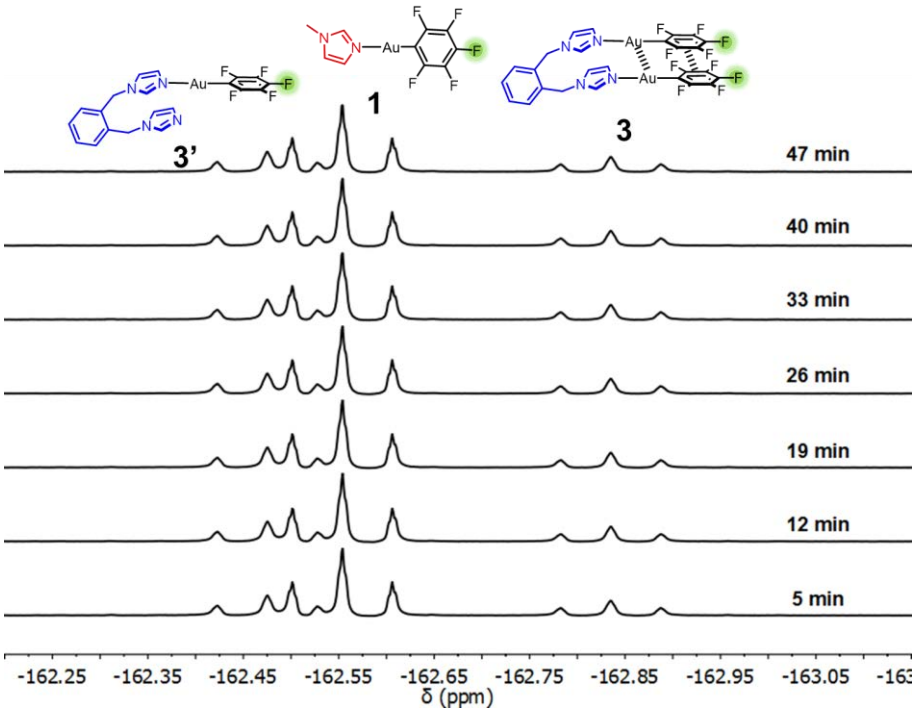

Figure 2.15 Variable-time ^{19}F NMR spectra of ligand-exchange experiments showing the exchange equilibrium is reached in 5 minutes.

Having known the initial concentrations $[\mathbf{1}]_0$ and $[\mathbf{BIMB}]_0$, the concentrations of all related species can be calculated (see Experimental 2.10.4 for calculation details) based on the NMR integrals of complexes **1**, **3'**, and **3**. The equilibrium constants K_1 and K_2 can thus be obtained by equations 1 and 2. The Gibbs free energies ΔG_1, ΔG_2, and $\Delta\Delta G$ can thus be calculated through equation 3–4. See Experimental for calculation details.

The equilibrium constant for the first step is given by:

$$2K_1 = \frac{[\mathbf{3'}][\mathbf{MI}]}{[\mathbf{1}][\mathbf{BIMB}]} \tag{1}$$

where [**1**], [**3'**], [**MI**], and [**BIMB**] are the molar concentrations of complexes **1**, **3'**, **MI**, and **BIMB**. Similarly, the equilibrium constant for the second step is:

$$1/2K_2 = \frac{[\mathbf{3}][\mathbf{MI}]}{[\mathbf{3'}][\mathbf{1}]} \tag{2}$$

where [**3**] is the concentration of complex **3**.

Gibbs free energies ΔG for each step are calculated using equation 3.

$$\Delta G = -RT\ln K \tag{3}$$

where R is the gas constant, T is the temperature.

The energy difference between the two steps, $\Delta\Delta G$, thus provides an estimate of the total energy of the aurophilic interactions and aromatic stacking (equation 4).

$$\Delta\Delta G = \Delta G_2 - \Delta G_1 = RT\ln(K_1/K_2) \tag{4}$$

2.6.2 Results and discussion

The positions of the ligand-exchange equilibria were assessed in several solvents to assess solvent effects. Ligand-exchange experiments were performed at least three times in each solvent examined and an average energy values were then calculated from the NMR integrals as described in the previous section. The obtained energies ΔG_1, ΔG_2 and $\Delta\Delta G$ in different solvents are depicted in **Figure 2.16**. In acetone, the ΔG_1 and ΔG_2 are found to be +1.4 kJ mol^{-1} and +1.7 kJ mol^{-1}, respectively. A $\Delta\Delta G$ for the total aurophilic and stacking interactions of +0.3 kJ mol^{-1} is thus determined (errors are reported as two standard deviations in the measurements). The ΔG_1 and

ΔG_2 values determined in other solvents are all small and positive (< +3 kJ mol^{-1}). Small $\Delta\Delta G$ of positive or negative values (± 2 kJ mol^{-1}) are yielded depending on the values of ΔG_1 and ΔG_2.

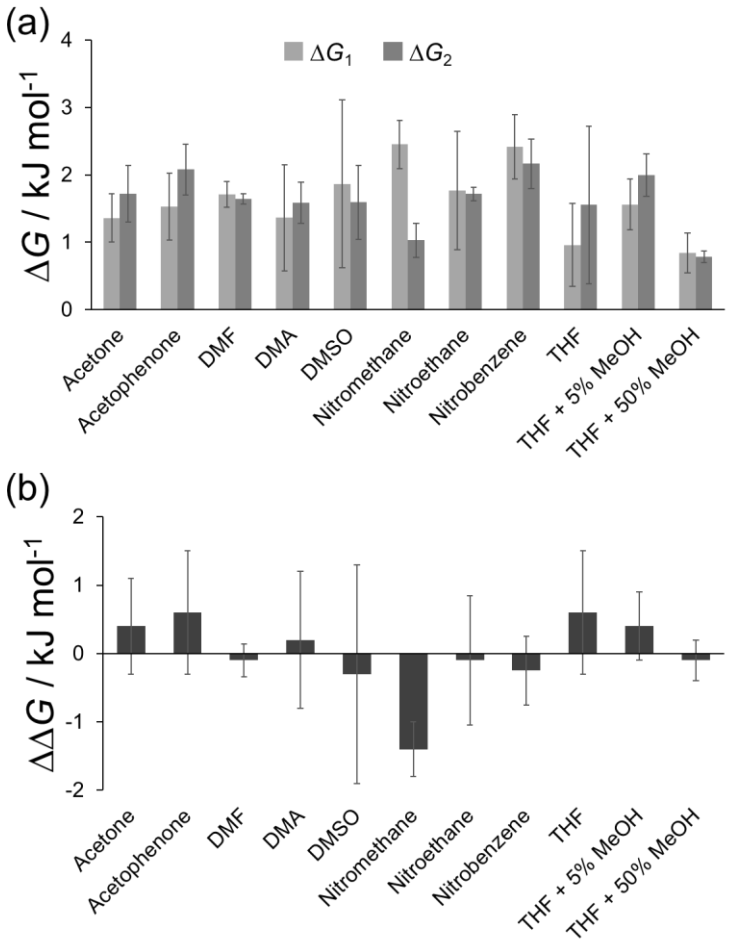

Figure 2.16 ΔG_1, ΔG_2, and $\Delta\Delta G$ in different solvents obtained from ligand-exchange experiments. Errors are 2 standard deviations.

The positive values of ΔG_1 in equilibrium step 1 suggest that the replacement of ligand MI in complex **1** by ligand **BIMB** is not favoured at room temperature. Similarly, the positive values of ΔG_2 in step 2 reveal the transformation from complex **3'** to complex **3** is not favoured at room temperature either. The subtracted energies $\Delta\Delta G$ are the strength of potential interactions between two [Au(C_6F_5)] fragments. Positive values in some solvents indicate the interactions are repulsive, while negative values imply attractive interactions. The very small values of $\Delta\Delta G$ (± 2 kJ mol^{-1}) and large experimental errors in different solvents suggest that the overall attraction of

aurophilic and aromatic stacking are very weak and even become repulsive in some solvents. Hence the strength of aurophilic interactions are not strong enough to be well expressed in solution at room temperature.

The different values of $\Delta\Delta G$ in a range of solvents suggest solvent can influence the strength of $[Au(C_6F_5)]-[Au(C_6F_5)]$ interactions. Correlations between interaction strength and solvent properties, such as polarity and cohesive energy density, have been plotted. However, no good correlation was found (see Appendix A.2).

2.6.3 Reverse ligand-exchange experiments

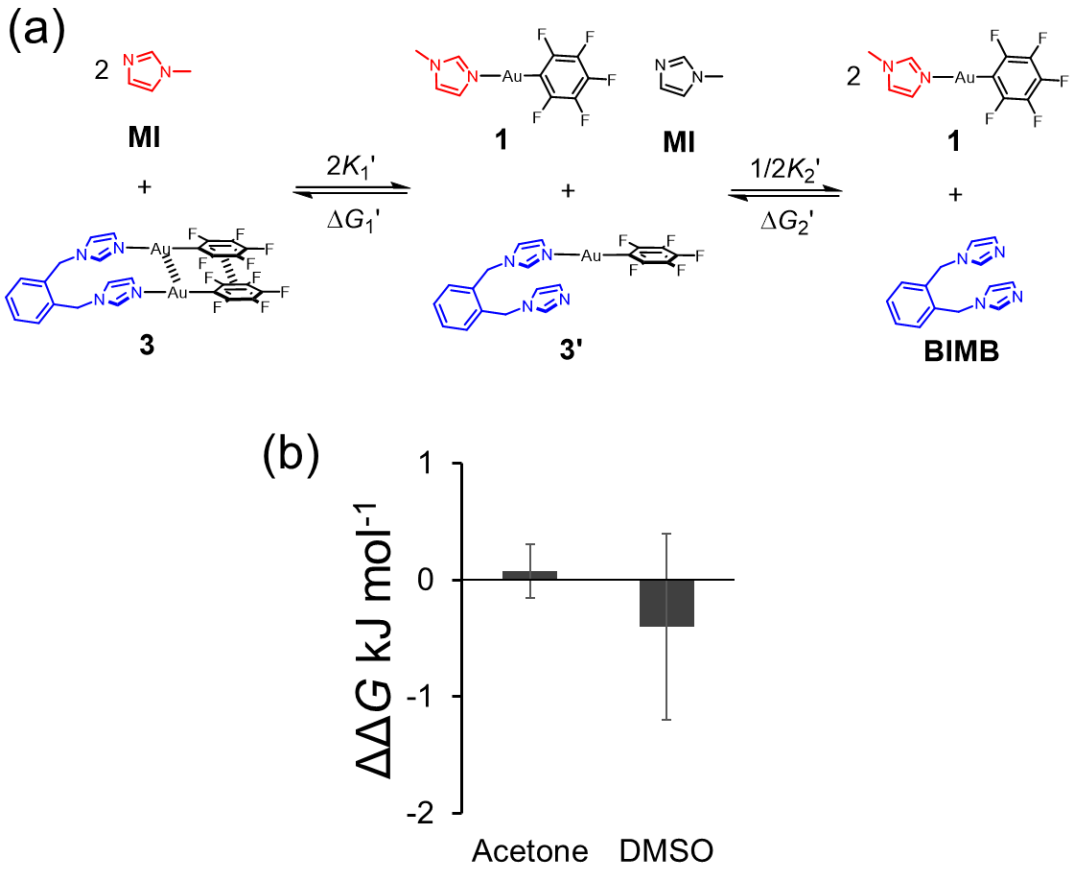

Figure 2.17 Reverse ligand-exchange experiments of adding two equivalents of ligand MI into a solution of complex **3** (a) and the obtained $\Delta\Delta G$' values in acetone and DMSO (b).

Reverse ligand-exchange experiments (**Figure 2.17a**) were also performed by adding ligand MI (2 equivalents) into the solution of complex **3** in acetone or DMSO. The equilibrium constants and Gibbs free energies were calculated using a similar method

to that described above (equations listed in Appendix A). The yielded $[Au(C_6F_5)]-[Au(C_6F_5)]$ $\Delta\Delta G$ values determined in acetone and DMSO by this alternative method were consistent with the results obtained in the forward ligand-exchange experiments, confirming the validity of the ligand-exchange approach and that the equilibrium endpoint of the system is independent of route.

Non-covalent interactions between two $[Au(C_6F_5)]$ fragments have been successfully measured by ligand-exchange approach. The measured interaction energies are very weak ($\pm$ 2 kJ mol^{-1}), and much smaller than theoretically determined values of aurophilic interactions (20–50 kJ mol^{-1}).[7,8] Different solvents show consistent weak interactions with little difference in the interaction energies. To understand and further dissect the aurophilic interactions from the $[C_6F_5]$–$[C_6F_5]$ interactions, further computational studies have been carried out.

2.7 Computational studies

The aurophilic interactions in the experimental systems were further examined through computational studies including electrostatic potential (ESP) maps, density slice, non-covalent interactions (NCI) index,[33] and energy decomposition analysis (EDA).[34–36] ESP maps were computed using the M06[37] functional and LACVP basis sets using *Spartan '14*. The LACVP series basis sets is a combination of the successful 6-31G basis set with the LANL2DZ effective core basis set.[38,39] Non-covalent interactions (NCI) analysis[33] was performed with the scalar-relativistic ZORA (zeroth-order regular approximation) Hamiltonian[40–42] and the GGA functional PBE[43] with the TZ2P basis set[44] using the *NCIPLOT* package.[45] Dispersion was accounted for using Grimme's D3 correction with Becke−Johnson damping.[46] This corresponds to a general notation of ZORA-PBE-D3BJ/TZ2P. Quantitative analysis was done using energy decomposition analysis (EDA)[34–36] embedded in the *ADF2017.110* package.[47,48] The same ZORA-PBE-D3BJ/TZ2P computational method was used for EDA calculation.

All of the single-point calculations were performed on crystal structures or modified crystal structures without geometry optimisation. Because minimisation would distort the geometries of the dimers, changing contributions from electrostatic interactions

and so on. For instance, the dimer **4'** (**Figure 2.18**), which was truncated based on the crystal structure of complex **4**, was optimised with the PBE functional and 6-31G* basis set for C, H, N, F, O, and the LANL2DZ basis set for Au using *Gaussian 09*.[49] Dispersion was accounted for using Grimme's D3 correction with Becke–Johnson damping. After optimisation, the monomer [(MBI)Au(C_6F_5)] was no longer found to be planar, and the two C_6F_5 and benzimidazole fragments do not stack. Hence, aromatic stacking and electrostatic interactions are very different from the original crystal structures, due to the lack of crystal packing influences in the gas-phase calculations on the isolated dimer.

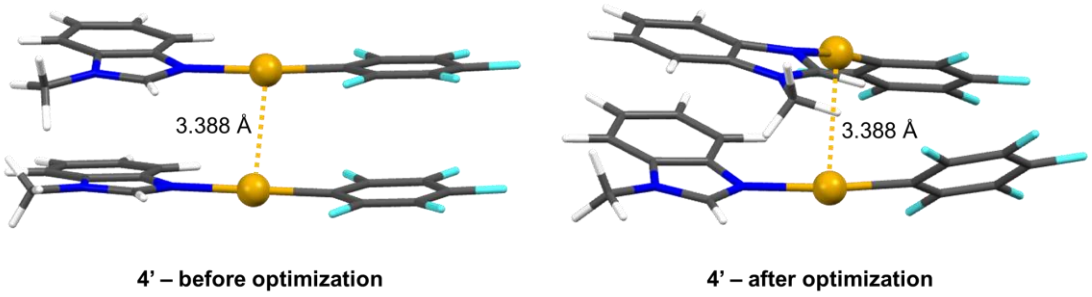

Figure 2.18 Geometries of dimer **4'** before (left) and after (right) optimisation. Optimisation method PBE/GD3BJ/LANL2DZ.

2.7.1 Electrostatic potential (ESP) maps

ESP maps of complexes **1–4** computed at DFT/M06/LACVP level of theory are shown in **Figure 2.19**. In complex **1**, the imidazole moiety is electron-poor (blue) due to a combination of both the charge and polarizing influence of the N-coordinated Au^I centre. In contrast, the C_6F_5 fragment is electron-rich (red) since this fragment bears a formal negative charge on the carbon bonded to the Au^I centre. The electrostatic attraction between the positive imidazole and negative C_6F_5 moieties makes them aggregate in an anti-parallel mode in the solid state. Similarly, complex **2** has an electron-rich C_6F_5 moiety and an electron-deficient *N*-methyl benzimidazole (MBI). Two monomers of complex **2** also dimerise in an anti-parallel mode in the solid state due to electrostatic attraction between the C_6F_5 and the MBI fragments.

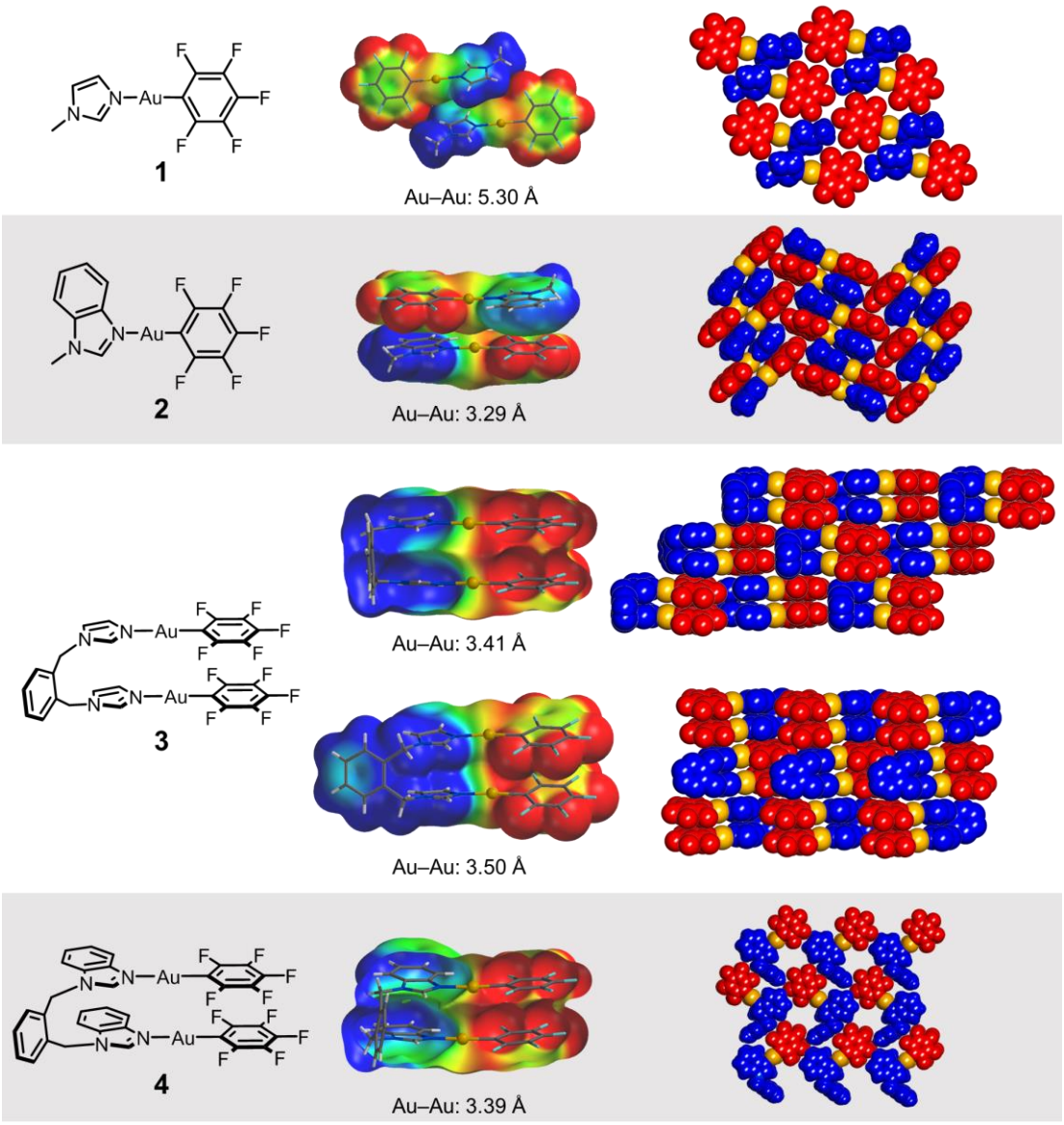

Figure 2.19 Structures (left), Electrostatic potential maps (middle) computed based on crystal structures at DFT/M06/LACVP level of theory using *Spartan '14*, and space-fill packing scheme of crystal structures (right) of complexes **1**–**4**. Electrostatic potential: < –120 kJ mol^{-1} electron-rich red, > 120 kJ mol^{-1} electron-poor blue. Space-fill crystal packing schemes: Au^{I} golden, pentafluorobenzene fragments red, imidazole fragments blue. Solvent molecules are omitted for clarity.

In contrast to complexes **1** and **2**, the two (MBI)Au(C_6F_5) arms in the half-supported complexes **3** and **4** adopt a parallel intermolecular packing mode in the solid state. The interactions between two C_6F_5 fragments or between two MI/MBI fragments are thus weaker or become repulsive. Consequently, the Au–Au distances in complexes **3** (3.41

Å and 3.50 Å) and **4** (3.39 Å) are longer than that in complex **2** (3.29 Å). Therefore, electrostatic interactions play a significant role in the molecular assembly of these complexes, and likely dominate any aurophilic interactions present. The significance of electrostatic interactions in molecular assembly can be further confirmed by the crystal space-fill schemes (**Figure 2.19**), in which the negative C_6F_5 fragments (red) and positive imidazole derivative fragments (blue) aggregate in a staggered pattern. As mentioned in chapter 1, distance is not always reliable for assessing the presence of aurophilic interactions. Electron density slices were computed at DFT/M06/LACVP level of theory using *Spartan '14*. As shown in **Figure 2.20**, the electron density slices reveal overlap between Au^I centres in complexes **2–4**, which would be consistent with the presence of aurophilic interactions. In contrast, no overlap is observed in complex **1**, demonstrating the absence of aurophilic interactions, as expected given the large separation between the Au^I centres.

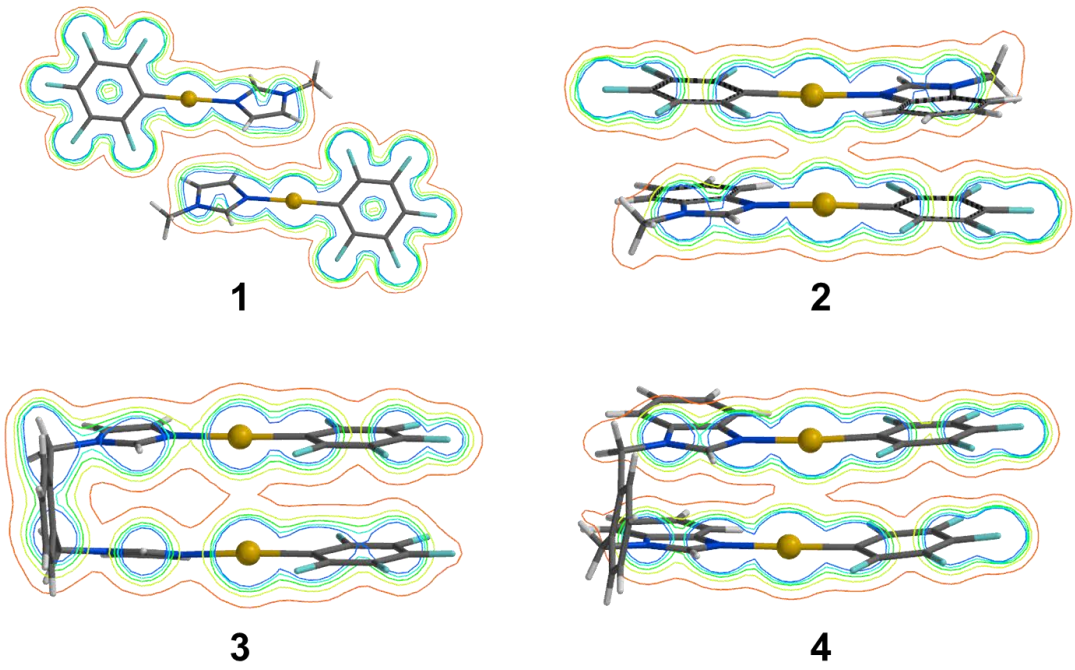

Figure 2.20 Electron density slice of complexes **1–4**. Electron densities 0.01 Bohrs/A^3 (red)–0.09 Bohrs/A^3 (blue).

2.7.2 Non-covalent interactions (NCI) analysis

For NCI analysis, the bridging phenyl group in complex **4** was deleted and replaced by two carbon-bonded hydrogen atoms to form a parallel packed dimer **4'**. Without

the conformational constraint of the phenyl bridge, the dimer **4'** would not remain in the parallel-packed structure upon geometry optimisation. Therefore, the calculations were performed on the dimer without further geometry optimisation. In order to compare the influence of packing modes on the interaction energies, the Au–Au distance in dimer **2** was shifted to 3.39 Å, matching the Au–Au distance in dimer **4'**, using *GaussView 6*.[50] The generated dimer was denoted as dimer **2'**. The similarity between dimer **2'** and dimer **4'** made it possible to study the influence of the packing mode. As we can see from **Figure 2.21**, the pale blue regions represent attraction, while red regions represent repulsion. Obviously, there are weak attractions between Au^{I} centres in both dimers, indicating the presence of aurophilic attraction. The colour in the anti-parallel packed dimer **2'** is slightly stronger than that in the parallel packed dimer **4'**, suggesting that electrostatic interactions might cooperatively strengthen intermolecular aurophilic interactions.

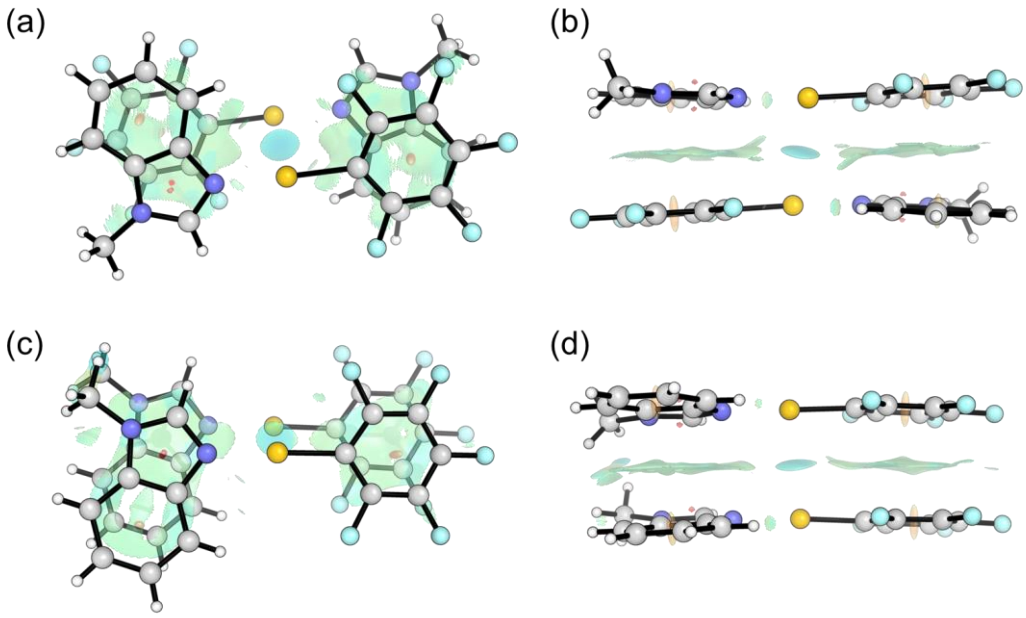

Figure 2.21 Non-covalent interactions (NCI) plots of complexes **2'** (a, b) and **4'** (c, d). Blue areas denote attractive interactions; red areas denote repulsive interactions.

2.7.3 Energy decomposition analysis (EDA)

Energy decomposition analysis (EDA)[34–36] can decompose the intermolecular interaction energy ΔE_{int} into four terms:

$$\Delta E_{int} = \Delta E_{elstat} + \Delta E_{disp} + \Delta E_{orb} + \Delta E_{Pauli}$$

ΔE_{elstat}, ΔE_{disp}, and ΔE_{orb} are electrostatic, dispersion and orbital attractions respectively. ΔE_{Pauli} is the repulsive exchange (Pauli) interaction between electrons of the two fragments having the same spin.

The complex **4** can be regarded as two fragments for EDA study. Three different types are shown in **Figure 2.22** depending on the ways of defining fragments. The black and green fragments are the two moieties used for EDA-NOCV studies. The **4a** gives the energies (ΔE_{4a}) of one N-Au coordination and the $[Au(C_6F_5)]_2$ interactions. Similarly, the **4b** provides the energies (ΔE_{4b}) of another N-Au coordination bond and the $[Au(C_6F_5)]_2$ interactions. Whereas, the energies (ΔE_{4ab}) of two N-Au dative bonds and the $[Au(C_6F_5)]_2$ interactions can be obtained from **4ab**. The interactions between two $[Au(C_6F_5)]$ moieties can thus be calculated using equation $\Delta\Delta E = \Delta E_{4a} + \Delta E_{4b} - \Delta E_{4ab}$.

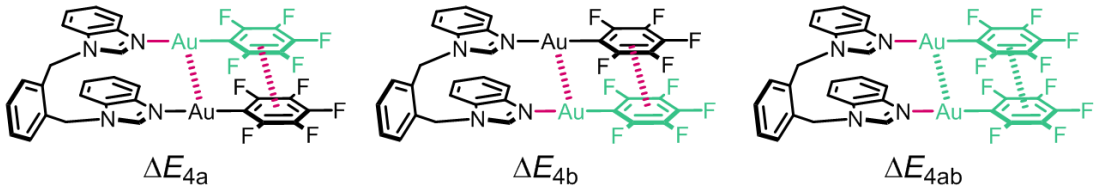

$$\Delta\Delta E = (\Delta E_{4a} + \Delta E_{4b} - \Delta E_{4ab}) / 2$$

Figure 2.22 Different regions (black and green fragments) used for energy decomposition analysis (EDA). Magenta solid and dash lines are the bonding/interactions dissected. The overall interactions $\Delta\Delta E$ between two $[Au(C_6F_5)]$ moieties are obtained using the displayed equation.

The results are shown in **Table 2.1**. The energy components of **4a** and **4b** are similar to each other. For the calculated interactions of $[Au(C_6F_5)]_2$, the attractive contributions decrease from dispersion (41%) to electrostatic (34%) to orbital (25%) components. The overall interaction energy is −25.0 kJ mol^{-1} once the strong Pauli repulsion (+57.9 kJ mol^{-1}) is also considered. This overall favourable energy is comparable to that of hydrogen bonds in the gas phase. It is very likely that this rather significant interaction energy might be cancelled in solution due to solvent competition. Indeed, the experimental data presented earlier confirm that this overall

interaction energy of −25.0 kJ mol^{-1} is certainly not well-preserved in a range of different solvents.

Table 2.1 Energy decomposition analysis results studied at ZORA/PBE-D3BJ/TZ2P. Energies in kJ mol^{-1}.

	ΔE_{int}	ΔE_{elstat}	ΔE_{disp}	ΔE_{orb}	ΔE_{Pauli}
4a	–221.7	–524.2	–49.8	–224.9	577.3
4b	–224.2	–552.9	–52.5	–233.4	614.6
4ab	–396.1	–1020.6	–34.8	–416.7	1076.0
(4a + 4b – 4ab) / 2	–25.0	–28.3 (34%)	–33.7 (41%)	–20.8 (25%)	57.9

To further isolate aurophilic interactions, the interactions in dimers **4'** and $[MBIAuH]_2$ have also been computed using EDA. Dimer $[MBIAuH]_2$ has been chosen as a control because the ESP surfaces of its MBI and C_6F_5 fragments are very similar to those in dimer **4'** (**Figure 2.23**). The intermolecular interactions between two $[MBI]_2$ fragments in $[MBIAuH]_2$ can thus be regarded as the same as those in dimer **4'**.

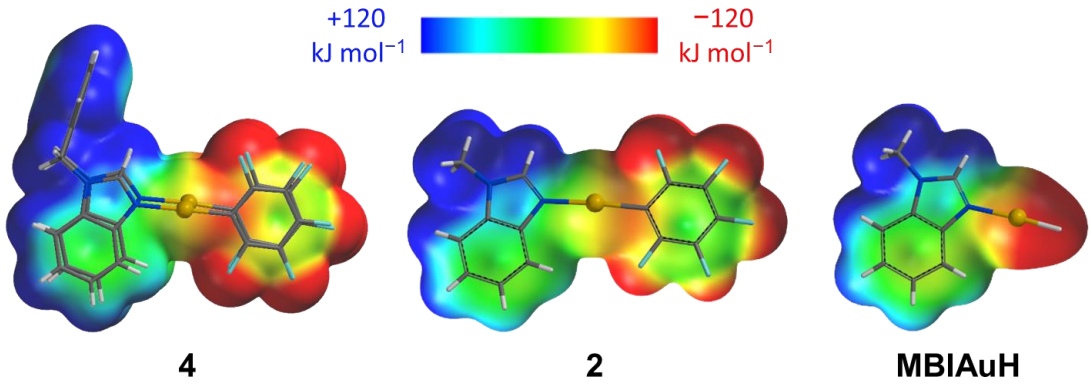

Figure 2.23 Electrostatic potential (ESP) surfaces of complexes **4**, **2** and MBIAuH calculated using Spartan '14 at M06/LACVP level.

Combining the EDA results of the dimer $[Au(C_6F_5)]_2$ (**Figure 2.22** and **Table 2.1**), the interactions for dimers $[C_6F_5]_2$, $[MBI]_2$, and $[Au]_2$ can be dissected using follow equations:

$$\Delta E_{[C6F5]2} = \Delta E_{\mathbf{4'}} - \Delta E_{[MBIAuH]2} \quad (5)$$

$$\Delta E_{[MBI]2} = \Delta E_{\mathbf{4'}} - \Delta E_{[AuC6F5]2} \quad (6)$$

$$\Delta E_{[Au]2} = \Delta E_{\mathbf{4'}} - \Delta E_{[C6F5]2} - \Delta E_{[MBI]2} \quad (7)$$

where $\Delta E_{\mathbf{4'}}$, $\Delta E_{[C6F5]2}$, $\Delta E_{[MBI]2}$, $\Delta E_{[MBIAuH]2}$, and $\Delta E_{[Au]2}$ are EDA calculated energies of dimers **4'**, $[C_6F_5]_2$, $[MBI]_2$, $[MBIAuH]_2$ and $[Au]_2$, respectively.

The results are summarised in **Figure 2.24**. In the dimer **2'**, electrostatic attraction (−92.0 kJ mol^{-1}) plays a dominant role though dispersion (−72.1 kJ mol^{-1}) and orbital delocalisation (−34.5 kJ mol^{-1}) also contribute significantly. The strong Pauli repulsion (+92.6 kJ mol^{-1}) results in an overall stabilising energy of −102.4 kJ mol^{-1}. In the dimer **4'**, the electrostatic attraction (−51.1 kJ mol^{-1}) is much weaker. The dispersion (−81.0 kJ mol^{-1}) and orbital interactions (−46.0 kJ mol^{-1}) are slightly increased. The Pauli repulsion (+153.6 kJ mol^{-1}) is much stronger. The total interaction energies (−24.5 kJ mol^{-1}) are significantly decreased. The different results of dimers **2'** and **4'** explain that the less stable parallel packing than anti-parallel stacking is mainly due to the weaker electrostatic attraction and the stronger Pauli repulsion. For dimer $[MBIAuH]_2$, the values of all the energy components become smaller, resulting an negligible overall interactions.

Surprisingly, the highly polarized $[C_6F_5]_2$ fragment has an overall favorable interaction (ΔE = −25 kJ mol^{-1}) and even has a favorable electrostatic component. Dispersion is the dominant attractive component and orbital component is quite weak. The overall energy of the $[C_6F_5]_2$ fragment is approximately the same as the $[AuC_6F_5]_2$ fragment and even the overall dimer **4'**, indicating that the intermolecular attraction in dimer **4'** is due solely to the presence of attraction between $[C_6F_5]$ fragments. Consequently, dimers $[MBI]_2$, and $[Au]_2$ display negligible overall interactions. Despite the overall negligible interaction, the attractive component of the aurophilic interaction is dominated by orbital interactions, with almost no contribution from dispersion.

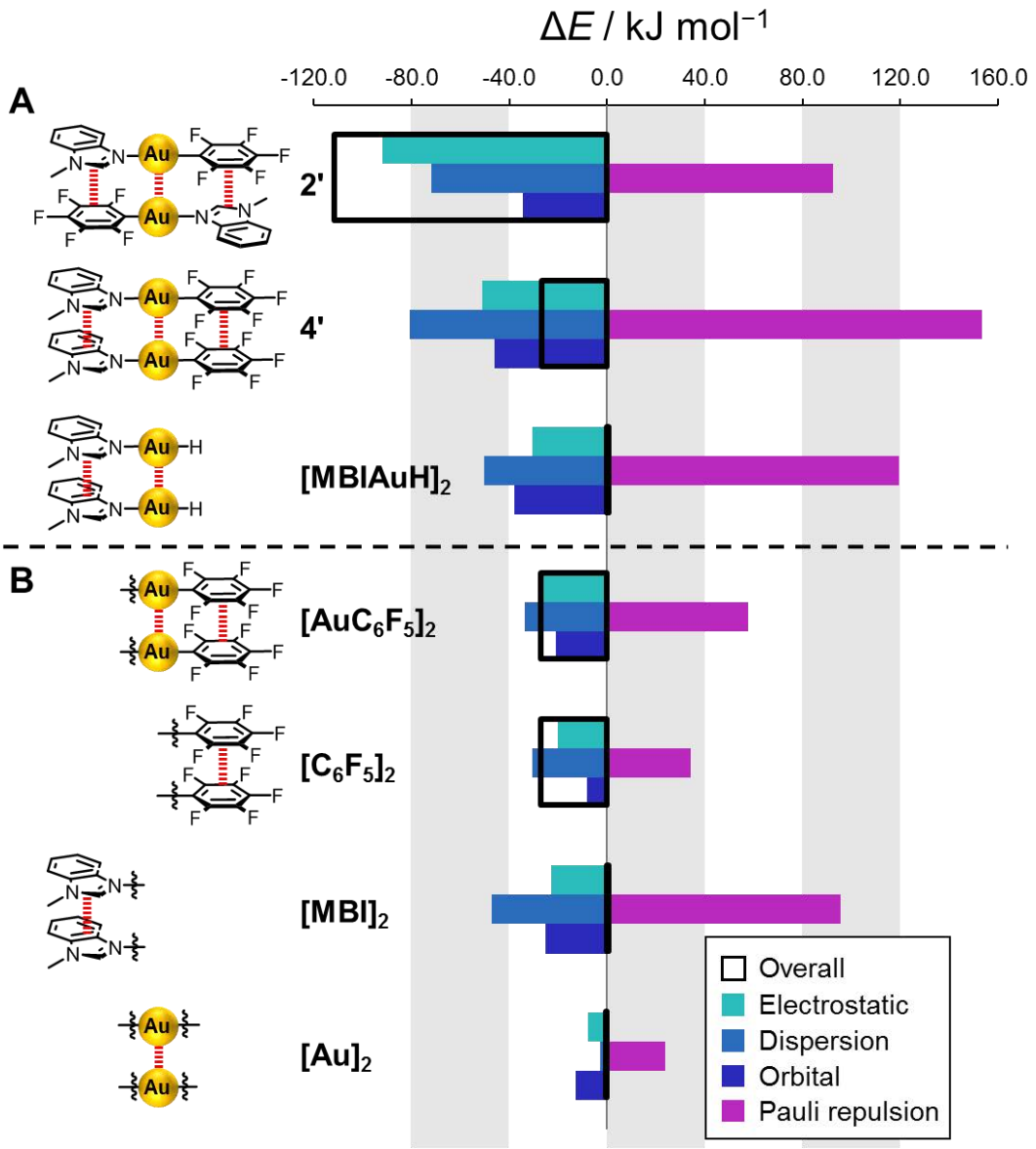

Figure 2.24 Energy decomposition analysis (EDA) results. The overall interactions (black empty) are decomposed into electrostatic interactions (cyan), dispersion interactions (pale blue), orbital interactions (dark blue), and Pauli repulsion (magenta). (**A**) EDA calculations were performed on dimers **2'**, **4'**, $[MBIAuH]_2$, which are computationally modified structures generated from the crystal structure of **4**. (**B**) Fragments dissected from complex **4,** dimer **4'**, and dimer $[MBIAuH]_2$. Computation performed using ADF2017.110 package at PBE-D3BJ/TZ2P/Scalar ZORA level.

The extended transition state method combined with natural orbitals for chemical valence (ETS-NOCV, also called EDA-NOCV),[51,52] as implemented in ADF, have also been computed to further study contributions to orbital interactions. The ΔE_{orb} is

decomposed into pairwise energy contributions for each pair of interacting orbitals. The deformation density (**Figure 2.25**) is used to describe the difference between the electron density of the fragments before and after interacting. Red areas denote electron density depletion, while blue areas denote density accumulation.

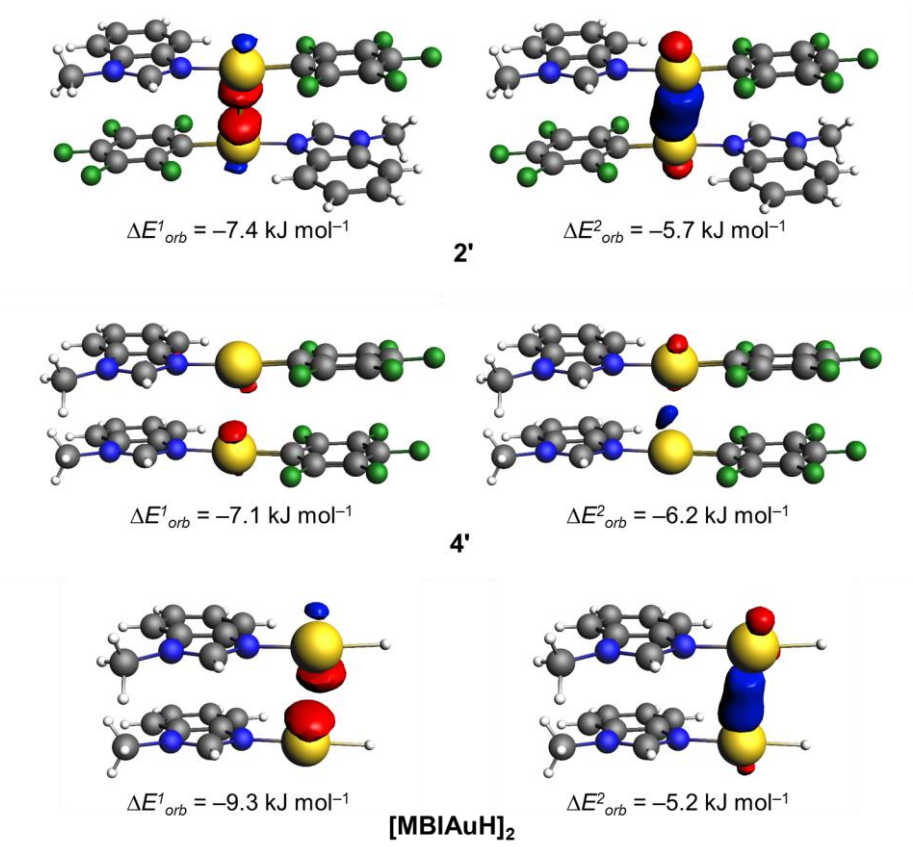

Figure 2.25 NOCVs for complexes **2'**, **4'**, and $[MBIAuH]_2$. Red areas denote electron density depletion, blue areas denote density accumulation. Cut-off value ±0.001 a.u. Atom colour codes: yellow Au, green F, blue N, grey C, white H. Computation performed using ADF2017.110 package at PBE-D3BJ/TZ2P/Scalar ZORA level.

In the dimer **2'**, the dominant NOCV (ΔE^1_{orb}) describes a depletion (red) of electron density between the Au centres and an accumulation (blue) at the outer side of the Au centres. Whereas the second significant NOCV (ΔE^2_{orb}) shows density flows from outer side of the Au–Au contacting to inner side. The first two NOCVs have a sum energy of −13.1 kJ mol^{-1}, contributing 39% to the total orbital interactions (−34.5 kJ mol^{-1}). The NOCVs of dimer **4'** show similar electron depletion and accumulation in the 1st and 2nd NOCVs. The orbital energies are −7.1 and −6.2 kJ mol^{-1}, which are similar to those of dimer **2'**. The NOCVs of dimer $[(MBI)AuH]_2$ also give consistent

results that the most significant two orbital interactions are from Au–Au contact. Their energies are also close to those in dimers **2'** and **4'**.

Obviously, the most significant two NOCVs are all related to Au centres, revealing the dominant contribution of aurophilic interactions to orbital interactions. It also suggests that aurophilic interactions have an orbital nature (partially at least). The two NOCVs have a sum energy of –13 kJ mol^{-1} to –15 kJ mol^{-1}, which contributes about 40% to the total orbital interactions. In addition, the similar values of ΔE^1_{orb} and ΔE^2_{orb} in dimer **2'** and **4'** suggest that changing the packing mode from anti-parallel to parallel does not affect the strength of aurophilic interactions.

ESP studies qualitatively indicate that electrostatic interactions contribute significantly to molecular assembly. NCI analysis demonstrates the presence of weak aurophilic interactions and weak attractions in dimeric [MBI][C_6F_5], [MBI]$_2$, and [C_6F_5]$_2$ fragments. EDA computations allow a quantitative analysis of intermolecular interactions. The interactions in dimer [Au(C_6F_5)]$_2$ are around –25 kJ mol^{-1}. The relatively weak interactions in gas phase can be easily cancelled out by competitive solvation interactions. This explains why the experimentally measured energies of [Au(C_6F_5)]$_2$ are very weak. Pure aurophilic interactions are singled out to be almost 0 kJ mol^{-1}. The combination of these theoretical findings alongside the experimental ones strongly suggest that aurophilic interactions are very weak. Their energetic contribution to molecular assembly is insignificant. The nature of aurophilic interactions are attributed to orbital interactions, at least partially, based on the fact that the dominant NOCVs are all related to Au centres.

2.8 Other literature examples

The study of aurophilic interactions has been expanded to several selected literature examples[1,53,54] to examine the generality of our findings. Complexes **5** is the molecular balance utilised by Schmidbaur[1] to estimate the strength of aurophilic interactions. The ESP and EDA results have been summarised in **Figure 2.26**. As we can see from ESPs of complex **5**, the negative chloride atoms interact strongly with the positive PMe_3 group from the other molecule though the two chloride atoms seem to be repulsive

with each other. This suggests electrostatic interactions contribute significantly in structure construction.

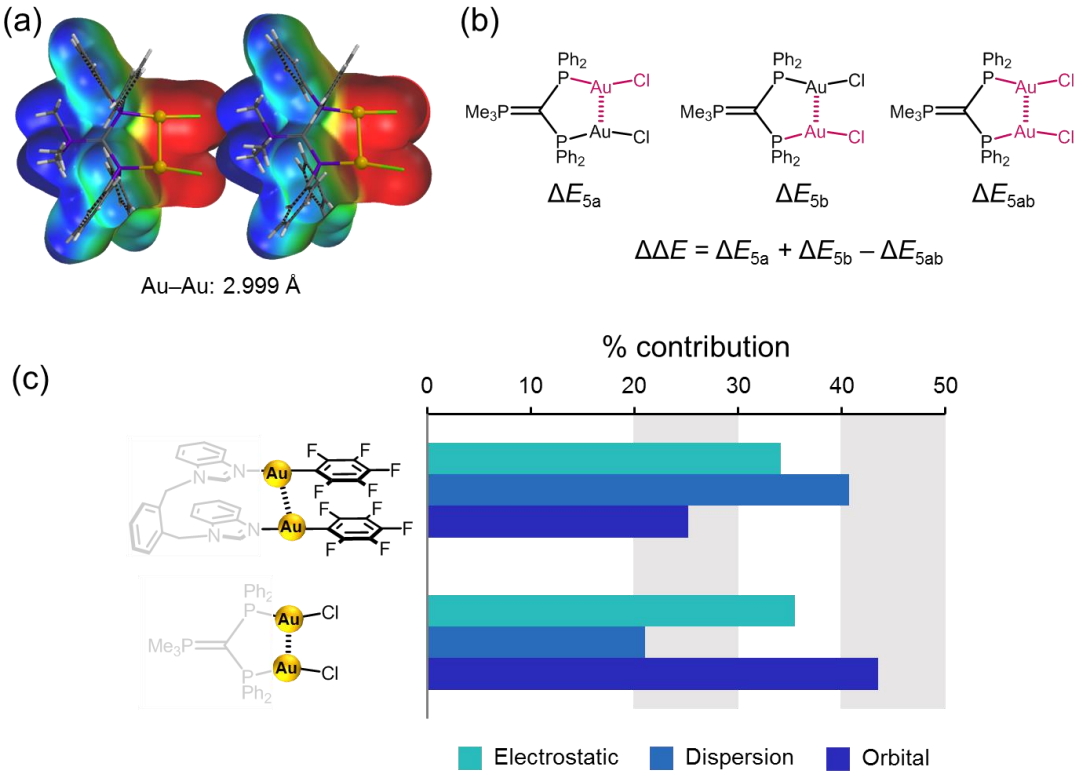

Figure 2.26 ESP maps (a), energy decomposition method (b) and of complexes **5**, and the percentage contribution of electrostatic, dispersion, and orbital interactions to the total attractions in the dimers $[AuCl]_2$ and $[AuC_6F_5]_2$ (c). The red and black fragments in (b) are the fragments defined for energy decomposition analysis. Electrostatic potential: < –120 kJ mol^{-1} electron-rich red, > 120 kJ mol^{-1} electron-poor blue.

The interactions in the dimer $[AuCl]_2$ are dissected out by the method shown in **Figure 2.26**b, and the results are compared with the interactions in the dimer $[AuC_6F_5]_2$ from complex **4** (**Figure 2.26**c). Since the Au–Au distances in the dimers $[AuCl]_2$ and $[AuC_6F_5]_2$ are different, percentage contribution of different energy components (electrostatic, dispersion, orbital) to the total attraction (sum of electrostatic, dispersion, orbital) are more appropriate for comparison. Electrostatic attraction plays a significant role though not the most important. This is reasonable since that the head-to-head packing (two electron-rich $[AuC_6F_5]$ fragments or two Cl atoms stack with each other) weakens the intermolecular electrostatic attraction. Dispersion contributes the most and orbital attraction contribute the least in the dimer $[AuC_6F_5]_2$. Whereas in

the dimer $[AuCl]_2$, a reverse trend is observed. The weaker dispersion in the dimer $[AuCl]_2$ is due to much less interacting area than that in the dimer $[AuC_6F_5]_2$.[55] The stronger orbital interactions is ascribed to the shorter Au–Au distance (3.4 Å for **4**, 3.0 Å for **5**).

The semi-perpendicularly packed complexes **6** and **7** dimerise perpendicularly so that the interference from the interactions except aurophilic interactions would be minimised (**Figure 2.27**). Their ESP maps still show attractions between positive and negative fragments. This is further confirmed by the dominant role of electrostatic attraction in the EDA results. Hence, electrostatic interactions help to stabilise the structure even in these semi-perpendicular packed dimers.

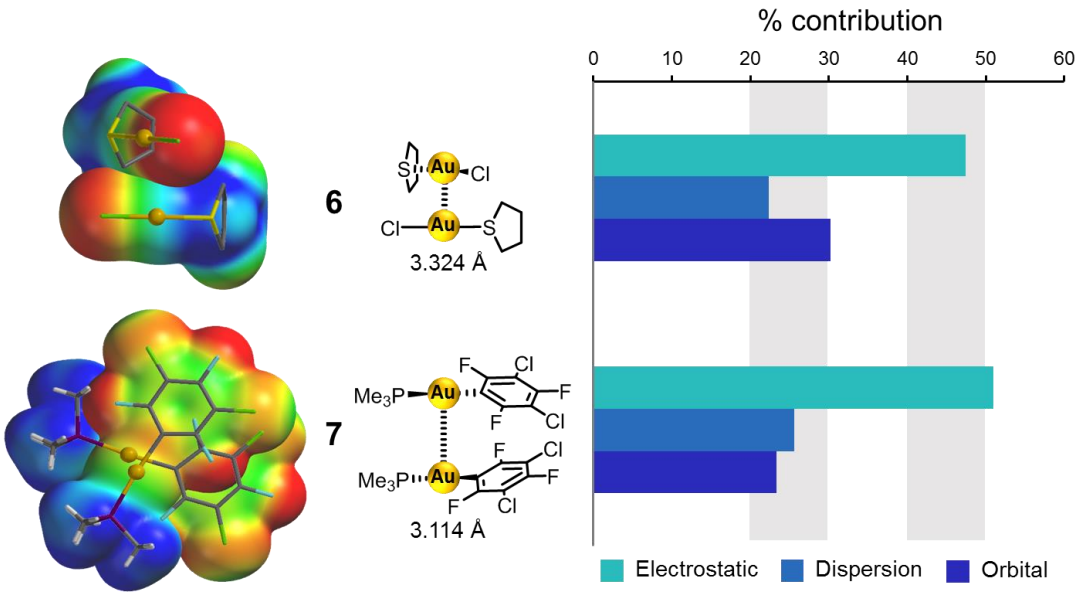

Figure 2.27 ESP maps and EDA results of complexes **6** and **7**.[54,55] Electrostatic potential: < –120 kJ mol^{-1} electron-rich red, > 120 kJ mol^{-1} electron-poor blue.

The NOCVs of complexes **6** and **7** (**Figure 2.28**) demonstrate the first and the second key orbital pairs are related to the depletion and accumulation of electron density between the gold centres, confirming the orbital nature of aurophilic interactions.

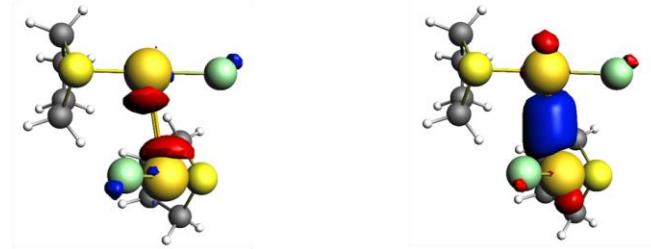

6

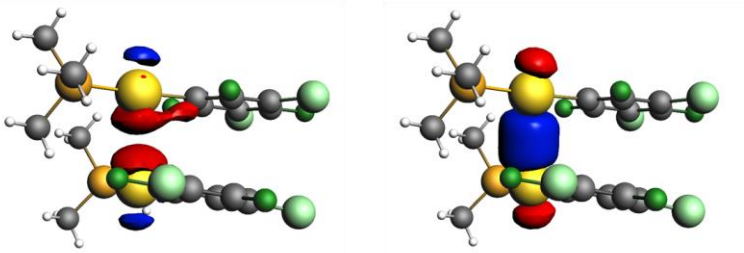

7

Figure 2.28 NOCVs for selected literature complexes. Red areas denote electron density depletion, blue areas denote density accumulation. Cut-off value ±0.001 a.u. Atom colour codes: golden Au, green F, pale green Cl, blue N, grey C, yellow S, white H.

These literature examples **5–7** show consistent results with complexes **1–4** that electrostatic attraction plays a dominant role rather than aurophilic interactions. The strength of aurophilic interactions is weak and this type of interaction is a key contributor to the orbital interactions.

2.9 Conclusions

Complexes **1**–**4** have been synthesised and employed to experimentally and computationally study the strength and nature of aurophilic interactions. Single-crystal structures indicate the presence of aurophilic interactions in complexes **2**–**4** in the solid state. The overall energies of aurophilic interactions and aromatic stacking (interactions in $[Au(C_6F_5)]_2$) have been estimated through NMR ligand-exchange experiments containing complexes **1** and **3**. The experimental measured energies are very small and negligible (±2 kJ mol^{-1}) in a range of different solvents. ESP maps, and the crystal packing modes of numerous X-ray structures demonstrate the dominant role of electrostatic interactions rather than aurophilic interactions in molecular assembly. NCI index studies illustrate the presence of weak attractive aurophilic interactions. EDA calculation confirm the dominant contribution from electrostatic interactions. The sum of aurophilic interactions and aromatic stacking in complex **4** in the gas phase is calculated to be of medium strength (−50 kJ mol^{-1}), but the isolated aurophilic interactions are found to be positive (+20.7 kJ mol^{-1}) which implies the weak strength of aurophilic interactions. The major attractive component between the Au centres is orbital interactions. EDA-NOCV studies show that aurophilic interactions contribute the most to orbital interactions. Further ESP and EDA-NOCV studies on selected literature complexes **5**–**7** illustrate consistent results, confirming that aurophilic interaction are weak and contribute little in molecular assembly. Instead, electrostatic interactions play a dominant role. Care should be paid in future studies of organometallic complexes to avoid potential overestimation of the energetic significance of aurophilic interactions.

2.10 Experimental

Chemicals and solvents were purchased from commercial suppliers and used without purification (unless stated otherwise). Dry solvents were obtained from the *PureSolv* solvent purification system. Analytical TLC was carried out on *Merck* aluminium sheets coated with silica gel 60F and visualized using UV light (254 nm). Melting points were obtained on a *Gallenkamp* melting point apparatus. Mass spectrometry was performed using the University of Edinburgh technician-supported mass spectrometry service, on a *ThermoElectron MAT XP* spectrometer for ESI-HRMS. UV-vis spectroscopy was performed on a Varian Cary 50 Scan UV Visible Spectrophotometer. Analytical solvents were used without further purification. ^{1}H, ^{13}C NMR and ^{19}F NMR spectra were measured on either 400 MHz Bruker Avance III spectrometer equipped with broadband BBFO+ ATMA probe or 500 MHz Bruker Avance III spectrometer equipped with carbon optimised dual ^{1}H/^{13}C DCH ATMA cryo-probe. Single-crystal X-ray diffraction was performed on an Agilent Technologies SuperNova diffractometer equipped with an Oxford Cryosystems Cryostream 700+ low-temperature apparatus operating at T = 120.0 K. Using **Olex2**[56], the structure was solved with the **ShelXS**[57] structure solution program, using the Patterson Method. The model was refined with **ShelXL**[57] using Least Squares minimisation. All non-hydrogen atoms were refined anisotropically. Hydrogen atom positions were calculated geometrically and refined using the riding model.

2.10.1 Synthesis

Preparation of complex 3

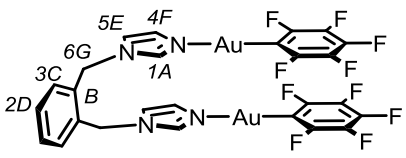

Ligand BIMB (0.095 g, 0.40 mmol) was dissolved in dry CH_2Cl_2 (2 mL) and added dropwise to a solution of $Au(C_6F_5)(tht)$ (0.090 g, 0.20 mmol) in CH_2Cl_2 (10 mL) under a nitrogen atmosphere. The mixture was heated and kept refluxing overnight. The resulted solution was concentrated (2 mL) and then Et_2O (2 mL) was added. After keeping in refrigerator (0–5 °C) overnight, the precipitated white solid was collected by filtration, washed with ether and dried under vacuum (0.109 g, 55%). M.p. 172 °C (decomposed). ^{1}H NMR (500 MHz, Acetone-d_6) δ 8.19

(t, J = 1.4 Hz, 2H, *1*), 7.57 – 7.51 (m, 2H, *2*), 7.48 (dd, J = 5.6, 3.5 Hz, 2H, *3*), 7.46 (t, J = 1.5 Hz, 2H, *4*), 7.26 (t, J = 1.4 Hz, 2H, *5*), 5.68 (s, 4H, *6*). ^{13}C NMR (126 MHz, Acetone-d_6) δ 140.42 (*A*), 134.60 (*B*), 131.41 (*C*), 130.70 (*D*), 129.87 (*E*), 121.76 (*F*), 49.73 (*G*). ^{19}F{^{1}H} NMR (376 MHz, Acetone-d_6) δ −116.31 – −116.50 (*o*-F, m), -162.86 (*p*-F, tt, J = 19.7, 1.3 Hz), −165.17 – −165.39 (*m*-F, m). Carbons of pentafluorophenyl ring cannot be assigned as they cannot be seen in ^{13}C NMR spectrum. MS (ESI) obtained *m/z* 989.0280 $[M+Na]^+$ (expected 989.0282), 799.0466 $[M-C_6F_5]^+$ (expected 799.0464), 603.0842 $[M-C_6F_5-Au+H]^+$ (expected 603.0877).

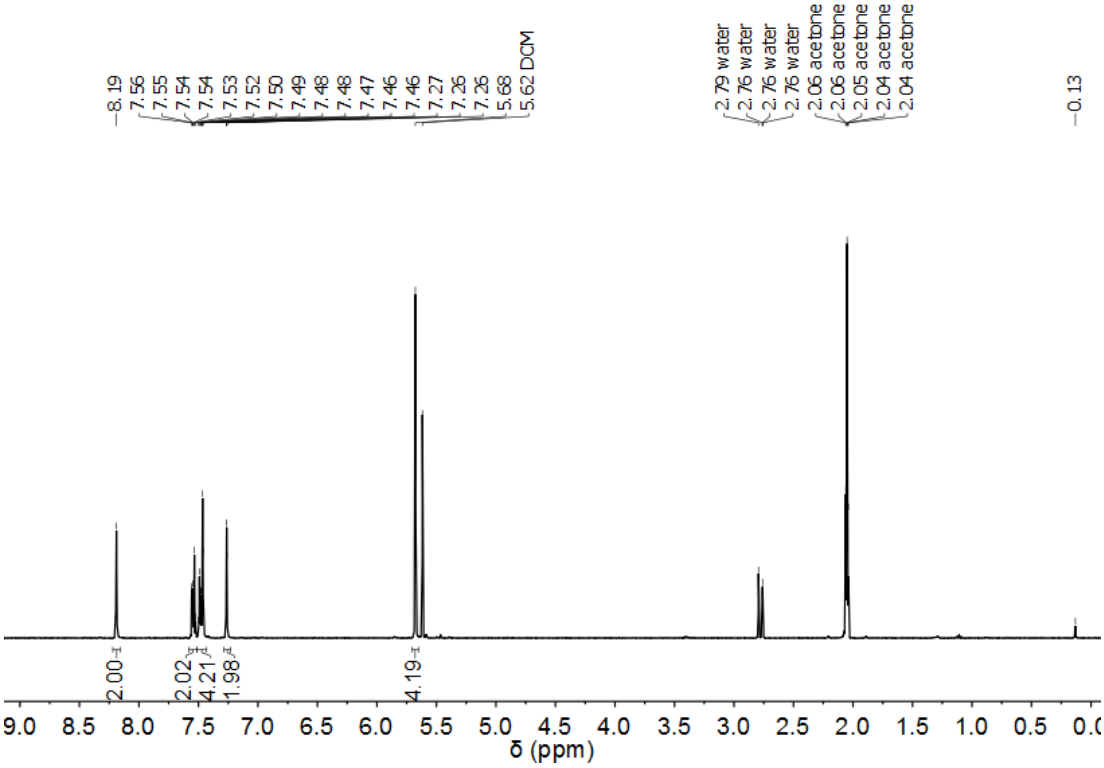

Figure 2.29 ^{1}H NMR spectra of complex **3** in acetone-d_6.

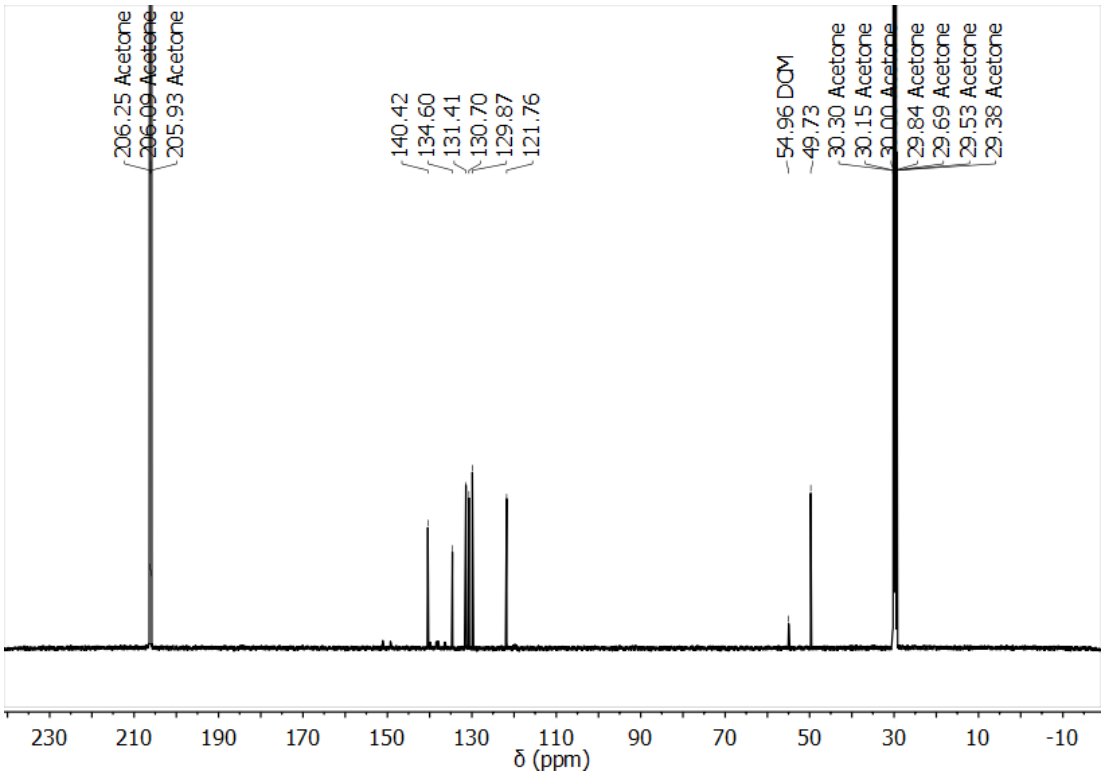

Figure 2.30 ^{13}C NMR spectra of complex **3** in acetone-d_6.

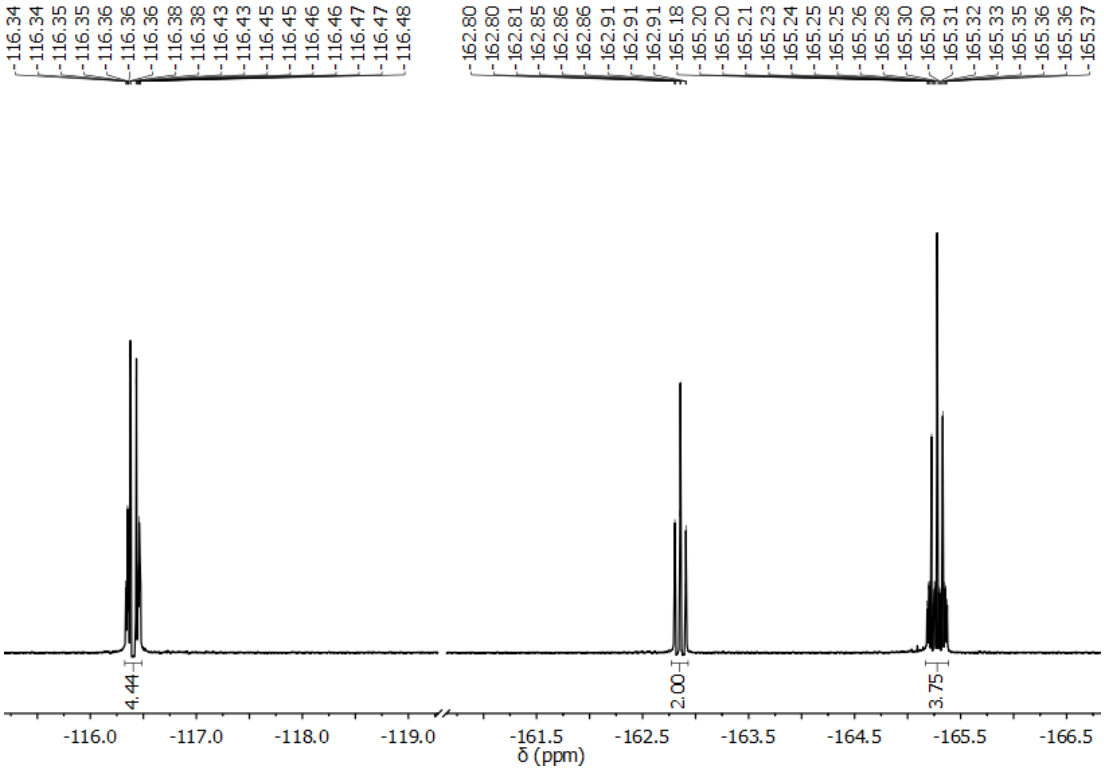

Figure 2.31 ^{19}F NMR spectra of complex **3** in acetone-d_6.

Preparation of 4

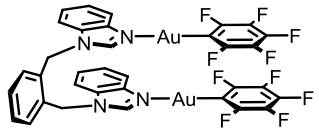

Complex **4** was prepared using the same procedure to complex **3**, except that ligand **BIMB** was replaced by ligand **BBIMB**. White solid (53 %) was obtained, m.p. 225 (decomposed). ^{1}H NMR (500 MHz, Acetone-d_6) δ 8.47 (s, 2H), 7.81 (dt, J = 8.2, 1.0 Hz, 2H), 7.66 – 7.57 (m, 6H), 7.42 – 7.35 (m, 2H), 7.36 – 7.29 (m, 2H), 5.94 (s, 4H, *8*). ^{13}C NMR (126 MHz, Acetone-d_6) δ 146.04, 141.11, 134.17, 133.30, 132.34, 131.12, 126.15, 125.55, 119.29, 112.66, 48.42. ^{19}F NMR (471 MHz, Acetone-d_6) δ −116.25 – −116.63 (m, *ortho*-F), −163.12 (t, J = 20.7 Hz, *para*-F), −165.18 – −165.64 (m, *meta*-F). MS (ESI) obtained *m/z* 703.1177 $[M–Au–C_6F_5+H]^+$ (expected 1066.0703 M^+, 703.1190 $[M–Au–C_6F_5+H]^+$).

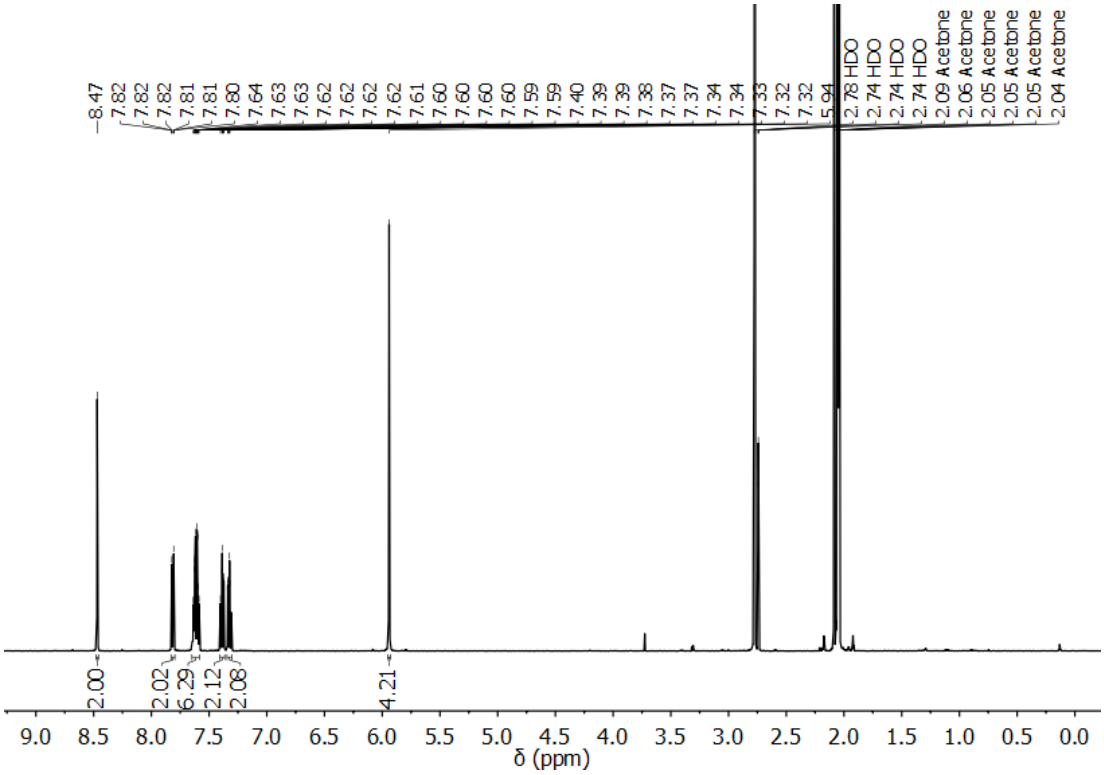

Figure 2.32 ^{1}H NMR spectra of complex **4** in acetone-d_6.

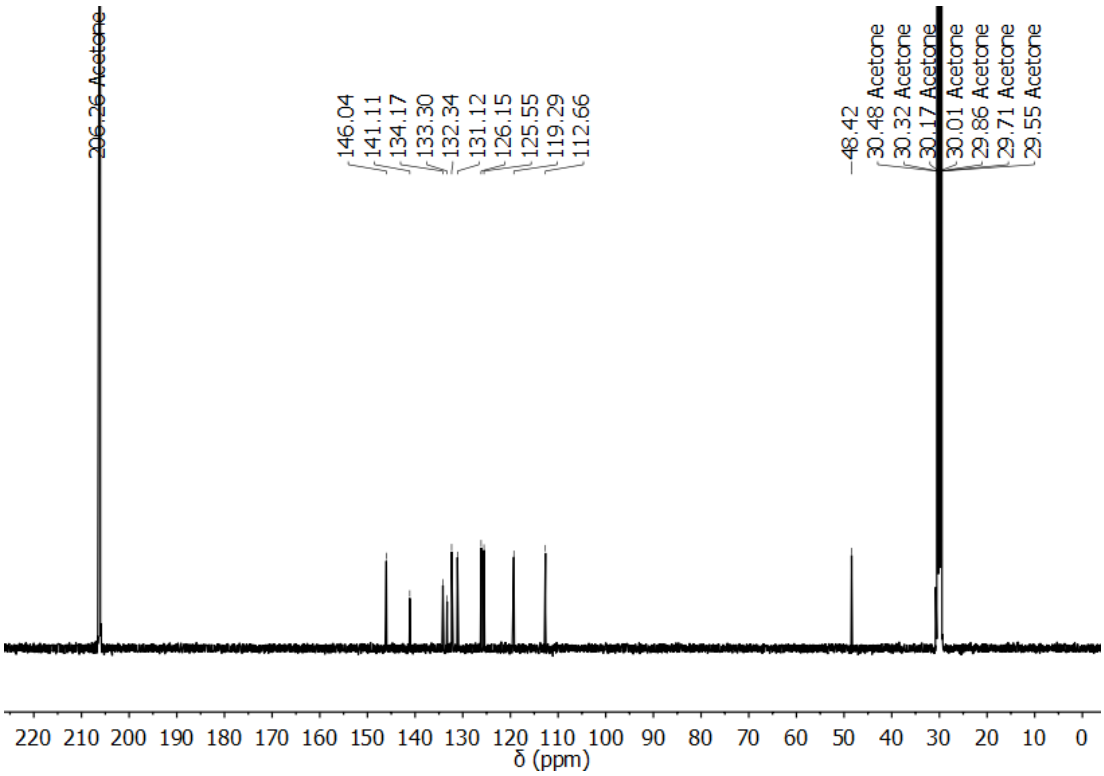

Figure 2.33 ^{13}C NMR spectra of complex **4** in acetone-d_6.

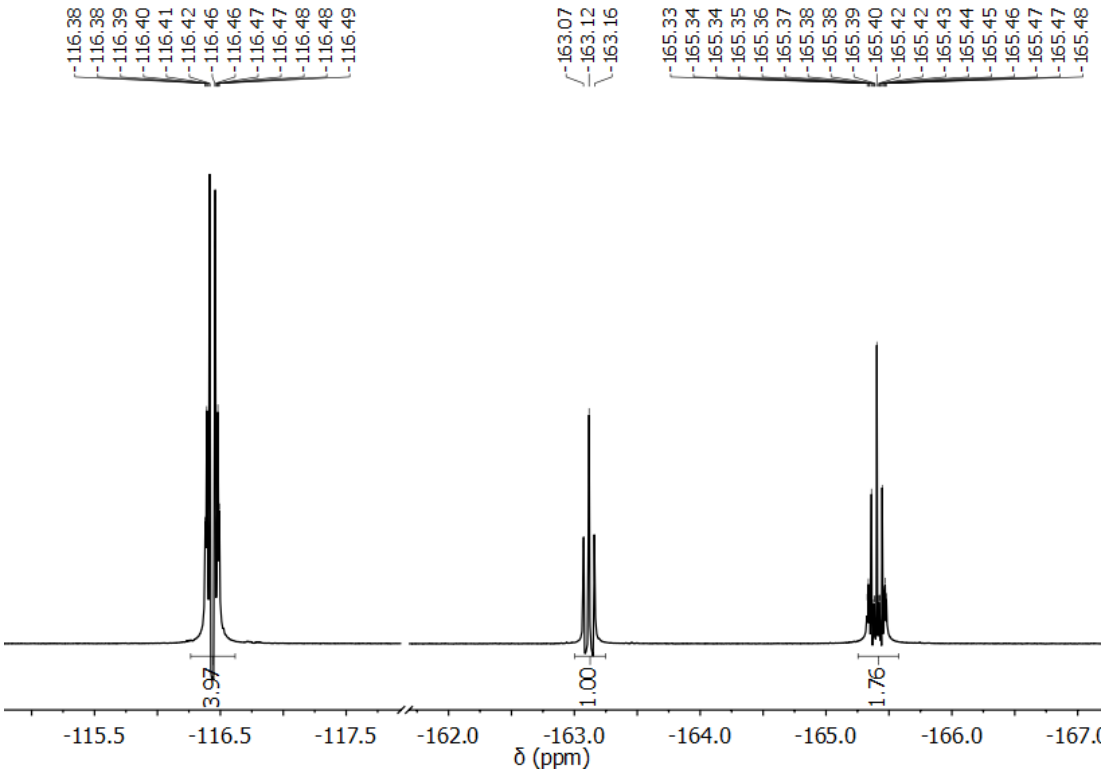

Figure 2.34 ^{19}F NMR spectra of complex **4** in acetone-d_6.

2.10.2 NMR dilution experiments

NMR tubes, precision glassware and glass syringes were dried under vacuum before use. Deuterated solvents were initially stood over activated 4 Å molecular sieves for a minimum of 24 h. Non-deuterated anhydrous solvents were used directly as commercially obtained anhydrous solvents or were distilled under reduced pressure from analytical-grade solvents. NMR dilution experiments were conducted in Wilmad screw-cap NMR tubes. Internal standards consisted of 25 mM trifluoroacetic acid in for C_6D_6 for ^1H and ^{19}F NMR studies, and were sealed in a glass capillary tube and then inserted into the NMR tube. NMR dilution experiments were only performed for complexes **2** and **3**, because the solubility of complex **4** was poor and complex **1** did not show aurophilicity even in the solid state.

Stock solutions of complexes **2** or **3** in acetone with almost saturated concentrations were prepared first. Then a known amount of the stock solution was added to a Willmad-cap NMR tube containing 350 μL of solvent and a sealed internal standard. ^1H and ^{19}F NMR spectra were recorded. Further amounts of the stock solution were added and spectra were measured. The procedure was repeated for several concentration points.

2.10.3 Ligand-exchange experiments

Solvents were processed the same way adopted in NMR dilution experiments. Wilmad screw-cap NMR tubes were dried under vacuum before use. Stock solutions (0.5 mL) containing complex **1** and ligand BIMB with a 2:1 ratio in different solvents were prepared. The concentration varied depending on the solubility of the related species, like **1**, **3**, **3'**, BIMB and MI. The solution was kept still for at least 10 mins to stabilise the equilibrium. Then the solution was transferred to a NMR tube for ^1H and ^{19}F NMR spectroscopy. Since the ^{19}F NMR spectra were much simpler and cleaner than the corresponding ^1H NMR spectra, ^{19}F NMR spectra were mainly used to monitor the exchange. ^1H NMR spectra served as complimentary proofs. Three partially overlapped peaks in ^{19}F NMR spectra were assigned to complexes **1**, **3** and **3'** by comparing with the ^{19}F NMR spectra of pure complexes **1** and **3** (**Figure 2.35**). The influence of concentration was investigated by dilution ^{19}F NMR spectra. As shown in **Figure 2.36**, the integrals of *para*-F in complexes **1**, **3** and **3'** kept the same upon

varying concentration. Therefore, the equilibrium of the ligand-exchange experiments were concentration independent.

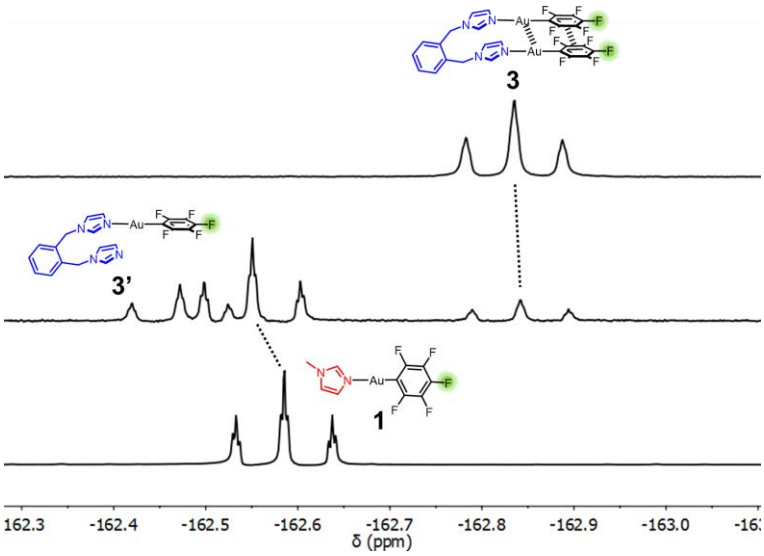

Figure 2.35 Partial ^{19}F NMR spectra (acetone-d_6, 298 K) showing peaks corresponding to *para*-F (highlighted in green) in complexes **1**, **3** and **3'**.

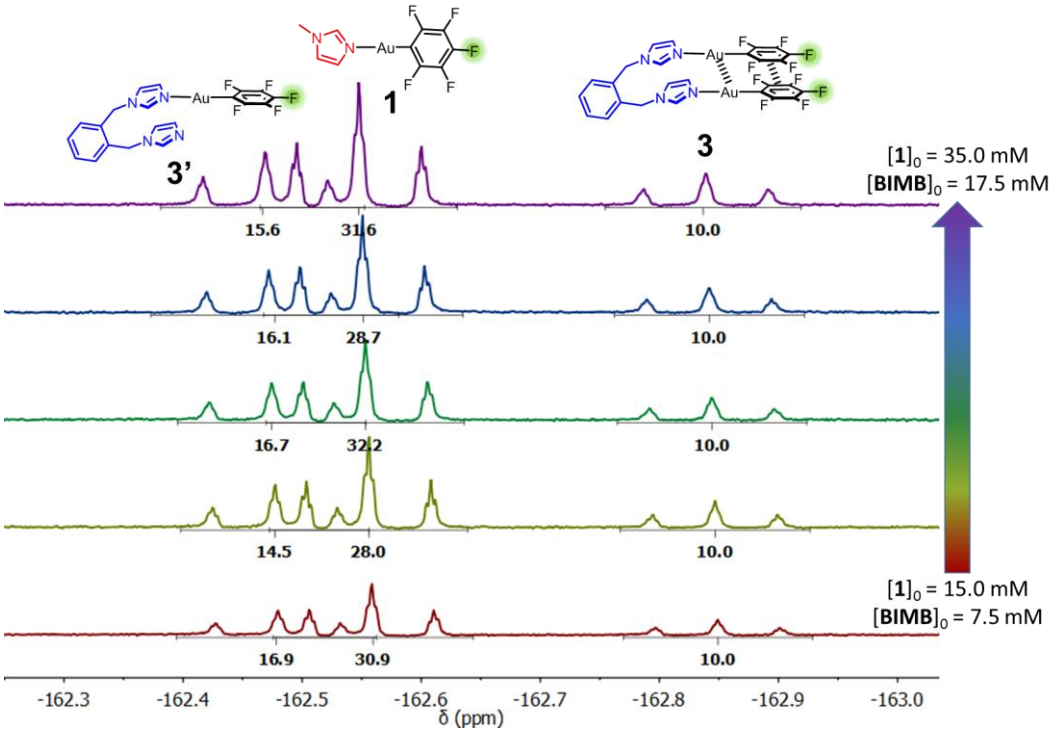

Figure 2.36 Variable-concentration ^{19}F NMR spectra (acetone-d_6, 298 K) showing peaks corresponding to *para*-F (highlighted in green) in complexes **1**, **3** and **3'**. The integrals of three different species basically keep the same upon changing concentration.

2.10.4 Calculation of equilibrium constants and energies

To simplify the calculation, the ligand-exchange experiment was modelled as the equilibria shown in **Figure 2.37**.

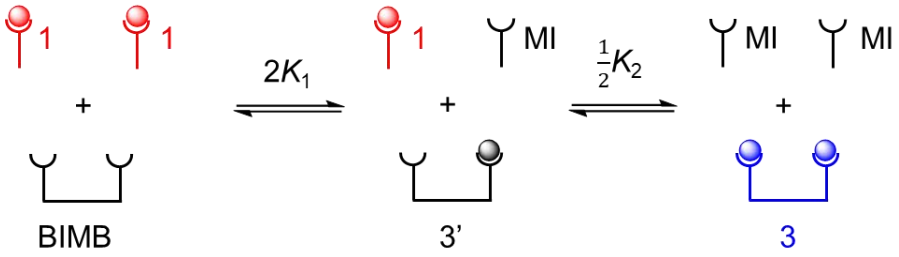

Figure 2.37 Simplified equilibria of the ligand-exchange experiments.

The concentration of all the components in the above equilibria can be obtained from the ^{19}F NMR based on the initial concentration $[\mathbf{1}]_0$ and $[\mathbf{BIMB}]_0$.

$$2[\mathbf{3}] + [\mathbf{1}] + [\mathbf{3'}] = [\mathbf{1}]_0 \quad (8)$$

$$2[\mathbf{3}] / ([\mathbf{1}] + [\mathbf{3'}]) = x \quad (9)$$

$$[\mathbf{1}] / [\mathbf{3'}] = y \quad (10)$$

where x, y are the ratios determined by integration of ^{19}F NMR spectra. For example, for the case in **Figure 2.35**, x = 10.00 / 50.36 = 0.20; y = 35.1 / 15.26 = 2.30.

From above equations we can get

$$[\mathbf{3}] = \frac{x}{2(x+1)}[\mathbf{1}]_0 \quad (11)$$

$$[\mathbf{1}] = \frac{y}{(x+1)(y+1)}[\mathbf{1}]_0 \quad (12)$$

$$[\mathbf{3'}] = \frac{1}{(x+1)(y+1)}[\mathbf{1}]_0 \quad (13)$$

Then, the concentrations of ligands **MI** and **BIMB** can be calculated.

$$[\mathbf{MI}] = [\mathbf{1}]_0 - [\mathbf{1}] \quad (14)$$

$$[\mathbf{BIMB}] = [\mathbf{BIMB}]_0 - [\mathbf{3}] - [\mathbf{3'}] \quad (15)$$

For a general equilibrium, The observed equilibrium constant K can be obtained from a statistical factor K_σ and a chemical constant K_{chem}.[58]

$$K = K_\sigma K_{chem} \tag{16}$$

Using the direct count method proposed by Bishop and Laidler,[59] the statistical factor K_σ is given by the ratio of symmetry numbers (σ) from reactant and product species in equilibrium (equation 2).

$$K_\sigma = \frac{\sigma_{reactants}}{\sigma_{products}} = \frac{l}{r} \tag{17}$$

where the l is the number of possible microspecies of product that can be formed, and the r is the number of possible microspecies of reactants that can be formed from products.

For the first step, $l = 4$, $r = 2$, so $K_{\sigma 1} = 4 / 2 = 2$.

For the second step, $l = 2$, $r = 4$, so $K_{\sigma 2} = 2 / 4 = 1/2$.

Therefore, the equilibrium constants of the two steps are $2K_1$ and $1/2K_2$ respectively.

Having known concentrations of all the species, the values of $2K_1$, $1/2K_2$, ΔG_1, ΔG_2, and $\Delta\Delta G$ can thus be calculated by equations 1–4 listed in section 2.6.1.

Reverse ligand-exchange

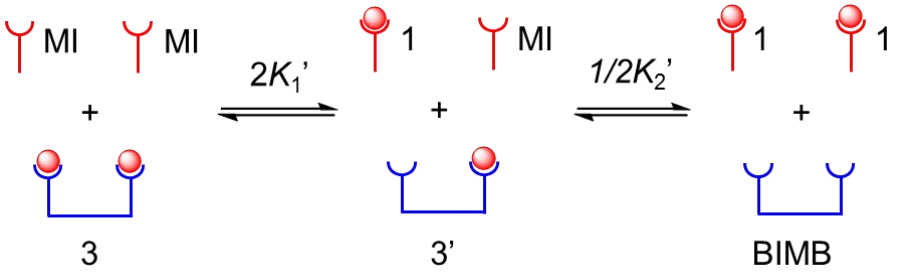

Figure 2.38 Simplified equilibria of the reverse ligand-exchange experiments.

The same procedure was carried out for reverse ligand-exchange experiments except that the starting stock solutions were changed to solutions (0.5 mL) containing complex **3** and two equivalents of ligand MI. The related concentrations, equilibrium constants, and Gibbs free energies were calculated by equations 18–28.

$$2[\mathbf{3}] + [\mathbf{1}] + [\mathbf{3'}] = 2[\mathbf{3}]_0 \tag{18}$$

$$\frac{2[\mathbf{3}]}{([\mathbf{1}] + [\mathbf{3'}])} = \mathrm{x} \tag{19}$$

$$\frac{[\mathbf{1}]}{[\mathbf{3'}]} = \mathrm{y} \tag{20}$$

$$[\mathbf{3'}] = \frac{2}{(\mathrm{x}+1)(\mathrm{y}+1)}[\mathbf{3}]_0 \tag{21}$$

$$[\mathbf{1}] = \frac{2\mathrm{y}}{(\mathrm{x}+1)(\mathrm{y}+1)}[\mathbf{3}]_0 \tag{22}$$

$$[\mathbf{3}] = \frac{\mathrm{x}}{\mathrm{x}+1}[\mathbf{3}]_0 \tag{23}$$

$$[\mathbf{MI}] = [\mathbf{MI}]_0 - [\mathbf{1}] \tag{24}$$

$$[\mathbf{BIMB}] = [\mathbf{3}]_0 - [\mathbf{3}] - [\mathbf{3'}] \tag{25}$$

$$2K_1' = \frac{[\mathbf{3'}][\mathbf{1}]}{[\mathbf{3}][\mathbf{MI}]} \tag{26}$$

$$1/2K_2' = \frac{[\mathbf{1}][\mathbf{BIMB}]}{[\mathbf{MI}][\mathbf{3'}]} \tag{27}$$

$$\Delta\Delta G' = \Delta G_1' - \Delta G_2' = -RT\ln(K_1'/K_2') = -\Delta\Delta G \tag{28}$$

2.11 References

1 H. Schmidbaur, W. Graf and G. Müller, *Angew. Chem. Int. Ed. Engl.*, 1988, **27**, 417–419.

2 V. Wing-Wah Yam and E. Chung-Chin Cheng, in *Photochemistry and Photophysics of Coordination Compounds II*, eds. V. Balzani and S. Campagna, Springer Berlin Heidelberg, Berlin, Heidelberg, 2007, pp. 269–309.

3 H. Schmidbaur and A. Schier, *Chem. Soc. Rev.*, 2008, **37**, 1931.

4 O. Crespo, in *Modern Supramolecular Gold Chemistry Gold Metal Interactions and Applications*, ed. A. Laguna, WILEY-VCH, Weinheim, 2008, pp. 65–117.

5 S. Coco and P. Espinet, in *Gold Chemistry: Applications and Future Directions in the Life Sciences*, ed. F. Mohr, WILEY-VCH, Weinheim, 2009, pp. 357–396.

6 C. M. Che and S. W. Lai, in *Gold Chemistry: Applications and Future Directions in the Life Sciences*, ed. F. Mohr, WILEY-VCH, Weinheim, 2009, pp. 249–281.

7 H. Schmidbaur and A. Schier, *Chem. Soc. Rev.*, 2008, **37**, 1931–1951.

8 H. Schmidbaur and A. Schier, *Chem. Soc. Rev.*, 2012, **41**, 370–412.

9 H. Schmidbaur, K. Dziwok, A. Grohmann and G. Müller, *Chem. Ber.*, 1989, **122**, 893–895.

10 D. E. Harwell, M. D. Mortimer, C. B. Knobler, F. A. L. L. Anet and M. F. Hawthorne, *J. Am. Chem. Soc.*, 1996, **118**, 2679–2685.

11 P. Casuso, A. Perez-San Vicente, H. Iribar, A. Gutierrez-Rivera, A. Izeta, I. Loinaz, G. Cabanero, H. J. Grande, I. Odriozola and D. Dupin, *Chem. Commun.*, 2014, **50**, 15199–15201.

12 R. Gavara, E. Aguiló, C. F. Guerra, L. Rodríguez and J. C. Lima, *Inorg. Chem.*, 2015, **54**, 5195–5203.

13 A. Himmelspach, M. Finze and S. Raub, *Angew. Chem. Int. Ed.*, 2011, **50**, 2628–2631.

14 A. Deák, T. Megyes, G. Tárkányi, P. Király, L. Biczók, G. Pálinkás and P. J. Stang, *J. Am. Chem. Soc.*, 2006, **128**, 12668–12670.

15 M. J. Katz, K. Sakai and D. B. Leznoff, *Chem. Soc. Rev.*, 2008, **37**, 1884–1895.

16 V. W.-W. Yam and E. C.-C. Cheng, *Chem. Soc. Rev.*, 2008, **37**, 1806.

17 H. Ito, T. Saito, N. Oshima, N. Kitamura, S. Ishizaka, Y. Hinatsu, M. Wakeshima, M. Kato, K. Tsuge and M. Sawamura, *J. Am. Chem. Soc.*, 2008, **130**, 10044–10045.

18 D. Weber and M. R. Gagné, in *Homogeneous Gold Catalysis*, ed. L. M. Slaughter, Springer International Publishing, Cham, 2015, pp. 167–211.

19 Y. Jiang, S. Alvarez and R. Hoffmann, *Inorg. Chem.*, 1985, **24**, 749–757.

20 P. Pyykkö and Y. Zhao, *Angew. Chem. Int. Ed. Engl.*, 1991, **30**, 604–605.

21 B. Pinter, L. Broeckaert, J. Turek, A. Růžička and F. De Proft, *Chem. Eur. J.*, 2014, **20**, 734–744.

22 L. Ray, M. M. Shaikh and P. Ghosh, *Inorg. Chem.*, 2008, **47**, 230–240.

23 O. Elbjeirami, S. Yockel, C. F. Campana, A. K. Wilson and M. A. Omary, *Organometallics*, 2007, **26**, 2550–2560.

24 F. Scherbaum, A. Grohmann, G. Müller and H. Schmidbaur, *Angew. Chem. Int. Ed. Engl.*, 1989, **28**, 463–465.

25 E. Andris, P. C. Andrikopoulos, J. Schulz, J. Turek, A. Růžička, J. Roithová and L. Rulí ek, *J. Am. Chem. Soc.*, 2018, **140**, 2316–2325.

26 E. J. Fernández, A. Laguna, J. M. López-de-Luzuriaga, M. Monge, M. Montiel, M. E. Olmos, J. Pérez and M. Rodríguez-Castillo, *Gold Bull.*, 2007, **40**, 172–183.

27 W. F. Gabrielli, S. D. Nogai, M. Nell, S. Cronje and H. G. Raubenheimer, *Polyhedron*, 2012, **34**, 188–197.

28 U. Rafael, L. Antonio, L. Mariano, B. D. A., M. H. H. and F. J. P., *Inorg. Synth.*, 2007.

29 M. Charbonneau, G. Addoumieh, P. Oguadinma and A. R. Schmitzer, *Organometallics*, 2014, **33**, 6544–6549.

30 J. Yang, J. Ma, Y. Liu, J. Ma and S. R. Batten, *Cryst. Growth Des.*, 2008, **8**, 4383–4393.

31 M. M. J. Smulders, M. M. L. Nieuwenhuizen, T. F. A. De Greef, P. Van Der Schoot, A. P. H. J. Schenning and E. W. Meijer, *Chem. Eur. J.*, 2010, **16**, 362–367.

32 E. Hartmann and R. M. Gschwind, *Angew. Chem. Int. Ed.*, 2013, **52**, 2350–2354.

33 E. R. Johnson, S. Keinan, P. Mori Sánchez, J. Contreras García, A. J. Cohen and W. Yang, *J. Am. Chem. Soc.*, 2010, **132**, 6498–6506.

34 K. Morokuma, *J. Chem. Phys.*, 1971, **55**, 1236–1244.

35 T. Ziegler and a Rauk, *Theor. Chim. Acta*, 1977, **46**, 1–10.

36 T. Ziegler and A. Rauk, *Inorg. Chem.*, 1979, **18**, 1558–1565.

37 Y. Zhao and D. G. Truhlar, *Theor. Chem. Acc.*, 2008, **120**, 215–241.

38 P. J. Hay and W. R. Wadt, *J. Chem. Phys.*, 1985, **82**, 270–283.

39 W. R. Wadt and P. J. Hay, *J. Chem. Phys.*, 1985, **82**, 284–298.

40 E. Van Lenthe, J. G. Snijders and E. J. Baerends, *J. Chem. Phys.*, 1996, **105**,

6505–6516.

41 E. van Lenthe, E. J. Baerends and J. G. Snijders, *J. Chem. Phys.*, 1993, **99**, 4597–4610.

42 E. Van Lenthe, E. J. Baerends and J. G. Snijders, *J. Chem. Phys.*, 1994, **101**, 9783–9792.

43 J. P. Perdew, K. Burke and M. Ernzerhof, *Phys. Rev. Lett.*, 1996, **77**, 3865–3868.

44 E. Van Lenthe and E. J. Baerends, *J. Comput. Chem.*, 2003, **24**, 1142–1156.

45 J. Contreras-García, E. R. Johnson, S. Keinan, R. Chaudret, J. P. Piquemal, D. N. Beratan and W. Yang, *J. Chem. Theory Comput.*, 2011, **7**, 625–632.

46 B. R. Brooks, C. L. B. III, J. A. D. Mackerell, L. Nilsson, R. J. Petrella, B. Roux, Y. Won, G. Archontis, C. Bartels, S. Boresch, A. Caflisch, L. Caves, Q. Cui, A. R. Dinner, M. Feig, S. Fischer, J. Gao, M. W. I. Hodoscek and M. Karplus, *J. Comput. Chem.*, 2009, **30**, 1545–1614.

47 G. te Velde, F. M. Bickelhaupt, E. J. Baerends, C. Fonseca Guerra, S. J. A. van Gisbergen, J. G. Snijders and T. Ziegler, *J. Comput. Chem.*, 2001, **22**, 931–967.

48 E. J. Baerends, T. Ziegler, A. J. Atkins, J. Autschbach, D. Bashford, O. Baseggio, A. Bérces, F. M. Bickelhaupt, C. Bo, P. M. Boerritger, L. Cavallo, C. Daul, D. P. Chong, D. V Chulhai, L. Deng, R. M. Dickson, J. M. Dieterich, D. E. Ellis, M. van Faassen, A. Ghysels, A. Giammona, S. J. A. van Gisbergen, A. Goez, A. W. Götz, S. Gusarov, F. E. Harris, P. van den Hoek, Z. Hu, C. R. Jacob, H. Jacobsen, L. Jensen, L. Joubert, J. W. Kaminski, G. van Kessel, C. König, F. Kootstra, A. Kovalenko, M. Krykunov, E. van Lenthe, D. A. McCormack, A. Michalak, M. Mitoraj, S. M. Morton, J. Neugebauer, V. P. Nicu, L. Noodleman, V. P. Osinga, S. Patchkovskii, M. Pavanello, C. A. Peeples, P. H. T. Philipsen, D. Post, C. C. Pye, H. Ramanantoanina, P. Ramos, W. Ravenek, J. I. Rodríguez, P. Ros, R. Rüger, P. R. T. Schipper, D. Schlüns, H. van Schoot, G. Schreckenbach, J. S. Seldenthuis, M. Seth, J. G. Snijders, M. Solà, S. M., M. Swart, D. Swerhone, G. te Velde, V. Tognetti, P. Vernooijs, L. Versluis, L. Visscher, O. Visser, F. Wang, T. A. Wesolowski, E. M. van Wezenbeek, G. Wiesenekker, S. K. Wolff, T. K. Woo and A. L. Yakovlev, .

49 M. J. Frisch, G. W. Trucks, H. B. Schlegel, G. E. Scuseria, M. A. Robb, J. R. Cheeseman, G. Scalmani, V. Barone, B. Mennucci, G. A. Petersson, H. Nakatsuji, M. Caricato, X. Li, H. P. Hratchian, A. F. Izmaylov, J. Bloino, G. Zheng, J. L. Sonnenberg, M. Hada, M. Ehara, K. Toyota, R. Fukuda, J. Hasegawa, M. Ishida, T. Nakajima, Y. Honda, O. Kitao, H. Nakai, T. Vreven, J. A. Montgomery, J. E. Peralta, F. Ogliaro, M. Bearpark, J. J. Heyd, E. Brothers, K. N. Kudin, V. N. Staroverov, R. Kobayashi, J. Normand, K. Raghavachari, A. Rendell, J. C. Burant, S. S. Iyengar, J. Tomasi, M. Cossi, N. Rega, J. M. Millam, M. Klene, J. E. Knox, J. B. Cross, V. Bakken, C. Adamo, J. Jaramillo, R. Gomperts, R. E. Stratmann, O. Yazyev, A. J. Austin, R. Cammi, C. Pomelli, J. W. Ochterski, R. L. Martin, K. Morokuma, V. G. Zakrzewski, G. A. Voth, P. Salvador, J. J. Dannenberg, S. Dapprich, A. D. Daniels, Farkas, J.

B. Foresman, J. V Ortiz, J. Cioslowski and D. J. Fox, 2009.

50 R. Dennington, T. A. Keith and J. M. Millam, 2016.

51 M. Mitoraj and A. Michalak, *J. Mol. Model.*, 2007, **13**, 347–355.

52 M. P. Mitoraj, A. Michalak and T. Ziegler, *J. Chem. Theory Comput.*, 2009, **5**, 962–975.

53 S. Ahrland, K. Dreisch, B. Norén and Å. Oskarsson, *Mater. Chem. Phys.*, 1993, **35**, 281–289.

54 T. Lasanta, J. M. Lõpez-De-Luzuriaga, M. Monge, M. E. Olmos and D. Pascual, *Chem. Eur. J.*, 2013, **19**, 4754–4766.

55 L. Yang, C. Adam, G. S. Nichol and S. L. Cockroft, *Nat. Chem.*, 2013, **5**, 1006–1010.

56 O. V Dolomanov, L. J. Bourhis, R. J. Gildea, J. A. K. Howard and H. Puschmann, *J. Appl. Crystallogr.*, 2009, **42**, 339–341.

57 G. M. Sheldrick, *Acta Crystallogr. Sect. A Found. Crystallogr.*, 2008, **64**, 112–122.

58 S. W. Benson, *J. Am. Chem. Soc.*, 1958, **80**, 5151–5154.

59 D. M. Bishop and K. J. Laidler, *J. Chem. Phys.*, 1965, **42**, 1688–1691.

Chapter 3: Understanding Metallophilic Interactions in Group 10 Metal-Complexes

Abstract

Complexes containing group 10 metal centres (Pt, Pd, Ni) have drawn much attention due to their various structures, intriguing luminescence, catalysis and bio-imaging properties. These structures and properties are often ascribed to the synergetic effects of metallophilic interactions, aromatic stacking, hydrogen bonding and other weak interactions. However, the nature and strength of metallophilic interactions of group 10 elements are still unclear. Here, a series of complexes **LM-X** (L = 1,3-di(5-hexyloxy-2-pyridyl)benzene, M = Pt^{II}, Pd^{II}, Ni^{II}, X = Cl or thiol derivatives) have been synthesised to understand metallophilic interactions and their contribution to molecular assembly. X-ray crystal structures provided evidence of close metal–metal contacts in complex **LPt-1** but not in other complexes, indicating that the crystal packing was sensitive to both metals and ligands. Solution-phase ^{1}H NMR spectroscopy revealed dimerisation of the complexes, however the measured binding constants were very weak and barely changed as the metal was varied, suggesting that the contribution of metallophilic interactions to the binding energy was negligible. The experimental results were supported by DFT calculation and energy decomposition analysis (EDA), which revealed that changing metal cations could affect the electrostatic attraction and Pauli repulsion of the dimers, but had little influence on the overall binding energies. Varying the substituents in the complexes yielded small changes in the dimerisation energies. However, no correlation between the binding energies and the donor-acceptor ability of the substituents was determined, suggesting that a complex interplay of steric and electrostatic factors was responsible for these small changes in dimerisation energies. Further natural orbitals for chemical valence analysis (EDA-NOCV) illustrated that metallophilic interactions originated (at least partially) from orbital interactions.

3.1 Introduction

Besides the earliest and the most widely studied metallophilic interactions between coinage metal centres (Au, Ag, Cu, see **Chapter 2**),[1–4] interactions between group 10 metal cations (Pt, Pd, Ni) are the second most significant series of metallophilic interactions.[5–9] Metallophilic interactions between square-planar metal complexes, especially Pt^{II}-complexes,[6,10,11] have been frequently described. It is easy to imagine how the planar structure lends itself to forming metallophilic complexes, strengthened through synergetic effects from other weak interactions, such as aromatic stacking. However, most studies purporting the formation of metallophilic interactions between such square-planar complexes focus on structure construction and photophysical behaviours. Detailed examination of the strength and nature of metallophilic interactions in these complexes is generally ignored. Indeed, metallophilic interactions as a contributing factor in the formation of such complexes is generally taken for granted with no or very limited evidence. Only one study from Alvarez and co-workers[12] into the nature and strength of metallophilic interactions between square-planar Pt^{II}-complexes has previously been reported (**Figure 3.1**). The study, which was purely computational, qualitatively and semi-quantitatively studied the nature of metallophilic interactions between square-planar ML_4 molecules by *ab initio* MP2 calculations using effective core potentials (ECP) and single-ζ or double-ζ basis sets.[13–15] The authors reported dimerisation energies of –38 kJ mol^{-1} and –83 kJ mol^{-1} for dimers $[PtCl_2(CO)_2]_2$ and $[PtCl_2\{HNCH(OH)\}_2]_2$, respectively. The Pt–Pt distances of the minimised structures were between 3.25 Å and 3.32 Å, which agreed with the experimental range of metallophilic interactions in the solid state.[8,16]

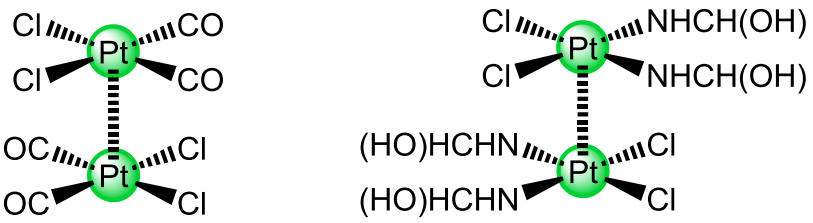

Figure 3.1 Complexes reported for computationally estimating Pt–Pt interactions.[12]

The absence of combined experimental and computational investigations into metallophilic interactions between group 10 metal cations is striking, given the relative abundance of systems which try to utilise such interactions. It is important to try and better understand both the nature and strength of such interactions to rationally exploit them.

3.2 Project aim and design

To estimate M–M (M = Pt^{II}, Pd^{II}, Ni^{II}) interactions, a range of organometallic complexes must be designed and synthesised. The complexes should ideally satisfy three criteria: I) The complexes should be neutral overall so that columbic attraction/repulsion and non-specific electrostatic interactions are minimised. II) The complexes should be planar structures with small functional groups such that steric effects are minimised. III) The complexes should be soluble and stable in a range of solvents (e.g. chloroform, acetonitrile, methanol) enabling the examination of their solution-phase behaviour and allowing for the evaluation of solvation effects.

Based on the above considerations, a series of cyclometalated complexes shown in **Figure 3.2** were designed. The neutral cyclometalated complexes are planar, which can allow them to potentially pack with each other with close metal–metal contacts. Hexane chains (hexyloxy) are attached to increase solubility. The complex without hexyloxy groups has been previously prepared by myself and shows poor solubility in common solvents like $CHCl_3$ and acetonitrile. The thiol ligand is also crucial to the system since it enables a diverse range of structures to be easily obtained to investigate substituent effects. Moreover, the presence of a slightly bulky thiol-ligand means that the compounds cannot stack beyond the formation of dimers (**Figure 3.3**), which simplifies the studies.

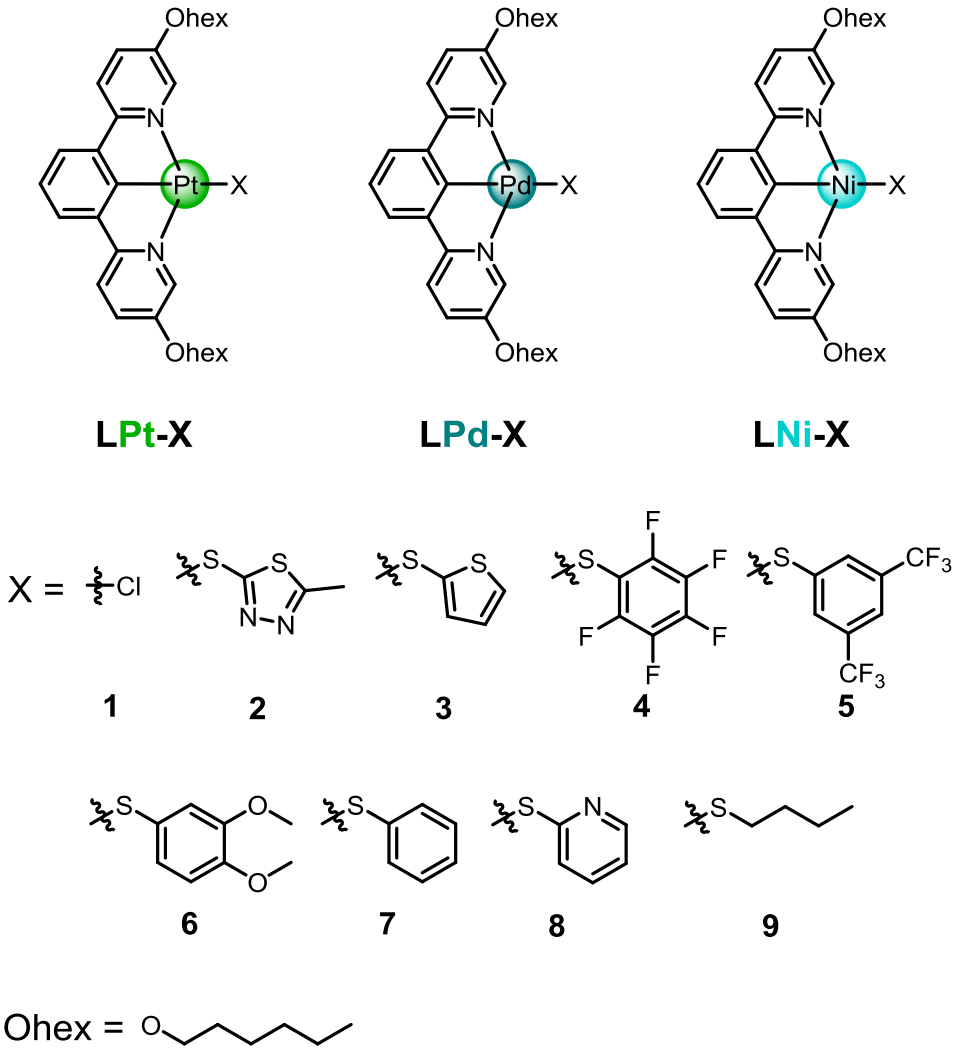

Figure 3.2 Structures of complexes **LM-X** (M = Pt, Pd, Ni) designed for the study of metallophilic interactions.

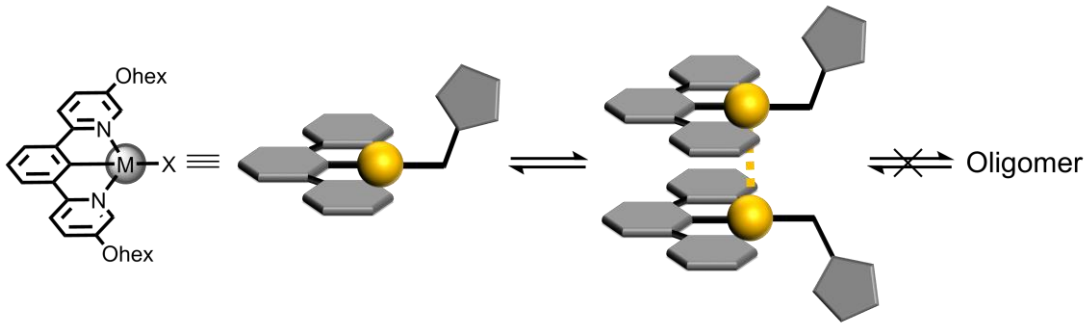

Figure 3.3 The presence of thiol ligands **X** prevents the dimer **[LM-X]$_2$** from further aggregation.

3.3 Synthesis, solubility and stability

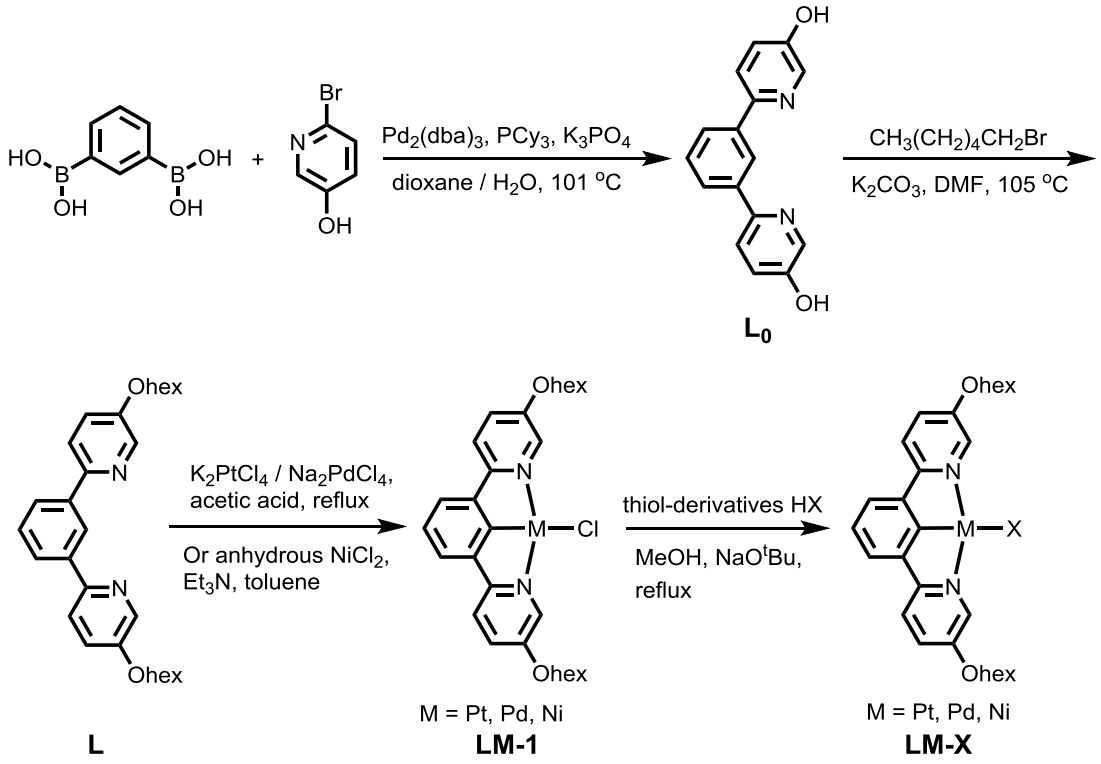

Figure 3.4 Synthetic routes for preparing complexes **LM-X**.

The desired complexes were prepared according to the synthetic routes displayed in **Figure 3.4**. Ligand **L** was accessed through a Suzuki-Miyaura cross-coupling reaction, followed by alkylation of the phenols. Ligand **L** was subsequently reacted with different metal salts (K_2PtCl_4, Na_2PdCl_4 or $NiCl_2$) to generate the complex **LM-1**. Finally, the target complexes **LM-X** were obtained by reacting complex **LM-1** with different thiol derivatives under basic conditions. The identities and purities of the complexes were confirmed by ^{1}H and ^{13}C NMR, mass spectrometry (ESI-MS) and single-crystal X-ray diffraction. See Appendix B for synthesis and characterisation details.

Ligands **2** (2-mercapto-5-methyl-1,3,4-thiadiazole) and **3** (2-thiophenethiol) were selected for comparing the influence of metals. A full series of Pt-, Pd- and Ni-complexes were synthesised with ligand **3**, while synthesis of **LNi-2** proved not possible as the ligand connected to the nickel centre through the nitrogen, rather than

the thiol sulfur (see crystal structure of **LNi-2** in Appendix B). Pt-complexes **LPt-X** with all the different thiol-ligands have been successfully prepared to study the influence of substituents.

All the complexes are found to be stable for weeks in the solid state at room temperature. They are soluble in chloroform. The ^{1}H NMR spectra of complex **LNi-3**, which is anticipated to be the least stable, in chloroform demonstrates that it is stable for at least 1 hour at room temperature (**Figure 3.5**). The stability of complexes **LPd-2**, **LPd-3**, **LPt-2**, and **LPt-4** (see Experimental 3.8.2) have also been examined and showed better stability than complex **LNi-3**. Therefore, complexes **LM-X** are soluble in chloroform and can be stable for at least 1 h, which is long enough for further NMR binding studies.

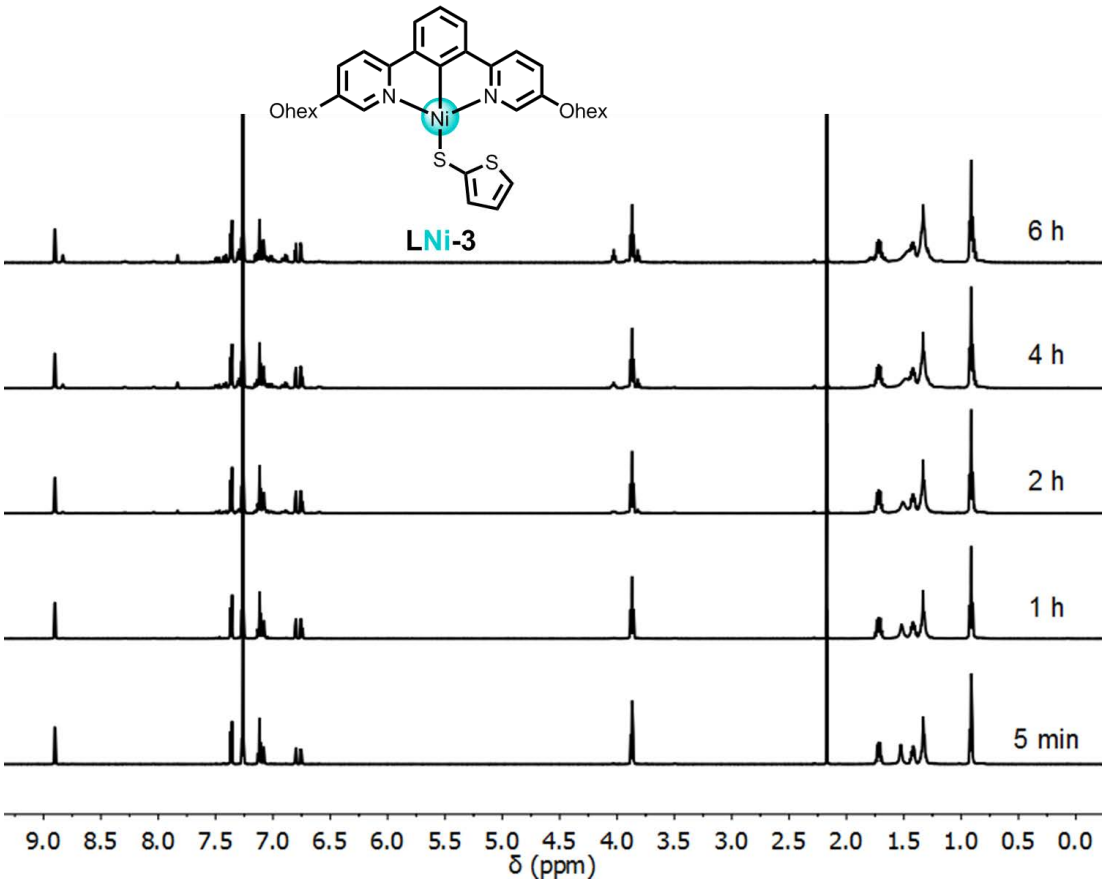

Figure 3.5 ^{1}H NMR spectra ($CDCl_3$, 500 MHz, 298 K) of complex **LNi-3** over time indicating its stability for >1 hour.

3.4 Crystallography

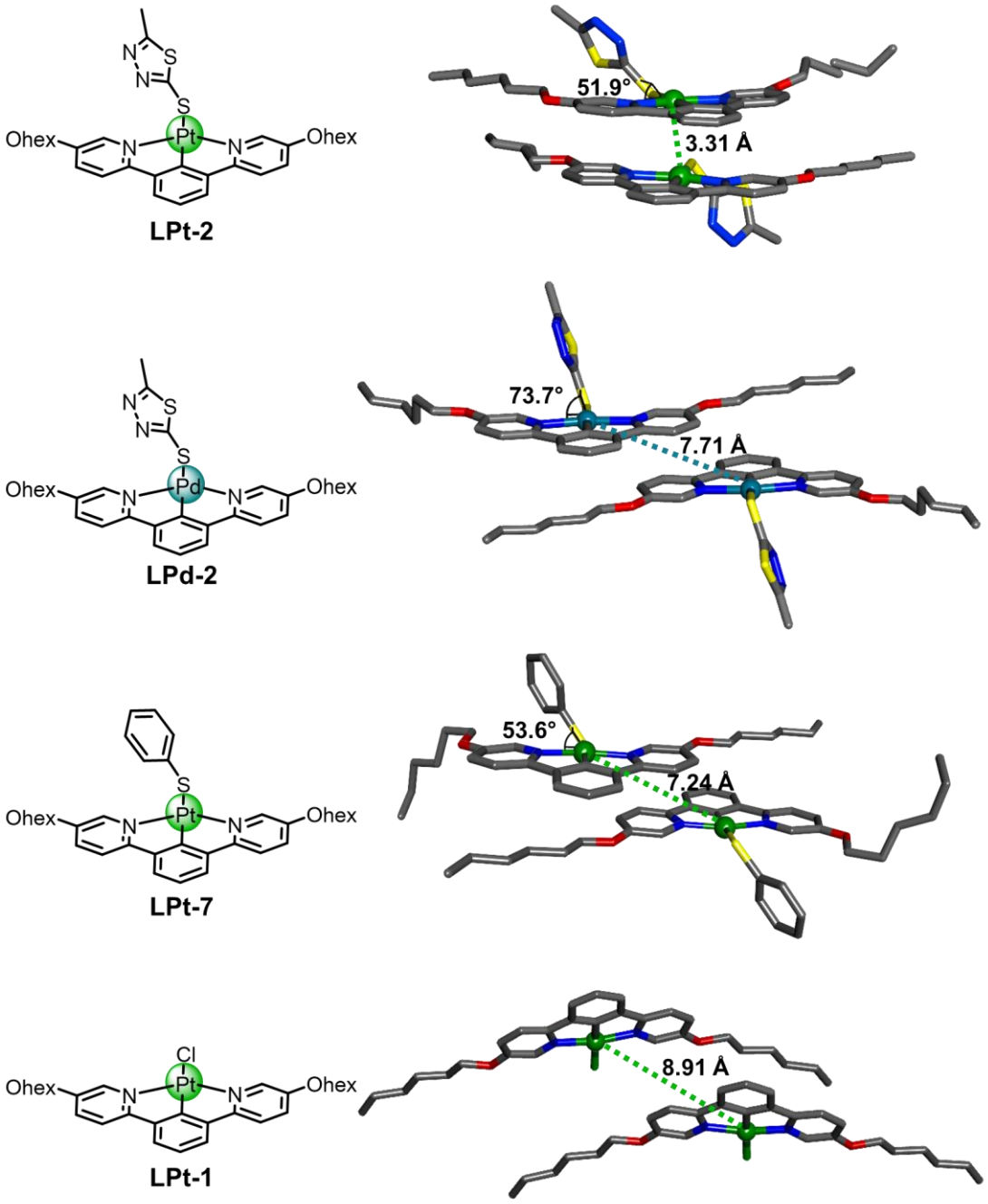

Figure 3.6 Structures (left) and crystal structures (right) of complexes **LPt-2** (a), **LPd-2** (b), **LPt-7** (c), and **LPt-1** (d). Metal-metal distances and N-M-S-C dihedral angles are shown in the crystal structures. Colour codes: green Pt, yellow S, blue N, red O, grey C, cyan Pd, pale green Cl. Hydrogens are omitted for clarity.

Crystals suitable for X-ray diffraction were only obtained for four complexes **LPt-1**, **LPt-2**, **LPt-7**, and **LPd-2**, by slow diffusion of diethyl ether vapour into a dichloromethane solution of the complexes. Unfortunately, poor stability in solution or the poor periodicity of the yielded solid precluded determination of the crystal structures of the other complexes. Nonetheless, the four complexes that did yield crystal structures could provide significant insight into the interactions in these complexes.

The crystal structures are depicted in **Figure 3.6**. For complex **LPt-2**, the Pt^{II} metal centre resides in a distorted square-planar environment connecting to a tridentate ligand **L** and a thiol derivative **2**. The ligand **2** is semi-perpendicular to the cyclometalated [LPt] moiety with a C-S-Pt-N dihedral torsion angle of is 51.9°. The nitrogen, rather than sulfur of the **2** orientates toward the Pt^{II} centre. Two adjacent **LPt-2** monomers dimerise with each other in a face-to-face mode. The Pt–Pt distance is 3.310 Å, indicating the presence of metallophilic interactions in the solid state. Notably, the semi-perpendicular orientation of the **2** ligand prevents the dimers from further aggregation, which would simplify subsequent binding studies in solution.

For the complex **LPd-2**, the Pd^{II} cation is also connected by a tridentate ligand **L** and a ligand **2**. The geometry of the complex monomer is similar to that of complex **LPt-2**, but the dihedral angle of C-S-Pd-N (73.7°) is larger in comparison. Two **LPd-2** monomers shift away from each other showing offset packing. As a result, [LPd] fragments overlay with the hexyloxy chains. Moreover, the orientation of the lower monomer is reversed relative to the upper monomer. The Pd–Pd distance is 7.709 Å, which is obviously too long for metallophilic interactions to form.

The complex **LPt-7** displays similar packing mode to that of complex **LPd-2**. Two monomers stack with reverse orientation, and [LPt] fragments overlay with hexyloxy chains. One hexyloxy chain stretches out of the plane of [LPt] moiety. The Pt–Pt distance is 7.244 Å, which indicates the absence of metallophilic interactions in the solid state. The precursor complex **LPt-1** also shows offset packing with a long Pt–Pt distance of 8.912 Å, indicating the absence of metallophilic interactions.

The presence of close Pt–Pt distance of 3.31 Å in complex **LPt-2** reveals the presence of metallophilic interactions in the solid state, enabling complex **LPt-2** being a

potential platform for estimating metallophilic interactions in solution. Complexes **LPt-1**, **LPt-7**, and **LPd-2** do not dimerise with close metal–metal contacts, suggesting that metallophilic interactions are not strong enough to dominate the crystal packing. Therefore, changing metals or ligands/substituents can tune the aggregation state. But how do they affect the assembly? Do metallophilic interactions play a significant role? To answer these questions, further experimental and computational investigations have been carried out.

3.5 Experimental estimation of binding energy in solution

3.5.1 Presence or not of metallophilic interactions in solution?

The presence of metallophilic interactions in the crystal structures of complex **LPt-2** suggests that the complex can be a potential platform to study metallophilic interactions in solution. Although the other complexes did not crystallise with close metal–metal contacts, metallophilic interactions may nonetheless be expressed in solution. UV-vis spectroscopy and fluorescence spectroscopy were utilised to examine whether metallophilic interactions were present in solution.

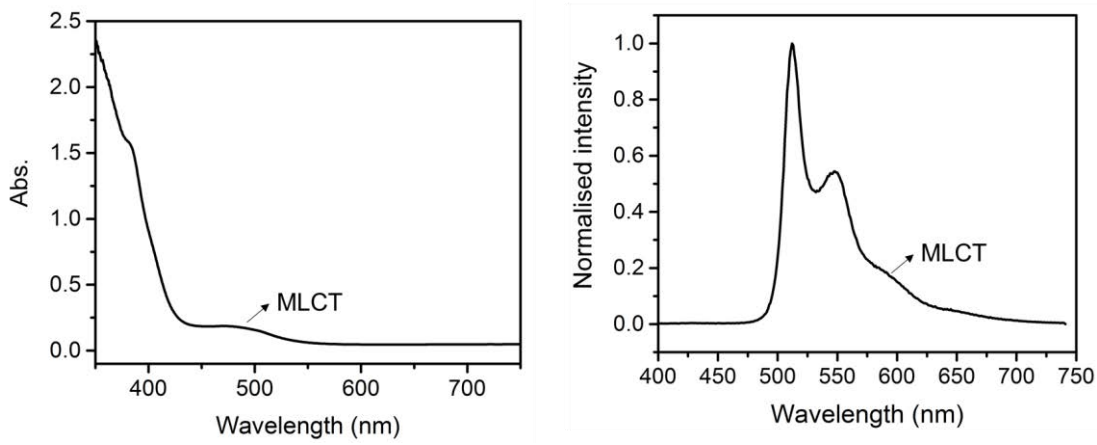

Figure 3.7 UV-vis spectrum (left) and fluorescence emission spectrum (right) of complex **LPt-2** in chloroform at room temperature.

The UV-vis spectrum of complex **LPt-2** in chloroform displays an absorption band at 480 nm (**Figure 3.7**), which is ascribed to metal-to-ligand charge transfer (MLCT). No lower energy absorption band that might correspond to metal-metal-to-ligand

charge transfer (MMLCT) is observed. An emission band of MMLCT is not found in the fluorescence emission spectra either. Hence, metallophilic interactions appear not to be preserved in solution at the relatively low concentration (< 1 mM) used for these UV-vis and fluorescence spectroscopic examinations. It remains possible that metallophilic interactions might be preserved at a higher concentrations. Thus, it became necessary to perform ^{1}H NMR dilution experiments to examine this possibility.

3.5.2 ^{1}H NMR dilution experiments

The presence of metallophilic interactions can be examined by dilution NMR spectra by looking at whether chemical shielding is observed upon increasing concentration. As shown in **Figure 3.8**, an equilibrium between complex monomers and dimers is reached at a certain range of concentration in solution. The presence of bulky a thiol-ligand **X** can prevent dimers from further aggregation such that only monomers and dimers exist in solution. Upon increasing the concentration of the complex **LM-X**, the ratio of dimers would be expected to increase if there are substantial interactions to drive formation of the dimer. The chemical shifts of dimers are anticipated to be more shielded than the monomers due to the shielding effects from the adjacent monomer. Consequently, the NMR peaks would be anticipated to shift upfield as the concentration was increased.

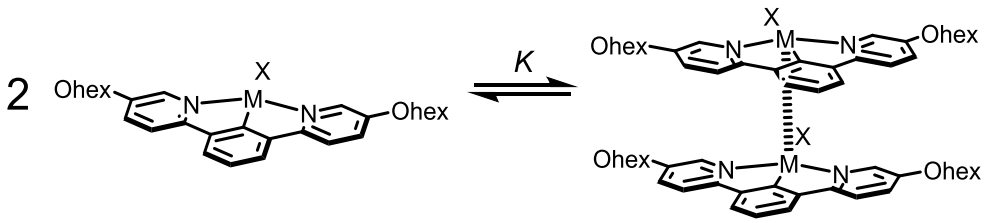

Figure 3.8 Proposed equilibrium between monomers and dimers of complex **LM-X** in solution.

The dilution ^{1}H NMR spectra ($CDCl_3$-*d*, 298 K) of complex **LPt-2** (**Figure 3.9**a) show obvious upfield shifts in the range of 7.0–9.1 ppm, corresponding to the aromatic protons, upon increasing concentration. This suggests that dimers of complex **LPt-2** are present in solution in which Pt–Pt interactions may be preserved.

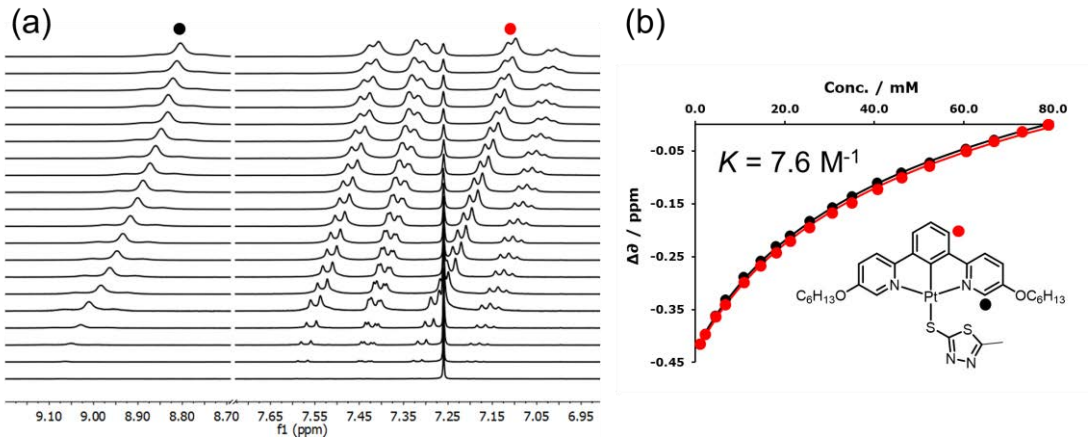

Figure 3.9 ^{1}H NMR spectra of dilution experiments for complex **LPt-2** in chloroform-*d* at 298 K (a) and the binding isotherms generated based on peaks around 8.9 ppm (black dot) and 7.2 ppm (red dot) (b). The corresponding protons in the structure are also noted using black and red dots.

The peaks at ~8.9 ppm (black dot, proton besides pyridine N) and 7.2 ppm (red dot, phenyl proton) have been utilised to generate a binding isotherm (**Figure 3.9b**) and to work out the binding constant K using a spreadsheet (14allMaster.xls) kindly supplied by Professor Christopher A. Hunter. Other peaks were not analysed because their chemical shift changes were too small to be fitted reliably. Given the binding constant K, the binding energy ΔG can be calculated using the equation $\Delta G = -RT\ln K$. The binding constant K and binding energy ΔG_{exp} of complex **LPt-2** are 7.6 ± 1.0 M^{-1} and –5.0 ± 0.3 kJ mol^{-1}, respectively. These values are small, suggesting the dimerisation interactions including metallophilic interactions and aromatic stacking are weak. ^{1}H NMR dilution spectra and the corresponding binding isotherms for other complexes are given in the Experimental section. Dilution experiments for each complex were repeated twice to gain average binding energies for each complex. The experimental error is reported as two standard deviations in these experimental measurements. The binding constants K and energies ΔG_{exp} for all the complexes are summarised in **Table 3.2**.

Table 3.2 Binding constant K and binding energy ΔG_{exp} obtained from ^{1}H NMR dilution experiments. Errors are reported as two standard deviations in the experimental values.

Complex	Ligand	K / M^{-1}	ΔG_{exp} / kJ mol^{-1}
LPt-2	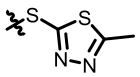	7.6 ± 1.0	−5.0 ± 0.3
LPd-2	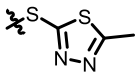	3.9 ± 1.5	−3.3 ± 0.7
LPt-3	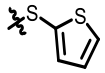	1.4 ± 0.3	−0.8 ± 0.6
LPd-3	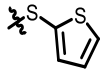	2.4 ± 0.5	−2.2 ± 0.5
LNi-3	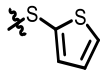	1.5 ± 0.5	−1.0 ± 0.9
LPt-4	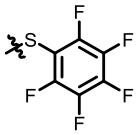	3.6 ± 0.8	−3.2 ± 0.6
LPt-5	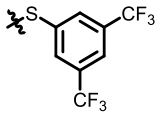	2.6 ± 0.8	−2.3 ± 0.8
LPt-6	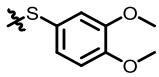	0.7 ± 0.3	+0.8 ± 1.0
LPt-7	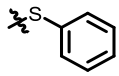	0.9 ± 0.4	+0.2 ± 1.2
LPt-8	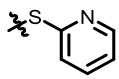	2.6 ± 0.4	−2.4 ± 0.4
LPt-9	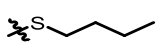	0.9 ± 0.4	+0.4 ± 0.6

Influence of metal cations

The influence of metal cations has been studied by comparing complexes with the same ligand but different metal cations. Two series of complexes including **LM-2** (M = Pt^{II} and Pd^{II}, **2** = 2-mercapto-5-methyl-1,3,4-thiadiazole) and **LM-3** (M = Pt^{II}, Pd^{II},

and Ni^{II}, **3** = 2-thiophenethiol) were employed for ^{1}H NMR dilution experiments. Unfortunately, the binding energies of complex **LNi-2** could not be used for comparison due to its different coordination mode (**Figure B.6**) in which Ni connects with N rather than S.

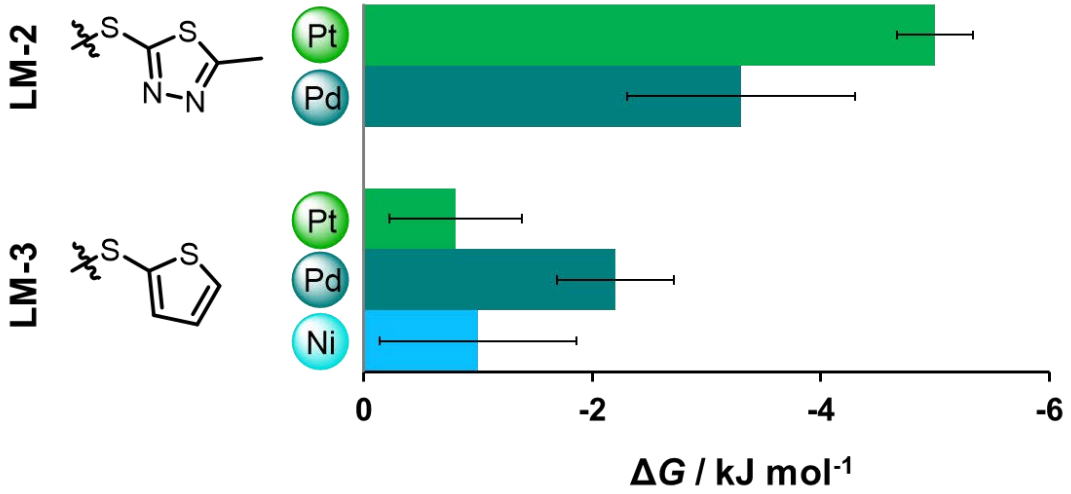

Figure 3.10 Experimental measured binding energies of complexes **LM-2** (M = Pt^{II}, Pd^{II}) and complexes **LM-3** (M = Pt^{II}, Pd^{II}, Ni^{II}) in chloroform-*d* at room temperature.

For the series of complexes **LM-2** (M = Pt^{II}, Pd^{II}), the complex **LPt-2** has a larger binding energy than the complex **LPd-2** (**Figure 3.10**). There are two possible explanations for this observation. One is that both complexes dimerise with the presence of metallophilic interactions. In this case, the larger binding energy for the complex **LPt-2** indicates Pt–Pt interactions are stronger than Pd–Pd interactions. The other explanation is that metallophilic interactions are preserved in the solution of complex **LPt-2**, but are not well expressed in the solution of complex **LPd-2**. This is supported by the fact that Pt–Pt interactions are present in the solid state, but Pd–Pd interactions are not (**Figure 3.6**). In this case, the absence of Pd–Pd interactions indicates that they are not strong enough to be preserved in solution, which also implies that they are weaker than Pt–Pt interactions.

To avoid the formation of Ni–N bonding, the ligand **3** (thiophene-2-thiol) without N atoms were used to replace the ligand **2** (2-mercapto-5-methyl-1,3,4-thiadiazole). In this way, the other series of complexes **LM-3** with three different metal cations (Pt^{II}, Pd^{II}, and Ni^{II}) were obtained. The binding energies for these three complexes laid in

the range of –1.1 to –2.5 kJ mol^{-1}. Although the complex **LPd-3** has a stronger binding energy than complexes **LPt-3** and **LNi-3**, the three binding energies can be regarded the same within error. There are alternative explanations for this observation. One is that the complexes **LM-3** dimerise in a face-to-face mode with the presence of very weak metallophilic interactions. The other explanation is that complexes **LM-3** pack in an offset, rather than face-to-face mode. However, irrespective of whether the complexes **LM-2** and **LM-3** assemble in a face-to-face or off-set mode, with or without the presence of metallophilic interactions in solution, the obtained weak binding constants and energies suggest metallophilic interactions are very weak and their contribution to molecular binding is negligible. This is also supported by the negligible change of binding energies upon changing metal centres.

Influence of substituents

^{1}H NMR dilution experiments of complexes **LPt-X** with different thiol derivatives have also been performed to study the influence of substituents. As shown in **Figure 3.11**, all the binding energies are very weak and in the range of +0.4 kJ mol^{-1} to –5.0 kJ mol^{-1}. The binding energies change slightly upon changing substituents.

Since the experimental binding energies (ΔG_{exp}) of complexes **LPt-X** are affected by different ligands, it is important to know whether these energies are correlated to the donor-acceptor ability of the substituents in ligands **2-9**. Electrostatic potential (ESP) is a good indicator of donor-acceptor ability. Electron-withdrawing group should pull away electron density over the protons and thus give larger positive potentials. Whereas electron-donating groups would result in smaller positive potentials. To better reflect the ESPs of the substituents, the SH groups in free ligands **2-9** were replaced by H forming free compounds **2'–9'**. The ESP values on H along H-C bonds were recorded (see section 3.6.1 for details). The ESP values decrease in the sequence **4** > **2** > **5** > **3** > **6** ≈ **7** > **8** > **9**. As displayed in **Figure 3.11**, the binding energies do not show a trend from the most electron-withdrawing ligand **4** to the most electron-donating ligand **9**. The plot of ESP values against ΔG_{exp} shown in **Figure 3.12** also give a poor correlation, suggesting that the binding energies are not simply influenced by electronic properties. It is therefore likely that a complex interplay of steric and electrostatic factors is responsible for these small changes in dimerisation energies.

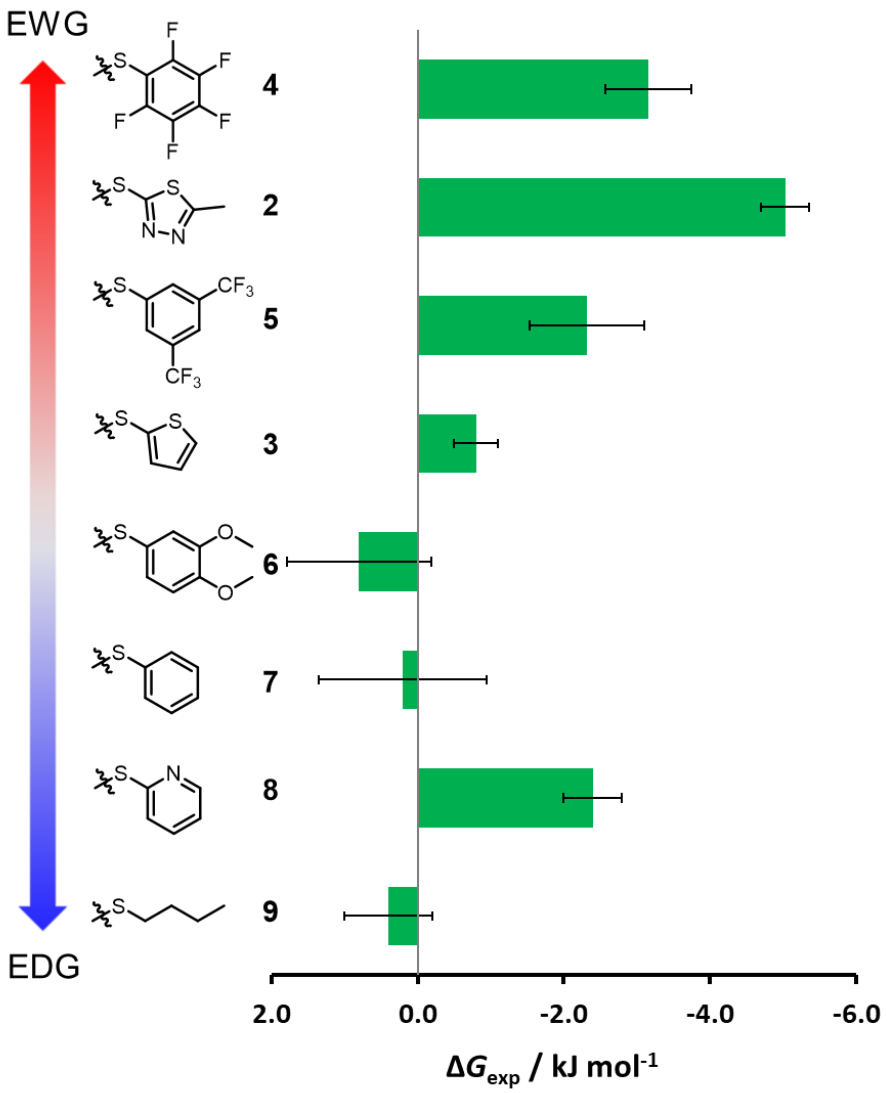

Figure 3.11 Experimental measured binding energies of complexes **LPt-X** in chloroform-*d* at room temperature.

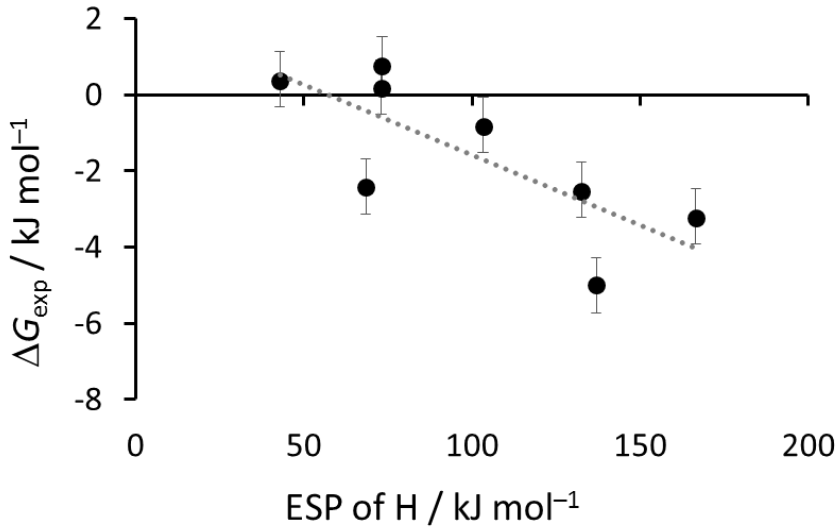

Figure 3.12 Graph of experimentally measured binding energy ΔG_{exp} against the ESP values taken over the proton H in compounds **2'-9'**.

3.6 Computational estimation of binding energy

Computational studies were performed to gain further insight into the experimental results and thereby metallophilic interactions involving group 10 elements. The *Gaussian 09* package[17] was employed for geometry optimisations, single-point energy calculations, both with and without solvation effects, and for electrostatic potential calculations. The Meta-GGA functional TPSSTPSS[18] with the def2-TZVP basis set[19] and density fitting, together with Grimme's D3 dispersion with Becke-Johnson damping[20] were employed for all the calculations. The general notation of the method is TPSSTPSS/def2TZVP/fit/GD3BJ. The energy decomposition analysis (EDA)[21–23] embedded in the *ADF2017.110* package[24,25] was utilised to quantify the contribution and the nature of metallophilic interactions. The calculations were performed using GGA functional PBE[26] with Grimme's D3 dispersion with Becke-Johnson damping[20]. The scalar relativistic ZORA[27–29] and TZ2P basis set[30] were employed. The general notation of the method is ZORA-PBE-GD3BJ/TZ2P.

3.6.1 ESP of substituents

As mentioned in section 3.5.2, the SH groups in free ligands **2-9** were replaced by H forming free compounds **2'–9'** to better understand the donor-acceptor ability of the ligands. The compounds **2'–9'** were optimised at B3LYP/6-31G* using Spartan '14 and the ESP values of H along H-C bonds were recorded. Take compound **2'** as an example, it was generated by replacing the SH in ligand **2** to H (**Figure 3.13**). The ESP on H along H-C bond was recorded to be 131 kJ mol^{-1}. Similarly, the ESP values of complexes **3'–9'** were taken and these ESP values decreased in a sequence **4'** > **2'** > **5'** > **3'** > **6'** ≈ **7'** > **8'** > **9'** (**Figure 3.14**).

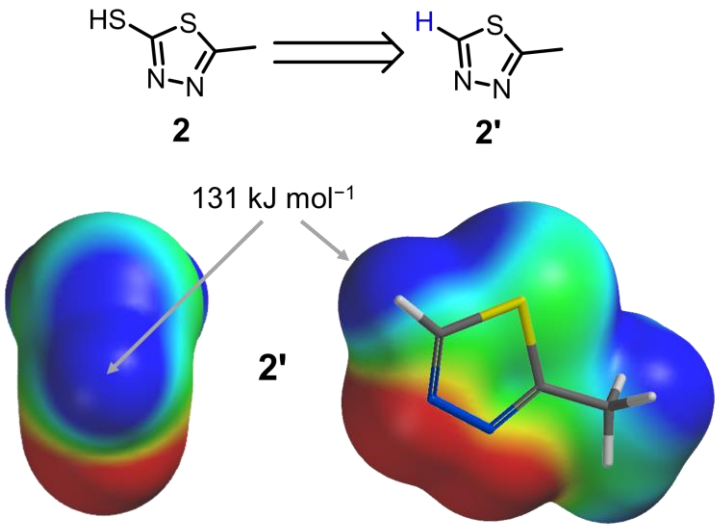

Figure 3.13 Compound **2** was transformed to compound **2'**, then ESP of H along H-C bond in compound **2'** was computed at B3LYP/6-31G* using Spartan '14. Blue areas are electron deficient and red areas are electron rich. Colour code: yellow S, blue N, grey C, and white H.

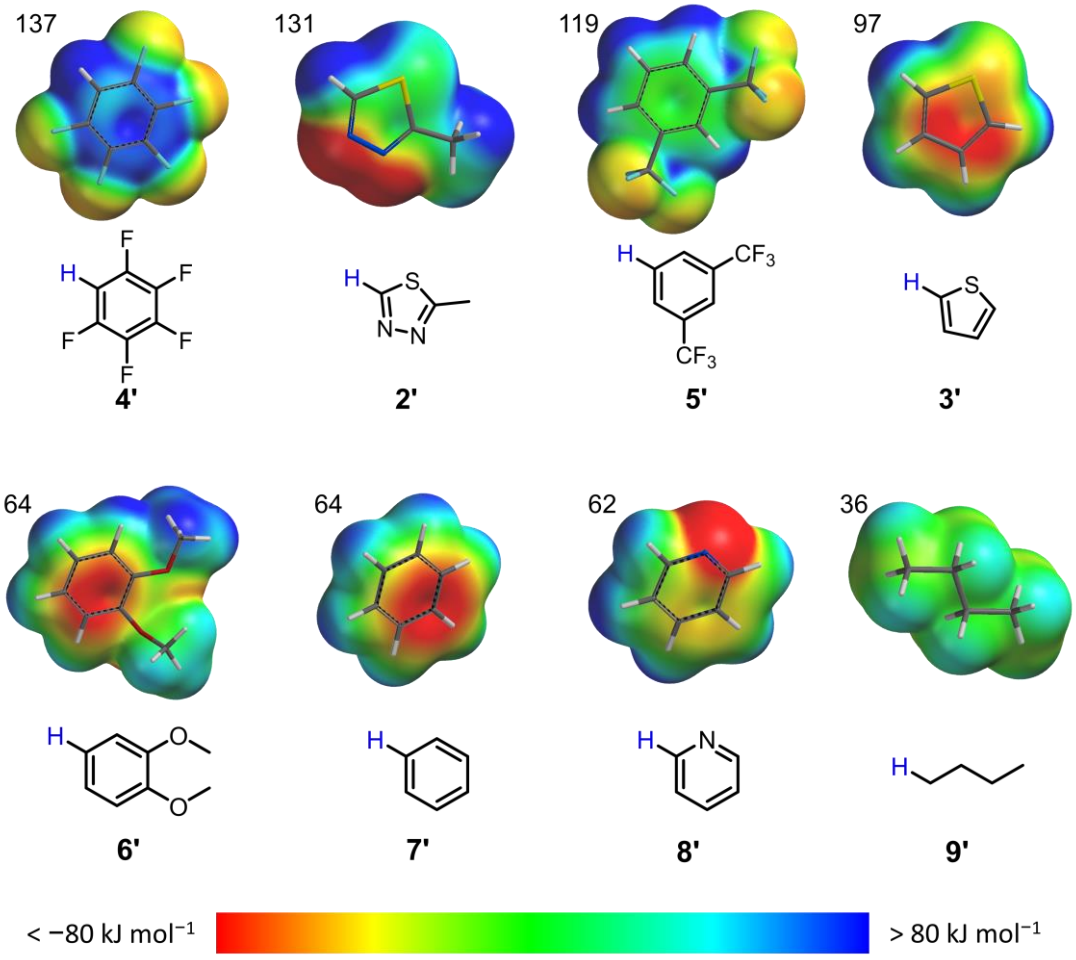

Figure 3.14 Electrostatic potential (ESP) maps of compounds **2'–9'** calculated at B3LYP/6-31G* using Spartan '14. ESP values of H (blue) along H-C bonds are noted in the figure.

3.6.2 Geometry optimisation

The complexes used for geometry optimisation were modified based on the crystal structure of the complex **LPt-2**. The long hexyl chain was replaced by a methyl group to save computational resources, since it is known that the substituent effects of a hexyl group and methyl group are very similar based on Hammett constants. The new ligand was denoted as ligand **L'** and the complex was thus denoted as **L'Pt-2**. By changing the Pt^{II} to Pd^{II} or Ni^{II}, geometries of complexes **L'Pd-2** and **L'Ni-2** were obtained and used for geometry optimisation. Similarly, by replacing the ligand **2** in complex **L'Pt-2** to other thiol-ligands, a series of Pt-complexes **L'Pt-X** were generated and then optimised. The dimer **[L'Pt-2]$_2$** was modified based on the crystallographic dimer **[LPt-2]$_2$**. Based on the geometry-optimised dimer **[L'Pt-2]$_2$**, different metal cations or

thiol ligands were introduced and then optimised. Optimisation for all these monomers and dimers were performed using the same method TPSSTPSS/def2TZVP/fit/GD3BJ.

The influence of metal cations was studied first. As depicted in **Figure 3.15**, the ligand **2** in the optimised geometries of the **L'Pt-2** monomer is semi-perpendicular to the planar fragment [L'Pt]. The N-Pt-S-C dihedral angle is 58.6°. The optimised structures of the **L'Pd-2** and **L'Ni-2** monomers were similar to that of the **L'Pt-2** monomer. But the dihedral angles increase to 61.7° in **L'Pd-2** and to 86.6° in **L'Ni-2**. The obviously increased N-Pt-S-C dihedral angle in **L'Ni-2** is attributed to the higher affinity of the Ni centre to the N in ligand **2**, which induces a shorter Ni-N distance (2.616 Å) and distorted tetragonal pyramidal geometry.

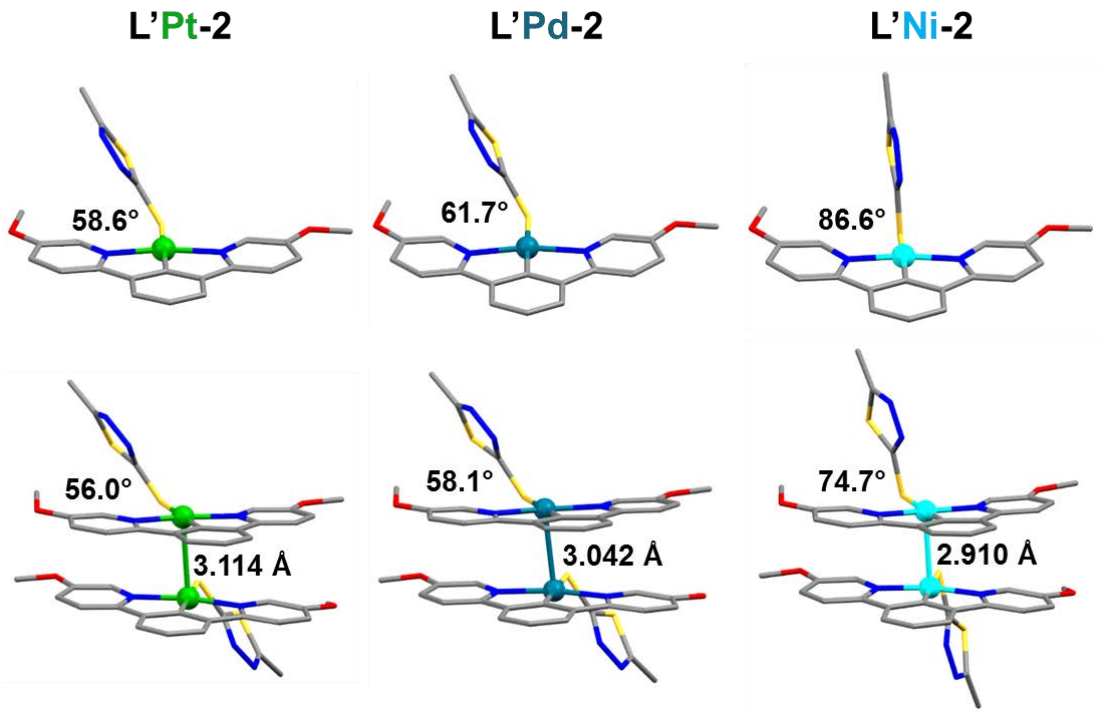

Figure 3.15 Optimised geometries of the monomers and dimers complexes **L'M-2** (M = Pt^{II}, Pd^{II}, and Ni^{II}) computed at TPSSTPSS/def2TZVP/fit/GD3BJ level of theory. Colour codes: green Pt, teal Pd, cyan Ni, blue N, red O, yellow S, grey C. Hydrogens are omitted for clarity.

After dimerisation, the dimers **[L'M-2]$_2$** with different metal cations display the same face-to-face stacking mode. The geometries of the monomers in these dimers retain similar geometries to monomeric **[L'M-2]**, except that the N-Pt-S-C dihedral angles become slightly smaller. The metal–metal distances in the dimers **[L'M-2]$_2$** decrease

in the sequence Pt^{II}–Pt^{II} (3.114 Å) > Pd^{II}–Pd^{II} (3.042 Å) > Ni^{II}–Ni^{II} (2.910 Å). These short metal–metal distances are consistent with the presence of metallophilic interactions. The decreasing trend can be ascribed to the smaller radii of Ni^{II} than Pd^{II} to Pt^{II}. The series of dimers **[L'M-3]$_2$** (**Figure 3.16**) show consistent results with metal–metal distances decreasing from Pt to Ni.

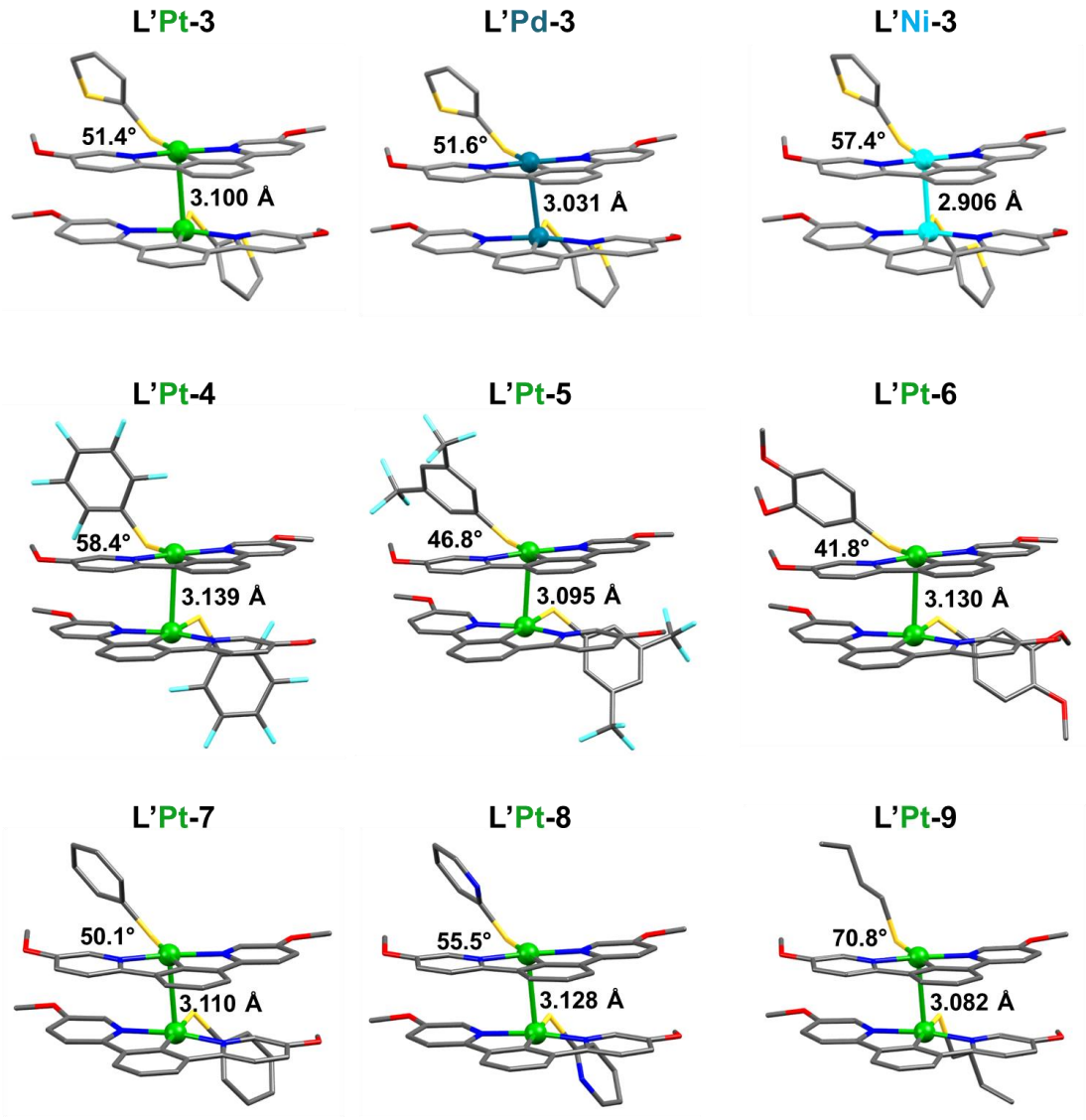

Figure 3.16 Optimised structure of complexes **L'Pt-X** (R = SC_6F_5, $SPhCF_3$, SPhOMe, SPh, SPy, SBu) computed at TPSSTPSS/def2TZVP/fit/GD3BJ level of theory. Colour codes: green Pt, blue N, red O, yellow S, cyan F, grey C. Hydrogens are omitted for clarity.

Dimers **[L'Pt-X]$_2$** with different thiol-ligands were also optimised and are shown in **Figure 3.16**. All the dimers show short Pt–Pt distances (3.08 – 3.14 Å). Different thiol-

ligands result in different Pt–Pt distances, suggesting dimerisation energies and metallophilic interactions can indeed affected by different substituents. The N-Pt-S-C dihedral angles changes slightly due to steric effects. In addition, the dihedral angles of C-Pt-Pt-C in the complexes **[L'Pt-4]$_2$**, **[L'Pt-5]$_2$**, and **[L'Pt-6]$_2$** are larger than those in other complexes. This is ascribed to the larger steric effects induced by the larger sizes of the substituents.

3.6.3 Dimerisation energy

Having the optimised monomers and dimers in hand, the binding energies of dimerisation in gas phase can be calculated using the equation 3.1.

$$\Delta G_{gas} = \Delta G_{dimer} - 2\Delta G_{mono} \quad (3.1)$$

where ΔG_{gas} is the binding energy of dimerisation in gas phase, ΔG_{mono} and ΔG_{dimer} are the sum of electronic and thermal free energies (Gibbs free energy) for the monomer and dimer respectively.

To compare with the experimentally measured dimerisation energies, solvation effects were also been taken into account by performing single point calculations at TPSSTPSS/def2TZVP/fit/GD3BJ level of theory using the continuum SMD solvation model in chloroform. The standard state used in the Gaussian solvation calculation is that of an ideal gas at 1 atm (denoted as $^{\ominus}$), which should be converted to the standard state of 1 M solution (denote as *).[31] The energy difference $\Delta G^{\ominus\rightarrow *}$ at 298 K is

$$\Delta G^{\ominus\rightarrow *} = -T\Delta S^{\ominus\rightarrow *} = RT\ln(V^{\ominus}/V^{*}) = 298R\ln(24.46/1) = 7.92 \text{ kJ mol}^{-1} \quad (3.2)$$

As only the SCF energy can be obtained in single point calculations, the Gibbs free energy ΔG^{*} at the standard state of 1 M solution can be calculated using equation 3.3.

$$\Delta G^{*} = \Delta E_{SCF} + \Delta E_{corr} + \Delta G^{\ominus\rightarrow *} \quad (3.3)$$

where the ΔE_{SCF} is the SCF energy, the ΔE_{corr} is the thermal correction to Gibbs free energy. The ΔE_{corr} can be obtained from the results of geometry optimisation. The Gibbs free energy for monomer (ΔG_{mono_sol}) and dimer (ΔG_{dimer_sol}) at standard state * in chloroform can thus be calculated. Then the dimerisation energy ΔG_{sol} in chloroform is calculated by equation 3.4.

$$\Delta G_{sol} = \Delta G_{dimer\_sol} - 2\Delta G_{mono\_sol} \quad (3.4)$$

The binding energies of these dimers **[L'M-X]$_2$** with and without solvation effects have been calculated using equations 3.1–3.4. The results are listed in **Table 3.3**.

Table 3.3 Computational results for complexes **L'M-X** computed at TPSSTPSS/def2TZVP/fit/GD3BJ using Gaussian 09. ΔG_{exp} is the experimentally measured binding energy of complexes **LM-X**. ΔG_{gas} and ΔG_{sol} are computational binding energies in the gas phase and in chloroform using SMD model. d_{Pt-Pt} is the Pt–Pt distance in optimised dimer, and d_{Pt-S} is Pt–S distance in the optimised monomer. ESP charge of S is obtained from monomeric complex.

Complex	ΔG_{exp} / kJ mol^{-1}	ΔG_{gas} / kJ mol^{-1}	ΔG_{sol} / kJ mol^{-1}	d_{Pt-Pt} / Å	d_{Pt-S} / Å	ESP charge of S
L'Ni-2	-	−54.6	−40.4	-	-	−0.369
L'Pd-2	-	−56.0	−38.3	-	-	−0.365
L'Pt-2	−5.0	−60.3	−42.7	3.114	2.439	−0.336
L'Pt-3	−0.8	−62.6	−41.8	3.100	2.421	−0.368
L'Pt-4	−3.2	−73.0	−48.2	3.139	2.445	−0.307
L'Pt-5	−2.5	−73.5	−43.0	3.095	2.428	−0.435
L'Pt-6	+0.8	−74.0	−38.9	3.130	2.414	−0.469
L'Pt-7	+0.2	−63.7	−42.8	3.110	2.415	−0.471
L'Pt-8	−2.4	−55.6	−36.5	3.128	2.429	−0.499
L'Pt-9	+0.4	−52.0	−31.1	3.082	2.422	−0.537

The gas phase dimerisation energy ΔG_{gas} varies from −51 kJ mol^{-1} to −74 kJ mol^{-1}, which is much larger than the experimentally measured dimerisation energy ΔG_{exp} (< −5 kJ mol^{-1}). After taking solvation effects into account (SMD, chloroform), the ΔG_{sol} decreases to −31 kJ mol^{-1} to −49 kJ mol^{-1}, which are closer to, but still somewhat larger than the experimental values. The energy difference between ΔG_{sol} and ΔG_{exp} is reasonable as the complexes **L'M-X** and **LM-X** used for experimental and computational studies respectively are not exactly the same, while continuum solvent models are known to have major limitations in regards to accuracy. Furthermore, long

hexyl chains in **LM-X** are replaced by methyl groups in **L'M-X** to save computational sources. The dimerisation energies ΔG_{sol} for complexes **L'M-2** with different metal centres are similar to each other. The small difference introduced by different metal cations suggest metallophilic interactions contribute little to the dimerisation energy.

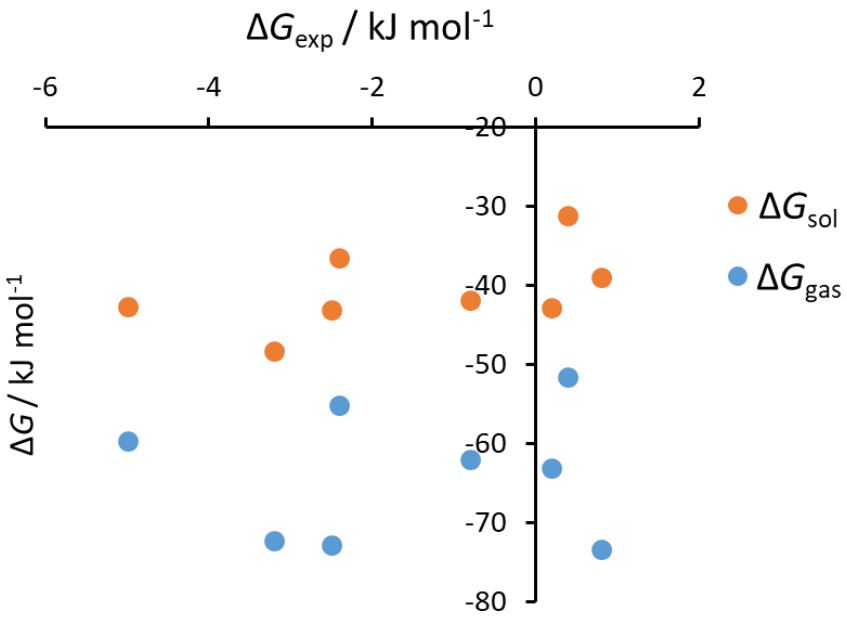

Figure 3.17 The relationship between computed binding energies ΔG_{gas}, ΔG_{sol} of complexes **L'Pt-X** and experimental measured binding energies ΔG_{exp} of complexes **LPt-X**.

The correlation between the experimental energies ΔG_{exp} and theoretical energies ΔG_{sol} in chloroform (**Figure 3.17**) are better than the correlation between ΔG_{exp} and ΔG_{gas} (though still not good). The poor correlation between ΔG_{exp} and ΔG_{sol} may be attributed to large experimental errors and estimation errors from the implicit SMD model.

Parameters including the electrostatic potential (ESP) charge of S in the monomeric **L'Pt-X**, Pt–Pt distance and Pt–S bond length have also been plotted against ΔG_{exp} or ΔG_{sol} (**Figure 3.18**). The poor correlations indicate the influence of substituents to dimerisation energies is complicated and is not simply affected by the electron-withdrawing properties of the substituents, Pt–Pt distance, or Pt–S bond length.

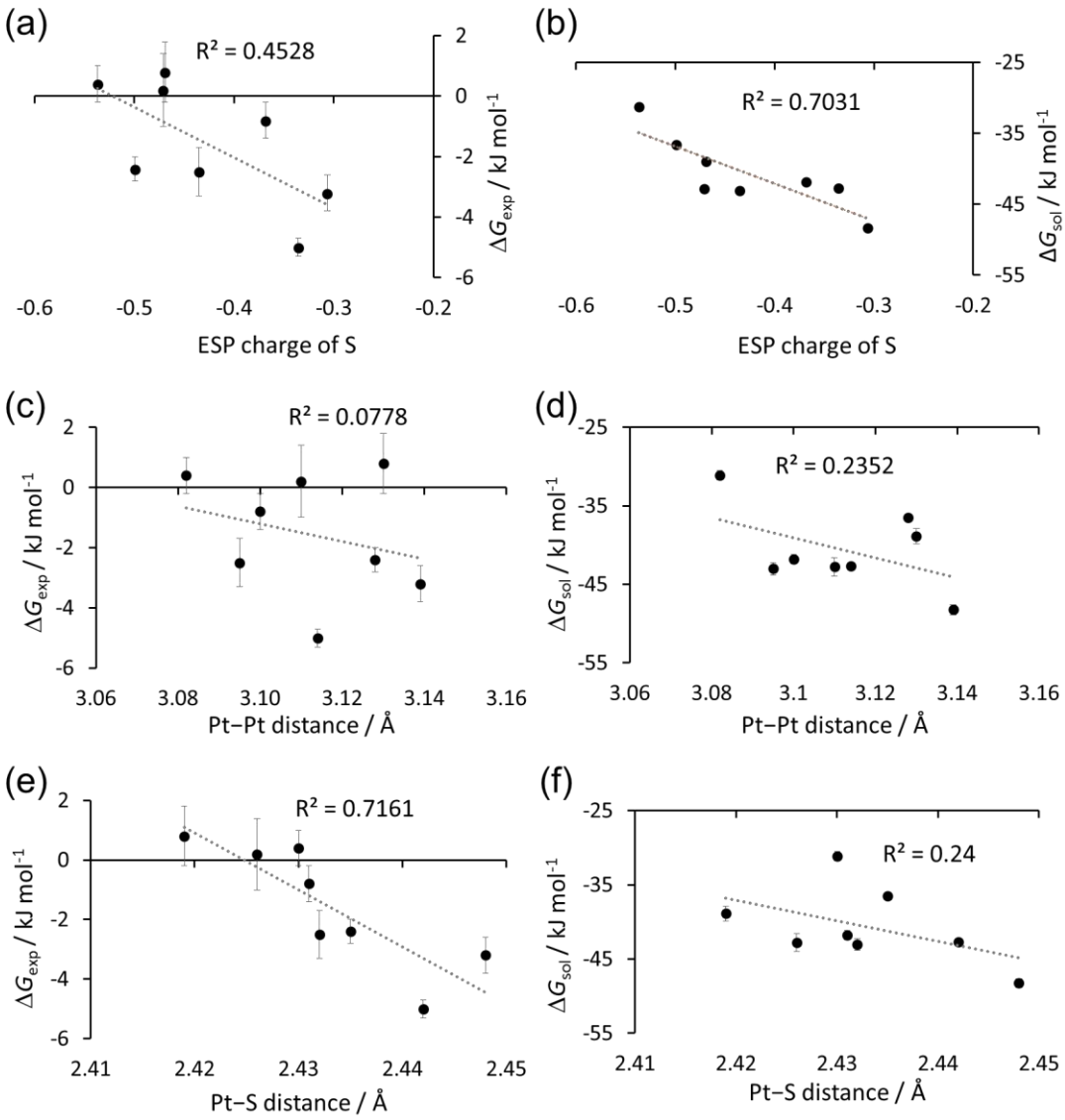

Figure 3.18 Plots showing the correlation of experimental dimerisation energies ΔG_{exp} and computed energy in chloroform ΔG_{sol} against (a, b) ESP charge of S, (c, d) Pt–Pt distance, and (e, f) Pt–S distance.

3.6.4 Energy decomposition analysis (EDA)

Energy decomposition analysis (EDA) embedded in the ADF package can decompose the overall interactions into electrostatic interactions, dispersion interactions, orbital interactions and Pauli repulsion. By varying the metal cations and substituents of the dimer **[L'M-X]$_2$**, the change in dimerisation interactions would hopefully shine some light on our understanding of metallophilic interactions. The results are listed in **Table B.12** in Appendix B.

EDA results from complexes **L'M-2** with different metals are displayed in **Figure 3.19**. The overall interactions ΔE_{int} (black empty bar) is decomposed into electrostatic interactions ΔE_{elstat} (cyan bar), dispersion interactions ΔE_{disp} (pale blue bar), orbital interactions ΔE_{orb} (dark blue bar) and Pauli repulsion ΔE_{Pauli} (magenta bar). Electrostatic attraction is the dominant attractive interaction, followed by dispersion and orbital interactions. Pauli repulsion is very strong due to the large size of the fragments in cyclometalated metal complex. When changing the Pt^{II} centre to Pd^{II} and Ni^{II}, the electrostatic interactions and Pauli repulsion are obviously reduced, while dispersion and orbital components are barely changed. However, the increase of the electrostatic attraction is offset by the Pauli repulsion resulting in the same overall interactions.

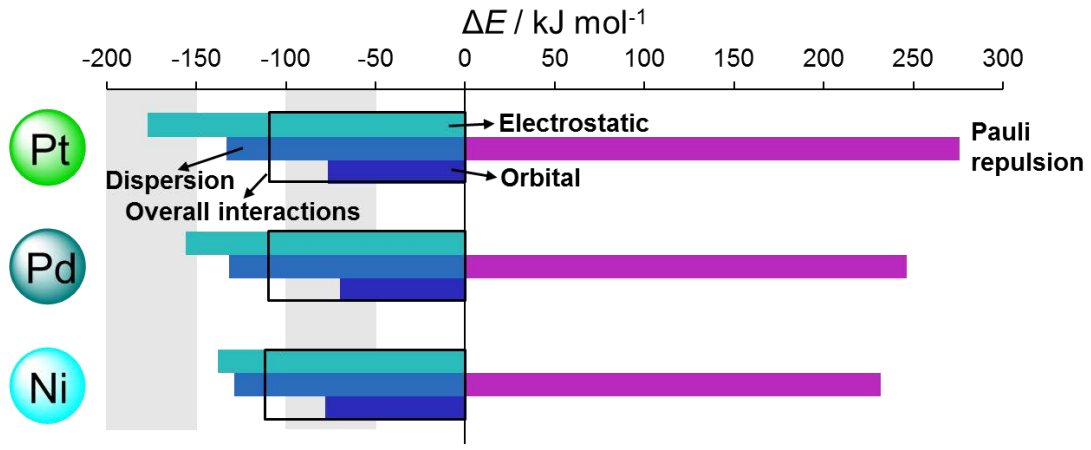

Figure 3.19 Energy decomposition analysis results of complexes **L'M-2** calculated at ZORA-PBE-GD3BJ/TZ2P level of theory.

The above discussion is based on the energies of complexes **L'M-2**, however, as the metal–metal distance decreases from Pt to Ni, the energies may not be suitable for direct comparison. Percentage contributions of ΔE_{elstat}, ΔE_{disp}, ΔE_{orb} to the total attraction may be more reliable for comparison. As shown in **Figure 3.20**, electrostatic is the dominant component and its contribution decreases slightly from Pt to Ni. The contributions from dispersion and orbital interactions are of similar value for different metal centres.

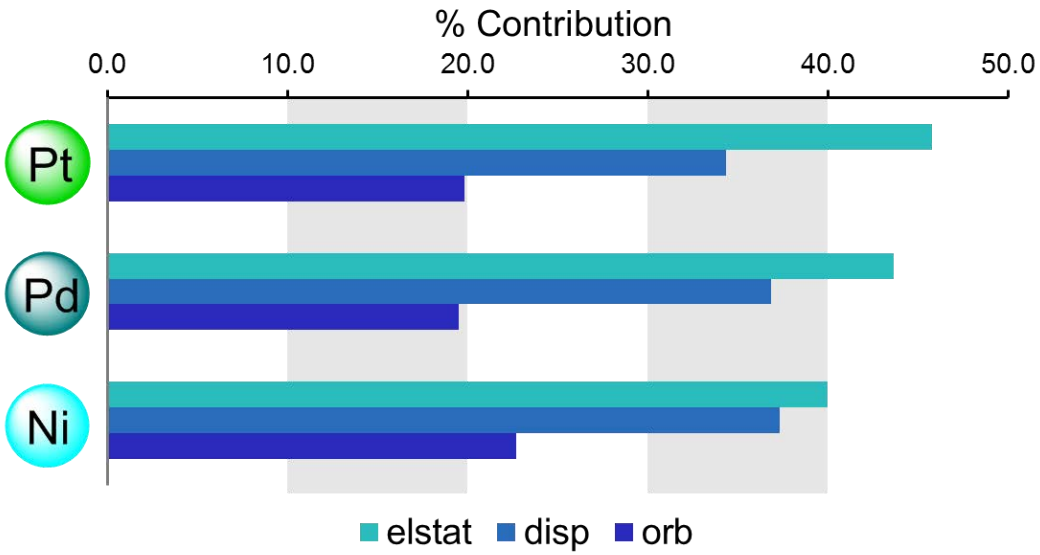

Figure 3.20 Percentage contributions of electrostatic interactions (blue-green), dispersion (pale blue), and orbital interactions (bright blue) to the attractive interactions in complexes **L'M-2** calculated at ZORA-PBE-GD3BJ/TZ2P level of theory.

These results shown in **Figure 3.19** and **Figure 3.20** suggest changing metals mainly affect electrostatic interactions. The change of dispersion and orbital interactions are tiny. The overall interactions are not affected by different metals, which means metallophilic interactions do not play a significant role in the dimerization. Otherwise, varying metal centres would change the dimerisation energy significantly.

When changing the substituents in ligands **2-9**, the electronic properties of S and Pt would be changed. The proposed Pt–Pt interactions would thus be changed. The EDA results of complexes **L'M-X** (**Figure 3.21**) demonstrate that the overall interactions and four components change slightly upon varying ligands. The interactions do not correlate with donor-acceptor ability of the ligands, which is consistent with the results obtained from Gaussian calculations. Percentage contributions in **Figure 3.22** demonstrate more clearly that varying ligands/substituents slightly change the contributions from electrostatic, dispersion, and orbital interactions. But no good

correlation with donor-acceptor is found, confirming that metallophilic interactions do not originate from electrostatic interactions.

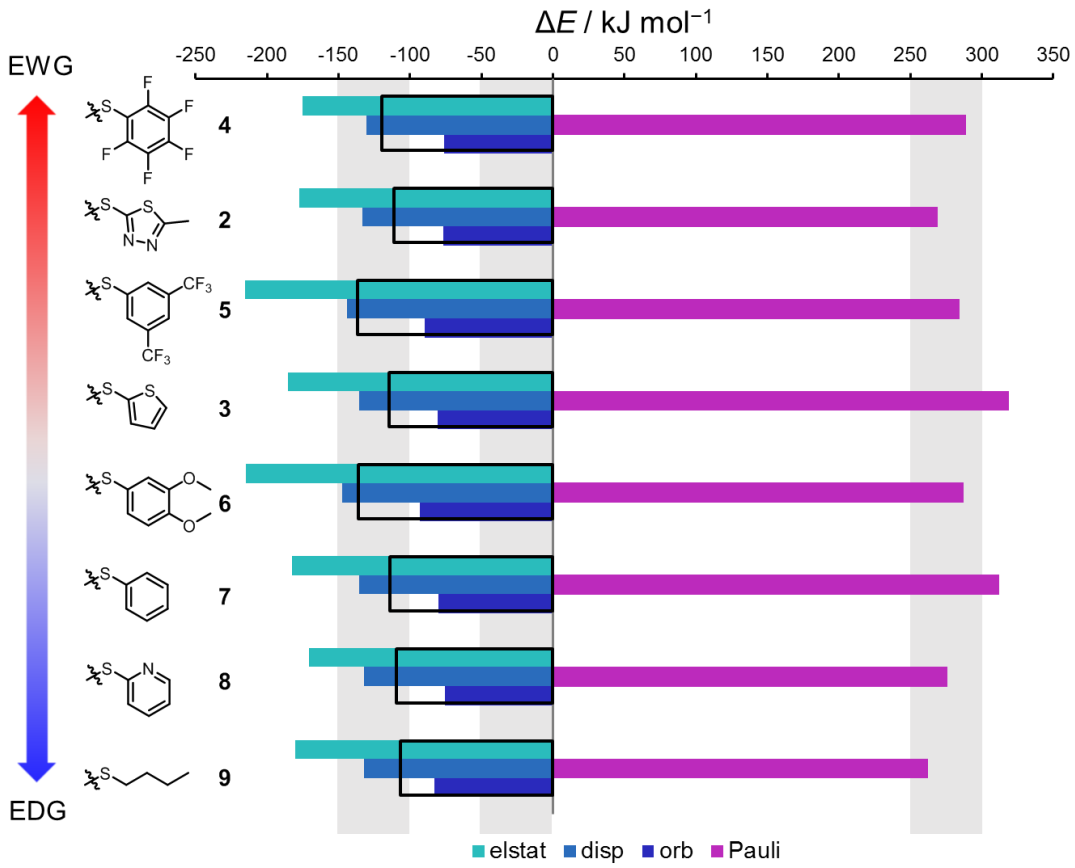

Figure 3.21 Energy decomposition analysis of complexes **L'Pt-X** performed at ZORA-PBE-GD3BJ/TZ2P level of theory.

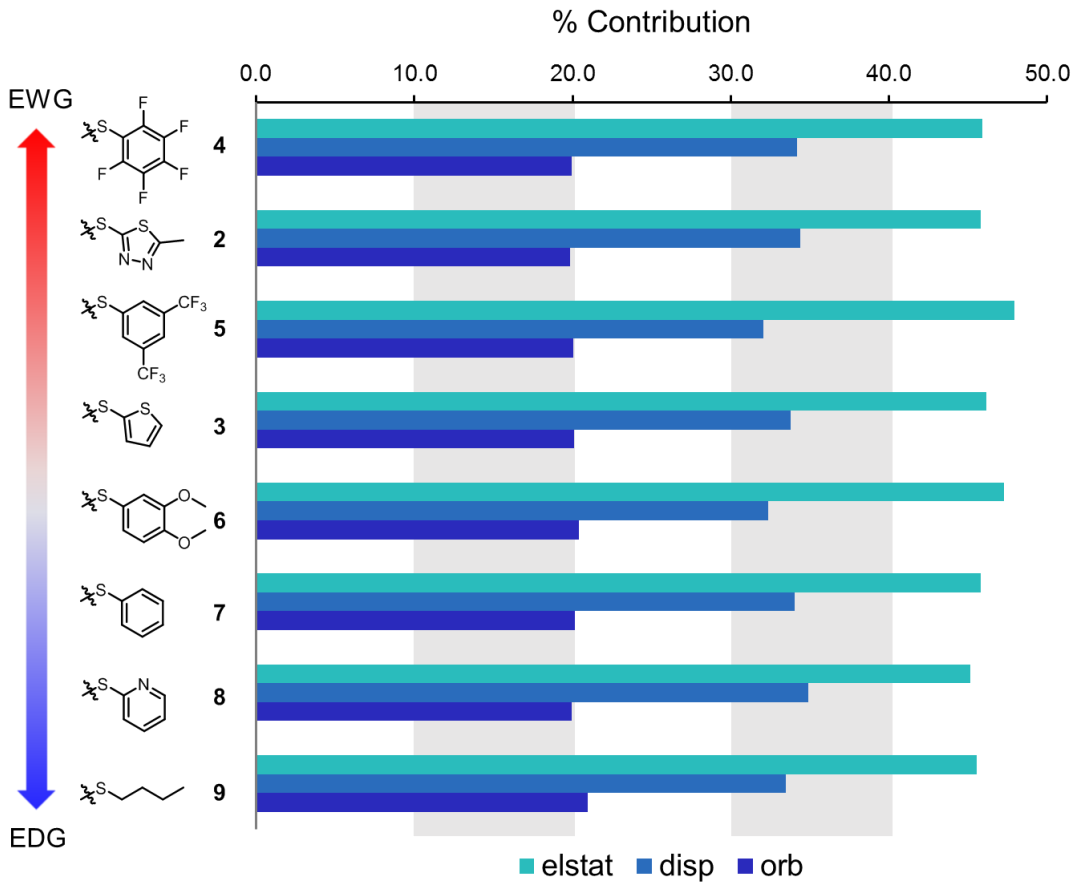

Figure 3.22 Percentage contributions of electrostatic interactions (blue-green), dispersion (pale blue), and orbital interactions (bright blue) to the attractive interactions in complexes **L'Pt-X** calculated at ZORA-PBE-GD3BJ/TZ2P level of theory.

Energy decomposition analysis combined with the natural orbitals for chemical valence theory (EDA-NOCV) enables identification of significant contributions from pairwise orbitals to orbital interactions. **Figure 3.23** shows the NOCV deformation densities computed for complexes **L'M-2** (M = Pt, Pd, Ni), in which charge flow takes place from red to blue. The first NOCV (ΔE^1_{orb}) describes a depletion (red) of electron density between the metal centres and an accumulation (blue) at the outer side of the metal centres. Whereas the second NOCV (ΔE^2_{orb}) illustrates density flows from the outer side of the metal–metal contact to inner side. The sum of ΔE^1_{orb} and ΔE^2_{orb} (–25 to –32 kJ mol^{-1}) contributes 35–42% of the orbital interactions, indicating the dominant role of metallophilic interactions to orbital interactions. These NOCV results also support the hypothesis that metallophilic interactions have an orbital nature (at

least partially). Other EDA-NOCV deformation densities and corresponding contributions are given in Appendix B and show consistent results.

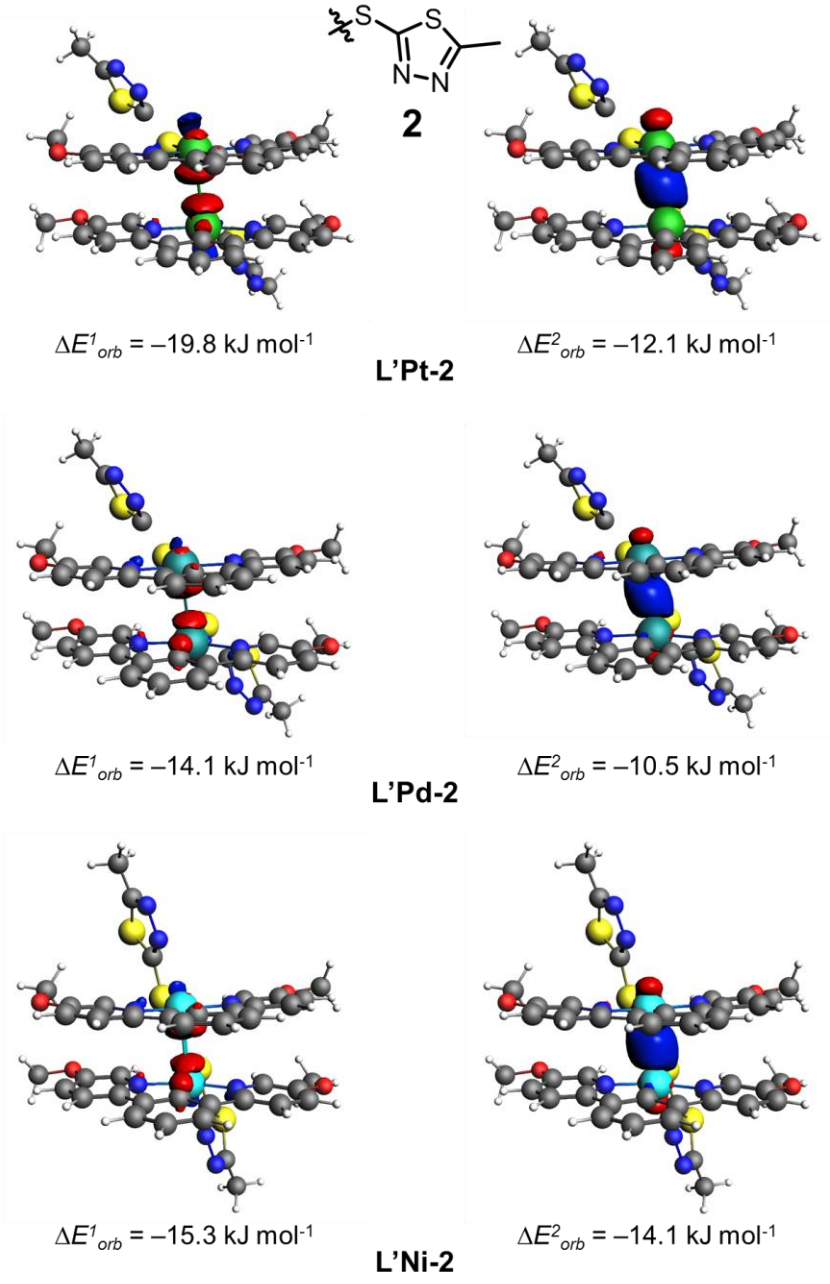

Figure 3.23 EDA-NOCV computed main deformation densities (Δρ) and corresponding energetic contributions for **L'Pt-2**, **L'Pd-2**, and **L'Ni-2**. Red: areas of charge depletion, blue: areas of charge accumulation.

3.7 Conclusions

A series of complexes **LM-X** (L = 1,3-di(5-hexyloxy-2-pyridyl)benzene, M = Pt^{II}, Pd^{II}, Ni^{II}, X = Cl or thiol derivatives) have been successfully synthesised. Metallophilic interactions are observed in the crystal structure of complex **LPt-2**, but not in complex **LPd-2** and complex **LPt-7**, which suggests metallophilic interactions are weak and can be easily tuned by metal centres and substituents. The weak strength is confirmed by weak binding in solution, as supported by ^{1}H NMR dilution spectra. The influence of different metal centres and different substituents are further investigated through computational studies. Binding energies have been computed, and energy decomposition analyses (EDA) have been performed. Changing the metal does not affect the overall dimerisation energies, and only influence electrostatic attraction and Pauli repulsion. Therefore, the contribution from metallophilic interactions to molecular assembly is weak, otherwise varying metal centres would change the dimerisation energy significantly. Varying substituents can slightly affect the dimerisation energy, but the change is poorly correlated with the donor-acceptor ability of the substituents, which indicates that metallophilic interactions do not have an electrostatic nature. Instead, the nature of metallophilic interactions is found to be orbital interactions (at least partially) as supported by EDA-NOCV studies. The weak strength and negligible contribution of metallophilic interactions alert us that future studies of metallophilic interactions in organometallic complexes should be treated with caution to avoid overestimation of their energetic significance.

3.8 Experimental

All the chemicals and solvents were purchased from commercial suppliers and used without purification unless stated otherwise. Dry solvents were obtained from a *PureSolv* solvent purification system. Melting points were measured in a *Gallenkamp* melting point apparatus. Mass spectrometry was performed using the University of Edinburgh technician-supported mass spectrometry service, on a *ThermoElectron MAT XP* spectrometer for ESI-HRMS. ^{1}H, ^{19}F and ^{13}C NMR spectra were recorded on either 400 or 500 MHz *Bruker Avance III* spectrometer. Single-crystal X-ray diffraction was performed on an Agilent Technologies SuperNova diffractometer equipped with an Oxford Cryosystems Cryostream 700+ low-temperature apparatus operating at T = 120.0 K. Using **Olex2**[32], the structure was solved with the **ShelXS**[33] structure solution program, using the Patterson Method. The model was refined with **ShelXL**[33] using Least Squares minimisation. All non-hydrogen atoms were refined anisotropically. Hydrogen atom positions were calculated geometrically and refined using the riding model.

3.8.1 Synthesis

Preparation of 1,3-di(5-hydroxy-2-pyridyl)benzene (L_0)

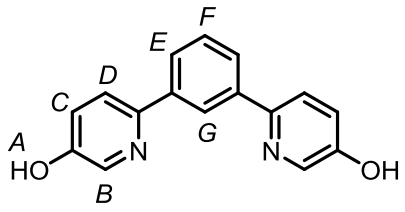

A mixture of 1,3-benzenediboronic acid (1.000 g, 6.0 mmol), 2-bromo-5-hydroxypyridine (2.300 g, 13.2 mmol), $Pd_2(dba)_3$ (0.110 g, 0.12 mmol), PCy_3 (0.084 g, 0.3 mmol), K_3PO_4 (4.320 g, 20.4 mmol), dioxane (40 mL) and H_2O (20 mL) was heated to 101 °C and kept refluxing for 24 hours under nitrogen atmosphere. The mixture was cooled and filtered, then 1M HCl and saturated $NaHCO_3$ were added into the filtrate to adjust pH to 7-8. The aqueous solution was washed with ethyl acetate (3 × 25 mL) and separated. The combined organic phase was dried over anhydrous $MgSO_4$. The solvent of the filtrate was removed under reduced pressure. The yellow crude solid was then recrystallized (hexane / ethyl acetate = 1 / 1) to yield a white solid (1.413 g, 89%). M.p. 232-235 °C. ^{1}H NMR (500 MHz, DMSO-d_6) δ 10.04 (s, br, 2H, H_A), 8.59 (t, J = 1.8 Hz, 1H, H_G), 8.25 (d, J = 2.9 Hz, 2H, H_B), 7.92 (dd, J = 7.8, 1.8 Hz, 2H, H_E), 7.87 (d, J = 8.6 Hz,

2H, H_D), 7.49 (t, J = 7.7 Hz, 1H, H_F), 7.26 (dd, J = 8.6, 2.9 Hz, 2H, H_C). ^{13}C NMR (126 MHz, DMSO-d_6) δ 153.11, 147.08, 139.09, 137.65, 128.90, 125.04, 123.06, 123.00, 120.84. MS-ESI: *m/z* 265.0991 $[MH]^+$ (expected 265.0972 $[MH]^+$).

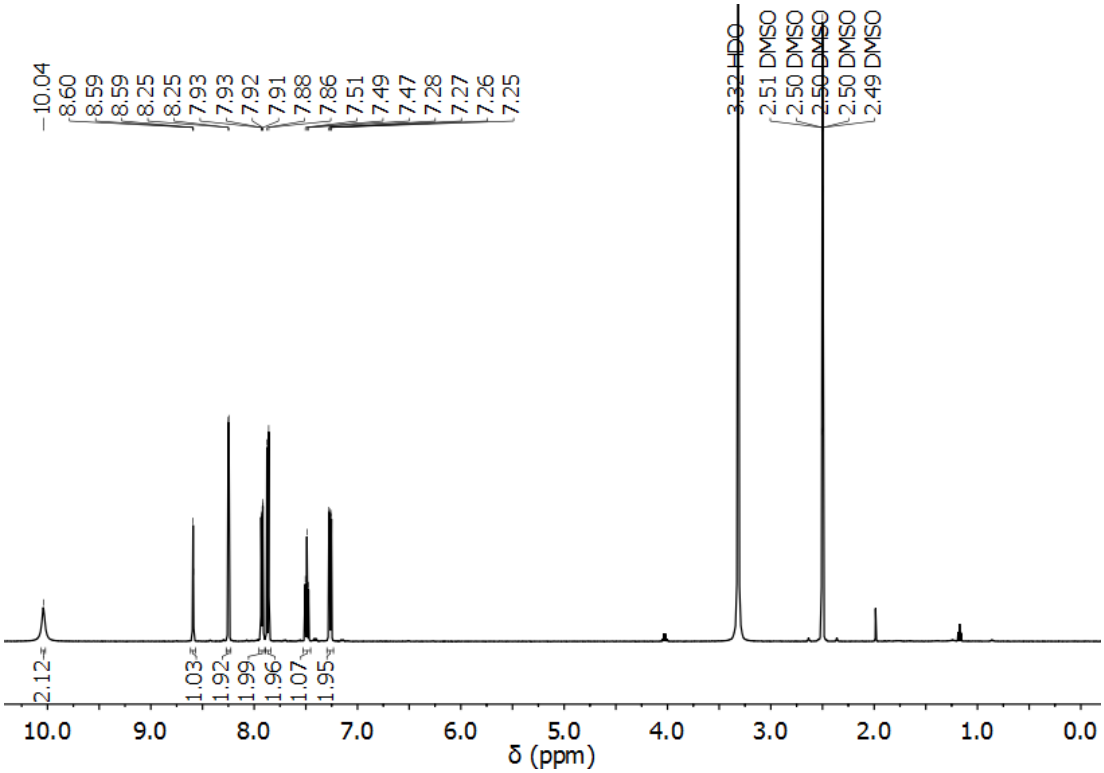

Figure 3.24 ^{1}H NMR spectrum of ligand $\mathbf{L_0}$ in DMSO-d_6.

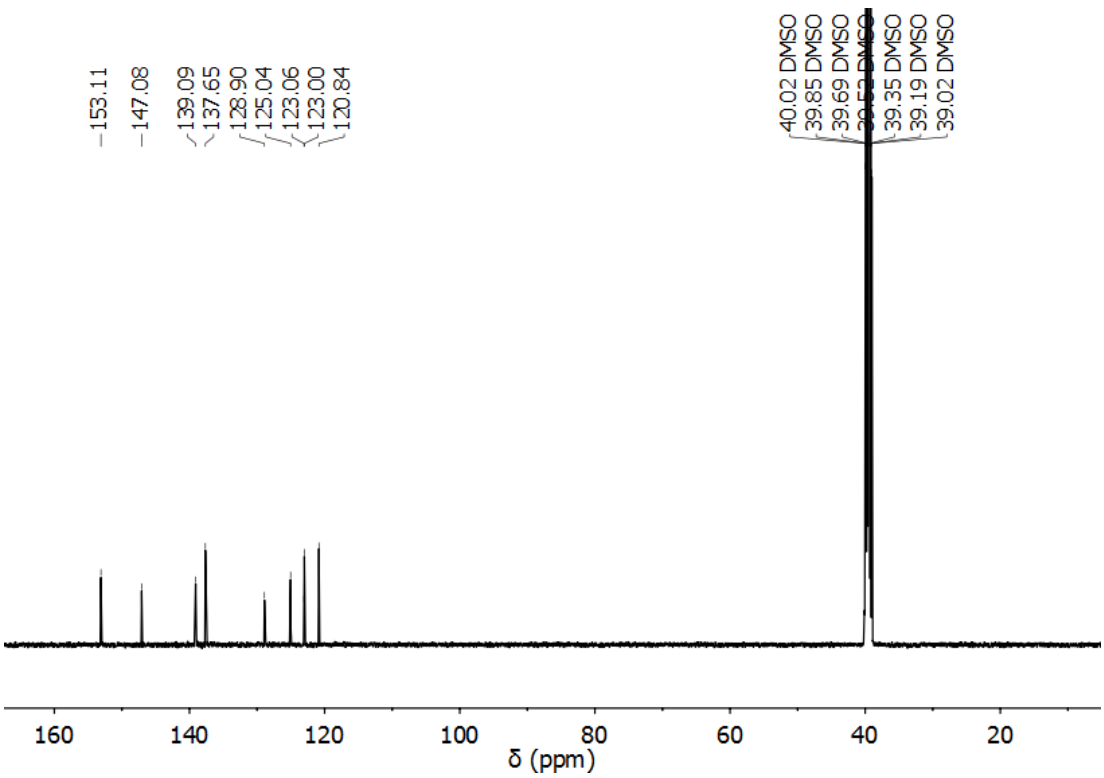

Figure 3.25 ^{13}C NMR spectrum of ligand $\mathbf{L_0}$ in DMSO-d_6.

Preparation of 1,3-di(5-hexyloxy-2-pyridyl)benzene (L)

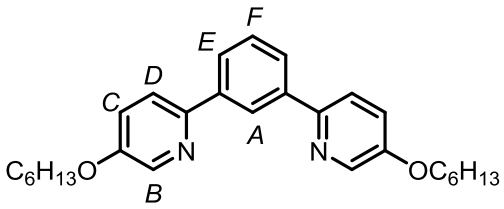

A mixture of 1,3-di(5-hydroxy-2-pyridyl)benzene ($\mathbf{L_0}$, 0.528 g, 2.0 mmol), potassium carbonate (1.656 g, 12.0 mmol) and 1-bromohexane (1 mL, 7.1 mmol) in DMF (30 mL) was stirred at 105 °C for 14 hours. Water (120 mL) was added, the precipitate was filtered, washed with water and methanol to yield a white solid (0.630 g, 73%). Melting point 78 °C. ^{1}H NMR (500 MHz, Chloroform-*d*) δ 8.49 (at, J = 1.8 Hz, 1H, H_A), 8.40 (d, J = 3.0 Hz, 2H, H_B), 7.94 (dd, J = 7.8, 1.8 Hz, 2H, H_E), 7.76 (d, J = 8.7 Hz, 2H, H_D), 7.52 (t, J = 7.7 Hz, 1H, H_F), 7.27 (dd, J = 9.0, 2.6 Hz, 2H, H_C), 4.05 (t, J = 6.5 Hz, 4H, OCH_2), 1.82 (dq, J = 8.0, 6.6 Hz, 4H, CH_2), 1.54 – 1.44 (m, 4H, CH_2), 1.36 (hept, J = 3.7, 3.2 Hz, 8H, CH_2), 0.94 – 0.90 (m, 6H, CH_3). ^{13}C NMR (126 MHz, $CDCl_3$) δ 154.63, 149.95, 139.76,

137.71, 129.22, 126.26, 124.54, 121.95, 121.10, 68.71, 31.72, 29.33, 25.80, 22.74, 14.18. MS-ESI: *m/z* 433.2876 $[MH]^+$ (expected 433.2850 $[MH]^+$).

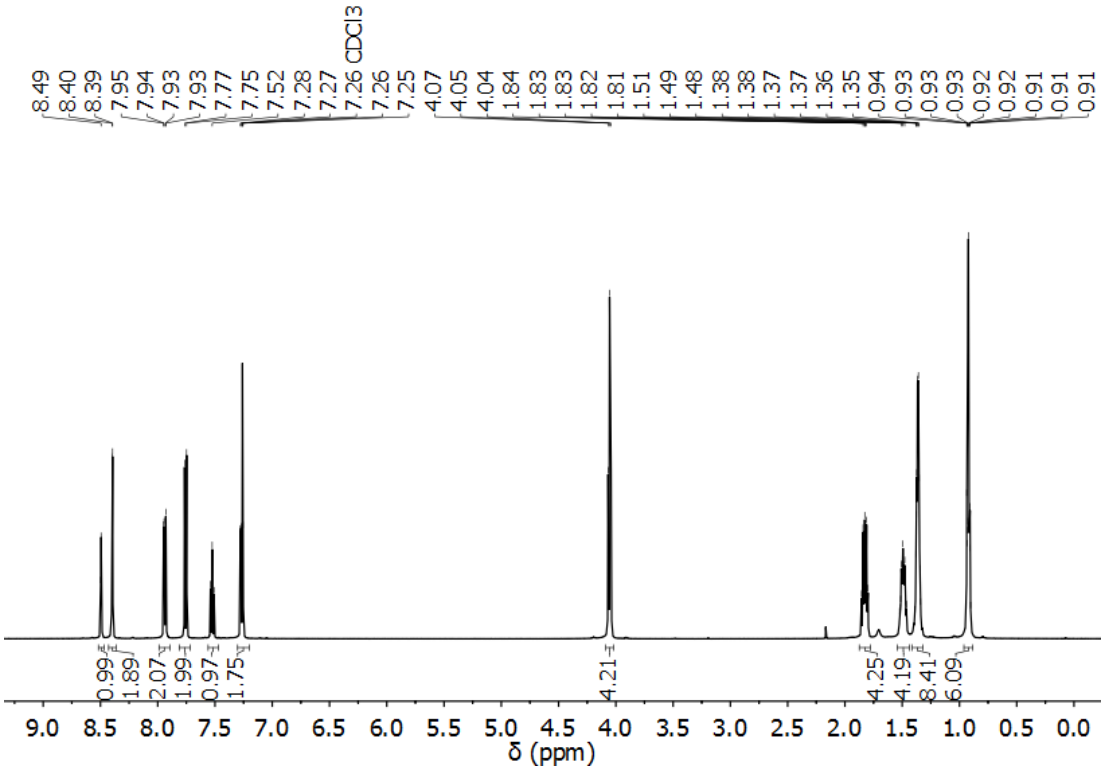

Figure 3.26 ^{1}H NMR spectrum of ligand **L** in $CDCl_3$-*d*.

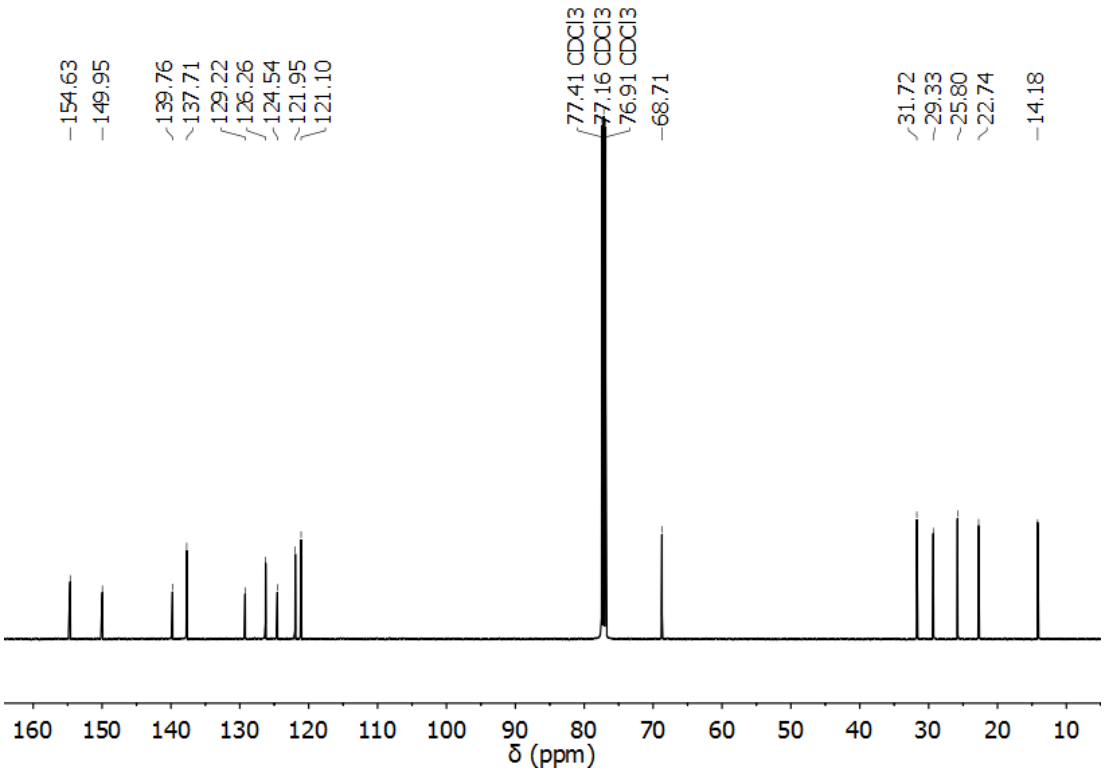

Figure 3.27 ^{13}C NMR spectrum of ligand **L** in $CDCl_3$-*d*.

Preparation of LPt-1

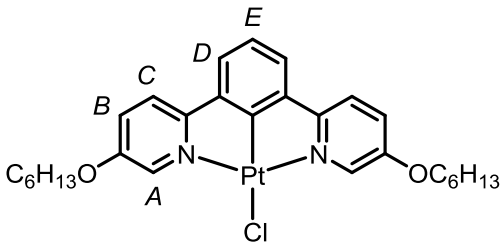

A mixture of the ligand **L** (0.432 g, 1.0 mmol), K_2PtCl_4 (0.415 g, 1.0 mmol) and acetic acid (100 mL) was heated under reflux for 3 days. Precipitated solid was filtered and washed with acetone. The crude solid was dissolved in chloroform and filtered to remove insoluble impurities. The filtrate was concentrated (5 mL) and was added acetone (10 mL) to gain yellow precipitate. The yellow powder (0.451 g, 68%) was then collected and dried under vacuum. M.p. 275 – 277 °C. ^{1}H NMR (500 MHz, Chloroform-*d*) δ 9.08 ($d_{satellite}$, J = 2.7 Hz, 2H, J (^{195}Pt-H) = 43.4 Hz, H_A), 7.57 (d, J = 8.8 Hz, 2H, H_C), 7.45 (dd, J = 8.8, 2.8 Hz, 2H, H_B), 7.27 (d, J = 7.6 Hz, 2H, H_D), 7.16 (dd, J = 8.1, 7.1 Hz, 1H, H_E), 4.10 (t, J = 6.4 Hz, 4H, OCH_2), 1.81 (ddt, J = 9.3, 7.9, 6.4 Hz, 4H, CH_2), 1.48 (ddd, J = 13.1, 7.2, 3.9 Hz, 4H, CH_2), 1.35 (ddd, J = 7.2, 4.6, 3.3 Hz, 8H, CH_2), 0.94 – 0.90 (m, 6H, CH_3). ^{13}C NMR (126 MHz, $CDCl_3$) δ 159.99, 158.65, 155.17, 141.08, 140.08, 124.91, 123.07, 121.99, 119.59, 69.40, 31.67, 29.18,

25.73, 22.73, 14.18. MS-ESI: *m/z* 626.2355 $[M–Cl]^+$, 1288.4383 $[2M–Cl]^+$ (expected 626.2346 $[M–Cl]^+$, 1288.4377 $[2M–Cl]^+$).

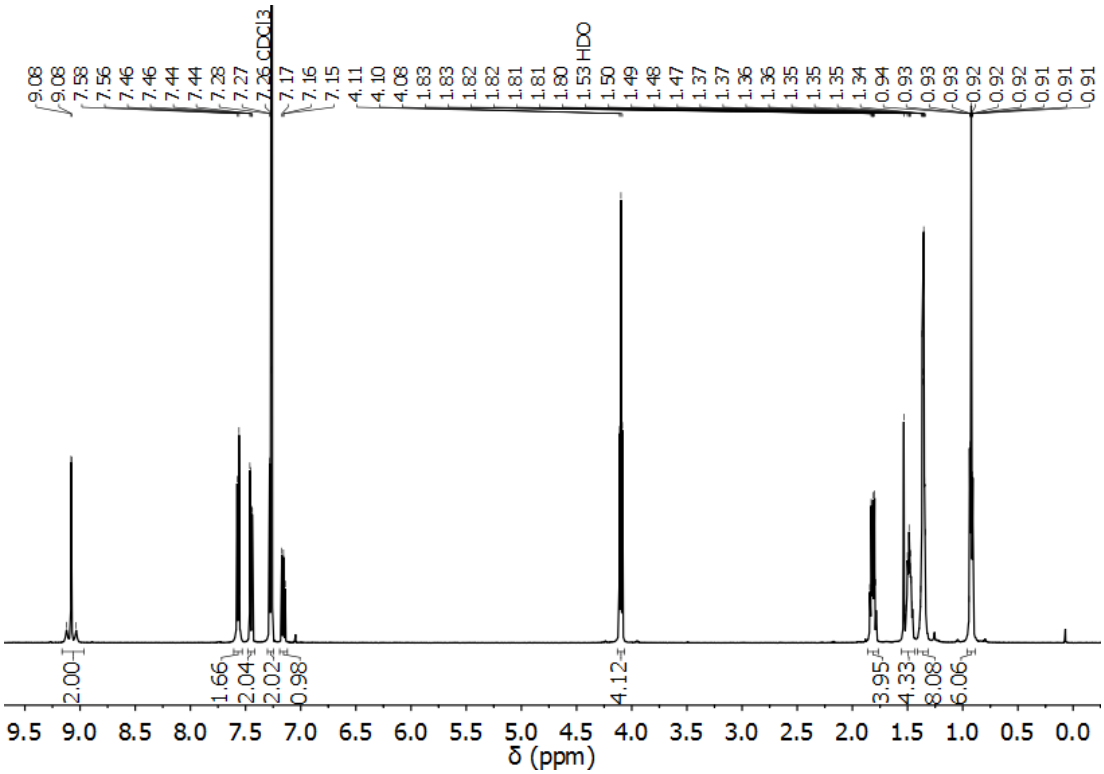

Figure 3.28 ^{1}H NMR spectrum of complex **LPt-1** in $CDCl_3$-*d*.

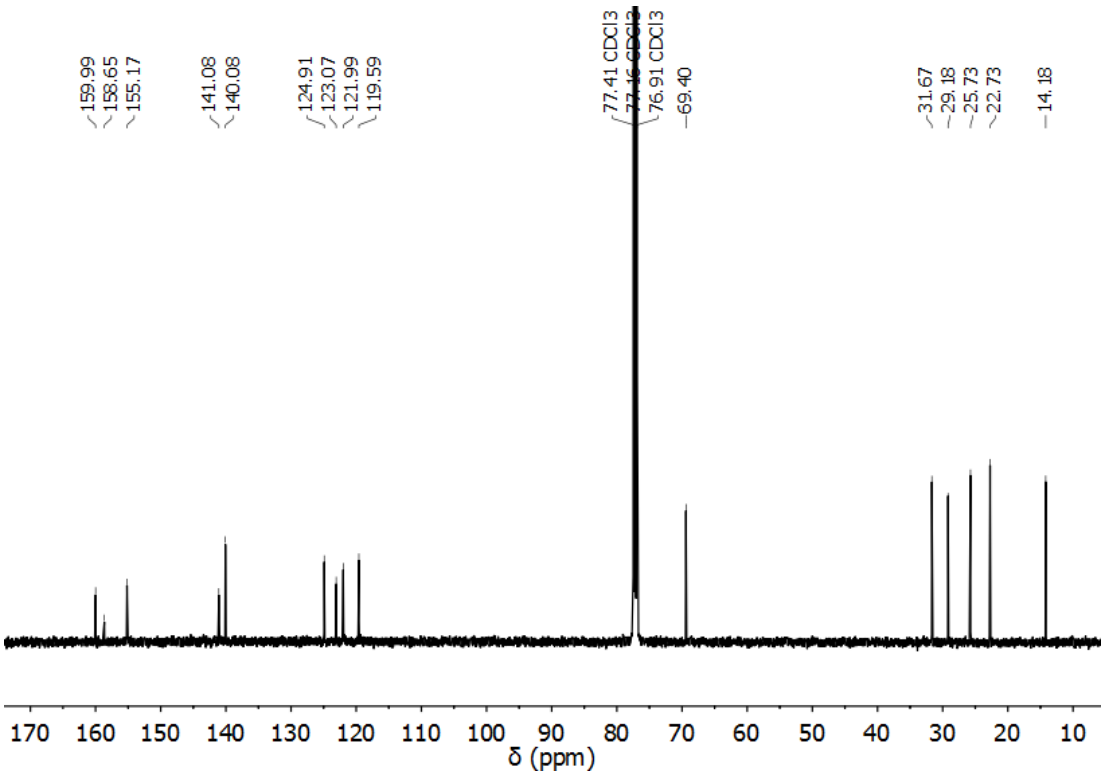

Figure 3.29 ^{13}C NMR spectrum of complex **LPt-1** in $CDCl_3$-*d*.

Preparation of LPd-1

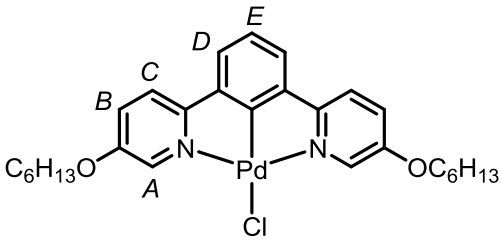

LPd-1 was synthesised using similar method to **LPt-1**, except the platinum salt was replaced by Na_2PdCl_4. Pale yellow solid (77%) was obtained. M.p. 205-206 °C. ^{1}H NMR (500 MHz, Chloroform-*d*) δ 8.79 (d, *J* = 2.7 Hz, 2H, H_A), 7.52 (d, *J* = 8.8 Hz, 2H, H_C), 7.35 (dd, *J* = 8.8, 2.8 Hz, 2H, H_B), 7.19 – 7.16 (m, 2H, H_D), 7.08 (dd, *J* = 8.2, 7.1 Hz, 1H, H_E), 4.06 (t, *J* = 6.4 Hz, 4H, OCH_2), 1.79 (ddt, *J* = 9.3, 7.9, 6.3 Hz, 4H, CH_2), 1.52 – 1.42 (m, 4H, CH_2), 1.38 – 1.32 (m, 8H, CH_2), 0.94 – 0.89 (m, 6H, CH_3). ^{13}C NMR (126 MHz, Chloroform-*d*) δ 169.69, 157.66, 154.89, 143.34, 140.34, 124.70, 124.40, 121.92, 119.25, 69.30, 31.66, 29.18, 25.72, 22.72, 14.18. MS-ESI: *m/z* 537.1732 $[M–Cl]^+$, 1111.3262 $[2M–Cl]^+$ (expected 537.1728 $[M–Cl]^+$).

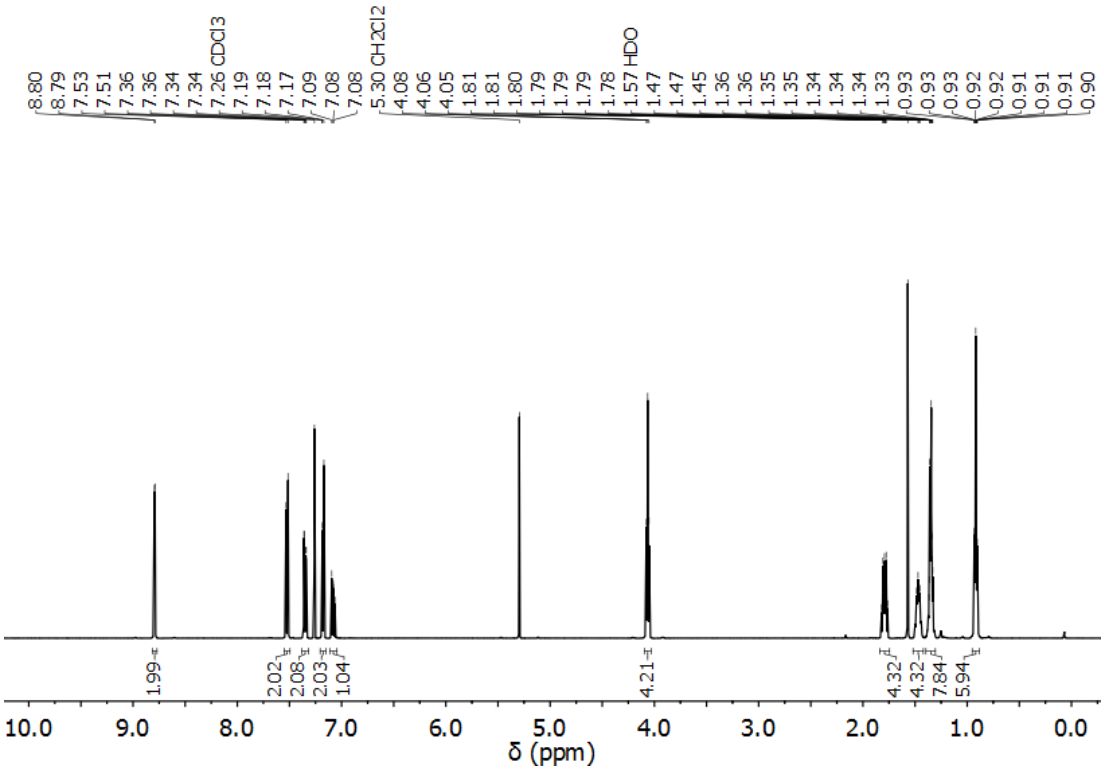

Figure 3.30 ^{1}H NMR spectrum of complex **LPd-1** in $CDCl_3$-*d*.

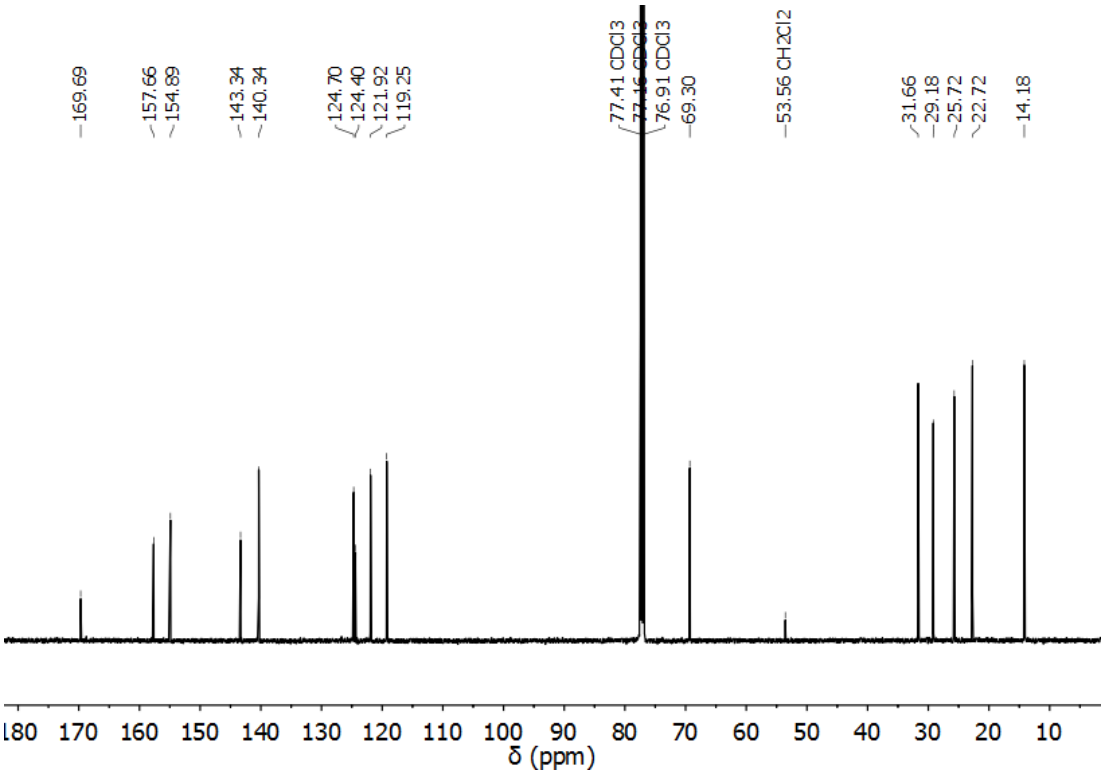

Figure 3.31 ^{13}C NMR spectrum of complex **LPd-1** in $CDCl_3$-*d*.

Preparation of LNi-1

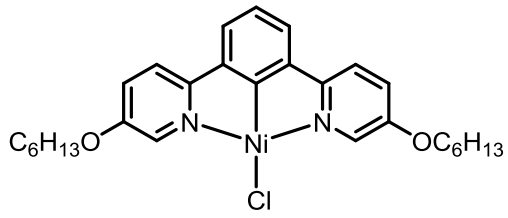

To a mixture of ligand **L** (0.2 mmol, 86.4 mg) and anhydrous $NiCl_2$ (38.9 mg, 0.3 mmol) in anhydrous toluene (20 mL) was added Et_3N (44 mL, 0.3 mmol). The reaction mixture was then refluxed for 48 hours. The mixture was cooled to room temperature and then filtered. Solvent of the filtrate was removed under reduced pressure. The residue was purified by flash column (light petroleum 60-80 / ethyl acetate = 5 / 1). Green solid (0.047 g, 45%) was obtained. ^{1}H NMR (500 MHz, Chloroform-*d*) δ 8.83 (s, 2H, PyH), 7.37 (d, *J* = 8.7 Hz, 2H, PyH), 7.29 (d, *J* = 8.8 Hz, 2H, PyH), 7.08 (s, 3H, PhH), 4.03 (t, *J* = 6.5 Hz, 4H, OCH_2), 1.83 – 1.74 (m, 4H, CH_2), 1.47 (dqd, *J* = 12.7, 7.1, 6.1, 3.7 Hz, 4H, CH_2), 1.40 – 1.30 (m, 8H, CH_2), 0.97 – 0.87 (m, 6H, CH_3). ^{13}C NMR (126 MHz, Chloroform-*d*) δ 167.330, 155.985, 154.413, 144.330, 141.803, 124.848, 124.756, 120.177, 118.019, 69.162, 31.663, 29.172, 25.724, 22.721, 14.174. MS-ESI: *m/z* 547.1623 $[M+Na]^+$ very weak intensity 1%, (expected 547.1633 $[M+Na]^+$). The complex decomposes significantly upon ionization.

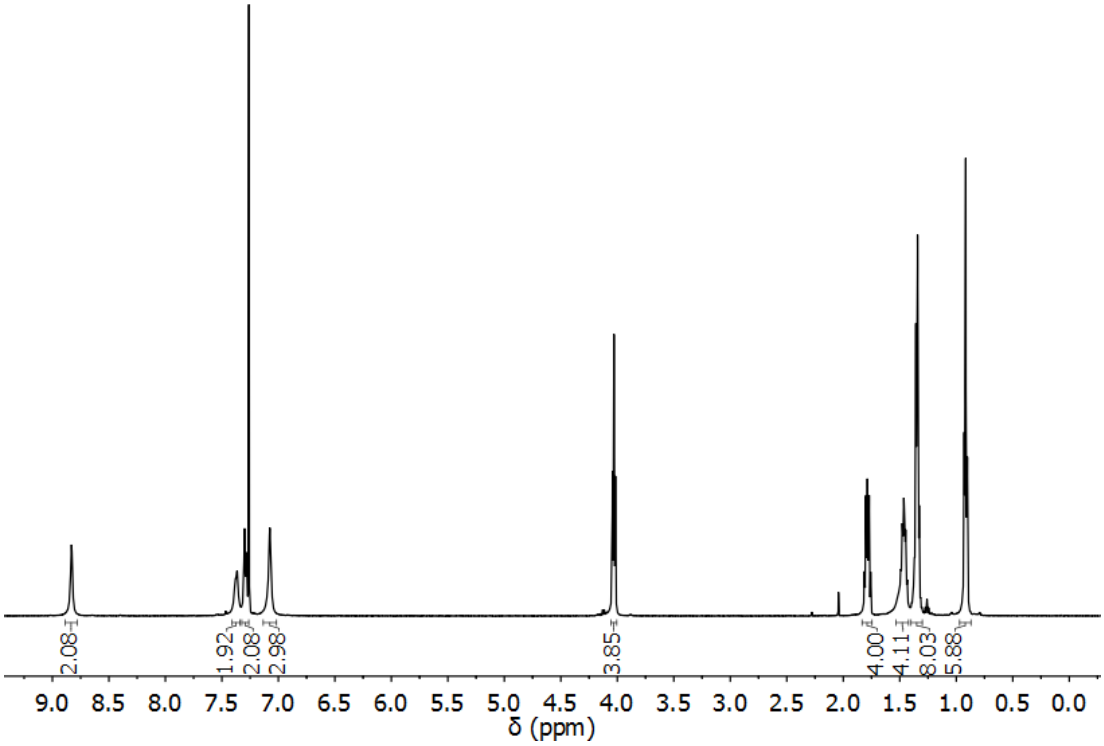

Figure 3.32 ^{1}H NMR spectrum of complex **LNi-1** in $CDCl_3$-*d* at 25 °C.

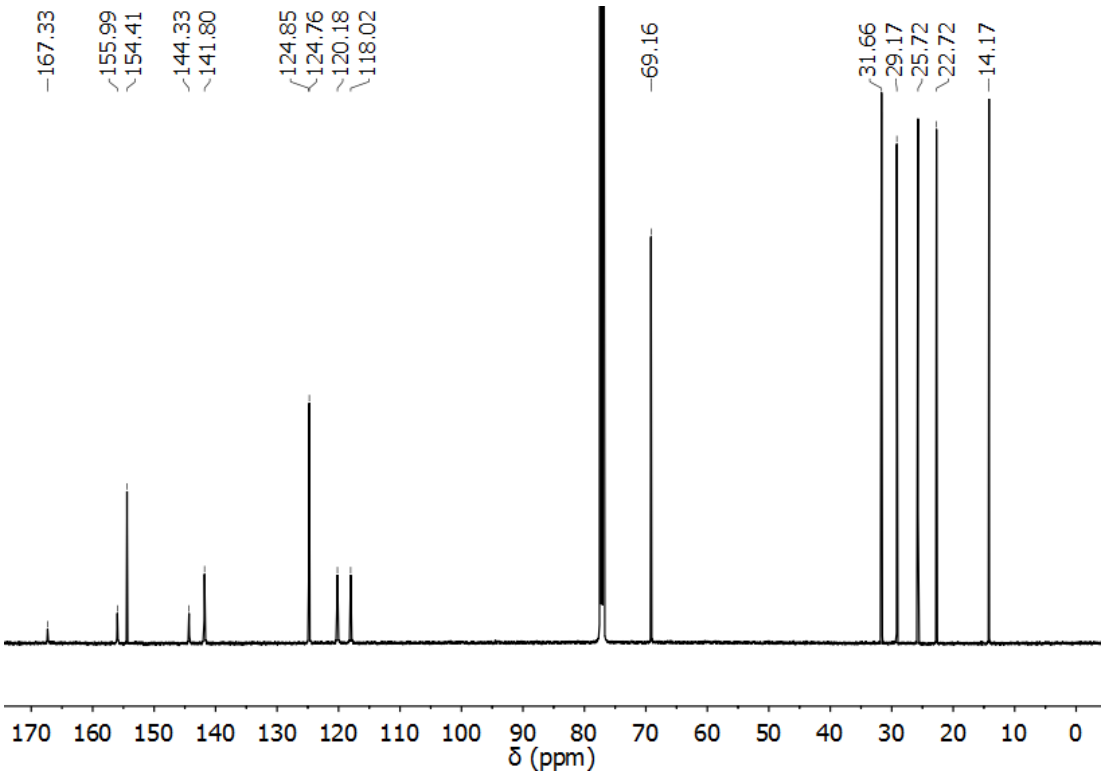

Figure 3.33 ^{13}C NMR spectrum of complex **LNi-1** in $CDCl_3$-*d* at 25 °C.

Preparation of LPt-2

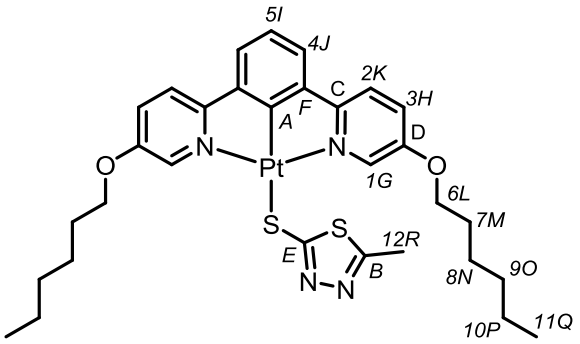

A mixture of **LPt-1** (0.264 g, 0.4 mmol), 2-mercapto-5-methyl-1,3,4-thiadiazole (STD, 0.078 g, 0.6 mmol) and NaO^{t}Bu (0.056 g, 0.6 mmol) in anhydrous methanol (5 mL) was refluxed overnight under a nitrogen atmosphere. Then solvent of the mixture was removed under reduced pressure. The obtained solid was dissolved in dichloromethane (5 mL) and then filtered to remove excess NaO^{t}Bu. The filtrate was concentrated (2 mL) and Et_2O (4 mL) was added to yield an orange precipitate. The orange solid (0.218 g, 72%) was collected and dried under vacuum. M.p. 159 – 160 °C. ^{1}H NMR (500 MHz, Chloroform-*d*) δ 9.05 – 8.89 ($s_{satellite}$, 2H, *J* (^{195}Pt-H) = 43.8 Hz, H_1), 7.52 (d, *J* = 8.8 Hz, 2H, H_2), 7.40 (dd, *J* = 8.8, 2.8 Hz, 2H, H_3), 7.24 (d, *J* = 7.7 Hz, 2H, H_4), 7.13 (t, *J* = 7.6 Hz, 1H, H_5), 3.96 (t, *J* = 6.4 Hz, 4H, H_6), 2.48 (s, 3H, H_{12}), 1.79 – 1.72 (m, 4H, H_7), 1.49 – 1.41 (m, 4H, H_8), 1.34 (hept, *J* = 5.0, 4.4 Hz, 8H, $H_{9,10}$), 0.95 – 0.88 (m, 6H, H_{11}). ^{13}C NMR (126 MHz, Chloroform-*d*) δ 164.31 (*A*), 162.11 (*C*), 155.18 (*D*), 152.02 (*E*), 141.64 (*F*), 140.76 (*G*), 124.89 (*H*), 123.98 (*I*), 121.90 (*J*), 119.79 (*K*), 69.29 (*L*), 31.68 (*O*), 29.12 (*M*), 25.74 (*N*), 22.71 (*P*), 15.67 (*R*), 14.18 (*Q*). MS-ESI: *m/z* 758.2125 $[MH]^+$ intensity 1%, 1383.4310 $[2M–STD]^+$ (expected 758.2157 $[MH]^+$, 1383.4426 $[2M–STD]^+$).

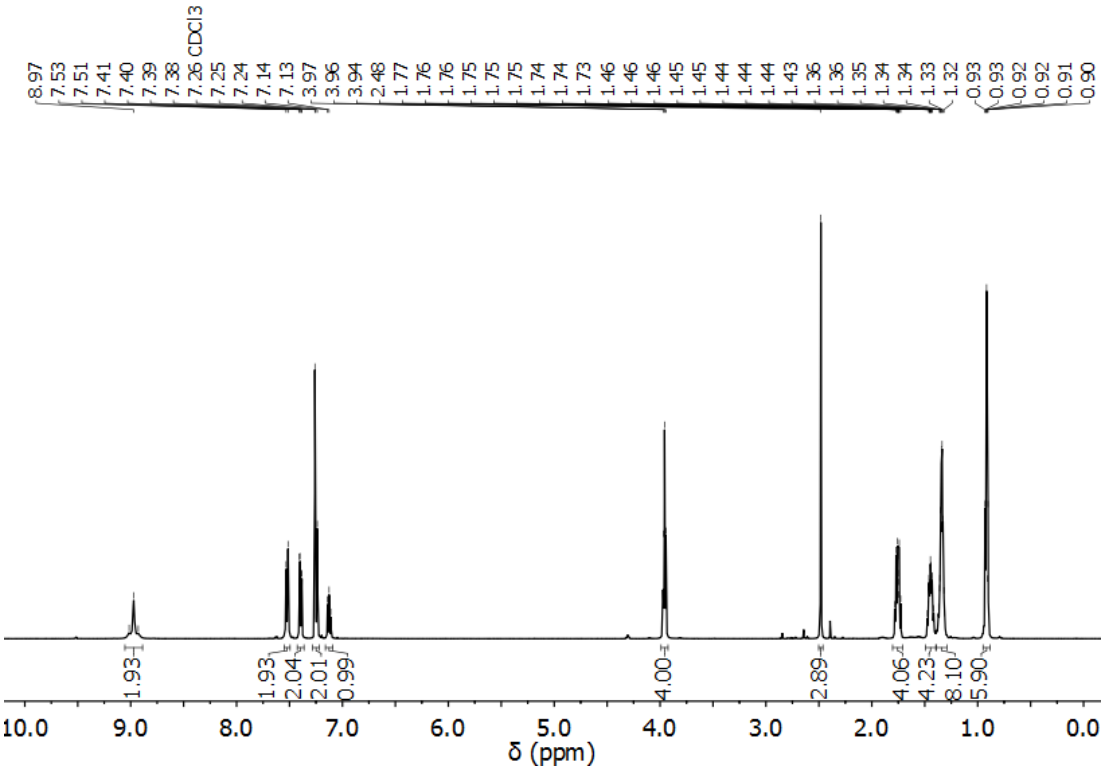

Figure 3.34 ^{1}H NMR spectrum of **LPt-2** in $CDCl_3$-*d*.

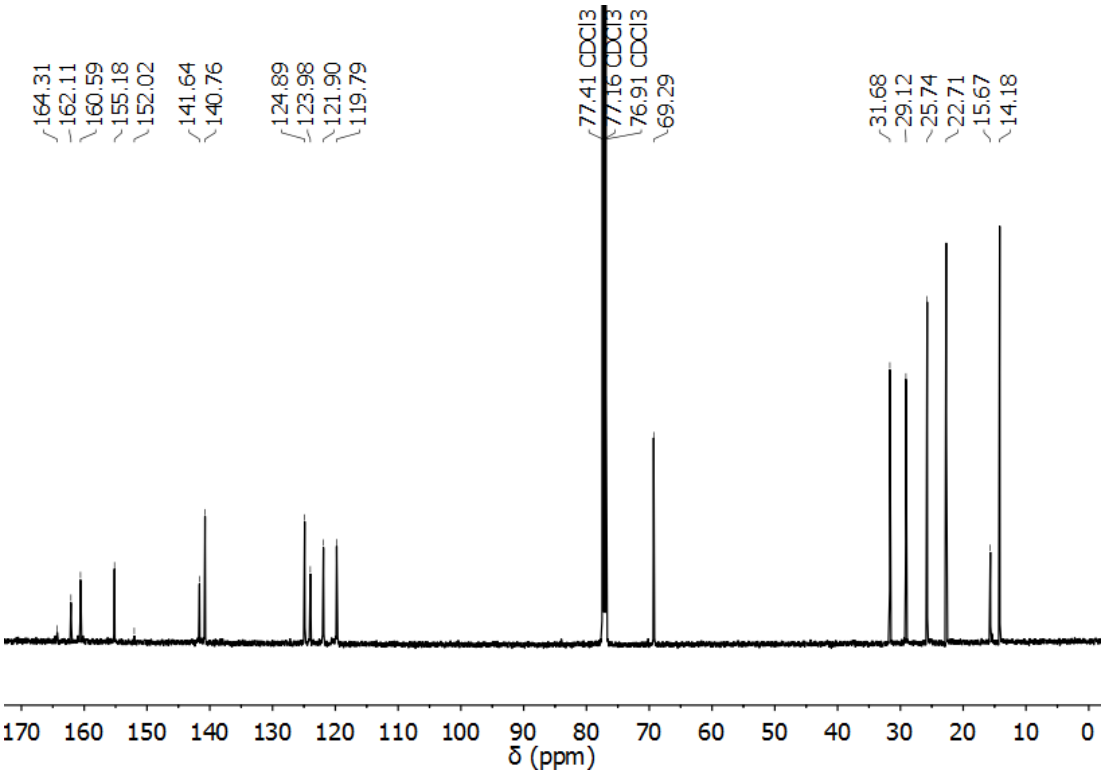

Figure 3.35 ^{13}C NMR spectrum of **LPt-2** in $CDCl_3$-*d*.

Preparation of LPd-2

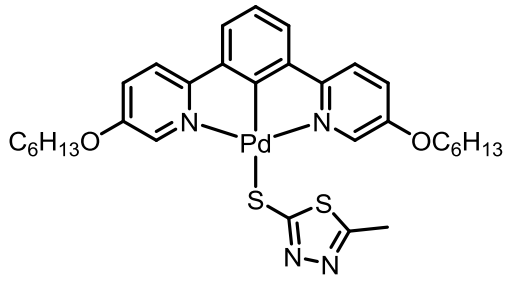

Same procedure to **LPt-2** was employed, except **LPt-1** was replaced by **LPd-1**. A yellow solid (75%) was obtained. M.p. 147-148 °C. ^{1}H NMR (500 MHz, Chloroform-*d*) δ 8.55 (s, 2H), 7.52 (d, *J* = 8.8 Hz, 2H), 7.34 (dd, *J* = 8.8, 2.8 Hz, 2H), 7.18 (d, *J* = 7.6 Hz, 2H), 7.10 (dd, *J* = 8.3, 6.9 Hz, 1H), 3.96 (t, *J* = 6.4 Hz, 4H), 2.53 (s, 3H), 1.79 – 1.72 (m, 4H), 1.48 – 1.41 (m, 4H), 1.34 (qt, *J* = 4.3, 2.0 Hz, 8H), 0.95 – 0.88 (m, 6H). ^{13}C NMR (151 MHz, Chloroform-*d*) δ 171.85, 162.48, 158.39, 154.97, 143.67, 140.71, 124.97, 121.95, 119.42, 69.30, 31.67, 29.12, 25.73, 22.72, 15.93, 14.19. MS-ESI: *m/z* 669.1546 $[M+H]^+$ intensity 0.6%, 1207.3184 $[2M–STD]^+$ intensity 100% (expected 669.1546 $[M+H]^+$, 1207.3203 $[2M–STD]^+$).

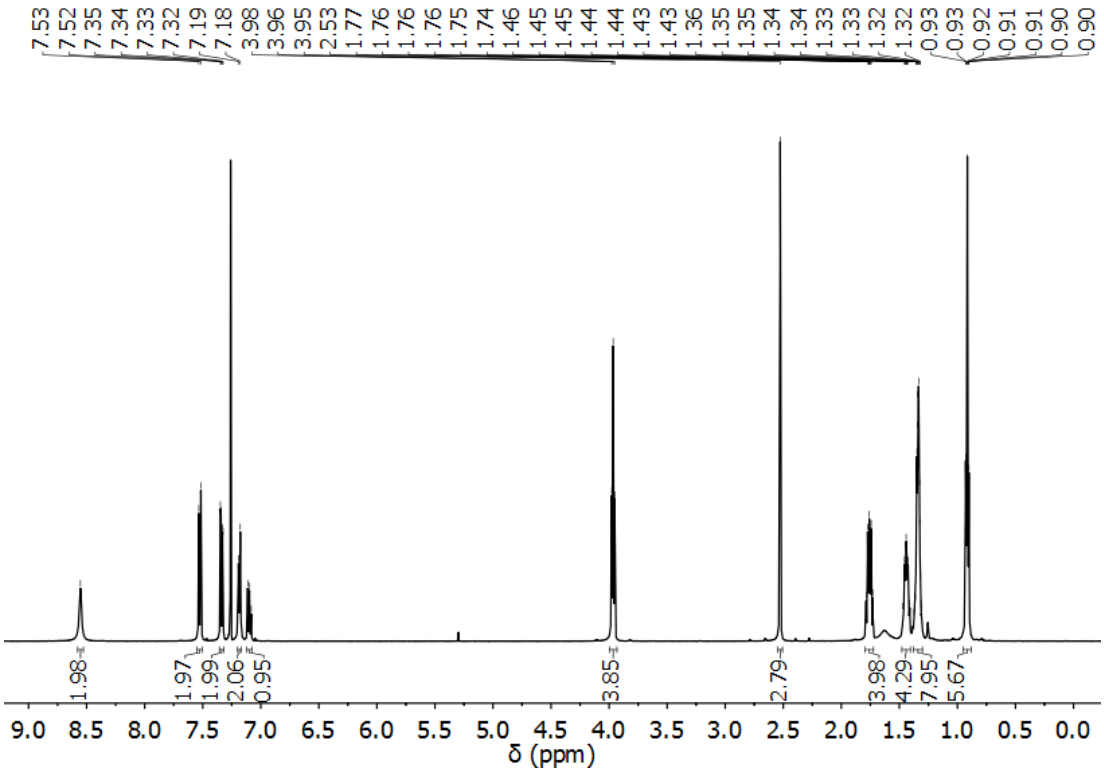

Figure 3.36 ^{1}H NMR spectrum of complex **LPd-2** in $CDCl_3$-*d*.

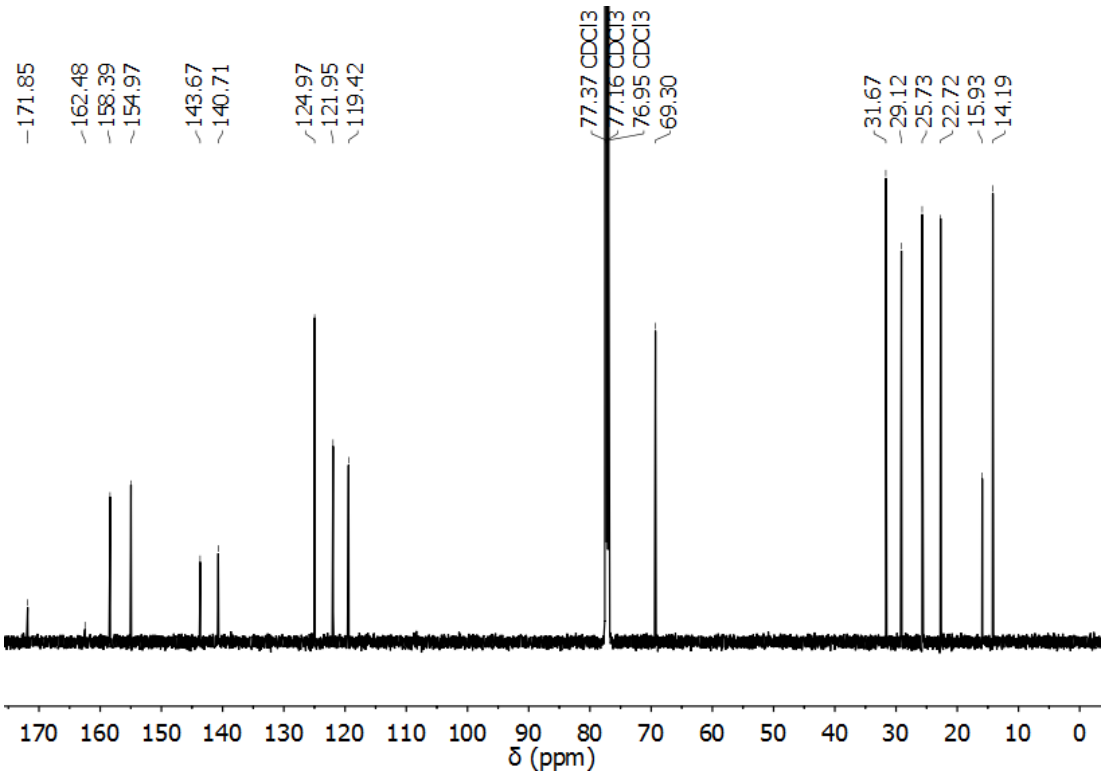

Figure 3.37 ^{13}C NMR spectrum of complex **LPd-2** in $CDCl_3$-*d*.

Preparation of complex LPt-3

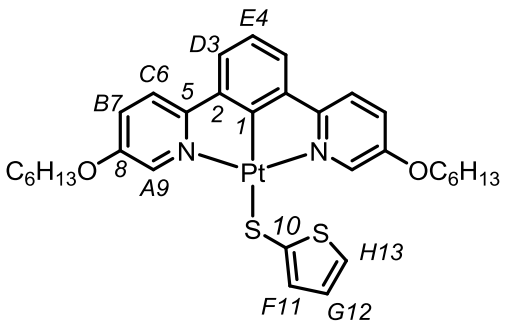

LPt-1 (0.099 g, 0.15 mmol), 2-thiophenethiol (0.026 g, 21 µL, 0.23 mmol) and NaO^{t}Bu (0.043 g, 0.45 mmol) were dissolved in anhydrous MeOH (5 mL). The mixture was refluxed overnight. The cooled green-yellow mixture was filtered and washed with MeOH to give an orange solid. The crude solid was dissolved in dichloromethane (2 mL). Methanol (4 mL) was added and then filtered to yield a pure orange product (0.080 g, 72%). ^{1}H NMR (400 MHz, Chloroform-*d*) δ 8.98 ($d_{satellite}$, J = 2.8 Hz, 2H, J (^{195}Pt-H) = 46.8 Hz, H_A), 7.53 (d, J = 8.8 Hz, 2H, H_C), 7.38 (dd, J = 8.9, 2.8 Hz, 2H, H_B), 7.29 (d, J = 7.6 Hz, 2H, H_D), 7.19 – 7.10 (m, 1H, H_E), 7.01 (dd, J = 3.4, 1.4 Hz, 1H, H_H), 6.82 – 6.70 (m, 2H, $H_{F,G}$), 3.84 (t, J = 6.4 Hz, 4H, OCH_2), 1.78 – 1.66 (m, 4H, CH_2), 1.42 (p, J = 6.9, 6.4 Hz, 4H, CH_2), 1.34 (dt, J = 8.1, 4.2 Hz, 8H, CH_2), 0.92 (t, J = 6.6 Hz, 6H, CH_3). ^{13}C NMR (126

MHz, Chloroform-*d*) δ 165.76 (C_1), 161.22 (C_5), 155.10 (C_8), 147.62 (C_{10}), 141.54 (C_2), 140.25 (C_9), 128.48 (C_{13}), 127.33 (C_{12}), 125.67 (C_7), 123.61 (C_4), 121.97 ($C_{3,11}$), 119.62 (C_6), 69.18 (OC), 31.65 (H_2C), 29.16 (H_2C), 25.67 (H_2C), 22.73 (H_2C), 14.19 (H_3C). MS-ESI: *m/z* 1367.4374 $[2M–STP]^+$ (1367.4363 $[2M–STP]^+$).

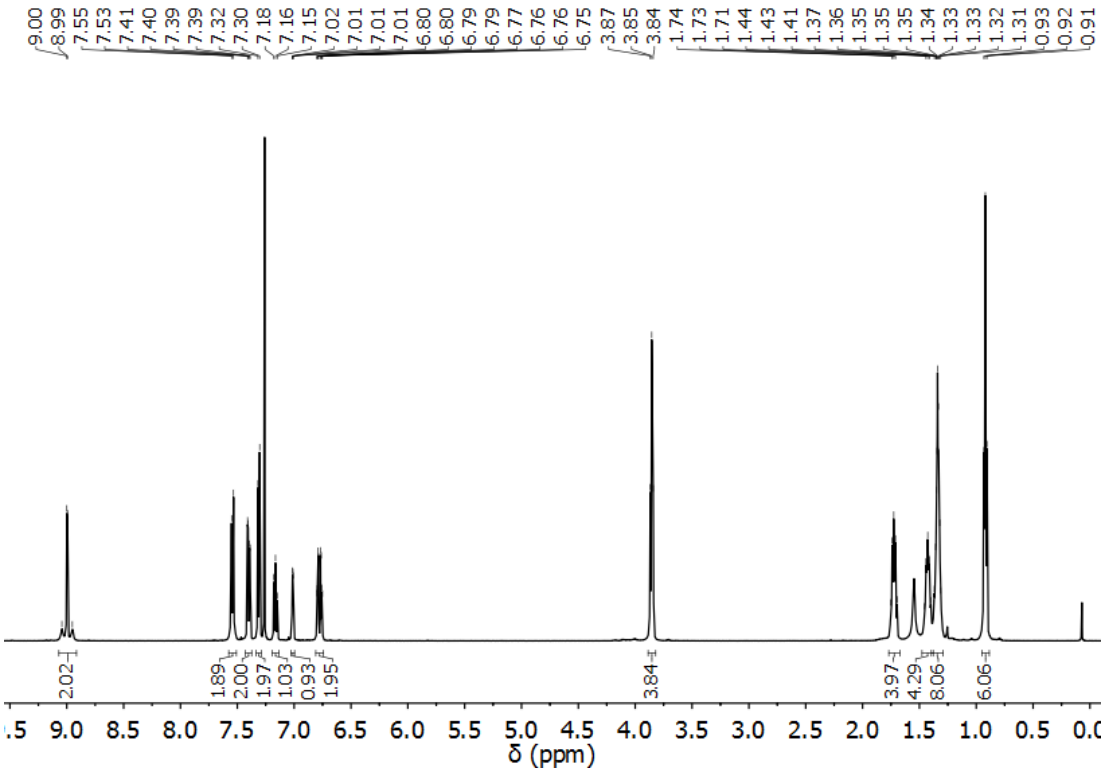

Figure 3.38 ^1H NMR spectrum of complex **LPt-3** in $CDCl_3$-*d*.

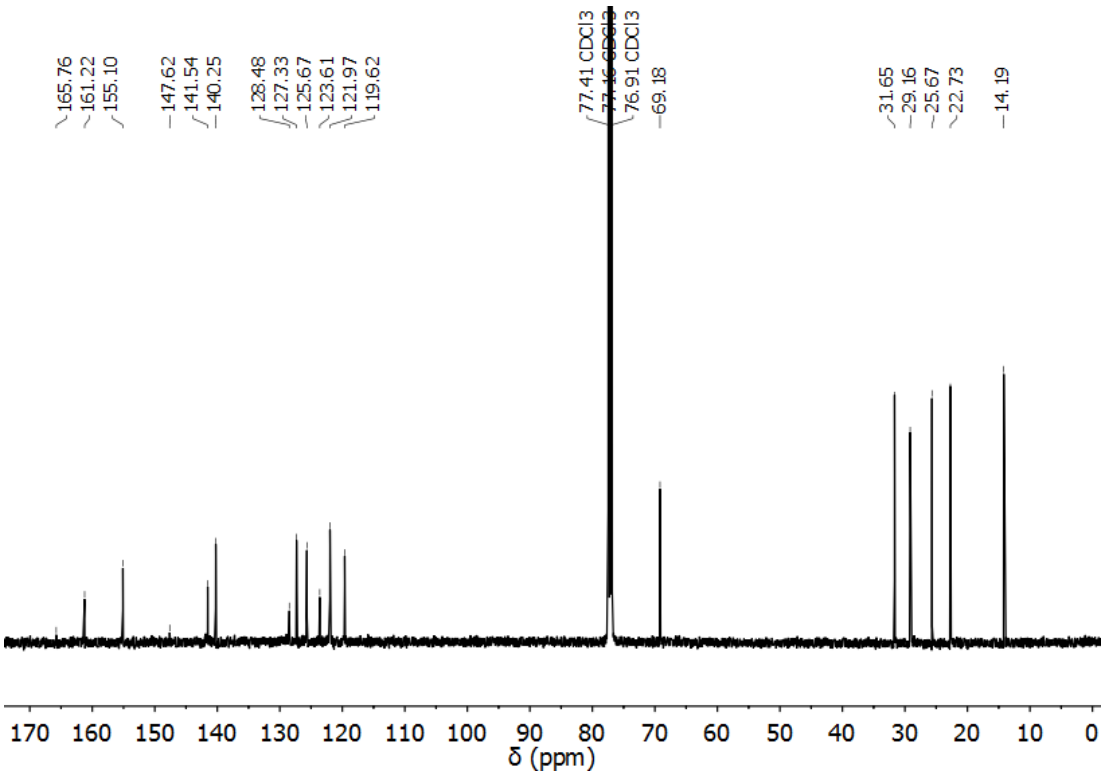

Figure 3.39 ^{13}C NMR spectrum of complex **LPt-3** in $CDCl_3$-*d*.

Preparation of LPd-3

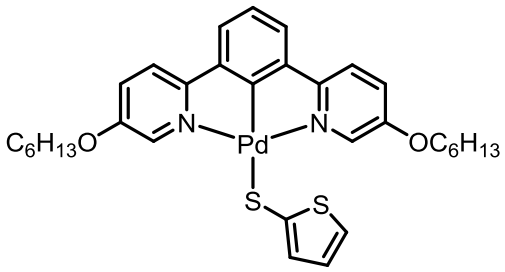

LPd-1 (0.115 g, 0.20 mmol), 2-thiophenethiol (0.035 g, 28 µL, 0.30 mmol) and NaO^{t}Bu (0.058 g, 0.60 mmol) were dissolved in anhydrous MeOH (8 mL). The mixture was refluxed overnight. The cooled green-yellow mixture was filtered and washed with MeOH to give a yellow-green solid. The crude solid was dissolved in dichloromethane (2 mL). Methanol (4 mL) was added and then filtered to yield a pure yellow green product (0.107 g, 80%). M.p. 159-161 °C. ^{1}H NMR (500 MHz, Chloroform-*d*) δ 8.71 (d, *J* = 2.8 Hz, 2H), 7.53 (d, *J* = 8.7 Hz, 2H), 7.34 (dd, *J* = 8.8, 2.8 Hz, 2H), 7.26 – 7.22 (m, 2H), 7.13 (dd, *J* = 8.2, 7.1 Hz, 1H), 6.99 (dd, *J* = 3.4, 1.3 Hz, 1H), 6.78 (dd, *J* = 5.4, 1.3 Hz, 1H), 6.74 (dd, *J* = 5.4, 3.4 Hz, 1H), 3.88 (t, *J* = 6.4 Hz, 4H), 1.73 (dq, *J* = 7.8, 6.4 Hz, 4H), 1.48 – 1.39

(m, 4H), 1.34 (qd, J = 5.3, 4.4, 2.8 Hz, 8H), 0.95 – 0.90 (m, 6H). MS-ESI: *m/z* 1191.3109 $[2M–STP]^+$, (expected 1191.3142 $[2M–STP]^+$).

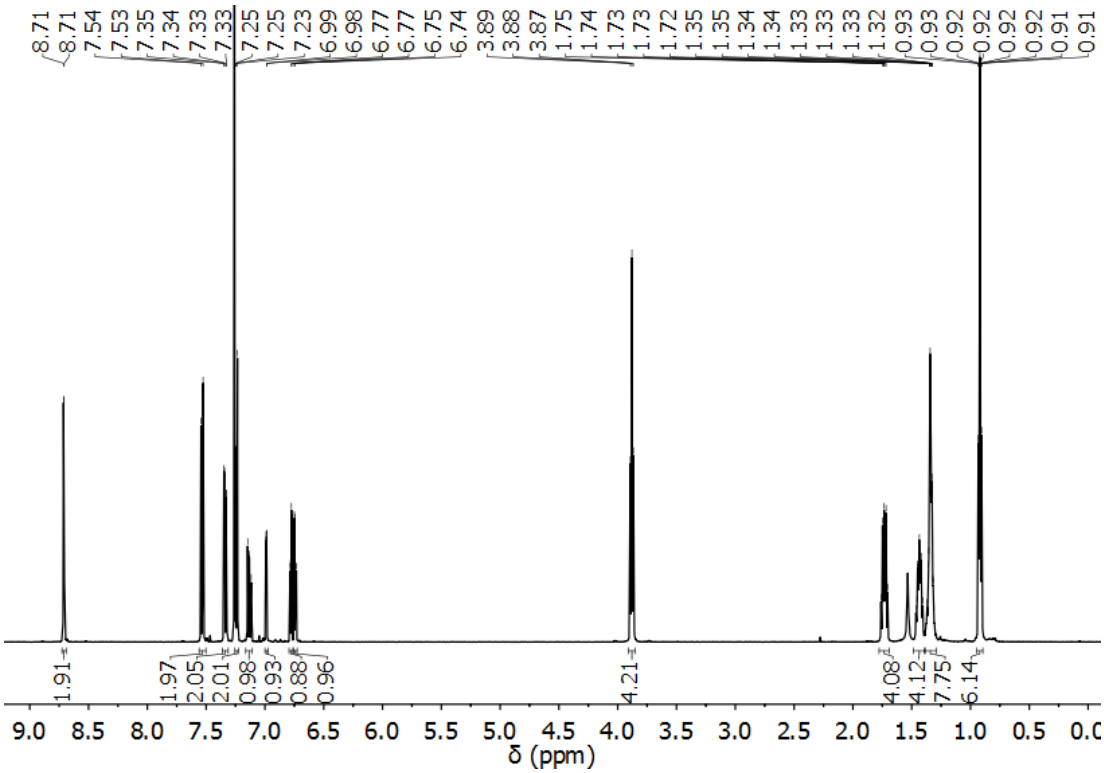

Figure 3.40 ^{1}H NMR spectrum of complex **LPd-3** in $CDCl_3$-*d*.

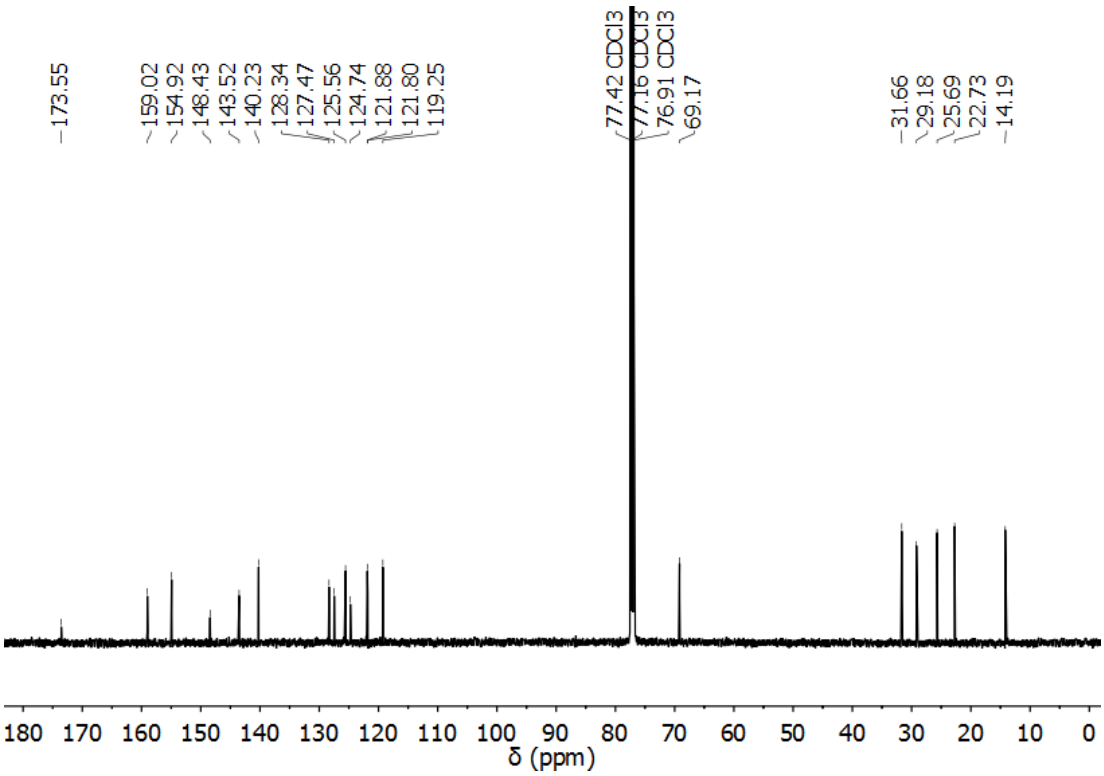

Figure 3.41 ^{13}C NMR spectrum of complex **LPd-3** in $CDCl_3$-*d*.

Preparation of LNi-3

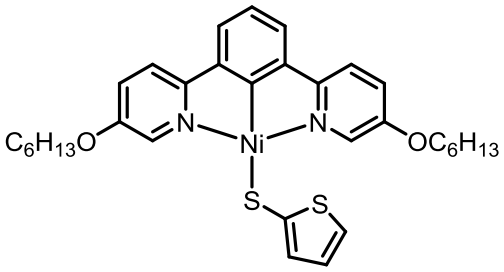

LNi-1 (0.079 g, 0.15 mmol), 2-thiophenethiol (0.026 g, 21 µL, 0.23 mmol) and ^{t}BuONa (0.043 g, 0.45 mmol) were dissolved in anhydrous MeOH (5 mL). The mixture was stirred overnight at room temperature. The brown mixture was filtered and washed with MeOH to give a yellow-green solid (0.077 g, 85%). M.p. 127-128 °C. ^{1}H NMR (601 MHz, Chloroform-*d*) δ 8.89 (d, *J* = 2.7 Hz, 2H), 7.35 (d, *J* = 8.6 Hz, 2H), 7.28 – 7.22 (m, 2H), 7.13 – 7.05 (m, 4H), 6.80 (dd, *J* = 5.4, 1.1 Hz, 1H), 6.75 (dd, *J* = 5.4, 3.5 Hz, 1H), 3.86 (t, *J* = 6.5 Hz, 4H), 1.71 (p, *J* = 6.8 Hz, 4H), 1.42 (p, *J* = 7.2 Hz, 4H), 1.33 (qt, *J* = 7.4, 3.6 Hz, 8H), 0.91 (t, *J* = 6.7 Hz, 6H). ^{13}C NMR (151 MHz, Chloroform-*d*) δ 170.041, 157.144, 154.541, 147.151, 144.484, 142.528, 128.181, 127.484, 125.321, 125.212, 121.959, 120.178, 118.022, 69.104, 31.666, 29.168, 25.703, 22.730, 14.188. MS-ESI: *m/z* 604.1727 $[M]^+$ intensity 0.9%, (expected 604.1723 $[M]^+$). The complex decomposes significantly upon ionization.

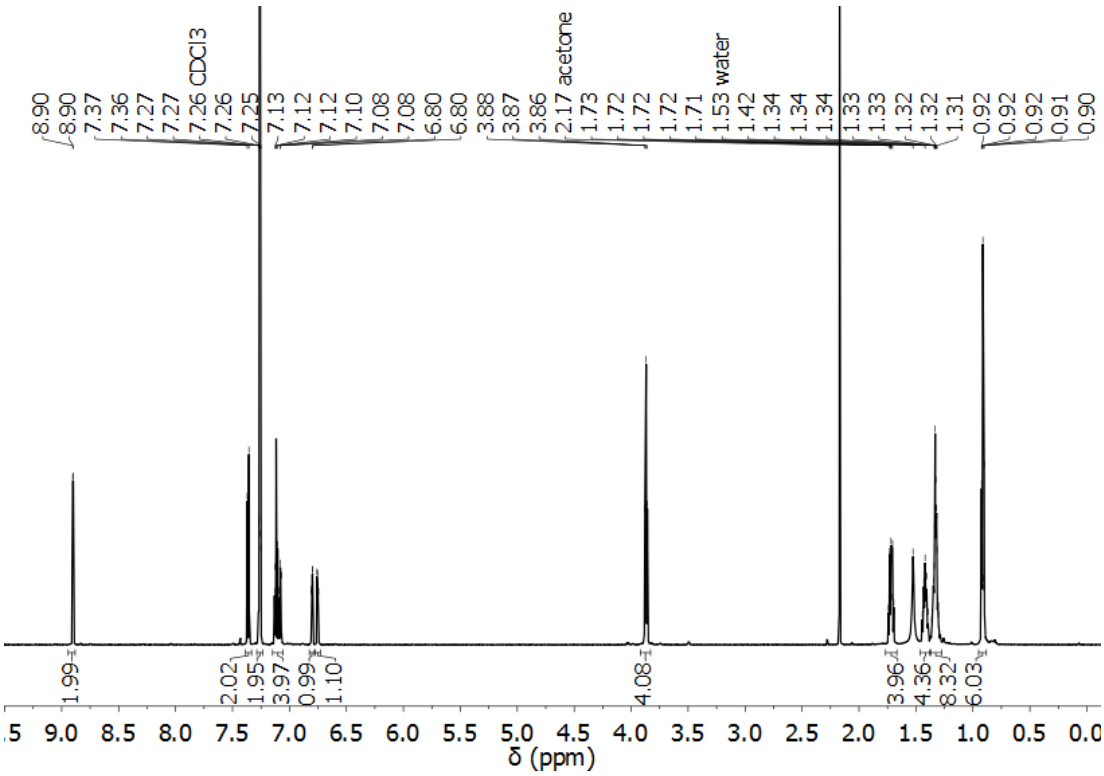

Figure 3.42 ^{1}H NMR spectrum of complex **LNi-3** in $CDCl_3$-*d* at 25 °C.

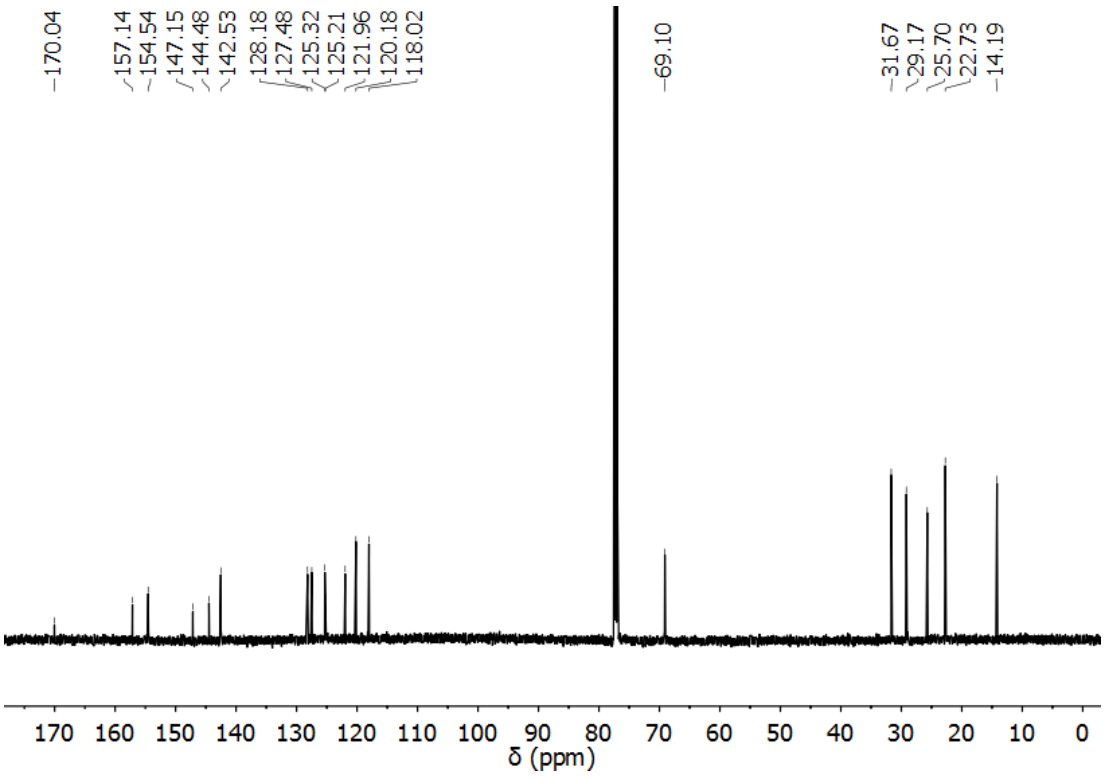

Figure 3.43 ^{13}C NMR spectrum of complex **LNi-3** in $CDCl_3$-*d* at 25 °C.

Preparation of LPt-4

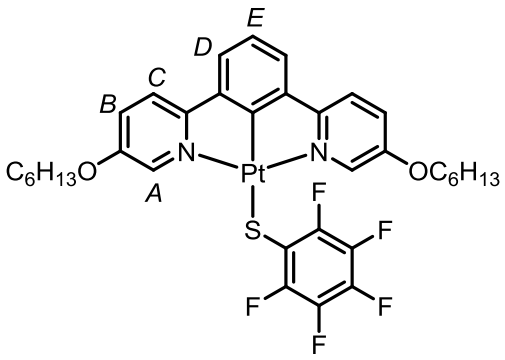

Complex **LPt-1** (0.099 g, 0.15 mmol), pentafluorothiolphenol (0.040 g, 27 μL, 0.20 mmol) and NaO^{t}Bu (0.029 g, 0.30 mmol) were dissolved in anhydrous MeOH (6 mL) under a nitrogen atmosphere. The mixture was filtered and washed with methanol to yield an orange solid (0.108 g, 87%). M.p. 172 °C. ^{1}H NMR (500 MHz, Chloroform-*d*) δ 9.22 (d, *J* = 2.7 Hz, *J* (^{195}Pt-H)= 45.3 Hz, 2H, H$_A$), 7.48 (d, *J* = 8.8 Hz, 2H, H$_C$), 7.40 (dd, *J* = 8.8, 2.8 Hz, 2H, H$_B$), 7.21 (d, *J* = 7.6 Hz, 2H, H$_D$), 7.10 (t, *J* = 7.6 Hz, 1H, H$_E$), 4.03 (t, *J* = 6.4 Hz, 4H, OCH$_2$), 1.85 – 1.76 (m, 4H, CH$_2$), 1.48 (t, *J* = 7.6 Hz, 4H, CH$_2$), 1.40 – 1.32 (m, 8H, CH$_2$), 0.96 – 0.89 (m, 6H, CH$_3$). ^{13}C NMR (126 MHz, Chloroform-*d*) δ 164.041, 160.762, 155.156, 141.604, 140.252, 125.507, 123.874, 121.898, 119.686, 69.293, 31.656, 29.205, 25.653, 22.715, 14.142. ^{19}F NMR (376 MHz, Chloroform-*d*) δ –132.97 – –133.18 (m, *o*-F), –164.25 (t, *J* = 21.4 Hz, *p*-F), –164.71 – –164.97 (m, *m*-F). MS-ESI: *m/z* 848.1882 [M+Na]$^+$ (expected 848.1881).

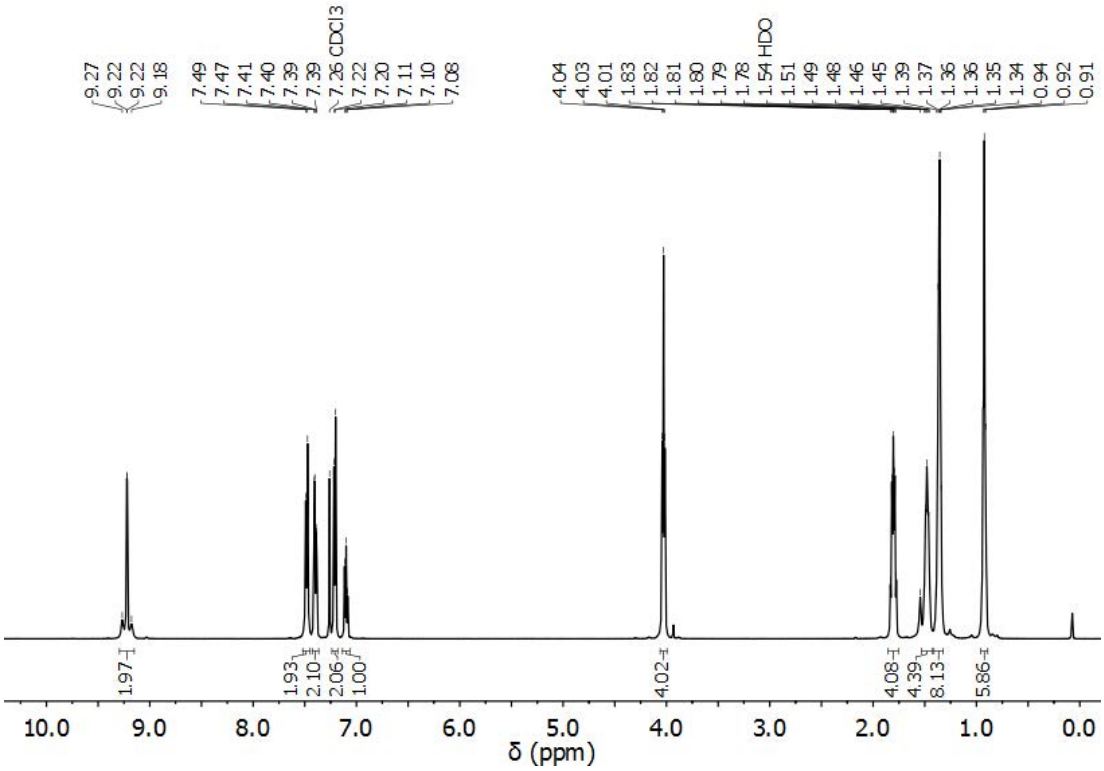

Figure 3.44 ^{1}H NMR spectrum of complex **LPt-4** in $CDCl_3$-*d*.

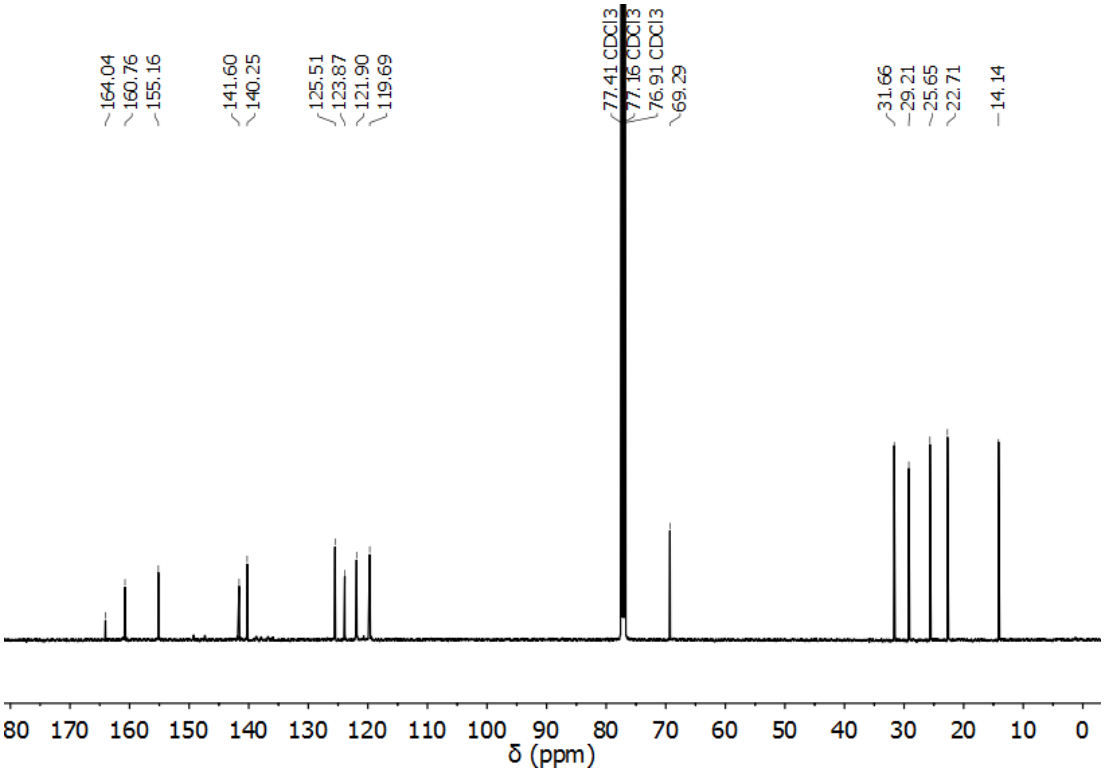

Figure 3.45 ^{13}C NMR spectrum of complex **LPt-4** in $CDCl_3$-*d*.

Preparation of LPt-5

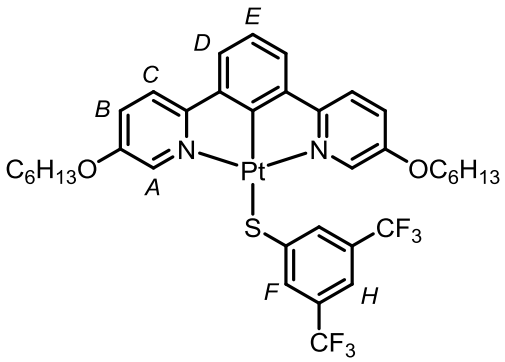

Complex **LPt-1** (0.099 g, 0.15 mmol), 3,5-bis(trifluoromethyl)thiophenol (0.049 g, 34 μL, 0.20 mmol) and NaO^tBu (0.029 g, 0.30 mmol) were dissolved in anhydrous MeOH (6 mL) under a nitrogen atmosphere. The mixture was filtered and washed with methanol to yield a yellow solid (0.108 g, 83%). M.p. 160-162 °C. ^1H NMR (400 MHz, Chloroform-*d*) δ 8.90 ($d_{satellite}$, J = 2.7 Hz, J (^{195}Pt-H) = 46.9 Hz, 2H, H_A), 8.19 (s, 2H, H_F), 7.57 (d, J = 8.8 Hz, 2H, H_C), 7.42 (dd, J = 8.9, 2.8 Hz, 2H, H_B), 7.38 – 7.31 (m, 2H, H_D), 7.33 – 7.28 (m, 1H, H_H), 7.21 (dd, J = 8.2, 7.1 Hz, 1H, H_E), 3.76 (t, J = 6.3 Hz, 4H, OCH_2), 1.67 (dq, J = 8.1, 6.4 Hz, 4H, CH_2), 1.43 – 1.22 (m, 12H, CH_2), 0.94 – 0.86 (m, 6H, CH_3). ^{13}C NMR (126 MHz, Chloroform-d) δ 165.59, 161.13, 155.10, 153.05, 141.53, 140.58, 132.45, 132.42, 130.49 (q, J = 32.4 Hz, C-CF_3), 123.83 (q, J = 272.8 Hz, CF_3), 125.49, 123.88, 122.14, 119.81, 114.79, 114.75, 114.72, 69.09, 31.57, 29.00, 25.59, 22.64, 14.11. ^{19}F NMR (376 MHz, Chloroform-d) δ -62.97. MS-ESI: *m/z* 894.2094 $[M+Na]^+$ intensity < 1%, (expected 894.2094 $[M+Na]^+$ 894.2098). The complex decomposes significantly upon ionization.

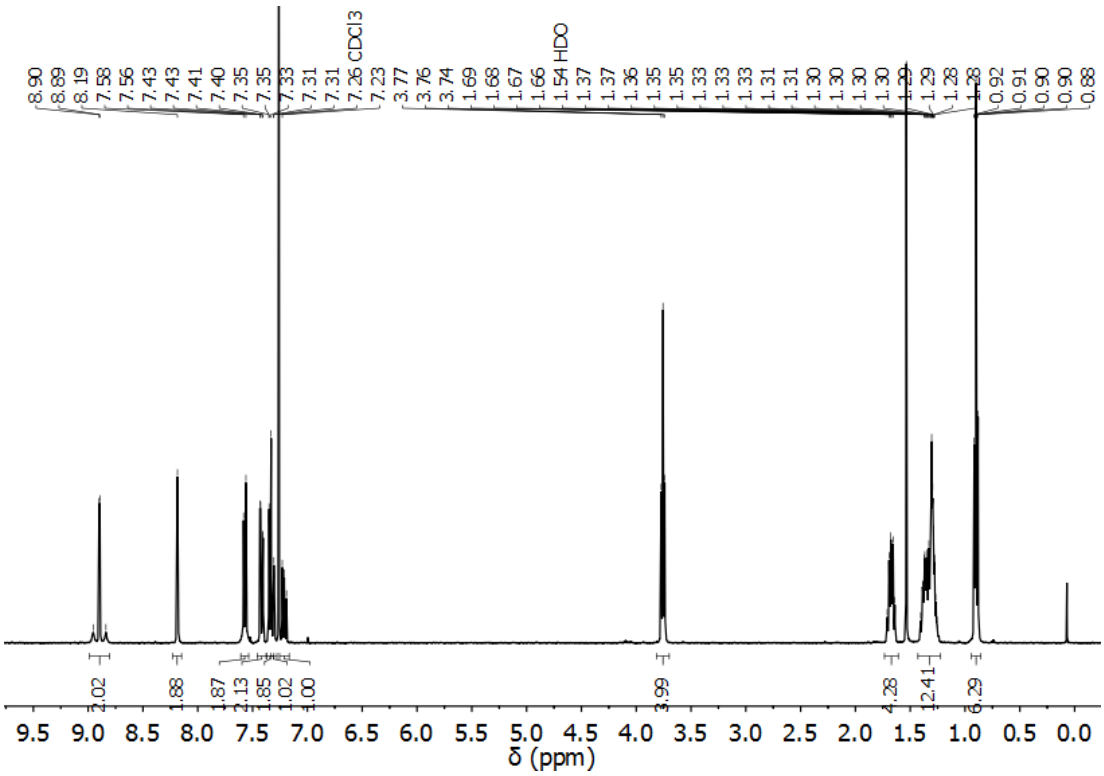

Figure 3.46 ^{1}H NMR spectrum of complex **LPt-5** in $CDCl_3$-*d*.

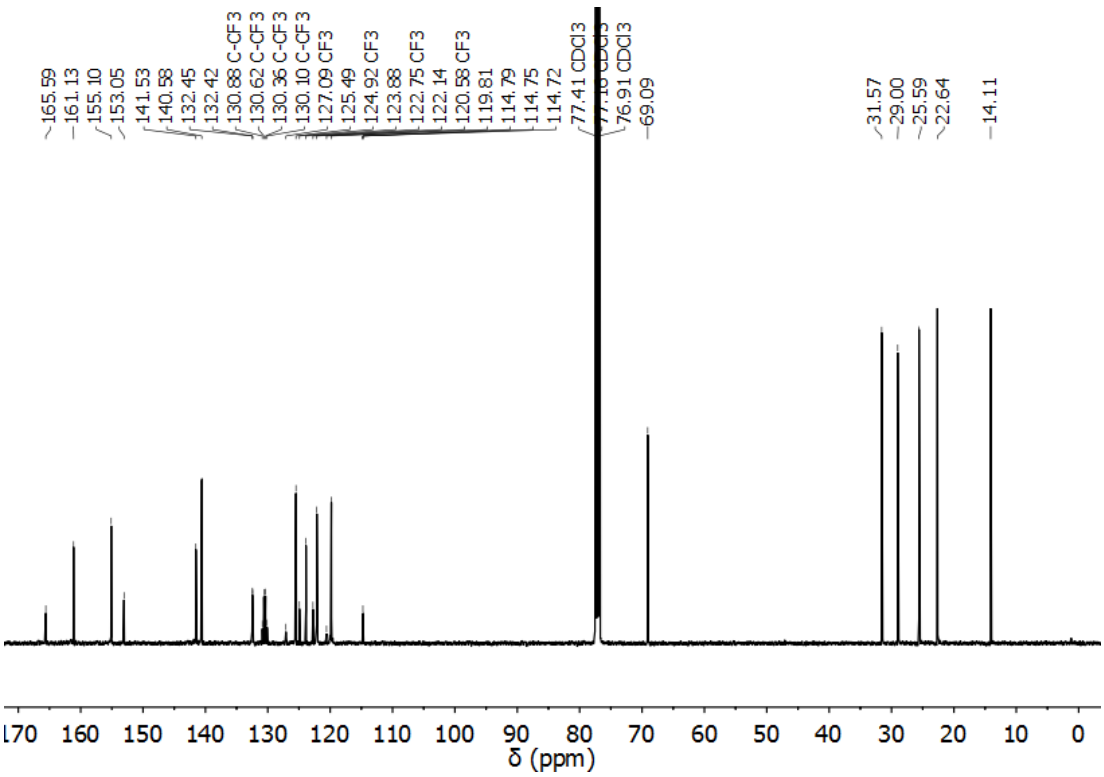

Figure 3.47 ^{13}C NMR spectrum of complex **LPt-5** in $CDCl_3$-*d*.

Preparation of LPt-6

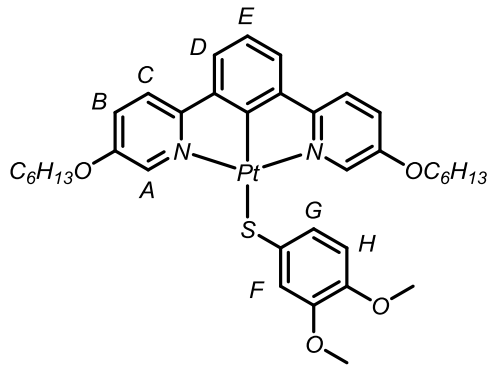

Complex **LPt-1** (0.099 g, 0.15 mmol), 3,4-dimethoxythiophenol (0.034 g, 29 μL, 0.20 mmol) and NaO^tBu (0.029 g, 0.30 mmol) were dissolved in anhydrous MeOH (6 mL) under a nitrogen atmosphere. The mixture was filtered and washed with methanol to yield an orange solid (0.107 g, 90%). M.p. 185-186 °C. ^{1}H NMR (500 MHz, Chloroform-*d*) δ 8.98 ($d_{satellite}$, J = 2.7 Hz, J (^{195}Pt-H) = 46.4 Hz, 2H, H_A), 7.56 (d, J = 8.8 Hz, 2H, H_C), 7.40 (dd, J = 8.8, 2.8 Hz, 2H, H_B), 7.38 – 7.32 (m, 3H, $H_{D,F}$), 7.31 (dd, J = 8.3, 2.1 Hz, 1H, H_G), 7.19 (dd, J = 8.0, 7.2 Hz, 1H, H_E), 6.60 (d, J = 8.3 Hz, 1H, H_H), 3.78 (s, 3H, OCH_3), 3.77 – 3.71 (m, 7H, OCH_2&OCH_3), 1.74 – 1.61 (m, 4H, CH_2), 1.46 – 1.22 (m, 12H, CH_2), 0.91 (t, J = 6.9 Hz, 6H, CH_3). ^{13}C NMR (126 MHz, Chloroform-*d*) δ 166.52, 161.39, 154.99, 148.59, 145.71, 141.45, 140.44, 138.35, 125.64, 125.60, 123.36, 122.03, 119.56, 117.37, 111.75, 77.41, 77.36, 77.16, 76.91, 69.08, 56.17, 55.91, 31.66, 29.17, 25.66, 22.72, 14.18. MS-ESI: *m/z* 1421.4958 $[2M–SPh(OMe)_2]^+$ (expected 1421.4991 $[2M–SPh(OMe)_2]^+$).

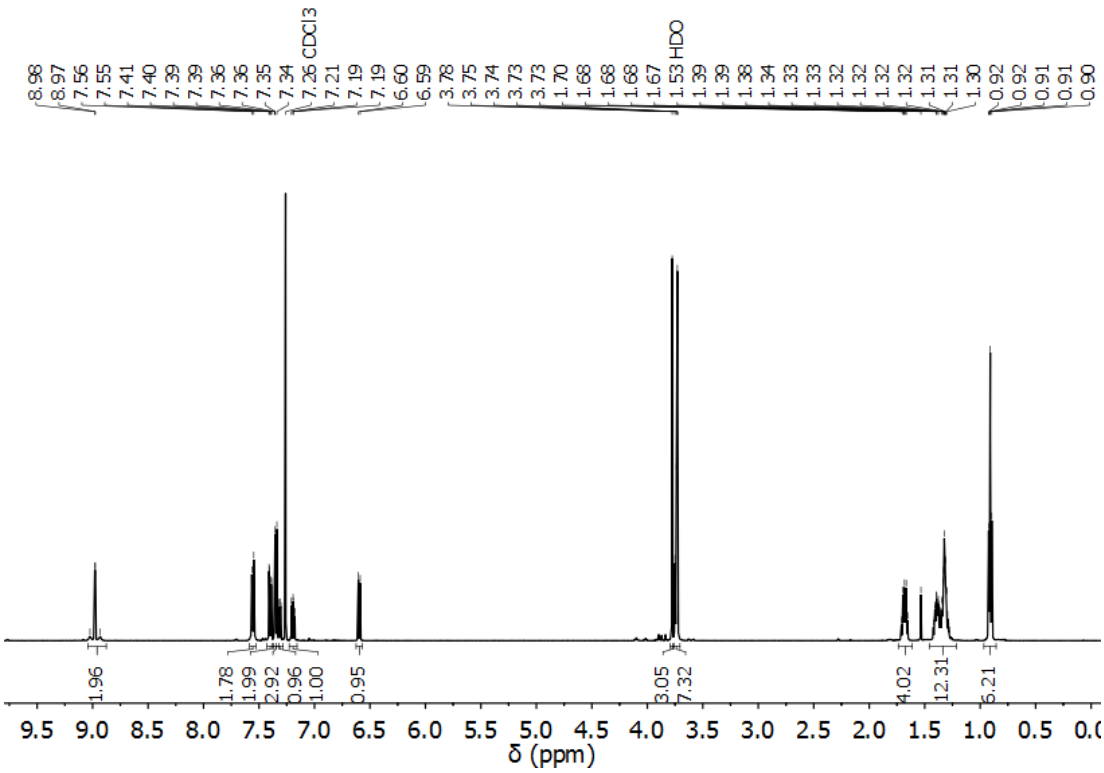

Figure 3.48 ^{1}H NMR spectrum of complex **LPt-6** in $CDCl_3$-*d*.

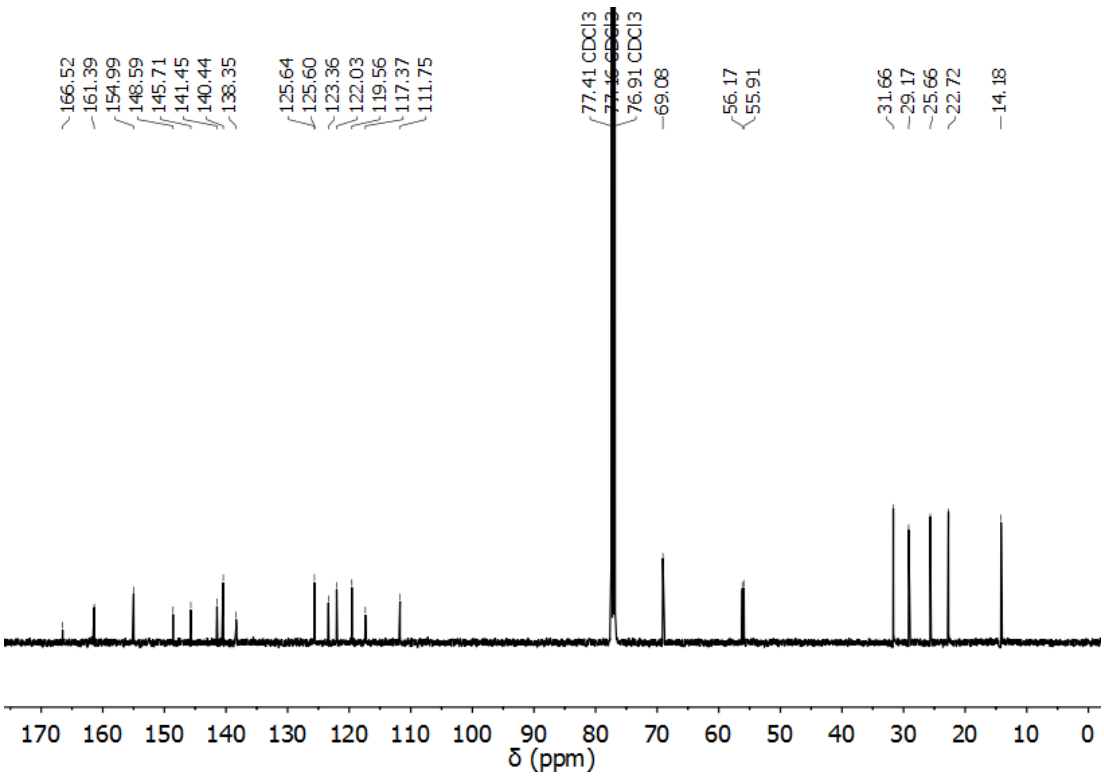

Figure 3.49 ^{13}C NMR spectrum of complex **LPt-6** in $CDCl_3$-*d*.

Preparation of LPt-7

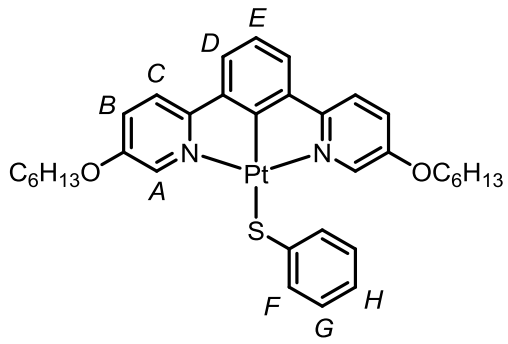

Complex **LPt-1** (0.099 g, 0.15 mmol), thiolphenol (HSPh, 0.022 g, 21 μL, 0.20 mmol) and NaO^{t}Bu (0.029 g, 0.30 mmol) were added into anhydrous MeOH (5 mL) under nitrogen atmosphere. The mixture was filtered and washed with methanol to yield a yellow solid (0.098 g, 89%). M.p. 186-188 °C. ^{1}H NMR (500 MHz, Chloroform-*d*) δ 9.01 (d, *J* = 2.7 Hz, 2H, H_A), 7.85 – 7.73 (m, 2H, H_F), 7.55 (d, *J* = 8.8 Hz, 2H, H_C), 7.39 (dd, *J* = 8.8, 2.8 Hz, 2H, H_B), 7.34 (d, *J* = 7.6 Hz, 2H, H_D), 7.19 (dd, *J* = 8.0, 7.3 Hz, 1H, H_E), 7.01 (t, *J* = 7.7 Hz, 2H, H_G), 6.91 – 6.85 (m, 1H, H_H), 3.70 (t, *J* = 6.4 Hz, 4H, OCH_2), 1.67 (p, *J* = 6.6 Hz, 4H, CH_2), 1.43 – 1.26 (m, 12H, CH_2), 0.91 (t, *J* = 6.9 Hz, 6H, CH_3). ^{13}C NMR (126 MHz, Chloroform-*d*) δ 166.486, 161.355, 155.031, 147.872, 141.571, 140.616, 133.740, 127.987, 125.686, 123.464, 122.168, 122.029, 119.577, 69.018, 31.633, 29.108, 25.627, 22.717, 14.177. MS-ESI: *m/z* 1361.4807 $[2M–SPh]^+$ (expected 1361.4799 $[2M–SPh]^+$).

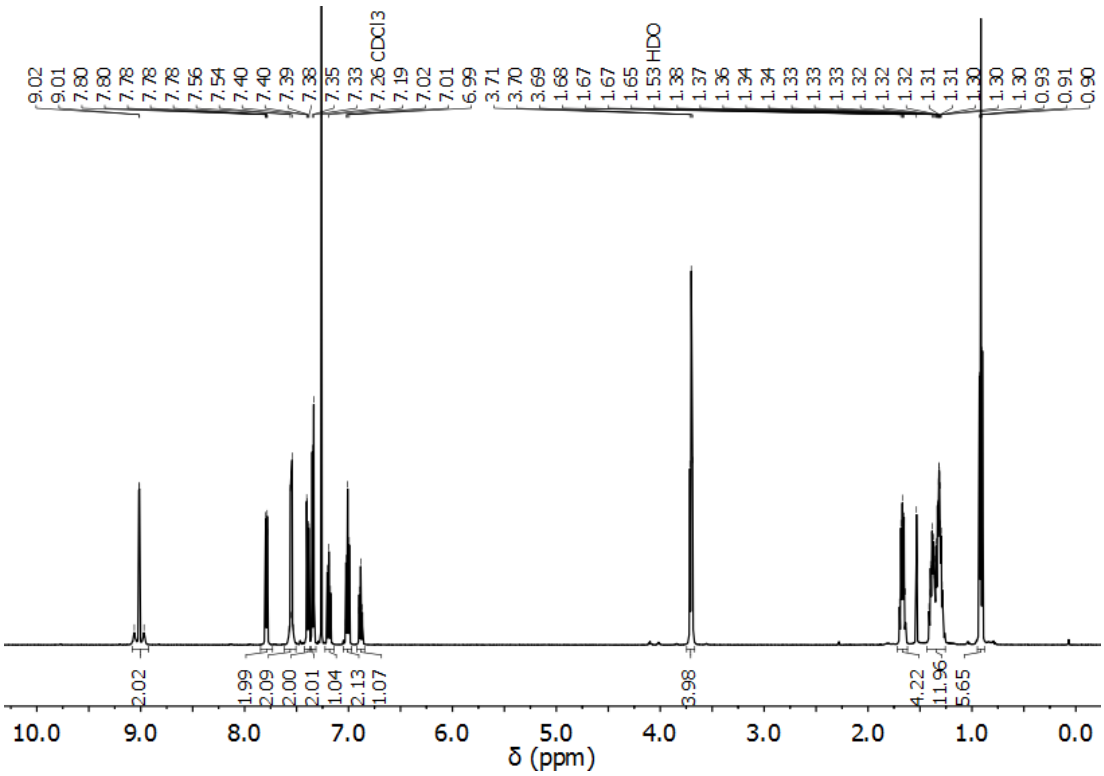

Figure 3.50 ^{1}H NMR spectrum of complex **LPt-7** in chloroform-*d*.

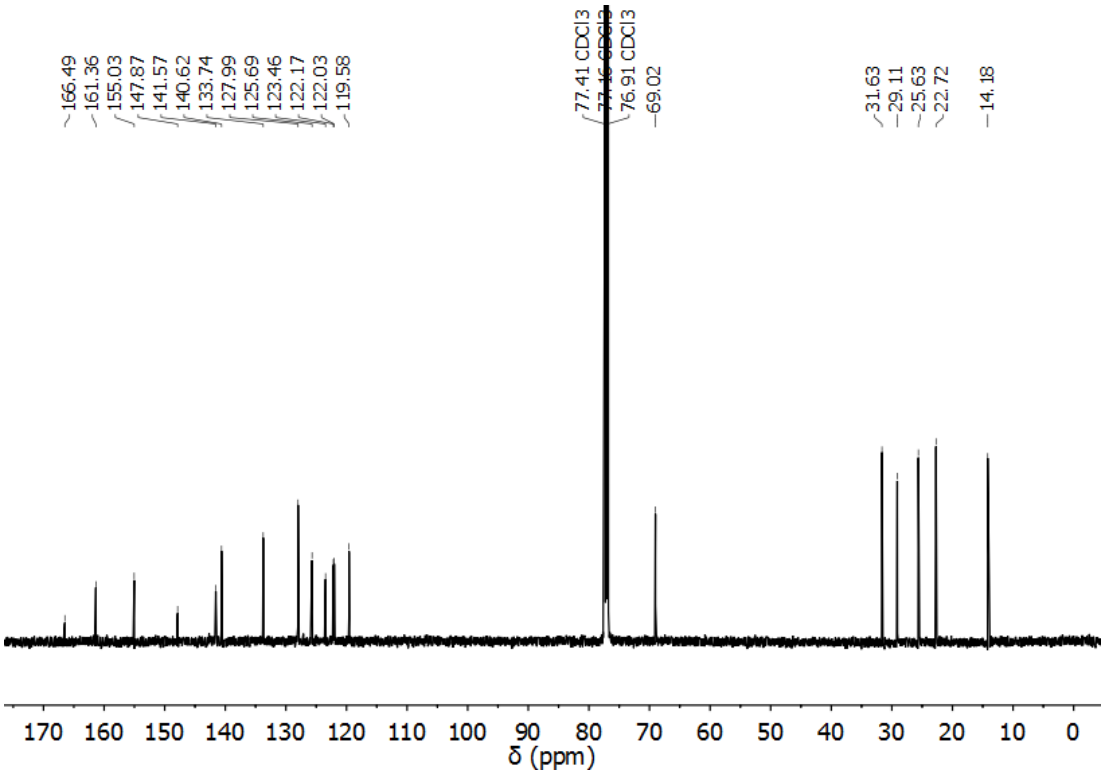

Figure 3.51 ^{13}C NMR spectrum of complex **LPt-7** in chloroform-*d*.

Preparation of LPt-8

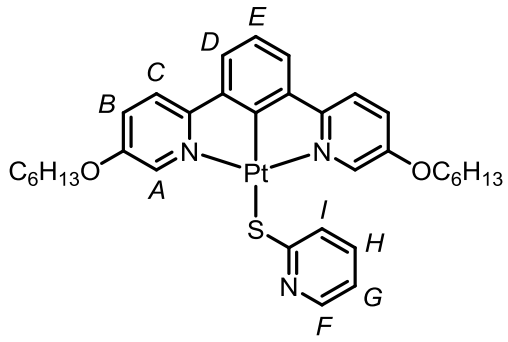

A mixture of **LPt-1** (0.132 g, 0.20 mmol), 2-mercaptopyridine (HSPy, 0.033 g, 0.30 mmol) and NaO^tBu (0.029 g, 0.45 mmol) in anhydrous methanol (6 mL) was refluxed overnight under a nitrogen atmosphere. The mixture was filtered and washed with methanol to yield a bright yellow solid (0.135 g, 92%). ^{1}H NMR (500 MHz, Chloroform-*d*) δ 9.11 ($d_{satellite}$, J = 2.8 Hz, J (^{195}Pt-H) = 46.3 Hz, 2H, H_A), 8.29 – 8.22 (m, 1H, H_F), 7.80 – 7.74 (m, 1H, H_I), 7.55 (d, J = 8.8 Hz, 2H, H_C), 7.40 (dd, J = 8.8, 2.8 Hz, 2H, H_B), 7.33 (d, J = 7.6 Hz, 2H, H_D), 7.22 – 7.13 (m, 2H, H_E and H_G), 6.72 (ddd, J = 7.4, 4.9, 1.1 Hz, 1H, H_H), 3.81 (t, J = 6.4 Hz, 4H, OCH_2), 1.69 (dt, J = 14.6, 6.6 Hz, 4H, CH_2), 1.39 (p, J = 7.2 Hz, 4H, CH_2), 1.36 – 1.24 (m, 8H, CH_2), 0.91 (t, J = 6.9 Hz, 6H, CH_3). ^{13}C NMR (126 MHz, Chloroform-*d*) δ 171.653, 166.344, 161.175, 154.993, 149.089, 141.604, 141.158, 134.410, 128.353, 125.174, 123.523, 121.946, 119.551, 116.511, 69.071, 31.608, 29.075, 25.636, 22.690, 14.158. MS-ESI: *m/z* 1362.4767 $[2M–SPy]^+$ (expected 1362.4752 $[2M–SPy]^+$).

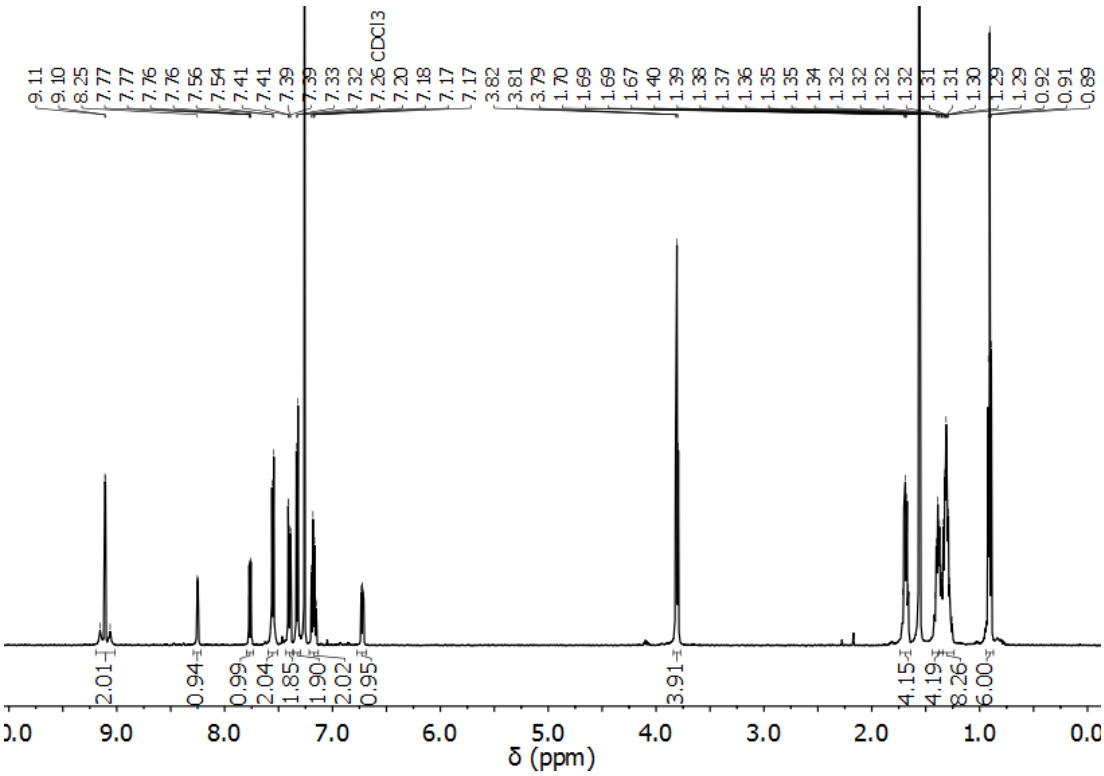

Figure 3.52 ^{1}H NMR spectrum of complex **LPt-8** in chloroform-*d*.

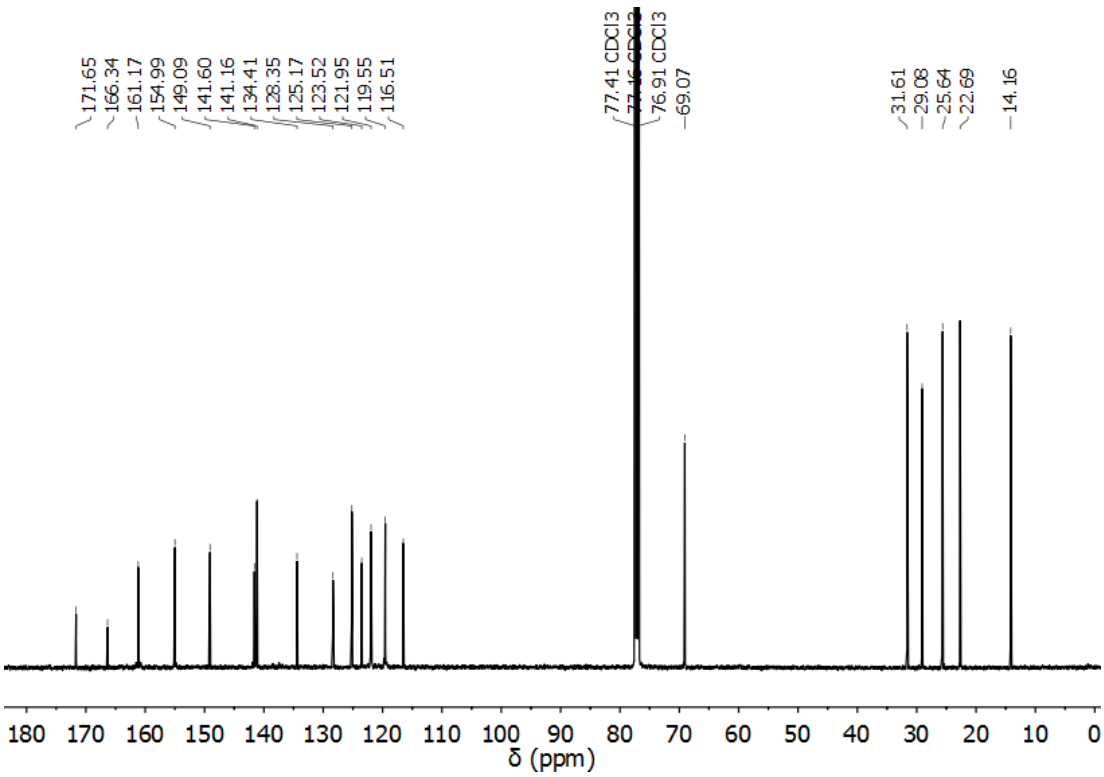

Figure 3.53 ^{13}C NMR spectrum of complex **LPt-8** in chloroform-*d*.

Preparation of LPt-9

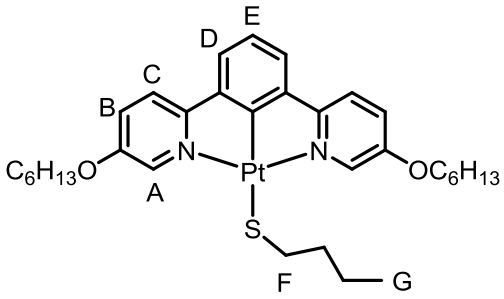

A mixture of **LPt-1** (0.099 g, 0.15 mmol), 1-butanethiol (HSBu, 24.5 μL, 0.23 mmol) and NaO^tBu (0.022 g, 0.23 mmol) in anhydrous methanol (5 mL) was refluxed overnight under a N2 atmosphere. The mixture was filtered and washed with methanol and diethyl ether to yield an orange solid (0.079 g, 74%). M.p. 170 °C. ^{1}H NMR (400 MHz, Chloroform-*d*) δ 9.50 ($d_{satellite}$, J = 2.8 Hz, 2H, J (^{195}Pt-H) = 48.0 Hz, H_A), 7.57 (d, J = 8.8 Hz, 2H, H_C), 7.45 (dd, J = 8.8, 2.8 Hz, 2H, H_B), 7.35 (d, J = 7.6 Hz, 2H, H_D), 7.16 (dd, J = 8.0, 7.2 Hz, 1H, H_E), 4.11 (t, J = 6.4 Hz, 4H, OCH_2), 2.89 (p, J = 7.1, 6.0 Hz, 2H, H_F), 1.88 – 1.75 (m, 6H, CH_2), 1.48 (dt, J = 9.5, 6.5 Hz, 6H, CH_2), 1.36 (h, J = 3.6 Hz, 8H, CH_2), 0.92 (td, J = 6.0, 5.0, 2.6 Hz, 6H, CH_3), 0.87 (t, J = 7.4 Hz, 3H, H_G). ^{13}C NMR (126 MHz, Chloroform-*d*) δ 161.61, 155.08, 141.48, 141.22, 124.60, 123.11, 121.95, 119.57, 77.41, 77.16, 76.91, 69.35, 39.79, 31.67, 30.23, 29.19, 25.74, 22.99, 22.72, 14.17, 14.12. MS-ESI: *m/z* 1341.5063 $[2M–SBu]^+$ (expected 1341.5091 $[2M–SBu]^+$).

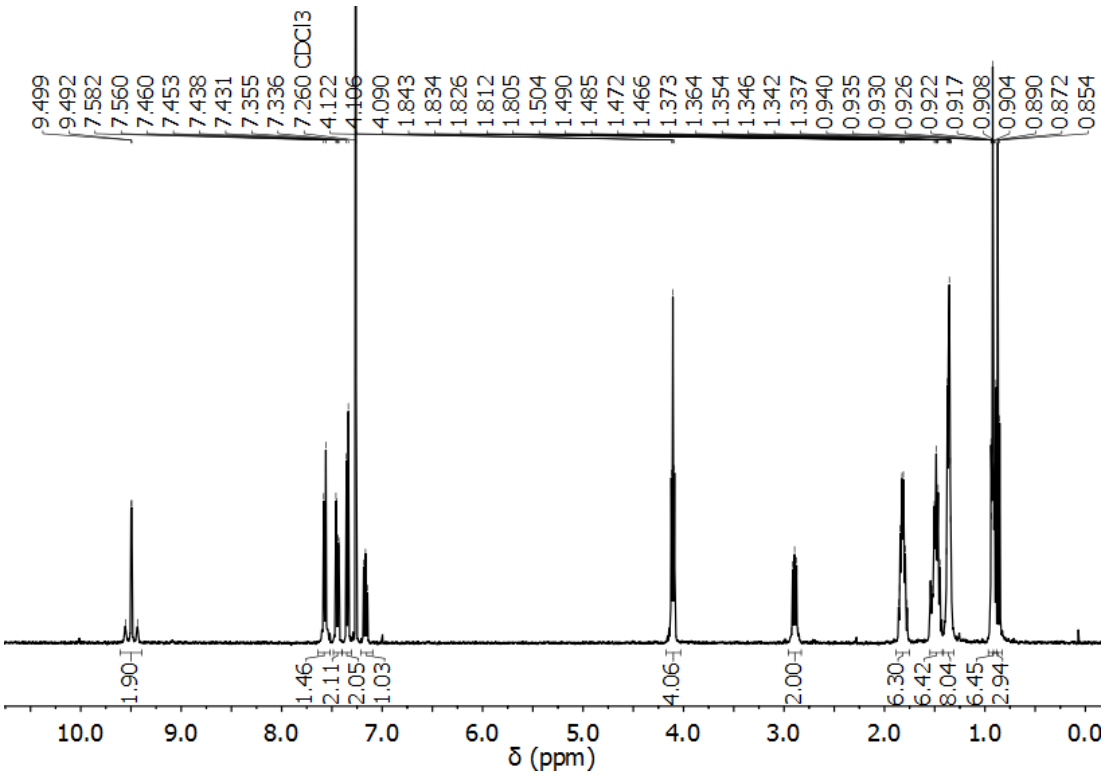

Figure 3.54 ^{1}H NMR spectrum of complex **LPt-9** in chloroform-*d*.

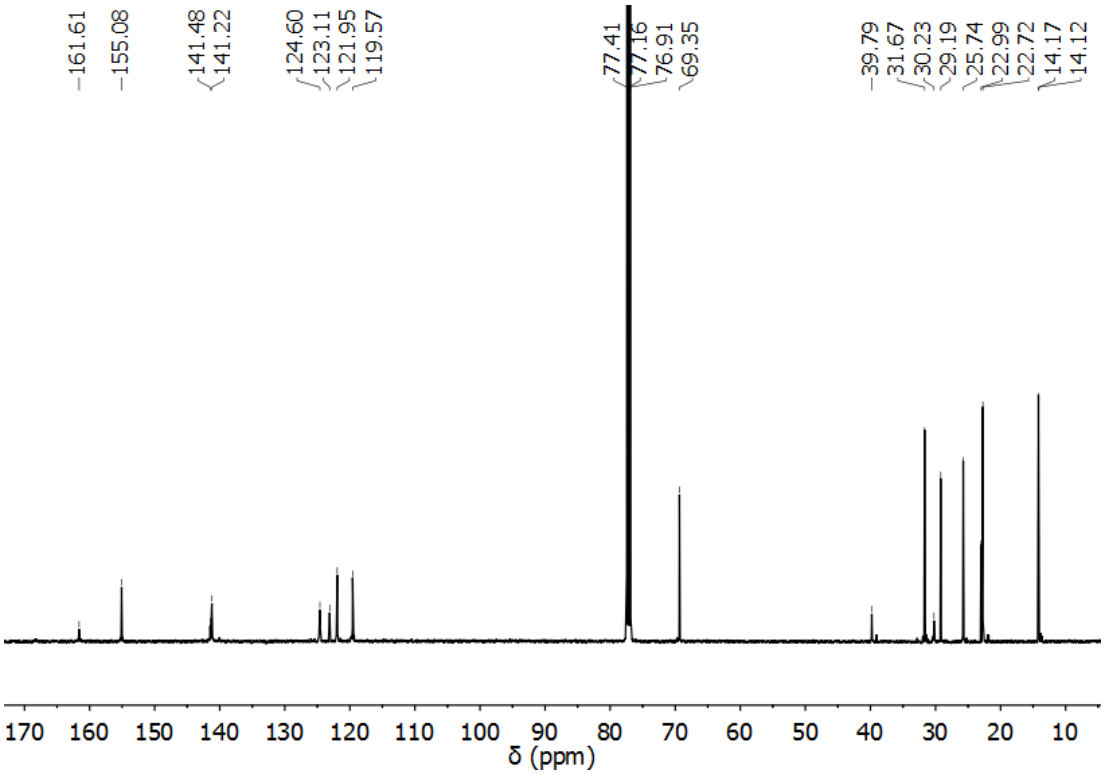

Figure 3.55 ^{13}C NMR spectrum of complex **LPt-9** in chloroform-*d*.

3.8.2 NMR stability and dilution experiments

NMR tubes, precision glassware and glass syringes were dried under vacuum before use. Deuterated solvents were used without further purification. NMR dilution experiments were conducted in Wilmad screw-cap NMR tubes. Stock solutions of complexes **LM-X** in $CDCl_3$-*d* at high concentrations (depending on solubility) were prepared first. Then a known amount of the stock solution was added to a Wilmad screw-cap NMR tube containing 350 µL of solvent. ^{1}H NMR spectra were recorded. Further amounts of the stock solution was added and spectra were measured sequentially. The procedure was repeated for several concentration points.

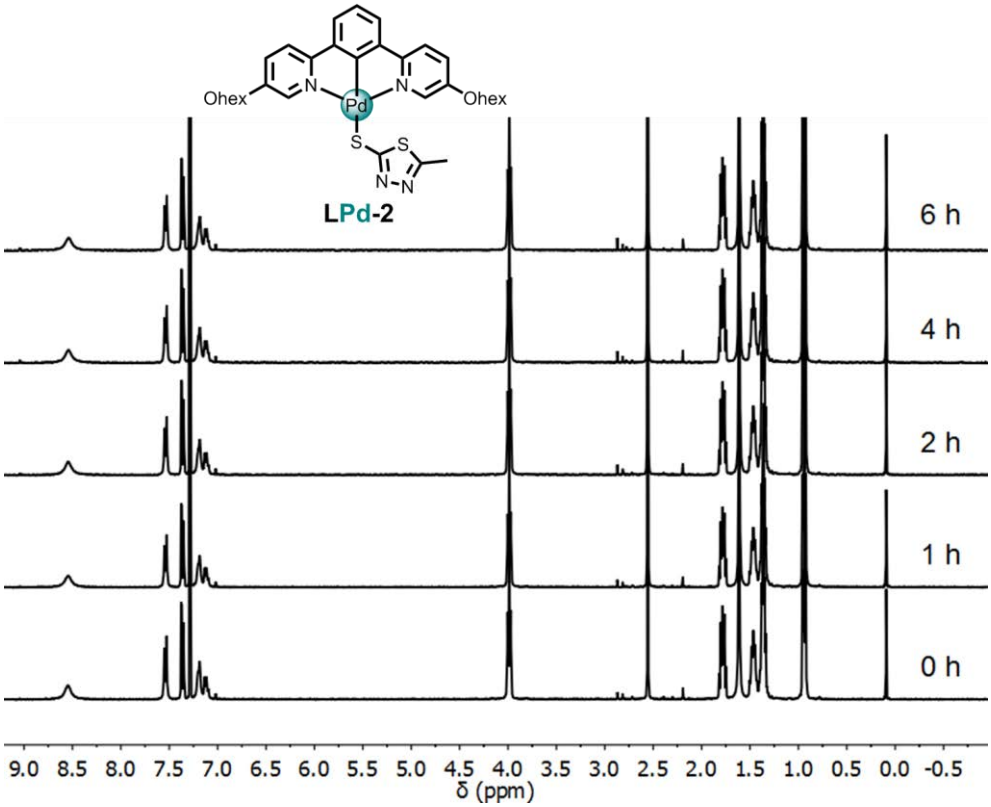

Figure 3.56 Variable-time ^{1}H NMR spectra ($CDCl_3$-*d*, 298 K) of complex **LPd-2**.

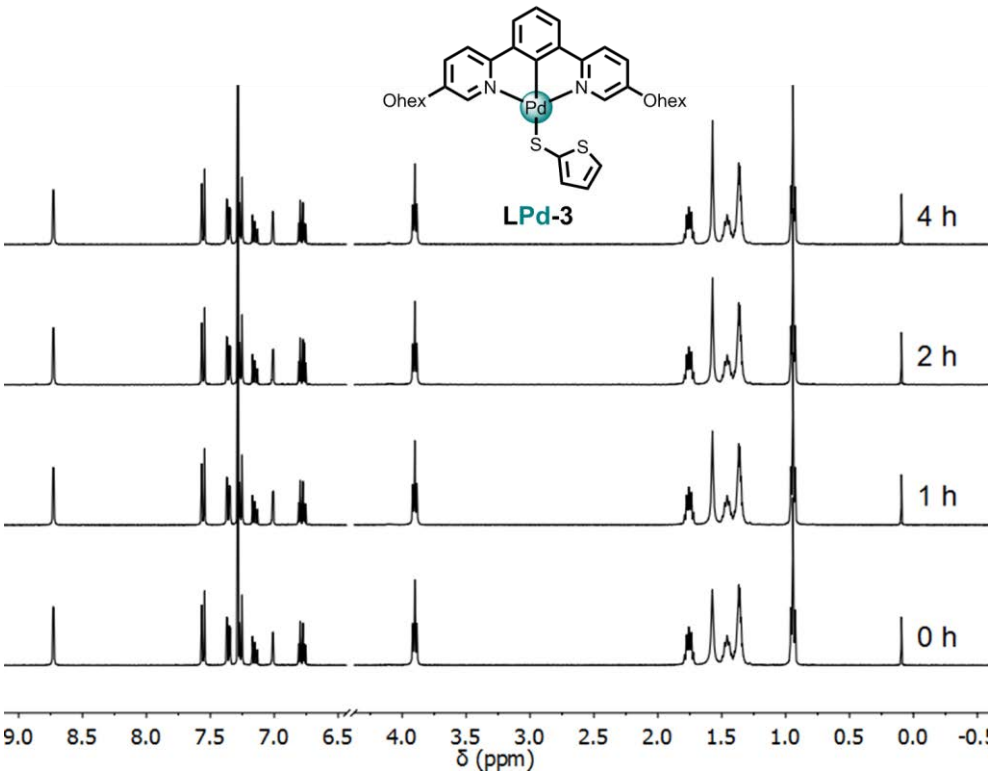

Figure 3.57 Variable-time ^{1}H NMR spectra ($CDCl_3$-*d*, 298 K) of complex **LPd-3**.

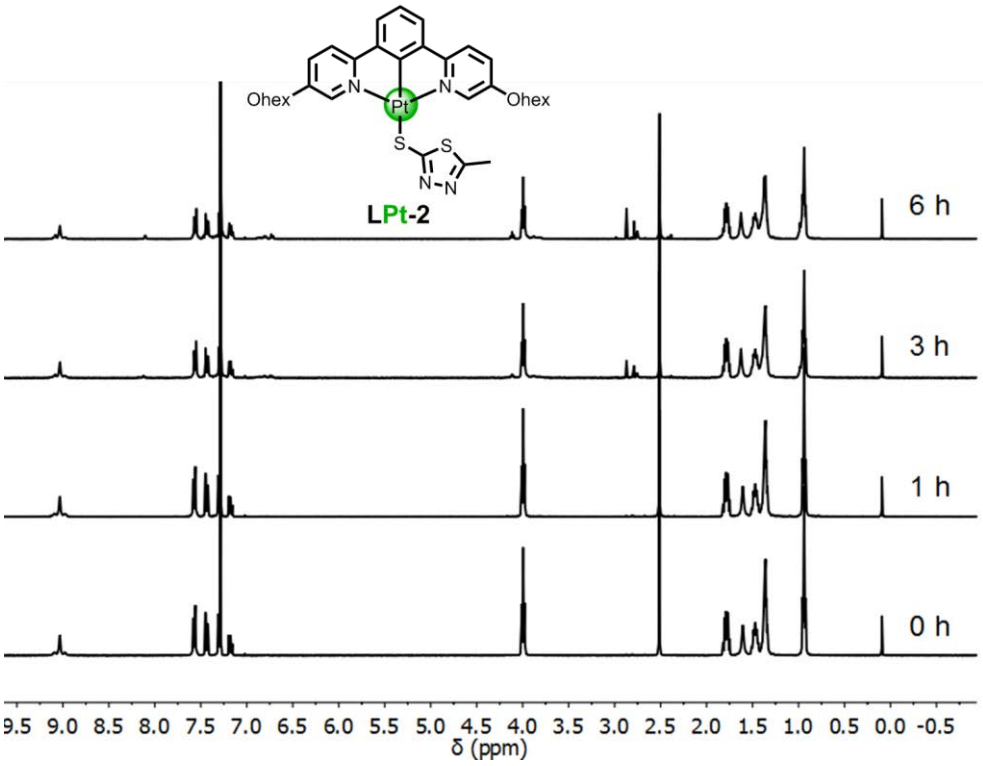

Figure 3.58 Variable-time ^{1}H NMR spectra ($CDCl_3$-*d*, 298 K) of complex **LPt-2**.

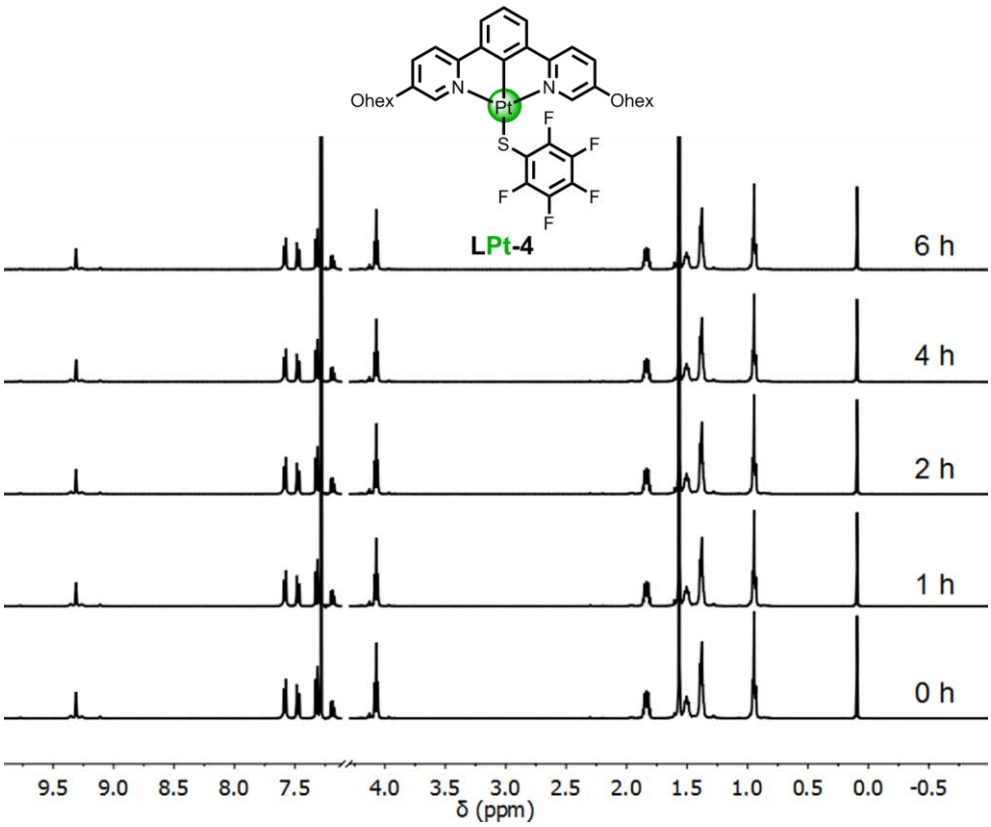

Figure 3.59 Variable-time ^{1}H NMR spectra ($CDCl_3$-*d*, 298 K) of complex **LPt-4**.

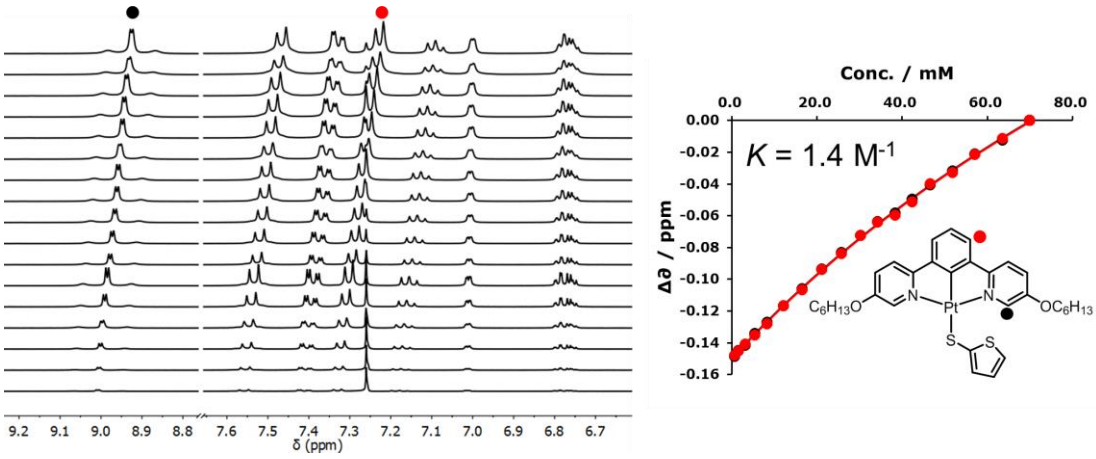

Figure 3.60 ^{1}H NMR dilution spectra of complex **LPt-3** in $CDCl_3$-*d* at 298 K and the corresponding binding isotherms.

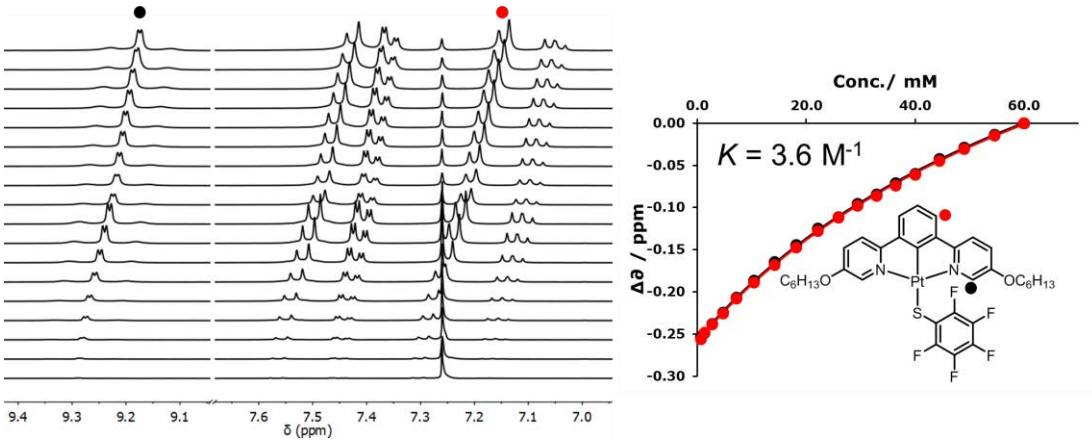

Figure 3.61 ^{1}H NMR dilution spectra of complex **LPt-4** in $CDCl_3$-*d* at 298 K and the corresponding binding isotherms.

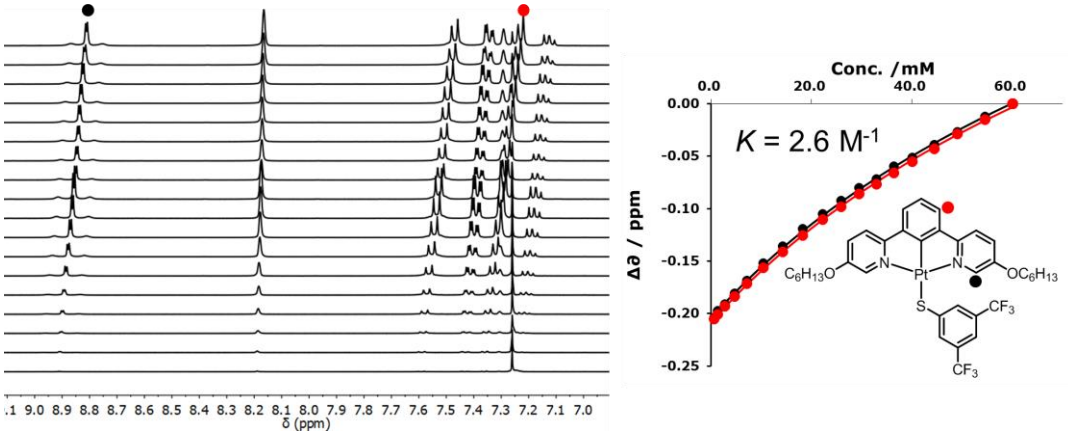

Figure 3.62 ^{1}H NMR dilution spectra of complex **LPt-5** in $CDCl_3$-*d* at 298 K and the corresponding binding isotherms.

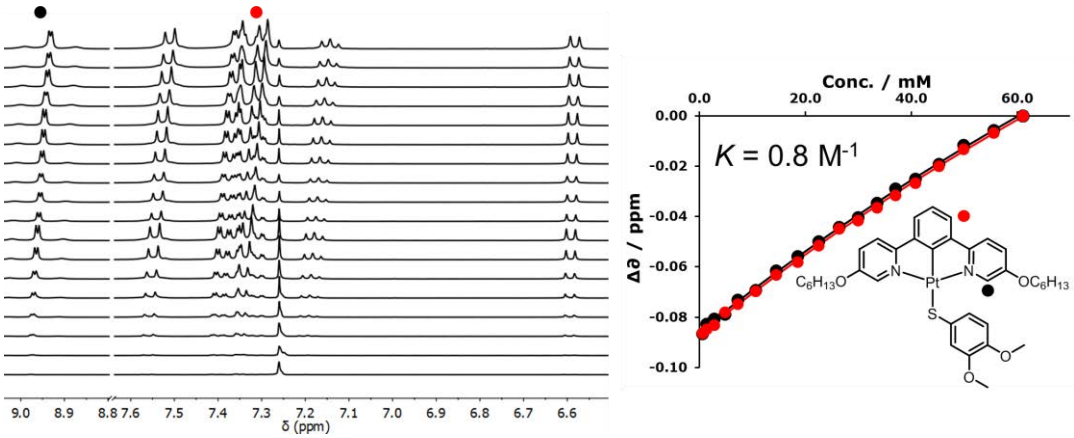

Figure 3.63 ^{1}H NMR dilution spectra of complex **LPt-6** in $CDCl_3$-*d* at 298 K and the corresponding binding isotherms.

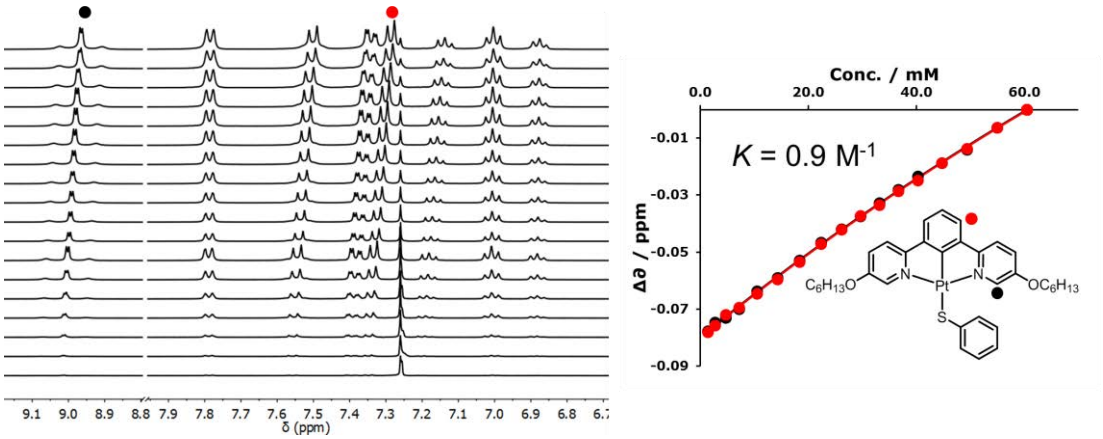

Figure 3.64 ^{1}H NMR dilution spectra of complex **LPt-7** in $CDCl_3$-*d* at 298 K and the corresponding binding isotherms.

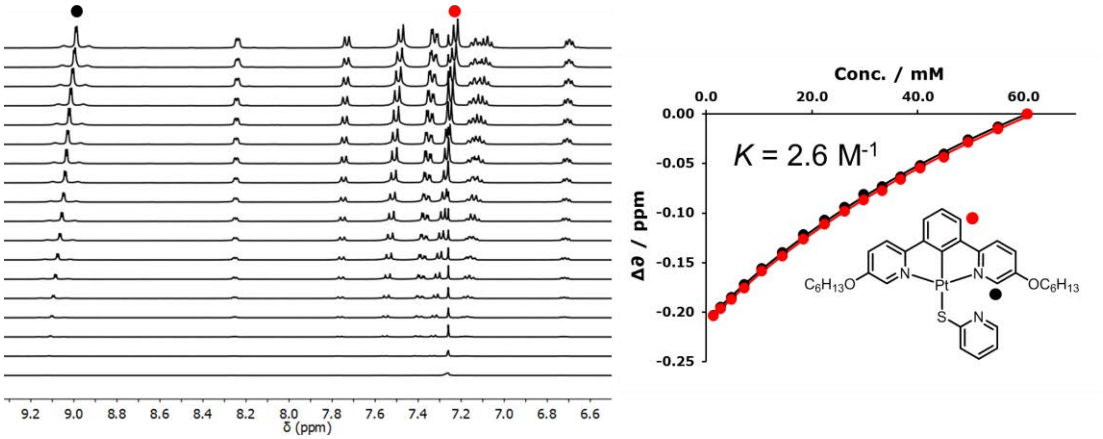

Figure 3.65 ^{1}H NMR dilution spectra of complex **LPt-8** in $CDCl_3$-*d* at 298 K and the corresponding binding isotherms.

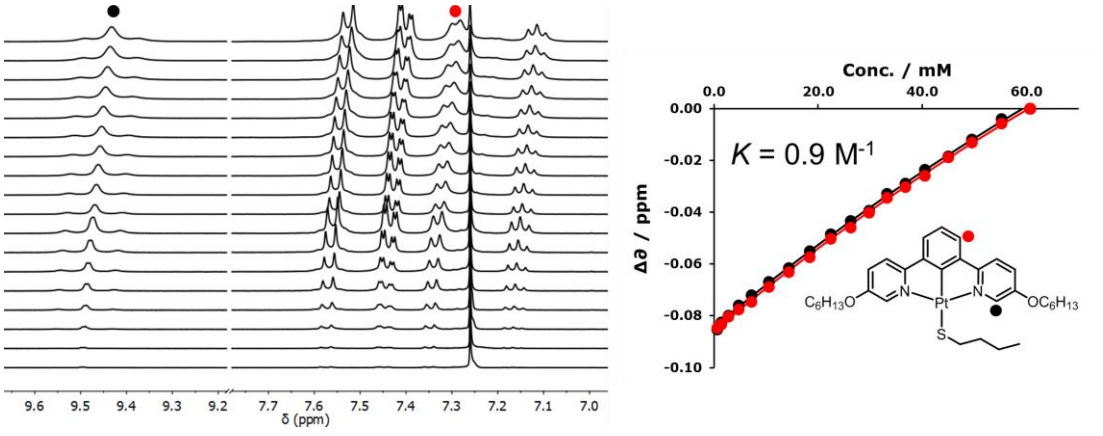

Figure 3.66 ^{1}H NMR dilution spectra of complex **LPt-9** in $CDCl_3$-*d* at 298 K and the corresponding binding isotherms.

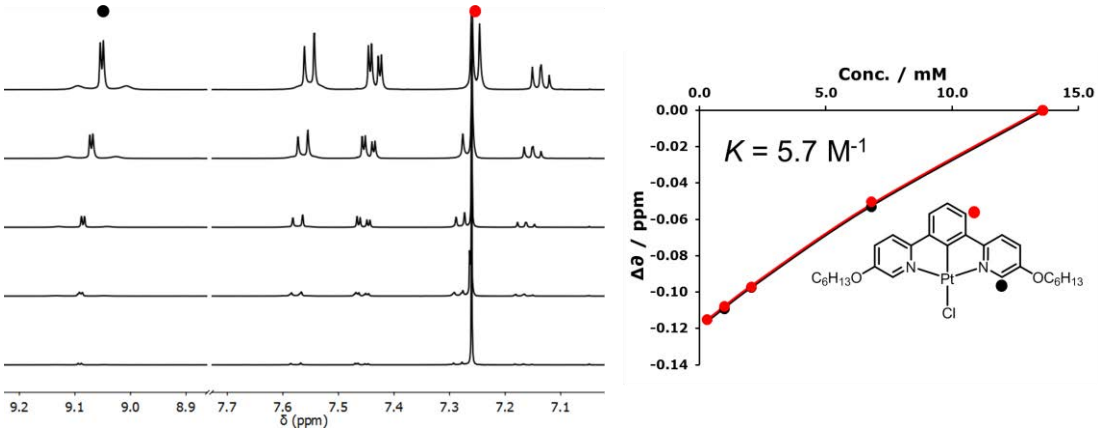

Figure 3.67 ^{1}H NMR dilution spectra of complex **LPt-1** in $CDCl_3$-*d* at 298 K and the corresponding binding isotherms.

3.9 References

1 H. Schmidbaur and A. Schier, *Chem. Soc. Rev.*, 2012, **41**, 370–412.

2 H. Schmidbaur and A. Schier, *Angew. Chem. Int. Ed.*, 2015, 54, 746–784.

3 M. A. Carvajal, S. Alvarez and J. J. Novoa, *Chem. Eur. J.*, 2004, **10**, 2117–2132.

4 E. O'Grady and N. Kaltsoyannis, *Phys. Chem. Chem. Phys.*, 2004, **6**, 680–687.

5 B. H. Xia, C. M. Che, D. L. Phillips, K. H. Leung and K. K. Cheung, *Inorg. Chem.*, 2002, **41**, 3866–3875.

6 A. Aliprandi, D. Genovese, M. Mauro and L. De Cola, *Chem. Lett.*, 2015, **44**, 1152–1169.

7 I. M. Sluch, A. J. Miranda, O. Elbjeirami, M. A. Omary and L. M. Slaughter, *Inorg. Chem.*, 2012, **51**, 10728–10746.

8 M. Yoshida and M. Kato, *Coord. Chem. Rev.*, 2018, **355**, 101–115.

9 Y. Kajitani, K. Tsuge, Y. Sasaki and M. Kato, *Chem. Eur. J.*, 2012, **18**, 11196–11200.

10 K. M.-C. Wong and V. W.-W. Yam, *Acc. Chem. Res.*, 2011, **44**, 424–434.

11 K. Li, G. S. Ming Tong, Q. Wan, G. Cheng, W.-Y. Tong, W.-H. Ang, W.-L. Kwong and C.-M. Che, *Chem. Sci.*, 2016, **7**, 1653–1673.

12 J. J. Novoa, G. Aullón, P. Alemany and S. Alvarez, *J. Am. Chem. Soc.*, 1995, **117**, 7169–7171.

13 E. G. Hope, W. Levason and N. A. Powell, *Inorg. Chim. Acta*, 1986, **115**, 187-192.

14 P. J. Hay and W. R. Wadt, *J. Chem. Phys.*, 1985, **82**, 270–283.

15 W. R. Wadt and P. J. Hay, *J. Chem. Phys.*, 1985, **82**, 284–298.

16 K. Sakai and H. Ozawa, *Coord. Chem. Rev.*, 2007, **251**, 2753–2766.

17 M. J. Frisch, G. W. Trucks, H. B. Schlegel, G. E. Scuseria, M. A. Robb, J. R. Cheeseman, G. Scalmani, V. Barone, B. Mennucci, G. A. Petersson, H. Nakatsuji, M. Caricato, X. Li, H. P. Hratchian, A. F. Izmaylov, J. Bloino, G. Zheng, J. L. Sonnenberg, M. Hada, M. Ehara, K. Toyota, R. Fukuda, J. Hasegawa, M. Ishida, T. Nakajima, Y. Honda, O. Kitao, H. Nakai, T. Vreven, J. A. Montgomery, J. E. Peralta, F. Ogliaro, M. Bearpark, J. J. Heyd, E. Brothers, K. N. Kudin, V. N. Staroverov, R. Kobayashi, J. Normand, K. Raghavachari, A. Rendell, J. C. Burant, S. S. Iyengar, J. Tomasi, M. Cossi, N. Rega, J. M. Millam, M. Klene, J. E. Knox, J. B. Cross, V. Bakken, C. Adamo, J. Jaramillo, R. Gomperts, R. E. Stratmann, O. Yazyev, A. J. Austin, R. Cammi, C. Pomelli, J. W. Ochterski, R. L. Martin, K. Morokuma, V. G. Zakrzewski, G. A. Voth, P. Salvador, J. J. Dannenberg, S. Dapprich, A. D. Daniels, Farkas, J.

B. Foresman, J. V Ortiz, J. Cioslowski and D. J. Fox, 2009.

18 J. Tao, J. P. Perdew, V. N. Staroverov and G. E. Scuseria, *Phys. Rev. Lett.*, 2003, **91**, 3–6.

19 F. Weigend and R. Ahlrichs, *Phys. Chem. Chem. Phys.*, 2005, **7**, 3297.

20 B. R. Brooks, C. L. B. III, J. A. D. Mackerell, L. Nilsson, R. J. Petrella, B. Roux, Y. Won, G. Archontis, C. Bartels, S. Boresch, A. Caflisch, L. Caves, Q. Cui, A. R. Dinner, M. Feig, S. Fischer, J. Gao, M. W. I. Hodoscek and M. Karplus, *J. Comput. Chem.*, 2009, **30**, 1545–1614.

21 K. Morokuma, *J. Chem. Phys.*, 1971, **55**, 1236–1244.

22 T. Ziegler and a Rauk, *Theor. Chim. Acta*, 1977, **46**, 1–10.

23 T. Ziegler and A. Rauk, *Inorg. Chem.*, 1979, **18**, 1558–1565.

24 E. J. Baerends, T. Ziegler, A. J. Atkins, J. Autschbach, D. Bashford, O. Baseggio, A. Bérces, F. M. Bickelhaupt, C. Bo, P. M. Boerritger, L. Cavallo, C. Daul, D. P. Chong, D. V Chulhai, L. Deng, R. M. Dickson, J. M. Dieterich, D. E. Ellis, M. van Faassen, A. Ghysels, A. Giammona, S. J. A. van Gisbergen, A. Goez, A. W. Götz, S. Gusarov, F. E. Harris, P. van den Hoek, Z. Hu, C. R. Jacob, H. Jacobsen, L. Jensen, L. Joubert, J. W. Kaminski, G. van Kessel, C. König, F. Kootstra, A. Kovalenko, M. Krykunov, E. van Lenthe, D. A. McCormack, A. Michalak, M. Mitoraj, S. M. Morton, J. Neugebauer, V. P. Nicu, L. Noodleman, V. P. Osinga, S. Patchkovskii, M. Pavanello, C. A. Peeples, P. H. T. Philipsen, D. Post, C. C. Pye, H. Ramanantoanina, P. Ramos, W. Ravenek, J. I. Rodríguez, P. Ros, R. Rüger, P. R. T. Schipper, D. Schlüns, H. van Schoot, G. Schreckenbach, J. S. Seldenthuis, M. Seth, J. G. Snijders, M. Solà, S. M., M. Swart, D. Swerhone, G. te Velde, V. Tognetti, P. Vernooijs, L. Versluis, L. Visscher, O. Visser, F. Wang, T. A. Wesolowski, E. M. van Wezenbeek, G. Wiesenekker, S. K. Wolff, T. K. Woo and A. L. Yakovlev, .

25 G. te Velde, F. M. Bickelhaupt, E. J. Baerends, C. Fonseca Guerra, S. J. A. van Gisbergen, J. G. Snijders and T. Ziegler, *J. Comput. Chem.*, 2001, **22**, 931–967.

26 J. P. Perdew, K. Burke and M. Ernzerhof, *Phys. Rev. Lett.*, 1996, **77**, 3865–3868.

27 E. van Lenthe, E. J. Baerends and J. G. Snijders, *J. Chem. Phys.*, 1993, **99**, 4597–4610.

28 E. Van Lenthe, E. J. Baerends and J. G. Snijders, *J. Chem. Phys.*, 1994, **101**, 9783–9792.

29 E. Van Lenthe, J. G. Snijders and E. J. Baerends, *J. Chem. Phys.*, 1996, **105**, 6505–6516.

30 E. Van Lenthe and E. J. Baerends, *J. Comput. Chem.*, 2003, **24**, 1142–1156.

31 C. P. Kelly, C. J. Cramer and D. G. Truhlar, *J. Chem. Theory Comput.*, 2005, **1**, 1133–1152.

32 O. V Dolomanov, L. J. Bourhis, R. J. Gildea, J. A. K. Howard and H. Puschmann, *J. Appl. Crystallogr.*, 2009, **42**, 339–341.

33 G. M. Sheldrick, *Acta Crystallogr. Sect. A Found. Crystallogr.*, 2008, **64**, 112–122.

Chapter 4: Solvent- and Temperature-Induced Colour Change of a Pt^{II}-Complex

Abstract

Square-planar cyclometalated Pt^{II}-complexes are easy to assemble into different structures, in which aromatic stacking and metallophilic interactions are proposed to play significant roles. These structures can be modulated by different stimuli, such as concentration, solvent composition, mechanical-grinding, temperature and counter ions, which are often associated with intriguing photophysical and spectroscopic changes. Here a complex **LPt-2** (L = 1,3-di(5-hexyloxy-2-pyridyl)benzene, **2** = 2-mercapto-5-methyl-1,3,4-thiadiazole) has been synthesised and employed to study the influence of solvent, concentration, and temperature. ^{1}H and ^{195}Pt NMR suggest that the complex is stable in chloroform, but transforms into other Pt^{II}-complexes in methanol. This is confirmed by UV-vis spectra and different solution colours. The complex solution displays a yellow colour in chloroform, but blue in methanol. The transformation in methanol was reached after 3 hours, which was supported by time-dependent NMR, UV-vis spectra and visible colour change. The stabilised solution in methanol illustrated colour change upon varying concentration and temperature. UV-vis spectra reveal that the colour change is due to the change of absorbance intensity at 475 nm and 570 nm, which correspond to metal-to-ligand charge transfer (MLCT) and metal-metal-to-ligand charge transfer (MMLCT) respectively. Therefore, metallophilic interactions present in methanol and contribute to the colour change. Varying solvent, concentration, and temperature can effectively tune metallophilic interactions, molecular assembly and the corresponding colour of the solution.

4.1 Introduction

Cyclometalated Pt^{II}-complexes have drawn much attention due to their potential applications in optoelectronic devices,[1] chemosensing,[2–4] photocatalysis,[5–7] and bioimaging.[8,9] The square-planar geometries of these complexes enable them to aggregate with each other due to synergetic effects from Pt–Pt interactions, π–π stacking and other weak interactions.[10,11] Several excellent reviews on the role of metallophilic interactions to photophysical properties of metal complexes have been reported.[1,12,13] The interactions in these aggregates are often weak, these Pt-complexes can be easily interrupted by different stimuli, inducing different morphologies with interesting spectroscopic and photophysical properties.[14–16] Such stimuli include concentration,[17,18] solvent composition,[10,19,20] organic vapours,[2,3,21] mechanical-grinding,[21] temperature,[22,23] counter ions,[24,25] pH[23,26] and so on.

4.2 Project aims

Chapter 3 revealed that metallophilic interactions are weak and contribute little to the assembly of the complex **LM-X** (M = Pt, Pd, and Ni, L = 1,3-di(5-hexyloxy-2-pyridyl)benzene, X = Cl or thiol derivatives). The assembly is sensitive to internal adjustments including different metals and substituents. Thus, the questions arise: What about external stimuli, such as solvent and temperature? How can they affect molecular aggregation and photophysical properties?

As the only complex displaying Pt–Pt interactions in the solid state, complex **LPt-2** (**2** = 2-mercapto-5-methyl-1,3,4-thiadiazole) is chosen as the model complex to investigate the influence of external stimuli to metallophilic interactions and molecular assembly. The benefits of using this complex are: i) the presence of S and N in ligand **2** may be sensitive to different solvents by forming/breaking hydrogen bonding with solvent molecules, ii) the flexible orientation of the thiol ligand enables the complex to be easily affected by external stimuli.

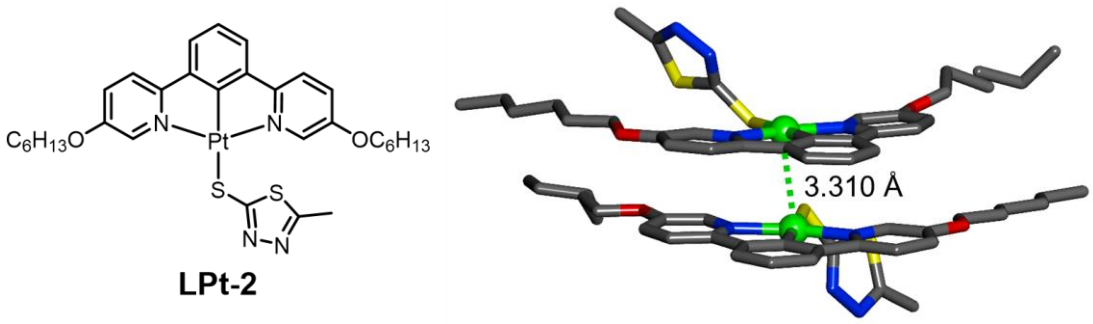

Figure 4.1 Complex **LPt-2** and its crystal structure. Colour codes: green Pt, yellow S, blue N, red O, grey C, cyan Pd. Hydrogens are omitted for clarity.

4.3 Results and discussion

4.3.1 Influence of solvent

The complex **LPt-2** can be dissolved in several organic solvents, including $CHCl_3$, CH_2Cl_2, MeOH, EtOH, MeCN, and DMSO. It is poorly soluble in acetone (< 5mM), benzene (< 2.5 mM), ethyl acetate, Et_2O, *n*-hexane, and is insoluble in water. The stability of complex **LPt-2** in different solvents have been examined by ^{1}H NMR spectroscopy. As shown in **Figure 4.2**, the spectrum in $CDCl_3$-*d* shows a characteristic satellite peak at ~ 9.0 ppm due to the ^{1}H-^{195}Pt coupling between H_a (proton besides pyridine N) and ^{195}Pt. The ratio of the integrals between OCH_2- (at ~4.0 ppm) from ligand L and CH_3 (at ~ 2.5 ppm) from ligand **2** is 4:3, which corresponds well with the complex. Therefore, the complex **LPt-2** is stable in $CDCl_3$-*d*. The spectrum in benzene-d_6 gives similar a spectrum to that in $CDCl_3$-*d* with proton *a* becoming more deshielded and other protons being more shielded. In acetone-d_6, the character satellite peak at ~9.0 ppm is preserved, but impurity peaks appear, suggesting the complex **LPt-2** partially decomposes in acetone. Whereas in DMSO-d_6, CDCN-d_3, and CD_3OD-d_4, the peak corresponding to H*a* overlaps with ^{1}H-^{195}Pt satellite peaks. The

extra peaks present in the range of 3.5–8.0 ppm suggest some new complexes appear in these solvents.

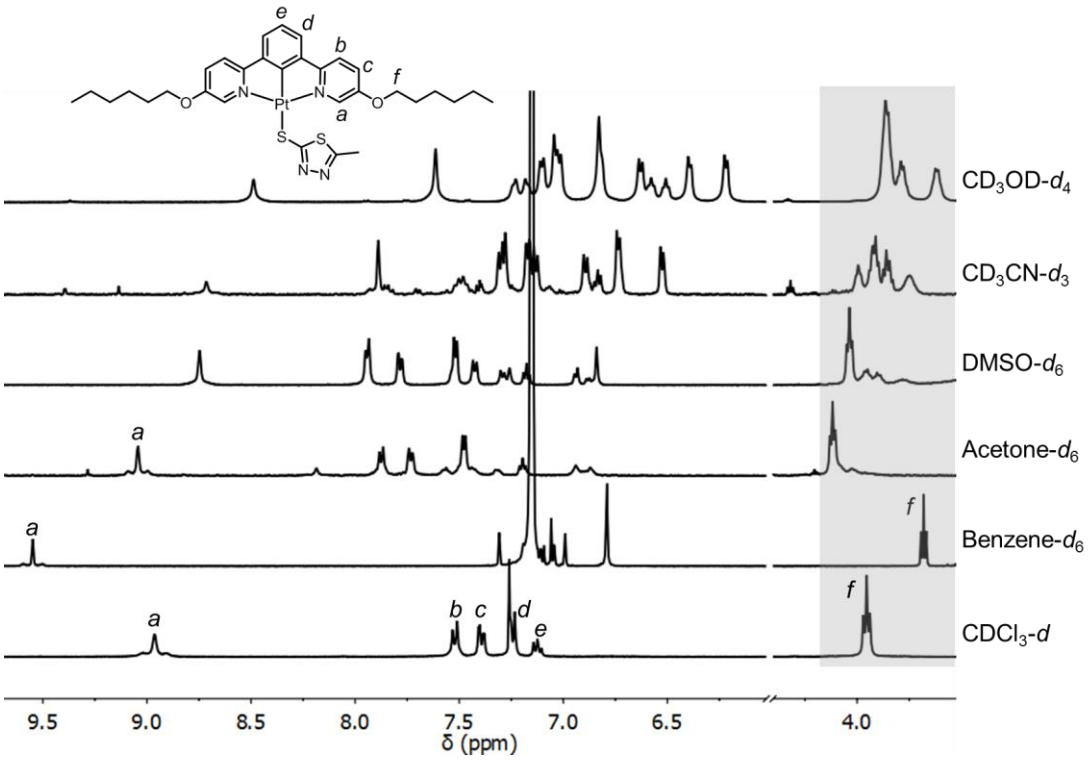

Figure 4.2 Partial ^{1}H NMR spectra of complex **LPt-2** in different solvents at 298 K.

The influence induced by different solvent can be observed more directly by showing different colour. As illustrated in **Figure 4.3**, the complex **LPt-2** in $CHCl_3$, CH_2Cl_2, benzene, hexane, and Et_2O gives a yellow/orange colour. While in acetonitrile, ethanol, and DMSO, the solutions display brown to red colour. In methanol, the solution containing transformed species is blue.

The colour change induced by different solvents can be monitored by UV-vis spectroscopy. As displayed in **Figure 4.4**, complex **LPt-2** in different solvents show different UV-vis absorption spectra. In DCM, THF and Et_2O, only absorption bands before 400 nm corresponding to intra-ligand absorption are observed. Whereas in $CHCl_3$, MeOH, and MeCN, an absorption band at around 475 nm appears. This band is assigned to $\pi_S/d_{Pt}\rightarrow\pi^*_L$ charge-transfer (MLCT),[27] which is the transition from sulfur or platinum to the ligand L. A low energy absorption band at 570 nm is only found in

methanol, which is ascribed to metal-metal-to-ligand charge transfer (MMLCT), suggesting Pt–Pt interactions is preserved in methanol.

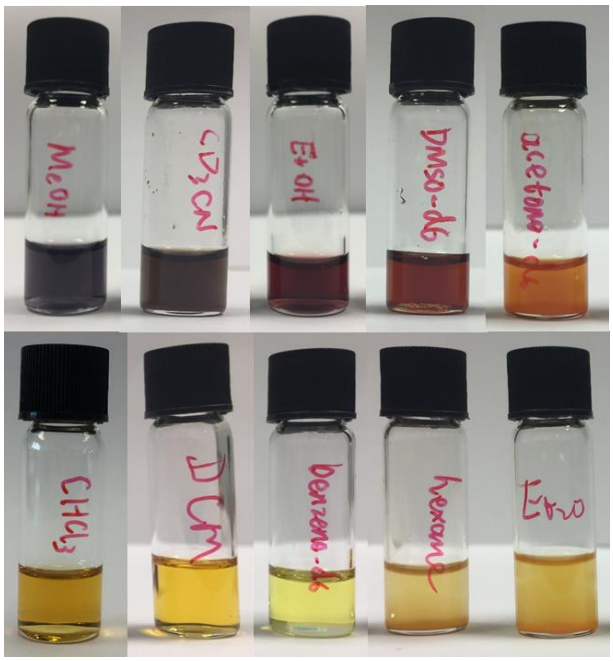

Figure 4.3 Images for solutions of complex **LPt-2** in different solvents under ambient light at room temperature.

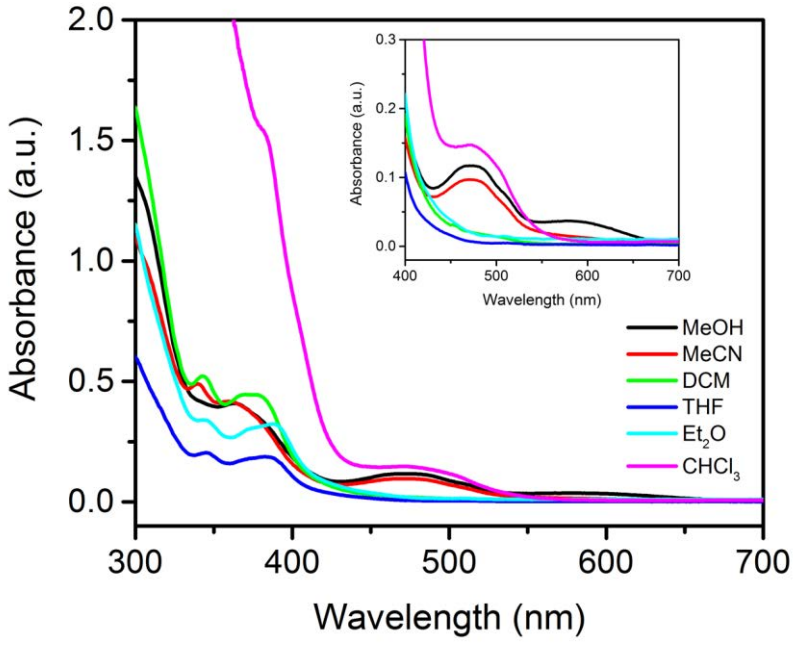

Figure 4.4 UV-vis absorption spectra of complex **LPt-2** in different solvents.

The UV-vis spectrum and the blue colour of the methanol solution is quite unique and interesting. To figure out what the complexes are in methanol and how the new species affect solution colour, further NMR spectroscopy and UV-vis spectroscopy studies have been performed.

4.3.2 Influence of time

Time-dependent ^{1}H NMR spectra of complex **LPt-2** (0.5 mM) in methanol were performed first to examine the stability of the solution (**Figure 4.5**). The freshly made solution displayed some small peaks which then gradually disappeared over 3 hours. The solution remained the same in the following 24 hours. The change of the spectra implies that the transformation from complex **LPt-2** to other species takes 3 hours. The transformation is accompanied by visible colour change. The freshly made solution was yellow/brown, but after 12 hours, the solution changed to pale green.

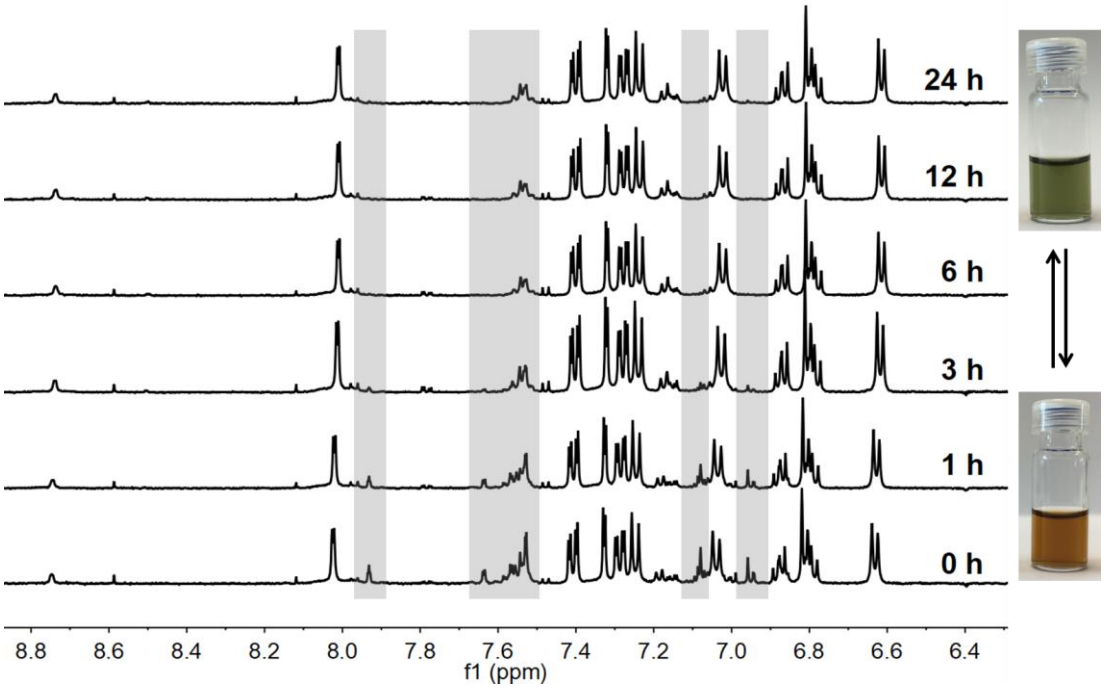

Figure 4.5 Time-dependent ^{1}H NMR spectra of complex **LPt-2** (0.5 mM) in methanol at room temperature. Changed peaks are indicated by grey areas. Images are the solution after 0 h and 12 h.

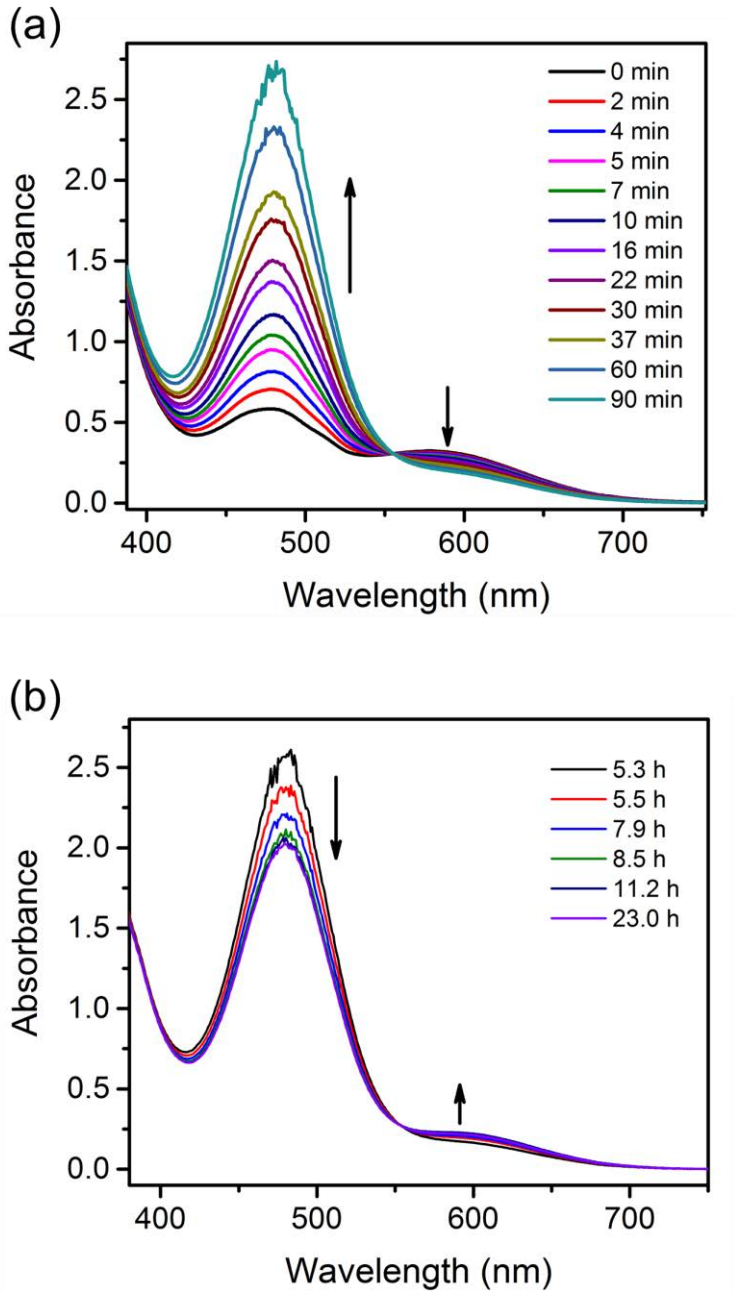

Figure 4.6 Time-dependent UV-vis spectra of complex **LPt-2** in methanol (0.25 mM) at room temperature.

Time-dependent UV-vis spectra of complex **LPt-2** in methanol has also been performed at room temperature. As depicted in **Figure 4.6**, the absorption band at 475 nm increases significantly and the peak at 570 nm decreases slightly in the first 90 minutes. In other words, absorption of blue and green light (450 – 560 nm) increases, and absorption of yellow and orange light (570 – 650 nm) decreases. Consequently,

the solution becomes a deeper yellow/brown colour. The spectra after 2 hours are not shown here because the absorbance at 475 nm after 2 hours is too strong (> 10). After 5 hours, reverse trends of decreasing absorbance at 475 nm and of increasing absorbance at 570 nm are observed. The solution thus shows a green-ish colour. Therefore, the visible colour change shown in **Figure 4.8** is caused by the change of absorbance at 475 nm and 570 nm. In addition, the tiny change of absorbance at 570 nm (MMLCT) also indicates that the contribution from metallophilic interactions is small.

4.3.3 Influence of concentration

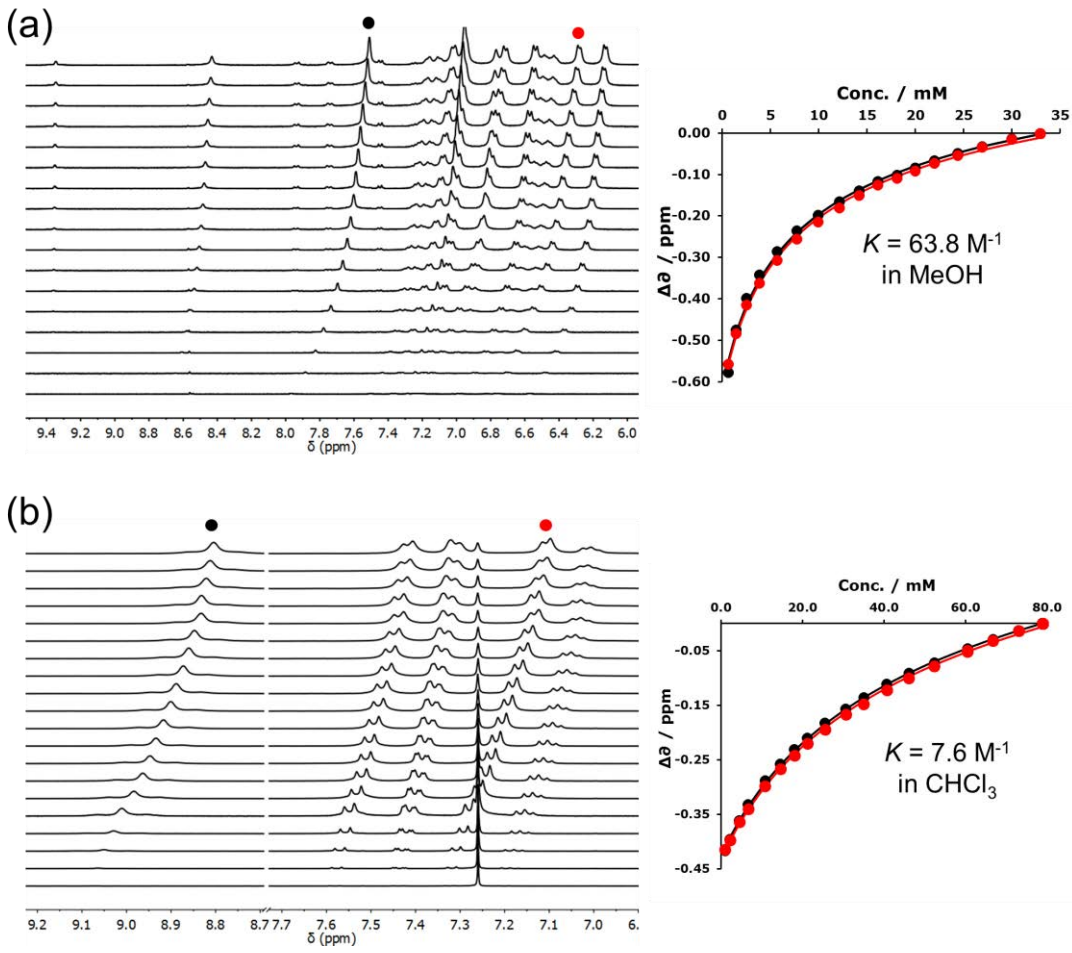

Figure 4.7 Concentration-dependent ^{1}H NMR spectra and corresponding binding isotherms of complex **LPt-2** in MeOH (a) and $CHCl_3$ (b).

Dilution ^{1}H NMR experiments were carried out to investigate the influence of concentration (**Figure 4.7**). Upon increasing the concentration of complex **LPt-2**

dissolved in MeOH and $CHCl_3$, upfield shifts were observed in the ^1H NMR spectra, suggesting the occurrence of aggregation. The fitted binding isotherms gave a binding constant of 63.8 M^{-1} in MeOH and a K of 7.6 M^{-1} in $CHCl_3$. Obviously, the binding constant K in methanol is about one order of magnitude higher than that in $CHCl_3$, indicating that the complexes aggregate more easily in methanol.

Images of the methanol solution at different concentrations are displayed in **Figure 4.8**. The freshly made methanol solution is transparent and shows a pale brown colour at 0.05 mM. Upon increasing concentration, the solution colour becomes darker. Whereas the solutions stabilised for 12 hours changes to a pale green colour at 0.05 mM and dark blue at 2 mM. Concentration-dependent UV-vis spectra (**Figure 4.9**) demonstrate that the absorbance of all the peaks increases with increasing concentration. The absorption band at 570 nm (MMLCT) is not linearly correlated to concentration, which doesn't obey Beer's law. This observation indicates that aggregation occurs in methanol and Pt–Pt interactions play a significant role in varying the photochemical properties.

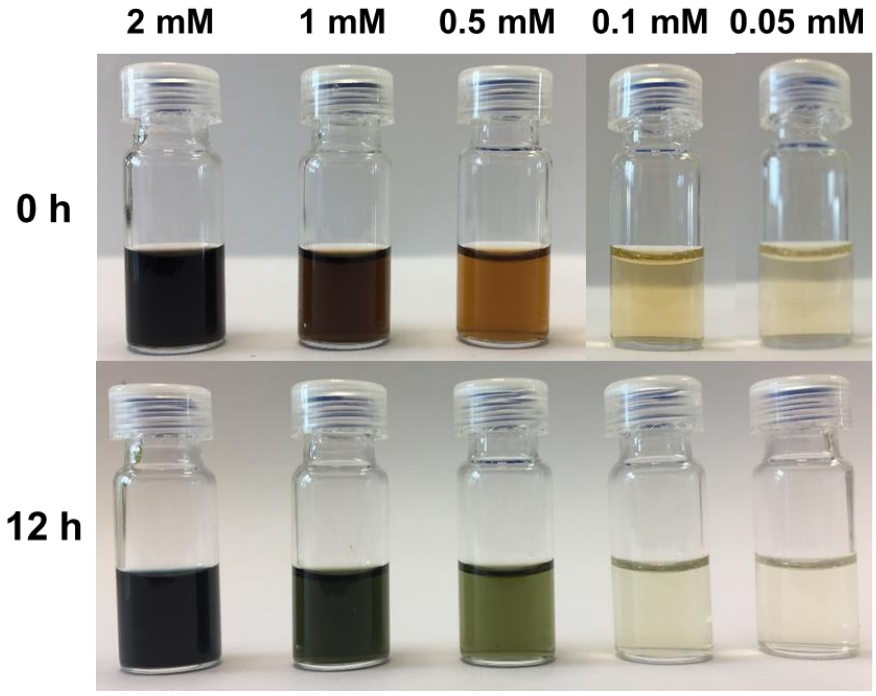

Figure 4.8 Images for the solution of complex **LPt-2** in methanol at different concentrations and the colour change over time.

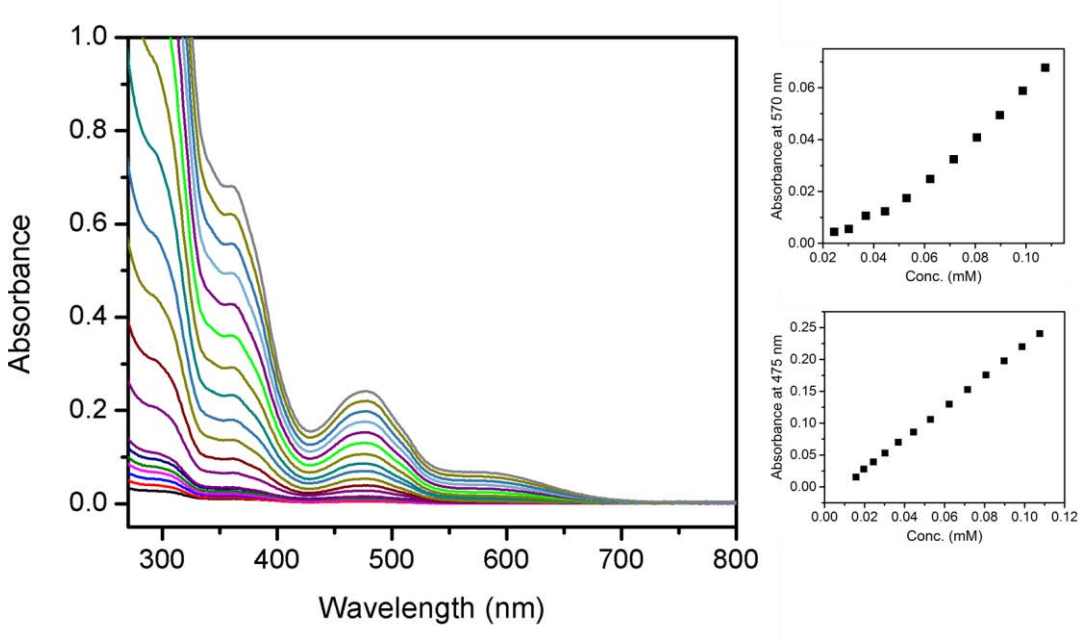

Figure 4.9 Concentration-dependent UV-vis absorption spectra of complex **LPt-2** in MeOH, and the corresponding plots of absorbance at 570 nm and 475 nm against concentration.

4.3.4 Influence of temperature

At room temperature, the ^{1}H NMR spectra of complex **LPt-2** in chloroform-*d* show a single peak at ~9.0 ppm, which is assigned to protons Ha and Ha' (**Figure 4.10**). The peak is firstly broadened when decreasing temperature from 298 K to 268 K, and then the signal becomes sharper below 268 K. Therefore, the complex **LPt-2** in $CHCl_3$ is in fast exchange at room temperature then reaches medium-fast exchange at the coalescence temperature of 268 K where the exchange rate further slows down. While the VT ^{1}H NMR spectra in methanol-d_4 shows a different trend. The peaks at ~8.5 ppm and ~7.6 ppm, which correspond to the Hs beside Ns in pyridines, firstly become sharper and then broader upon decreasing temperature. This further confirms that the complex in methanol is not **LPt-2** anymore. Both multiple complexes and their self-assembly behaviour might be responsible for the line sharpening and broadening trend in methanol.

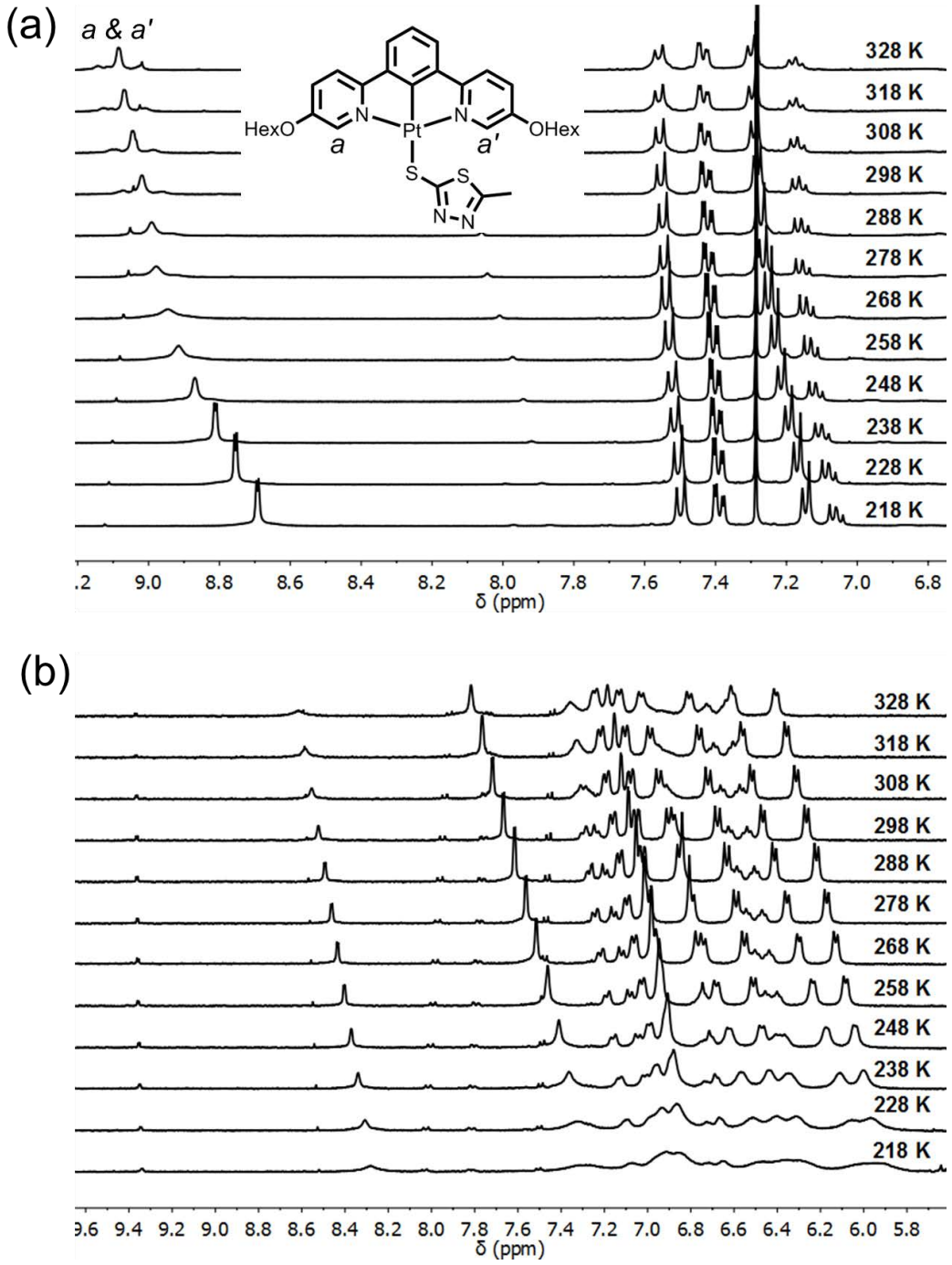

Figure 4.10 Temperature-dependent ^{1}H NMR spectra of complex **LPt-2** in chloroform-*d* (a) and methanol-d_4 (b) at concentration of 10 mM.

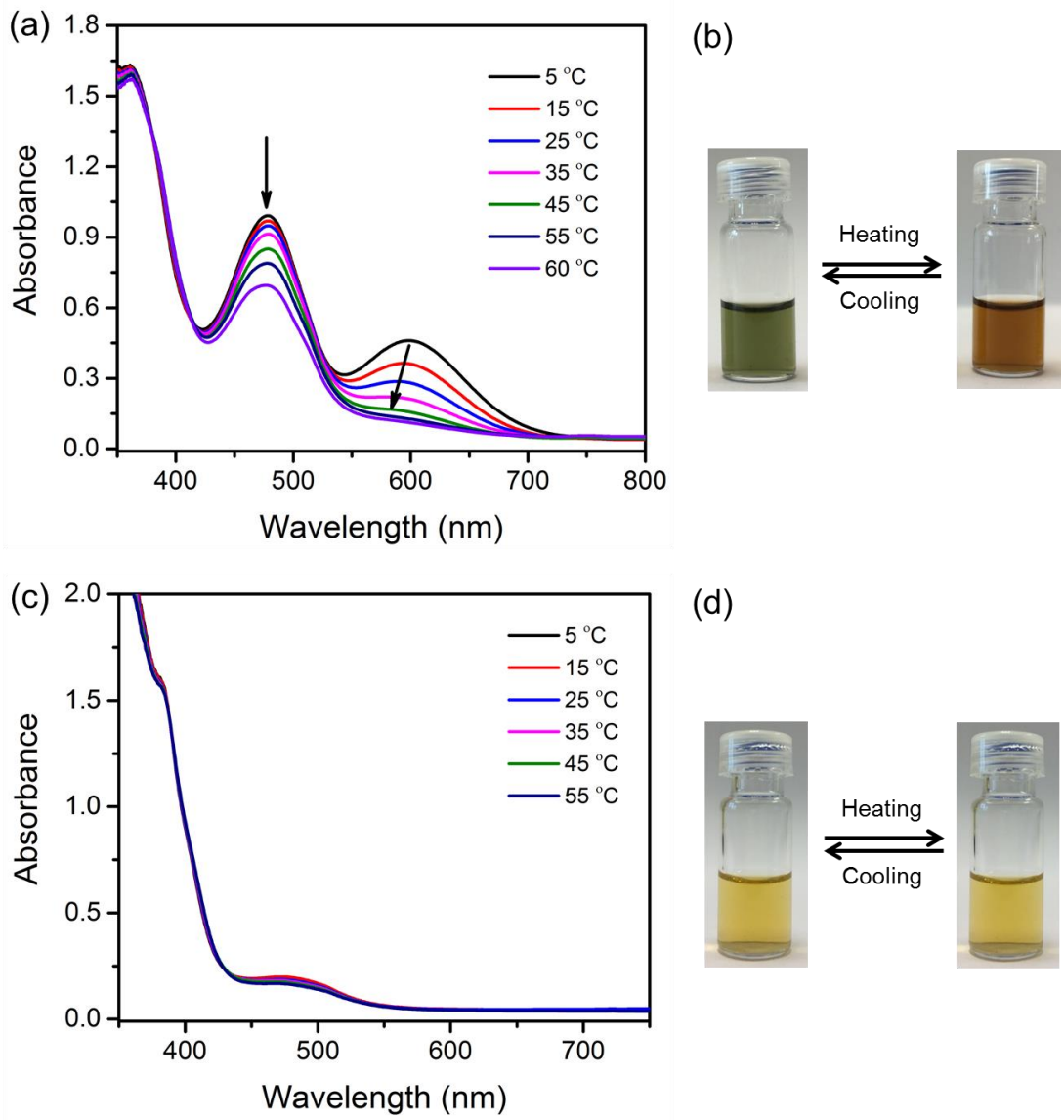

Figure 4.11 Temperature-dependent UV-vis spectra and the corresponding images of complex **LPt-2** (0.2 mM) in MeOH (a, b) and in $CHCl_3$ (c, d).

Knowing that the complex **LPt-2** in methanol is transforming to other species in the first 3 hours, a solution (0.2 mM) was stabilised overnight at room temperature. The stabilised solution was then examined in a temperature-dependent UV-vis spectroscopy study. The obtained results are summarised in **Figure 4.11**. Upon increasing temperature from 5 °C to 60 °C, both peaks at 475 nm and 570 nm decrease (**Figure 4.11a**). A small blue shift (~ 20 nm) at peak 570 nm is also observed. Due to the decrease of absorption bands and the blue shift, the green solution changed to a brown colour at higher temperature. The solution colour recovers to green after cooling

down. The corresponding reversible colour change is depicted in **Figure 4.11b**. The significant change of absorbance at 570 nm (MMLCT) suggest that metallophilic interactions are sensitive to temperature. The metal–metal distance can be easily tuned by varying temperature. The solution in $CHCl_3$ serves as a control (**Figure 4.11c&d**), in which no obvious spectroscopic and visible change have been observed.

4.3.5 What are the complexes in methanol?

Having known the interesting colour change in methanol induced by time, concentration, and temperature, it is essential to know what the new complexes are and how they affect the solution colour. The ^{1}H NMR spectra of the solution in methanol is compared to that in chloroform (**Figure 4.12**). The presence of three peaks at 3.5–4.0 ppm and three peaks at 2.2–2.8 ppm indicates that there are three different chemical environments for OCH_2 (from ligand L) and CH_3 (from ligand **2**), respectively. ^{195}Pt NMR spectroscopy (**Figure 4.13**) displays peaks at –3485 ppm, –3520 ppm, and –3645 ppm (very weak, may be noise), revealing there are two (or three) Pt-complexes in methanol. Since the $Pt^{II}S$-complexed halides generally display ^{195}Pt signal in the range of –3500 to –4200 ppm,[28] the complexes in methanol are expected to be $Pt^{II}S$-complexes, though they do not correspond to the original complex **LPt-2**.

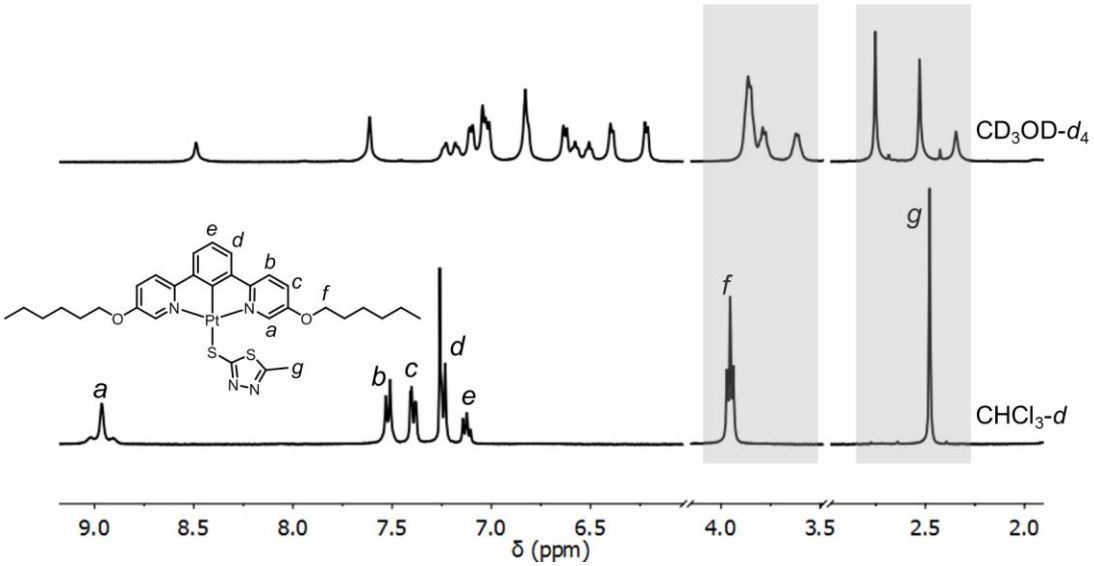

Figure 4.12 ^{1}H NMR spectra of complex **LPt-2** in $CHCl_3$-*d* and CD_3OD-d_4. Grey areas are peaks corresponding to OCH_2 (from ligand L) and CH_3 (from ligand **2**).

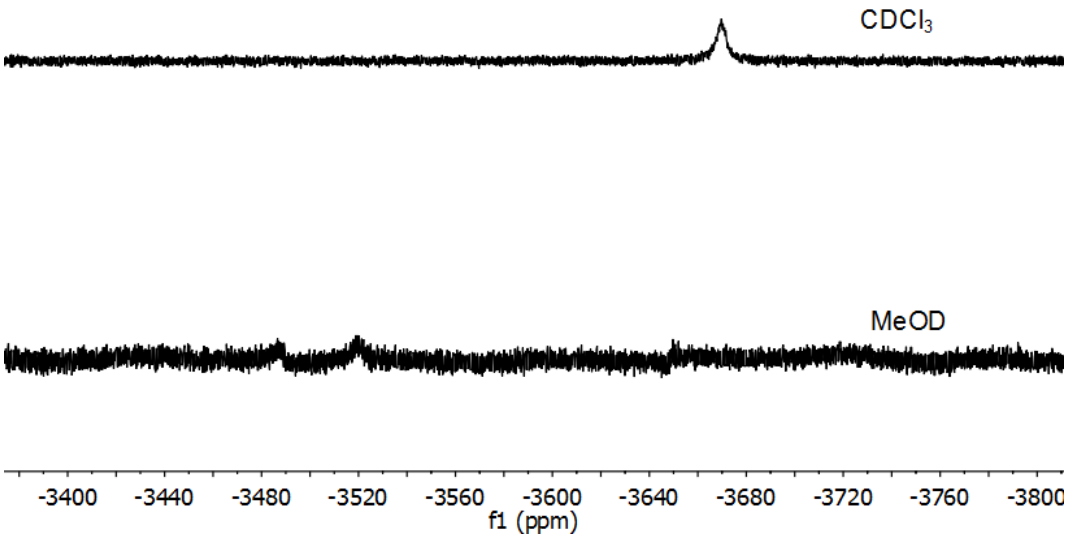

Figure 4.13 ^{195}Pt NMR spectra of complex **LPt-2** in chloroform-*d* and methanol-d_3.

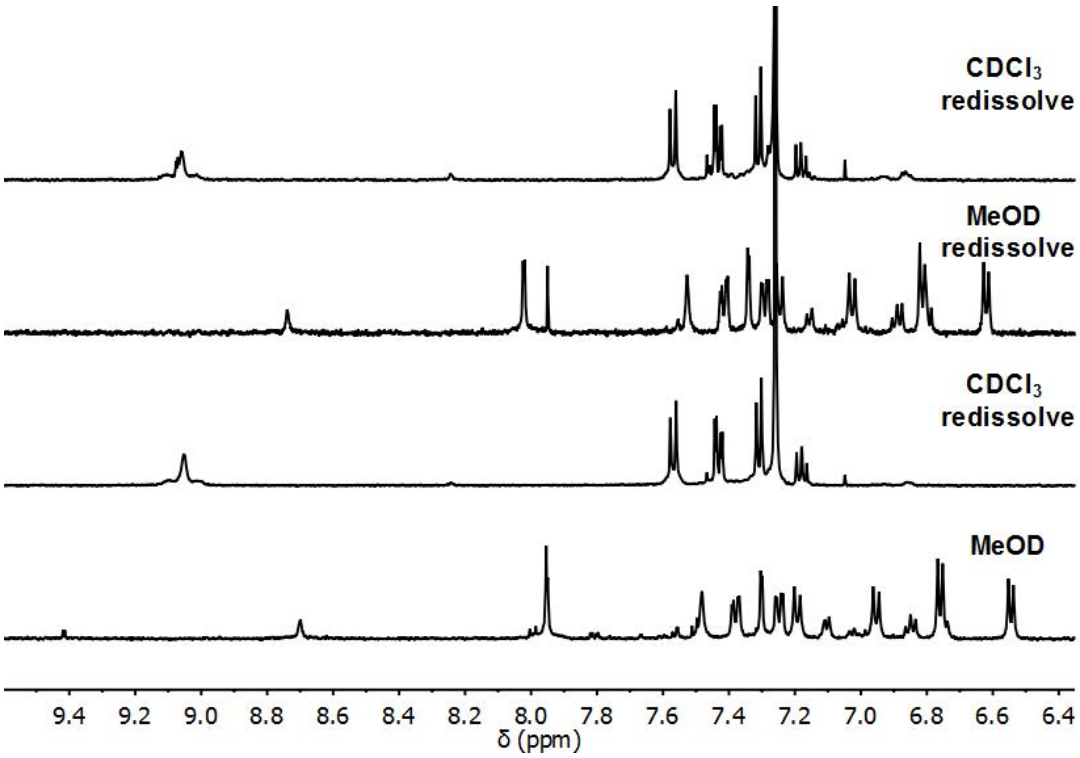

Figure 4.14 Reversible transformation of complex **LPt-2** in methanol-d_4 and in chloroform-*d* at 300 K.

Although the complex in methanol transforms to other species, the transformation is reversible and can be recovered by simply removing methanol. As illustrated in **Figure 4.14**, the complex **LPt-2** firstly shows complicated peaks in methanol. Removing the methanol using a rotary evaporator at ~ 40 °C to yield a solid, which was re-dissolved in chloroform gave an ^{1}H NMR spectrum corresponding to the recovered complex **LPt-2**.

The new species in methanol are probably due to decomposition, transformation, solvent coordination, and complex self-assembly. The reversible transformation shown in **Figure 4.14** excludes the possibility of complex decomposition, otherwise it would not be possible to recover the original complex by simply changing, or removing the solvent. Moreover, the insoluble ligand L (white powder) is not found in MeOH, confirming that the complex **LPt-2** is not fully decomposed to ligand L. It should be expected that alternative modes of self-assembly of the complex components would yield slightly shifted spectra rather than such different spectra. Therefore, it may

be hypothesised that the new species are due to complex transformation and/or solvent coordination.

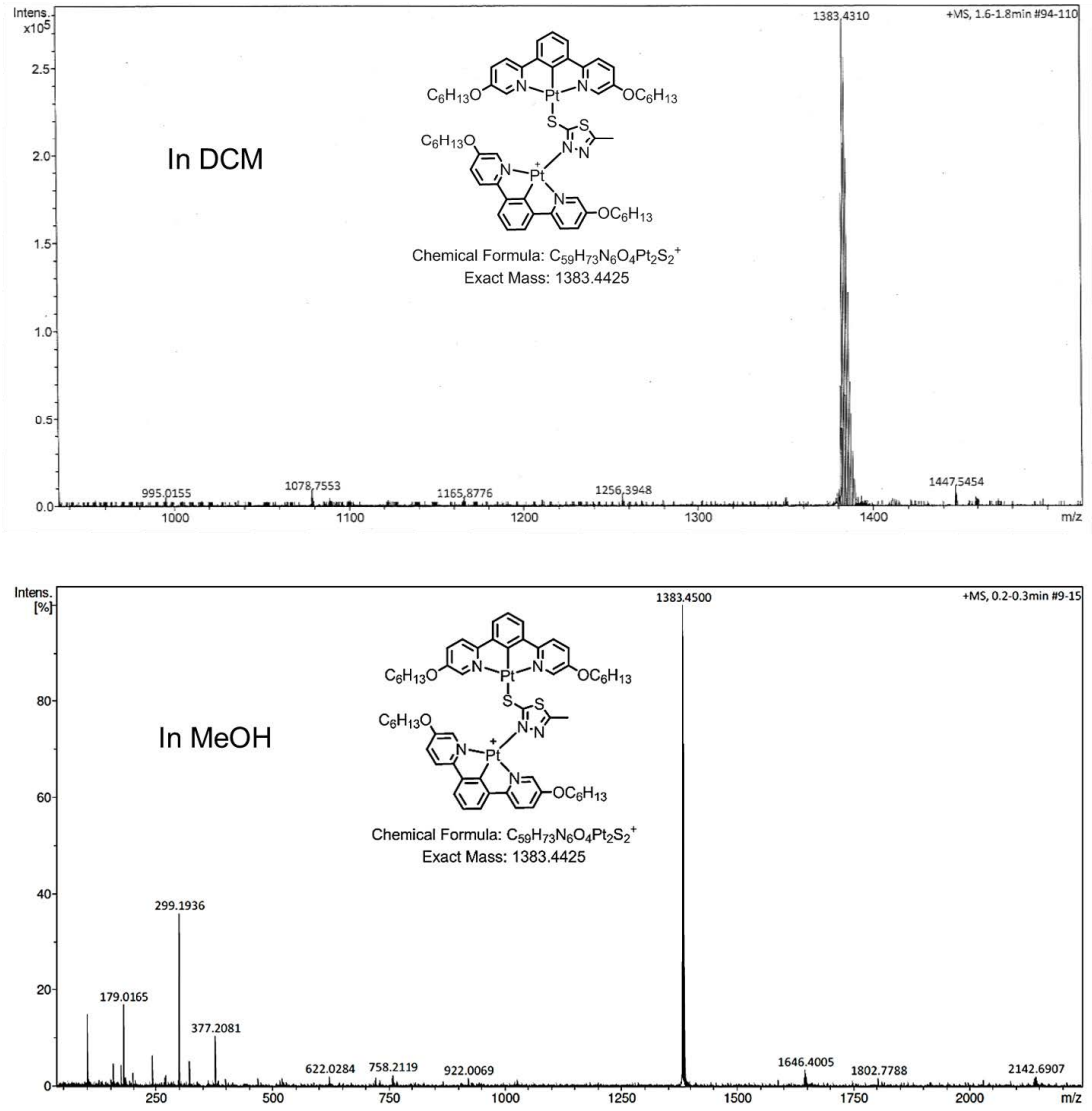

Figure 4.15 MS-ESI of complex **LPt-2** dissolved in DCM (upper) and MeOH (lower), respectively.

Electrospray ionisation mass spectrometry (MS-ESI) was also been performed to figure out what the Pt-complexes are in methanol. Unfortunately, both solutions of complex **LPt-2** in dichloromethane and methanol only showed same peak at ~ 1383.4 *m*/*z*, which corresponds to $\mathbf{[L_2Pt_2\text{-}2]^+}$ cation (**Figure 4.15**). Neither spectrum showed the molecular peak of the complex **LPt-2** or other Pt-complexes. MS-ESI is thus not a good method for this study.

Combining the above NMR and MS spectra, the new Pt-complexes in MeOH are proposed to be the complexes listed in **Figure 4.16**. The complicated ^{1}H NMR spectra in MeOH suggest the solution may be a mixture of the proposed complexes and the complex **LPt-2**.

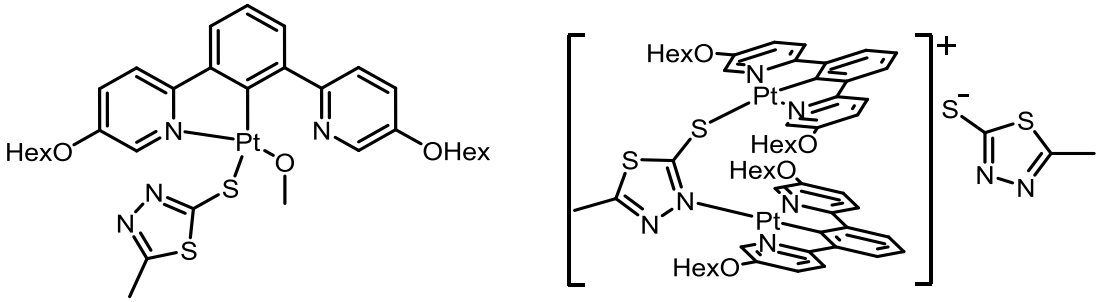

Figure 4.16 Possible complexes in methanol.

4.4 Conclusions

In summary, the complex **LPt-2** has been prepared and employed to investigate the influence of solvent, time, concentration, and temperature on complex assembly and corresponding changes in photochemical properties. The complex emits bright orange light under UV light in the solid state. After being dissolved in different solvents, different colours were observed. ^{1}H and ^{195}Pt NMR spectroscopy suggested that the unique blue/green colour of the solution in methanol is due to the transformation from the complex **LPt-2** to other $Pt^{II}S$-complexes. The transformation is reversible and is accompanied by a visible colour change. The colour of methanol solutions of the complex are also affected by time, concentration and temperature. Metallophilic interactions were found to be preserved in methanol and play a role in affecting the solution colour, which is evidenced by ^{1}H NMR spectra, UV-vis spectra and optical images. Therefore, varying solvent, concentration, and temperature can be effective methods for tuning metallophilic interactions, molecular assembly and corresponding colour.

4.5 References

1 J. Kalinowski, V. Fattori, M. Cocchi and J. A. G. Williams, *Coord. Chem. Rev.*, 2011, **255**, 2401–2425.

2 A. Kobayashi and M. Kato, *Eur. J. Inorg. Chem.*, 2014, **2014**, 4469–4483.

3 O. S. Wenger, *Chem. Rev.*, 2013, **113**, 3686–3733.

4 V. Guerchais and J. L. Fillaut, *Coord. Chem. Rev.*, 2011, **255**, 2448–2457.

5 D. Zhang, L. Z. Wu, L. Zhou, X. Han, Q. Z. Yang, L. P. Zhang and C. H. Tung, *J. Am. Chem. Soc.*, 2004, **126**, 3440–3441.

6 J. J. Zhong, Q. Y. Meng, G. X. Wang, Q. Liu, B. Chen, K. Feng, C. H. Tung and L. Z. Wu, *Chem. Eur. J.*, 2013, **19**, 6443–6450.

7 P. Du, J. Schneider, P. Jarosz and R. Eisenberg, *J. Am. Chem. Soc.*, 2006, **128**, 7726–7727.

8 M. Mauro, A. Aliprandi, D. Septiadi, N. S. Kehr and L. De Cola, *Chem. Soc. Rev.*, 2014, **43**, 4144–4166.

9 E. Baggaley, J. A. Weinstein and J. A. G. Williams, *Coord. Chem. Rev.*, 2012, **256**, 1762–1785.

10 H. L. Au-Yeung, S. Y. L. Leung, A. Y. Y. Tam and V. W. W. Yam, *J. Am. Chem. Soc.*, 2014, **136**, 17910–17913.

11 M. Yoshida and M. Kato, *Coord. Chem. Rev.*, 2018, **355**, 101–115.

12 K. M.-C. Wong and V. W.-W. Yam, *Acc. Chem. Res.*, 2011, **44**, 424–434.

13 V. W.-W. Yam and E. C.-C. Cheng, *Chem. Soc. Rev.*, 2008, **37**, 1806.

14 V. W.-W. Yam, V. K.-M. Au and S. Y.-L. Leung, *Chem. Rev.*, 2015, **115**, 7589–7728.

15 K. Li, G. S. Ming Tong, Q. Wan, G. Cheng, W.-Y. Tong, W.-H. Ang, W.-L. Kwong and C.-M. Che, *Chem. Sci.*, 2016, **7**, 1653–1673.

16 S. D. Cummings, *Coord. Chem. Rev.*, 2009, **253**, 449–478.

17 K. Wang, M. A. Haga, H. Monjushiro, M. Akiba and Y. Sasaki, *Inorg. Chem.*, 2000, **39**, 4022–4028.

18 J. A. G. Williams, A. Beeby, E. S. Davies, J. A. Weinstein and C. Wilson, *Inorg. Chem.*, 2003, **42**, 8609–8611.

19 V. W.-W. Yam, K. M.-C. Wong and N. Zhu, *J. Am. Chem. Soc.*, 2002, **124**, 6506–6507.

20 Z. L. Gong and Y. W. Zhong, *Inorg. Chem.*, 2016, **55**, 10143–10151.

21 B. Jiang, J. Zhang, J. Q. Ma, W. Zheng, L. J. Chen, B. Sun, C. Li, B. W. Hu, H. Tan, X. Li and H. B. Yang, *J. Am. Chem. Soc.*, 2016, **138**, 738–741.

22 K. H.-Y. Chan, H.-S. Chow, K. M.-C. Wong, M. C.-L. Yeung and V. W.-W. Yam, *Chem. Sci.*, 2010, **1**, 477.

23 C. Y. S. Chung and V. W. W. Yam, *Chem. Eur. J.*, 2013, **19**, 13182–13192.

24 S. D. Taylor, W. Howard, N. Kaval, R. Hart, J. a Krause and W. B. Connick, *Chem. Commun.* , 2010, **46**, 1070–1072.

25 Y. Chen, C.-M. Che and W. Lu, *Chem. Commun.*, 2015, **51**, 5371–5374.

26 C. K. Koo, B. Lam, S. K. Leung, M. H. W. Lam and W. Y. Wong, *J. Am. Chem. Soc.*, 2006, **128**, 16434–16435.

27 W. A. Tarran, G. R. Freeman, L. Murphy, A. M. Benham, R. Kataky and J. A. G. Williams, *Inorg. Chem.*, 2014, **53**, 5738–5749.

28 E. G. Hope, W. Levason and N. A. Powell, *Inorg. Chim. Acta*, 1986, **115**, 187-192.

Chapter 5: Overall conclusions

Metallophilic interactions have been widely observed in metal-complexes containing closed shell (d^{10}, s^2) or pseudo-closed shell (d^8) metal centres. In order to incorporate this type of interaction into rational system design, it is crucial to fully understand the nature and strength of metallophilic interactions and exploit their role in influencing molecular assembly and the corresponding properties. However, designing proper systems and utilising them to investigate the origin and strength of metallophilic interactions is very challenging. Solubility, stability, charge, geometry, and steric effects are all factors critical for assessing metallophilicity. This thesis have taken the challenge and aimed to perform a fundamental study of metallophilic interactions by both experimental and computational approaches.

Chapter 1 presents an up-to-date literature review of metallophilic interactions. A huge number of crystal structures that display the presence of metallophilic interactions have been reported. The interactions are purported to contribute significantly to supramolecular assembly, luminescence, catalysis, and so on. A considerable amount of computational work have been reported, which propose that metallophilic interactions are originated from either dispersion or orbital hybridisation. The strength of metallophilic interactions are calculated to be 20–50 kJ mol^{-1}. However, the number of experimental measurements of metallophilic interactions are very limited. The lack of experimental studies encourage me to gain insight into the nature, strength, and contribution of metallophilic interactions in metal-complexes.

Chapter 2 investigates the most widely and earliest studied aurophilic (Au^I–Au^I) interactions. Complexes **1**–**4** have been synthesised and employed to experimentally and computationally study the strength and nature of aurophilic interactions. The strength of binding energies, including aurophilic interactions and aromatic stacking, are experimentally measured by a ligand-exchange approach. The obtained energies are negligible (±2 kJ mol^{-1}) in all solvents examined. The weak strength of aurophilic interactions is confirmed by energy decomposition analysis (EDA). The results of the extended transition state (ETS) method combined with natural orbitals for chemical valence (EDA-NOCV or ETS-NOCV) support the idea that aurophilic interactions

originated from orbital interactions. Electrostatic attraction is found to contribute dominantly, which is also supported by electrostatic potential (ESP) maps and single crystal packing scheme. Further computation studies on several selected literature complexes illustrate consistent results, confirming that aurophilic interactions are weak and contribute little in molecular assembly.

Chapter 3 expands the study of metallophlic interactions to group 10 elements (Pt, Pd, Ni). A series of complexes **LM-X** (L = 1,3-di(5-hexyloxy-2-pyridyl)benzene, M = Pt^{II}, Pd^{II}, Ni^{II}, X = Cl or thiol derivatives) have been synthesised. The weak strength of metallophilic interactions is confirmed by weak binding in solution, as supported by ^{1}H NMR dilution spectra. Varying metal centres and substituents barely change the binding energies, implying metallophilic interactions contribute little to self-assembly of the complexes. Computation of dissociation energies and EDA studies reveal that changing the metals only influence electrostatic attraction and Pauli repulsion, but do not affect the overall interactions, which confirms that contribution from metallophilic interactions to complex assembly is weak. The influence of different substituents to the computed dimerisation energies is also quite small. The energies are poorly correlated to donor-acceptor ability of the substituents, which further confirms that metallophilic interactions are not originated from electrostatic interactions. Instead, the nature of metallophilic interactions is found to be orbital interactions (at least partially) as supported by EDA-NOCV studies.

Chapter 4 employs the complex **LPt-2** synthesised in chapter 3 to investigate the influence of solvent, time, concentration, and temperature to metallophilic interactions and to the aggregation behaviour of the complex. Methanol has been found to trigger reversible transformation of the complex **LPt-2** to other $Pt^{II}S$-complexes, inducing spectroscopic and photophysical change. The aggregation behaviour of the new $Pt^{II}S$-complexes in methanol changes upon varying concentration and temperature, suggesting metallophilic interactions are preserved in methanol and play a role in affecting the colour of the solution. Therefore, varying solvent, concentration, and temperature can be effective methods for tuning metallophilic interactions, molecular assembly and the corresponding colour.

The combined experimental and computational studies of Au^{I}-, Pt^{II}-, Pd^{II}-, Ni^{II}-complexes containing metallophilic interactions in this thesis has demonstrated that the strength of metallophilic interactions in metal-complexes containing aromatic ligands are very weak. The contribution of metallophilic interactions to the assembly of the complexes are negligible. Instead, electrostatic interactions play a dominant role. This thesis supports that the origin of metallophilic interactions is orbital interactions (at least partially). Caution should be exercised in future studies of metallophilic interactions in organometallic complexes to avoid potential overestimation of their energetic significance.

Appendix A (Chapter 2)

A.1 Crystallography

Table A.1 Crystallographic data of complexes **3** and **4**.

Compound	Complex 3 Form I	Complex 3 Form II	Complex 4
Formula	$C_{27}H_{16}Au_2Cl_2F_{10}N_4$	$C_{26}H_{14}Au_2F_{10}N_4$	$C_{37}H_{24}Au_2F_{10}N_4O$
$D_{calc.}$/ g cm^{-3}	2.426	2.571	2.131
μ/mm^{-1}	10.461	11.839	16.336
Formula Weight	1051.27	966.34	1124.53
Colour	colourless	colourless	colourless
Shape	block	plate	plate
Max Size/mm	0.49	0.18	0.14
Mid Size/mm	0.13	0.03	0.07
Min Size/mm	0.09	0.02	0.02
T/K	120.0	120.0	220.0
Crystal System	monoclinic	triclinic	monoclinic
Space Group	$P2_1/c$	P-1	$P2_1/c$
a/Å	9.59464(19)	8.2955(3)	12.15450(10)
b/Å	15.5274(3)	12.4758(3)	13.5983(2)
c/Å	19.3242(3)	12.7327(3)	42.4078(4)
α/°	90	86.4564(18)	90
β/°	91.3370(16)	71.984(2)	90.5490(10)
γ/°	90	85.603(2)	90
V/Å^3	2878.13(10)	1248.45(6)	7008.86(14)
Z	4	2	8
Z'	1	1	2
Θ_{min}/°	3.236	2.968	3.413
Θ_{max}/°	33.140	26.363	76.258
Measured Refl.	86906	39223	110212
Independent Refl.	10945	5103	14580
Reflections Used	9017	4319	12824
R_{int}	0.0725	0.0665	0.0871
Parameters	406	379	978
Restraints	0	72	0
Largest Peak	1.148	1.406	2.790
Deepest Hole	-1.367	-1.085	-1.917
GooF	1.056	1.050	1.176
wR_2 (all data)	0.0549	0.0612	0.1795
wR_2	0.0514	0.0584	0.1752
R_1 (all data)	0.0473	0.0429	0.0775
R_1	0.0339	0.0308	0.0702

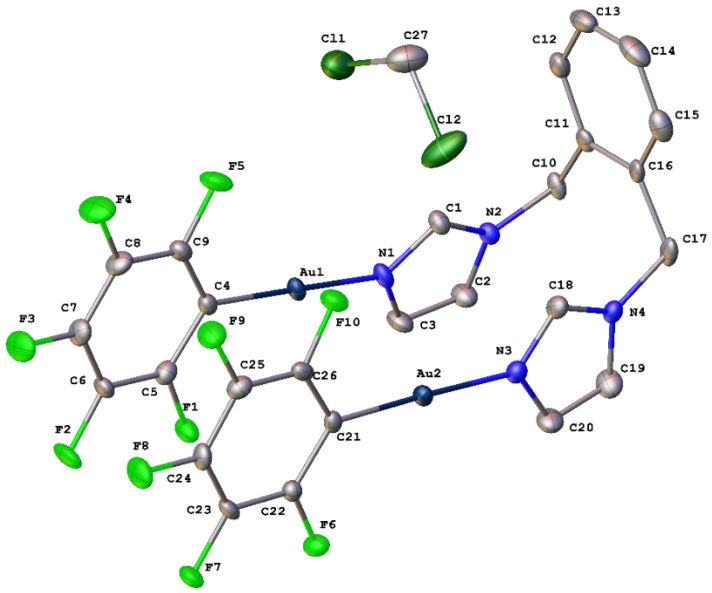

Figure A.1 The asymmetric unit of complex **3** Form I, with displacement ellipsoids at the 50 pc probability level and H atoms omitted.

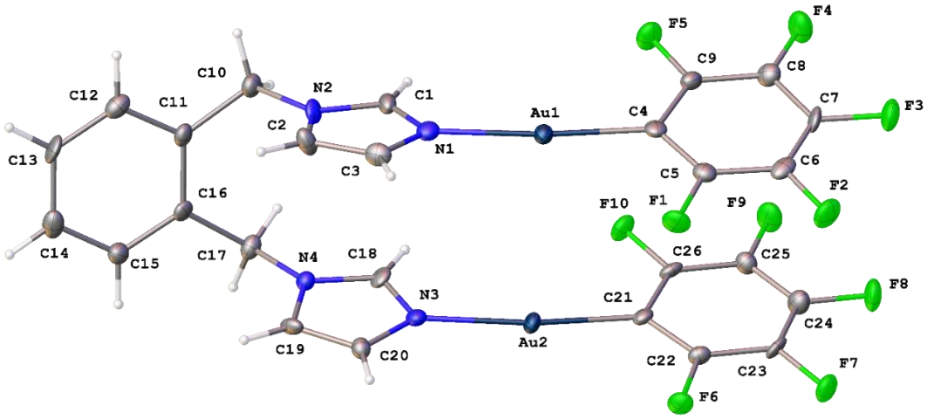

Figure A.2 The asymmetric unit of complex **3** Form II, with displacement ellipsoids at the 50 pc probability level.

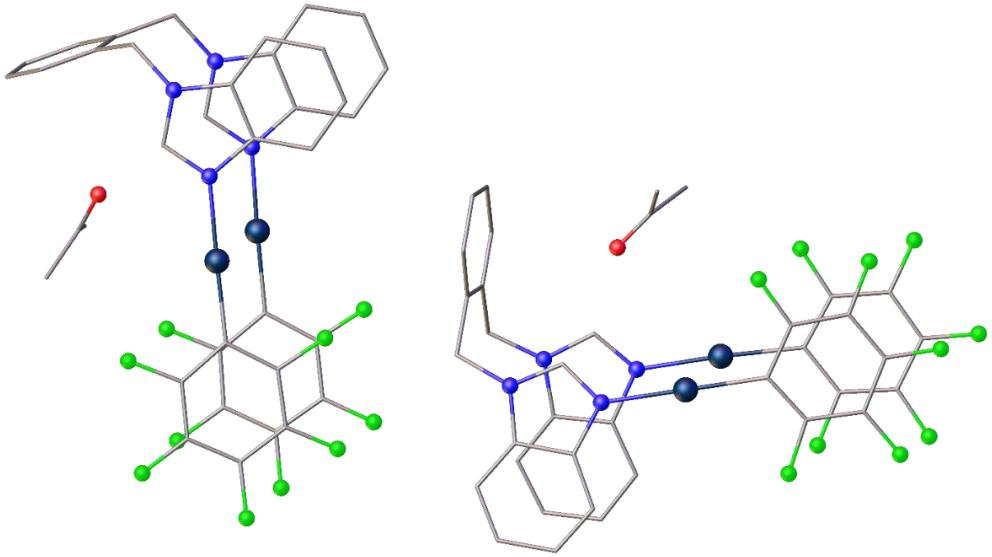

Figure A.3 Asymmetric unit of complex **4** with two independent molecules due to Z' value of 2.

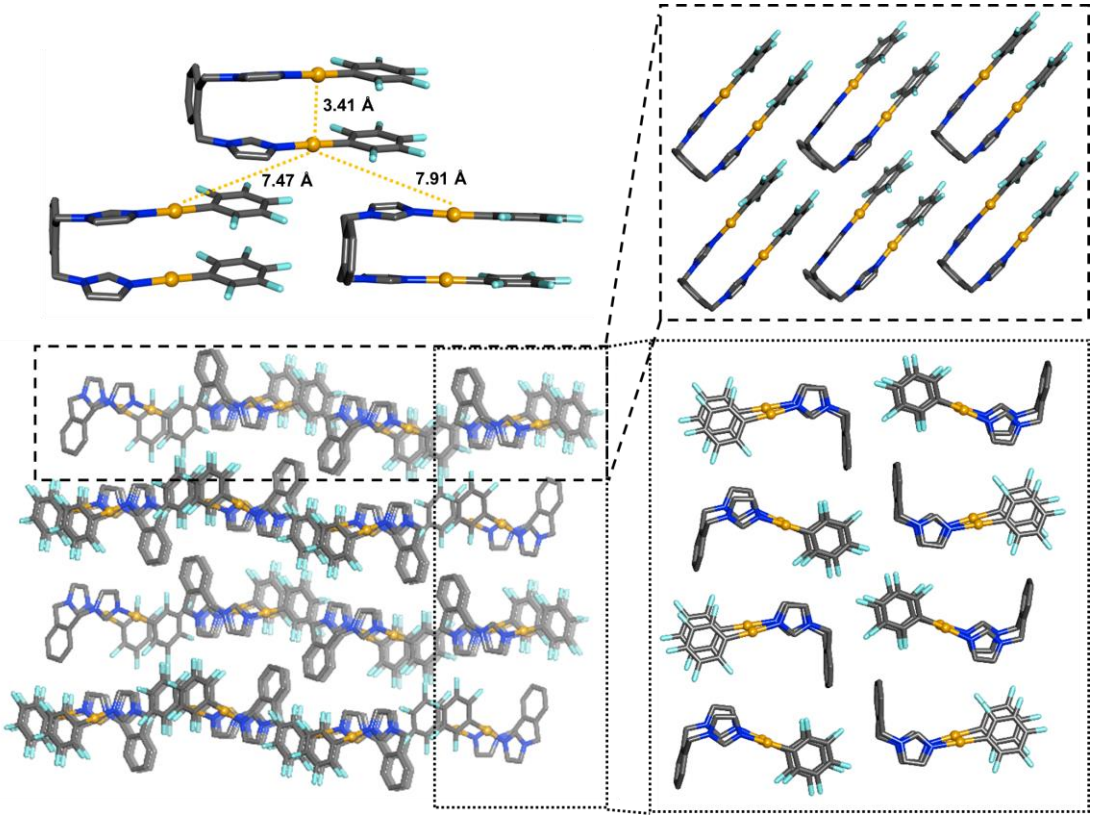

Figure A.4 Crystal packing structures of complex **3** form I.

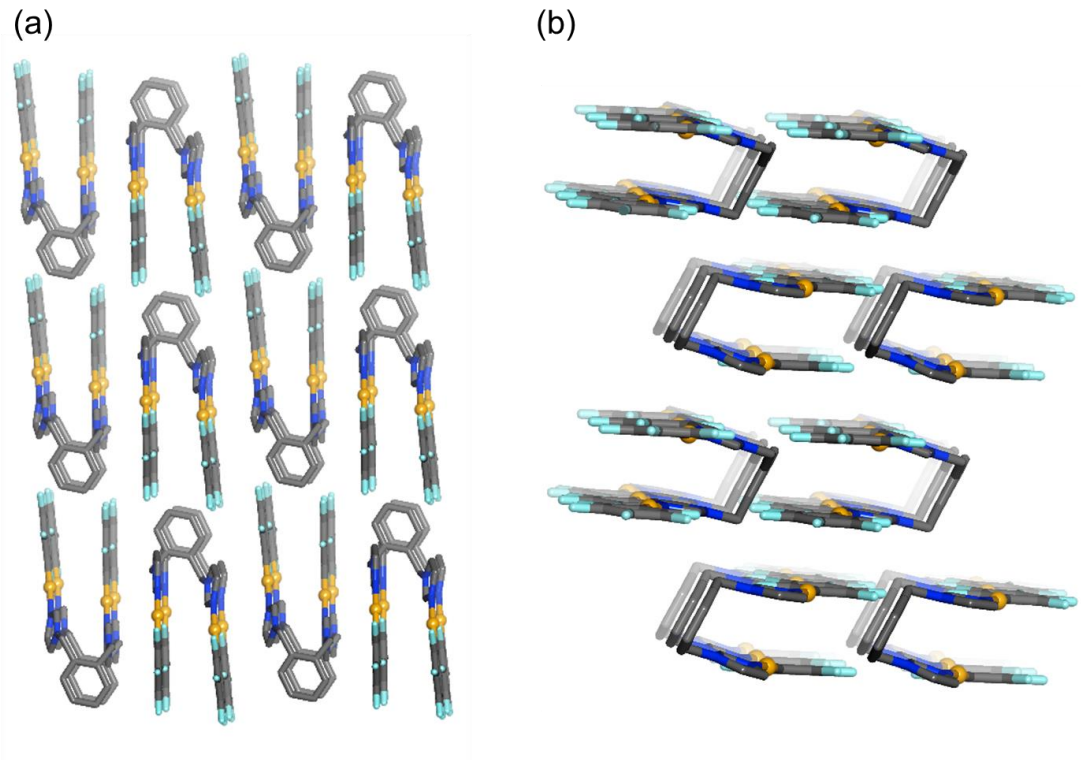

Figure A.5 Crystal packing structures of complex **3** form II along axis *a* (a) and axis *c* (b).

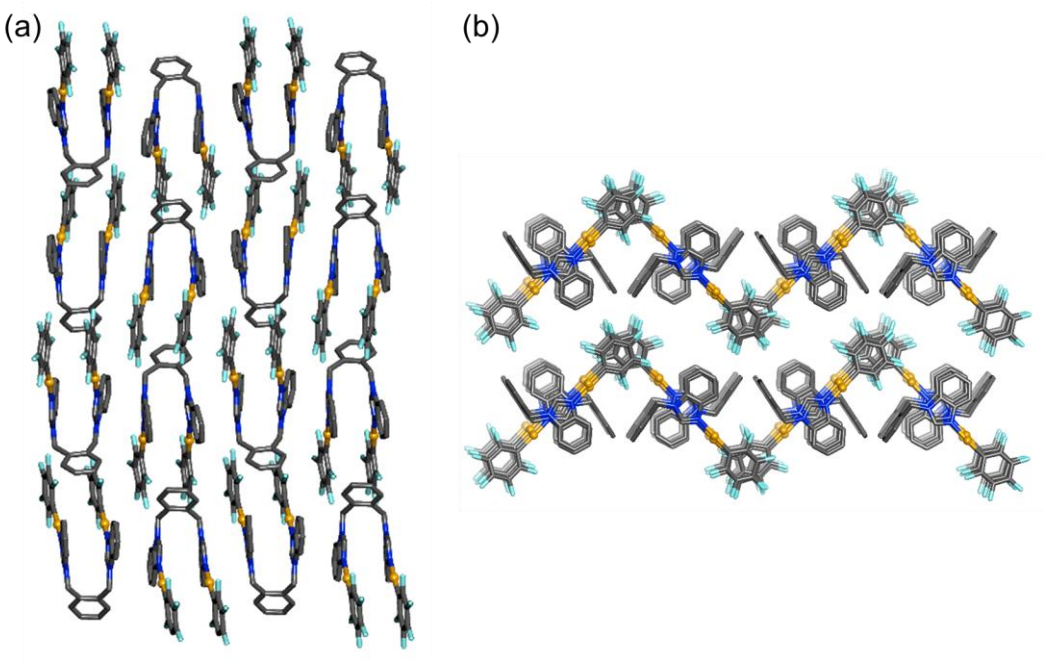

Figure A.6 Crystal packing structures of complex **4** along axis *a* (a) and axis *b* (b).

Table A.2 Selected bond lengths in Å for complex **3** Form I.

Atom	Atom	Length/Å
Au1	N1	2.049(3)
Au1	C4	2.001(3)
Au2	N3	2.043(3)
Au2	C21	1.993(3)
F1	C5	1.362(3)
F2	C6	1.354(4)
F3	C7	1.336(4)
F4	C8	1.344(4)
F5	C9	1.358(4)
F6	C22	1.368(3)
F7	C23	1.357(4)
F8	C24	1.346(4)

Atom	Atom	Length/Å
F9	C25	1.353(3)
F10	C26	1.358(4)
N1	C1	1.337(4)
N1	C3	1.380(4)
N2	C1	1.345(4)
N2	C2	1.368(4)
N2	C10	1.472(4)
N3	C18	1.332(4)
N3	C20	1.377(4)
N4	C17	1.471(4)
N4	C18	1.339(4)
N4	C19	1.364(4)

Table A.3 Selected bond angles in ° for complex **3** From I.

Atom	Atom	Atom	Angle/°
C4	Au1	N1	176.78(12)
C21	Au2	N3	178.23(11)
C1	N1	Au1	126.3(2)
C1	N1	C3	105.7(3)
C3	N1	Au1	127.9(2)
C1	N2	C2	107.8(3)
C1	N2	C10	126.7(3)
C2	N2	C10	125.4(3)
C18	N3	Au2	127.8(2)
C18	N3	C20	105.8(3)
C20	N3	Au2	126.4(2)
C18	N4	C17	127.0(3)

Atom	Atom	Atom	Angle/°
C18	N4	C19	107.2(3)
C19	N4	C17	125.7(3)
N1	C1	N2	110.1(3)
C3	C2	N2	106.7(3)
C2	C3	N1	109.6(3)
C5	C4	Au1	121.0(2)
C9	C4	Au1	125.9(2)
C9	C4	C5	113.1(3)
N2	C10	C11	112.4(3)
N4	C17	C16	113.4(3)
N3	C18	N4	110.9(3)
Cl1	C27	Cl2	112.2(2)

Table A.4 Bond Lengths in Å for complex **3** Form II.

Atom	Atom	Length/Å
Au1	N1	2.046(5)
Au1	C4	1.993(6)
Au2	N3	2.058(5)
Au2	C21	1.993(5)
F1	C5	1.354(7)
F2	C6	1.348(7)
F3	C7	1.349(6)
F4	C8	1.337(7)
F5	C9	1.358(7)
F6	C22	1.363(6)
F7	C23	1.343(6)
F8	C24	1.347(7)

Atom	Atom	Length/Å
F9	C25	1.348(6)
F10	C26	1.354(6)
N1	C1	1.325(7)
N1	C3	1.373(7)
N2	C1	1.341(7)
N2	C2	1.349(8)
N2	C10	1.482(7)
N3	C18	1.323(7)
N3	C20	1.374(7)
N4	C17	1.485(7)
N4	C18	1.343(7)
N4	C19	1.368(7)

Table A.5 Bond Angles in ° for complex **3** Form II.

Atom	Atom	Atom	Angle/°
C4	Au1	N1	175.2(2)
C21	Au2	N3	171.3(2)
C1	N1	Au1	123.2(4)
C1	N1	C3	106.8(5)
C3	N1	Au1	130.1(4)
C1	N2	C2	107.9(5)
C1	N2	C10	125.0(5)
C2	N2	C10	127.0(5)
C18	N3	Au2	118.0(4)
C18	N3	C20	106.0(5)
C20	N3	Au2	136.0(4)
C18	N4	C17	122.8(5)
C18	N4	C19	107.9(5)
C19	N4	C17	128.9(5)
N1	C1	N2	110.3(5)
N2	C2	C3	107.2(5)
C2	C3	N1	107.8(5)
C5	C4	Au1	125.0(4)
C9	C4	Au1	121.0(4)
N2	C10	C11	112.3(5)
N4	C17	C16	113.9(4)
N3	C18	N4	110.8(5)
C20	C19	N4	105.8(5)
C19	C20	N3	109.5(5)
C22	C21	Au2	127.1(4)
C26	C21	Au2	120.1(4)

Table A.6 Bond Lengths in Å for complex **4**.

Atom	Atom	Length/Å
Au1	N1	2.037(10)
Au1	C8	1.975(12)
Au2	N3	2.032(10)
Au2	C29	1.999(12)
F1	C9	1.344(13)
F2	C10	1.361(13)
F3	C11	1.347(13)
F4	C12	1.346(12)
F5	C13	1.360(13)
F6	C30	1.356(16)
F7	C31	1.371(16)
F8	C32	1.351(15)
F9	C33	1.359(15)
F10	C34	1.372(14)
N1	C1	1.304(16)
N1	C2	1.397(16)
N2	C1	1.360(15)
N2	C7	1.374(16)
N2	C14	1.480(14)
N3	C22	1.321(14)
N3	C23	1.409(15)
N4	C21	1.467(14)
N4	C22	1.359(15)
N4	C28	1.397(14)
Au51	N51	2.015(9)
Au51	C58	1.968(10)
Au52	N53	2.036(10)
Au52	C78	1.964(11)
F51	C59	1.370(11)
F52	C60	1.370(13)
F53	C61	1.354(12)
F54	C62	1.341(12)
F55	C63	1.354(13)
F56	C79	1.365(13)
F57	C80	1.355(14)
F58	C81	1.356(14)
F59	C82	1.343(13)
F60	C83	1.349(14)
N51	C51	1.330(14)
N51	C52	1.405(14)
N52	C51	1.342(13)
N52	C57	1.391(13)
N52	C64	1.487(13)
N53	C72	1.325(14)
N53	C73	1.404(15)
N54	C024	1.391(14)
N54	C71	1.467(14)
N54	C72	1.353(15)

Table A.7 Bond Angles in ° for complex **4**.

Atom	Atom	Atom	Angle/°
C8	Au1	N1	179.0(4)
C29	Au2	N3	175.6(4)
C1	N1	Au1	126.9(8)
C1	N1	C2	106.3(10)
C2	N1	Au1	126.8(8)
C1	N2	C7	107.1(10)
C1	N2	C14	128.1(11)
C7	N2	C14	124.8(10)
C22	N3	Au2	130.7(9)
C22	N3	C23	105.6(10)
C23	N3	Au2	123.7(7)
C22	N4	C21	127.2(10)
C22	N4	C28	107.8(9)
C28	N4	C21	125.0(10)
N1	C1	N2	113.3(11)
N1	C2	C7	107.7(10)
C3	C2	N1	132.2(12)
C3	C2	C7	120.2(12)
C4	C3	C2	118.4(14)
C3	C4	C5	121.6(14)
C6	C5	C4	121.6(13)
C5	C6	C7	117.1(13)
N2	C7	C2	105.6(10)
N2	C7	C6	133.3(11)
C6	C7	C2	121.0(12)
C9	C8	Au1	123.3(8)
C13	C8	Au1	123.7(9)
N2	C14	C15	111.2(10)
N4	C21	C20	113.5(9)
N3	C22	N4	112.5(11)
N4	C28	C23	104.9(9)
C30	C29	Au2	124.5(9)
C34	C29	Au2	122.3(9)
C58	Au51	N51	178.4(4)
C78	Au52	N53	176.8(4)

Atom	Atom	Atom	Angle/°
C51	N51	Au51	127.7(7)
C51	N51	C52	104.1(9)
C52	N51	Au51	128.2(7)
C51	N52	C57	107.7(9)
C51	N52	C64	128.1(10)
C57	N52	C64	124.2(9)
C72	N53	Au52	128.5(8)
C72	N53	C73	105.9(10)
C73	N53	Au52	125.6(8)
C024	N54	C71	126.1(10)
C72	N54	C024	107.5(9)
C72	N54	C71	126.3(10)
N54	C024	C73	105.5(10)
C77	C024	N54	133.4(11)
C77	C024	C73	121.1(12)
N51	C51	N52	113.6(9)
N51	C52	C57	109.9(9)
C53	C52	N51	129.1(10)
N52	C57	C52	104.7(9)
C59	C58	Au51	124.5(8)
C63	C58	Au51	123.4(8)
C63	C58	C59	112.1(10)
N52	C64	C65	112.5(9)
N54	C71	C70	111.5(9)
N53	C72	N54	112.5(10)
N53	C73	C024	108.4(10)
C79	C78	Au52	125.0(8)
C83	C78	Au52	123.3(9)
O1	C35	C36	123(2)
O1	C35	C37	118.7(19)
C36	C35	C37	118(2)
O51	C84	C85	120.9(16)
O51	C84	C86	119.1(17)
C85	C84	C86	119.9(16)

A.2 Correlation between experimental ΔΔ*G* and solvent parameters

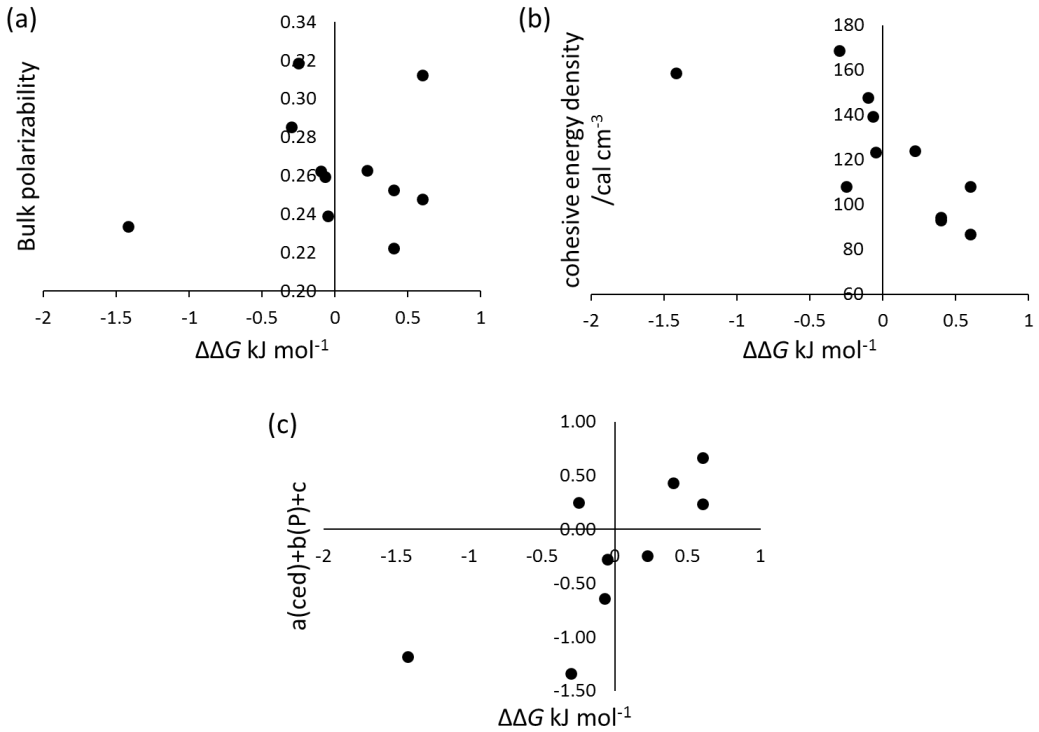

Figure A.7 Correlation between experimental measured [Au(C_6F_5)]–[Au(C_6F_5)] interactions ΔΔ*G* with bulk polarizability (P) (a), cohesive energy density (ced) (b), and model a(ced)+b(P)+c. a, b, and c are constants.

A.3 EDA results of literature examples

Table A.8 Energy decomposition analysis results of complex **5** computed at ZORA/PBE-D3BJ/TZ2P. Energies in kJ mol^{-1}.

	ΔE_{int}	ΔE_{elstat}	ΔE_{disp}	ΔE_{orb}	ΔE_{Pauli}
5a	–303.2	–745.0	–37.0	–349.2	827.9
5b	–296.4	–720.4	–36.01	–346.29	806.4
5ab	–560.6	–1438.1	–56.8	–662.0	1596.2
$[AuCl]_2$	–38.9	–27.3 (35%)	–16.2 (21%)	–33.5 (44%)	38.1

Appendix B (Chapter 3)

B.1 Crystallography

Table B.1 Crystallographic data of complexes **LM-2** (M = Pt, Pd, Ni), **LPt-7** and **LPt-1**.

Compound	**LPt-2**	**LPd-2**	**LNi-2**	**LPt-7**	**LPt-1**
Formula	$C_{63}H_{77}Cl_3N_8O_4Pt_2S_4$	$C_{31}H_{38}N_4O_2PdS_2$	$C_{30}H_{38}N_5NiO_2S_2$	$C_{34}H_{40}N_2O_2PtS$	$C_{28}H_{35}ClN_2O_2Pt$
$D_{calc.}$/ g cm^{-3}	1.673	1.442	1.406	1.616	1.759
μ/mm^{-1}	4.610	0.772	0.837	9.576	5.746
Formula Weight	1635.09	669.17	623.48	735.83	662.12
Colour	dark orange	light yellow	dark yellow	pale orange	yellow
Shape	plate	block	rhombus-shaped plate	needle	block
Size/mm^3	0.59×0.21×0.07	0.25×0.19×0.15	0.28×0.08×0.02	0.35×0.05×0.02	0.35×0.19×0.10
T/K	120.0	270.0	120.0	120.0	120.0
Crystal System	monoclinic	triclinic	triclinic	monoclinic	monoclinic
Space Group	$P2_1/c$	P-1	P-1	$P2_1/c$	$P2_1/c$
a/Å	9.2888(2)	10.2295(3)	10.5339(6)	42.921(4)	8.04770(19)
b/Å	38.0909(9)	11.6920(3)	11.1390(7)	10.1902(5)	30.5593(7)
c/Å	18.4079(3)	13.5235(5)	13.4327(7)	13.9468(6)	10.3792(3)
α/°	90	98.629(3)	104.545(5)	90	90
β/°	94.641(2)	95.968(3)	100.341(5)	97.386(6)	101.565(3)
γ/°	90	103.140(2)	97.871(5)	90	90
V/Å^3	6491.7(2)	1541.19(8)	1473.19(16)	6049.3(7)	2500.76(11)
Z	4	2	2	8	4
Z'	1	1	1	2	1
Wavelength/Å	0.71073	0.71073	0.71073	1.54178	0.71073
Radiation type	Mo Kα	Mo Kα	MoKα	CuKα	MoKα
Θ_{min}/°	2.723	2.828	2.835	4.154	2.830
Θ_{max}/°	26.372	29.735	29.710	76.574	31.225
Measured Refl.	107544	34948	26241	54166	39953
Independent Refl.	13261	7909	7310	12391	7493
Reflections Used	10289	5886	5759	9313	6708
R_{int}	0.0915	0.0680	0.0639	0.1334	0.0518
Parameters	699	364	364	666	309
Restraints	690	1	0	433	0
Largest Peak	3.359	0.710	0.482	5.475	2.554
Deepest Hole	-4.094	-0.622	-0.788	-4.450	-2.946
GooF	1.458	1.046	1.086	1.129	1.260
wR_2 (all data)	0.2128	0.1198	0.1011	0.3882	0.0783
wR_2	0.2082	0.1064	0.0940	0.3713	0.0761
R_1 (all data)	0.1275	0.0710	0.0815	0.1955	0.0518
R_1	0.1072	0.0481	0.0576	0.1664	0.0436

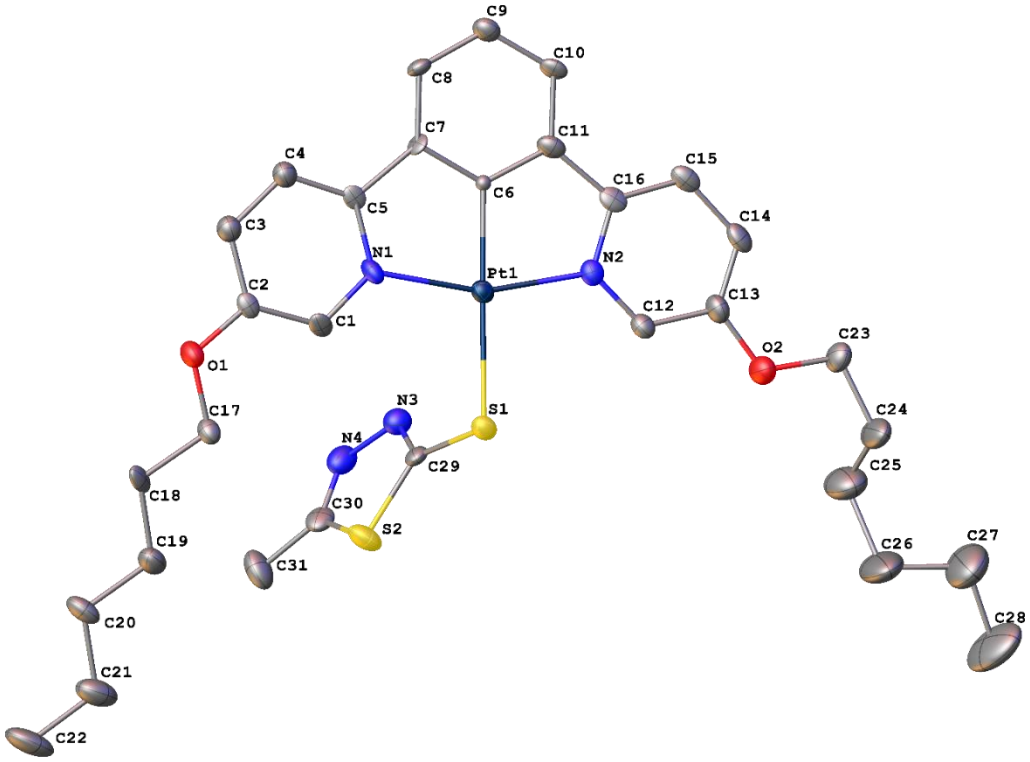

Figure B.1 The structure of one of the two Pt complexes in **LPt-2**. Displacement ellipsoids are at the 50% probability level and H atoms are not shown.

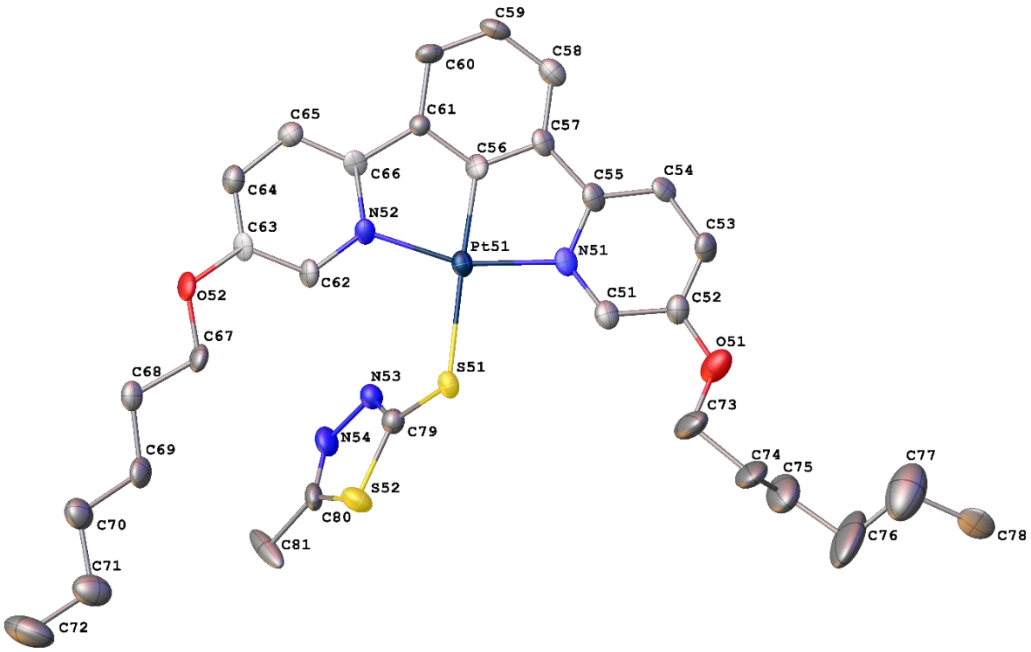

Figure B.2 The structure of the second of the two Pt complexes in **LPt-2**. Displacement ellipsoids are at the 50% probability level; disorder and H atoms are not shown.

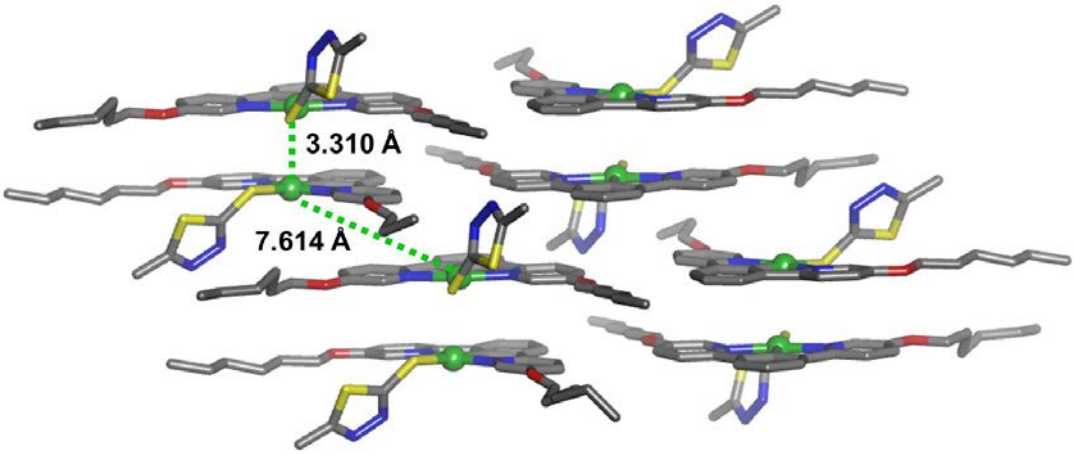

Figure B.3 The crystal-packing structure of the complex **LPt-2**. Hydrogens are omitted for clarity.

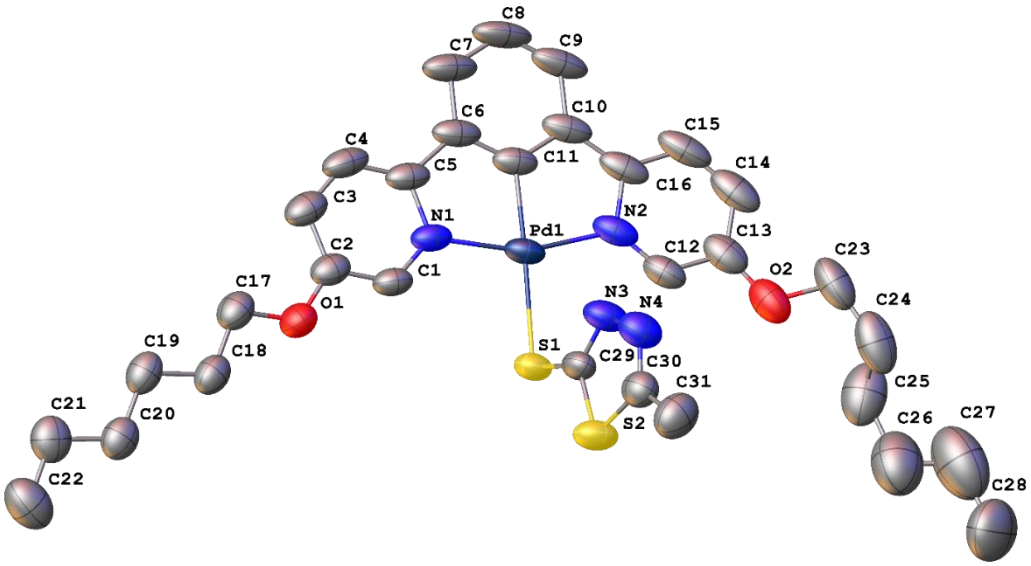

Figure B.4 The asymmetric unit of **LPd-2**. Displacement ellipsoids are at the 50% probability level.

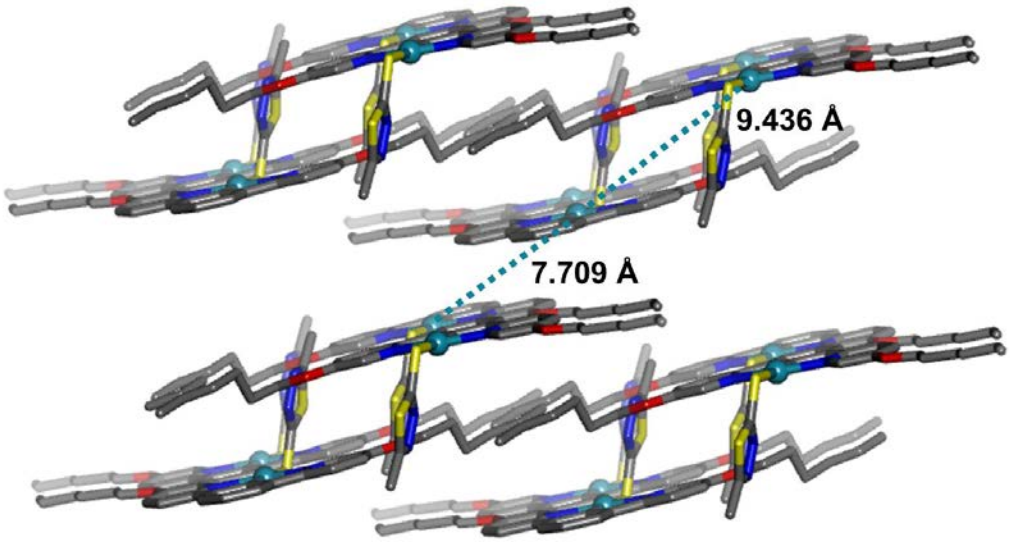

Figure B.5 The crystal-packing structure of the complex **LPd-2**. Hydrogens are omitted for clarity.

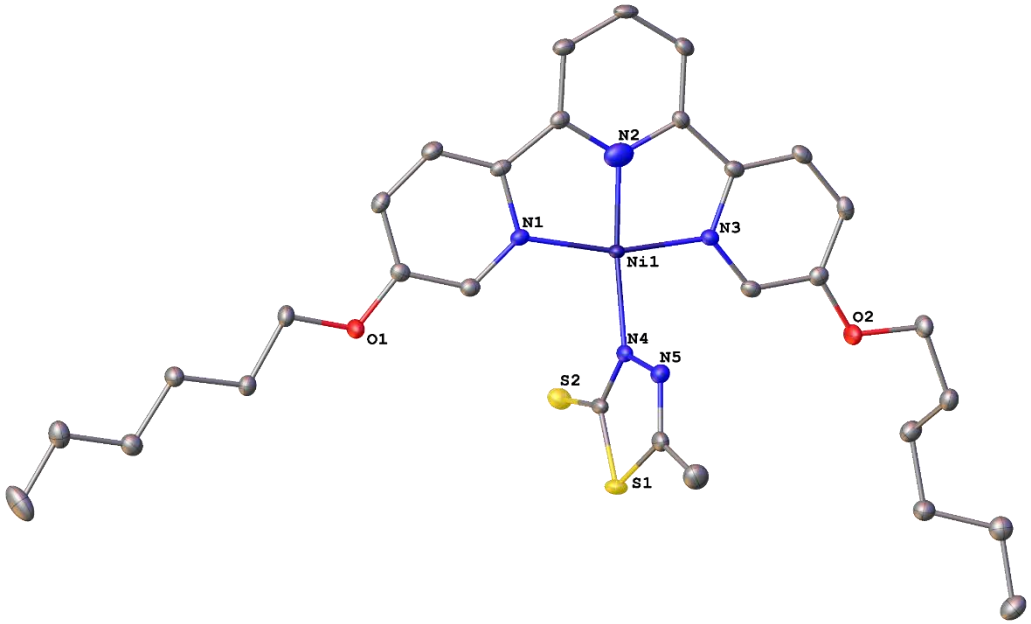

Figure B.6 The asymmetric unit of **LNi-2**. Displacement ellipsoids are at the 50% probability level.

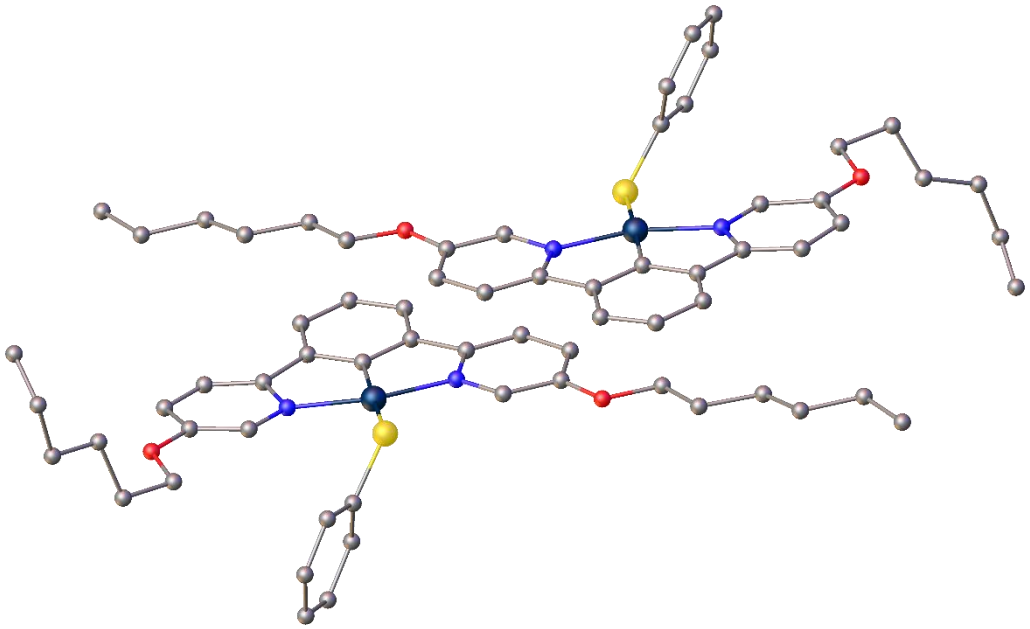

Figure B.7 The asymmetric unit of **LPt-7**, with displacement ellipsoids at the 30% probability level. Disorder and H atoms are not shown.

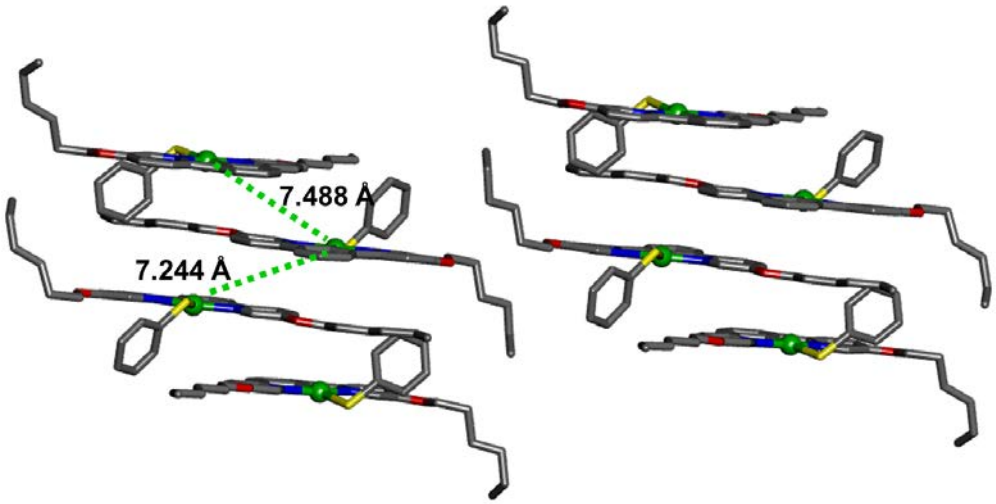

Figure B.8 The crystal-packing structure of the complex **LPt-7**. Hydrogens are omitted for clarity.

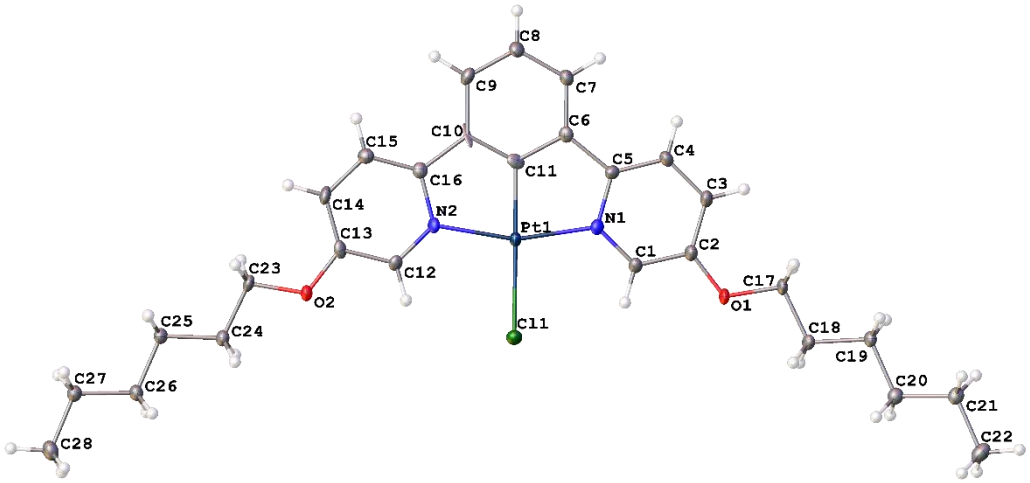

Figure B.9 The molecular structure of **LPt-1**. Displacement ellipsoids are at the 50% probability level.

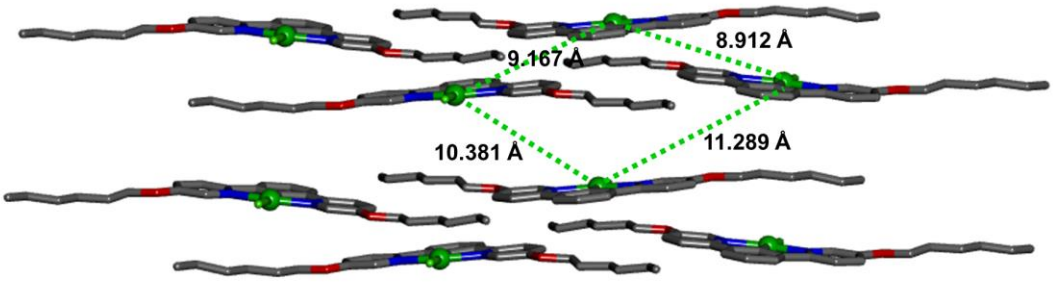

Figure B.10 The crystal-packing structure of the complex **LPt-1**. Hydrogens are omitted for clarity.

Table B.2 Bond Lengths in Å for **LPt-2**.

Atom	Atom	Length/Å
Pt1	S1	2.429(4)
Pt1	N1	2.054(12)
Pt1	N2	2.031(12)
Pt1	C6	1.938(13)
S1	C29	1.741(16)
S2	C29	1.740(16)
S2	C30	1.735(18)
O1	C2	1.358(18)
O1	C17	1.434(18)
O2	C13	1.37(2)
O2	C23	1.430(19)
N1	C1	1.353(19)
N1	C5	1.37(2)
N2	C12	1.34(2)
N2	C16	1.36(2)
N3	N4	1.401(19)
N3	C29	1.31(2)
N4	C30	1.28(2)
C1	C2	1.39(2)
C2	C3	1.41(2)
C3	C4	1.42(2)
C4	C5	1.35(2)
C5	C7	1.49(2)
C6	C7	1.400(18)
C6	C11	1.39(2)
C7	C8	1.38(2)
C8	C9	1.40(2)
C9	C10	1.42(2)
C10	C11	1.40(2)
C11	C16	1.47(2)
C12	C13	1.40(2)
C13	C14	1.33(2)
C14	C15	1.45(2)
C15	C16	1.38(2)
C17	C18	1.531(14)
C18	C19	1.516(15)
C19	C20	1.545(14)
C20	C21	1.526(15)
C21	C22	1.528(16)
C23	C24	1.52(3)
C24	C25	1.35(3)
C25	C26	1.64(4)
C26	C27	1.55(4)
C27	C28	1.56(4)
C30	C31	1.50(2)
Pt51	S51	2.424(4)
Pt51	N51	2.042(13)
Pt51	N52	2.014(13)
Pt51	C56	1.938(16)
S51	C79	1.721(16)
S52	C79	1.740(17)
S52	C80	1.715(19)
O51	C52	1.35(2)
O51	C73A	1.303(13)
O51	C73	1.334(14)
O52	C63	1.359(18)
O52	C67	1.43(2)
N51	C51	1.32(2)
N51	C55	1.39(2)
N52	C62	1.369(19)
N52	C66	1.36(2)
N53	N54	1.408(18)
N53	C79	1.32(2)
N54	C80	1.32(2)
C51	C52	1.40(2)
C52	C53	1.35(2)
C53	C54	1.41(2)
C54	C55	1.39(2)
C55	C57	1.47(2)
C56	C57	1.39(2)
C56	C61	1.39(2)
C57	C58	1.39(2)
C58	C59	1.41(2)
C59	C60	1.38(2)
C60	C61	1.42(2)
C61	C66	1.47(2)
C62	C63	1.40(2)
C63	C64	1.34(2)
C64	C65	1.43(2)
C65	C66	1.40(2)
C67	C68	1.52(2)
C68	C69	1.51(2)
C69	C70	1.53(3)
C70	C71	1.53(3)
C71	C72	1.52(3)
C73A	C74A	1.6128
C73	C74	1.5484
C74	C75	1.5308
C75	C76	1.5856
C76	C77	1.5423
C77	C78	1.5095
C74A	C75A	1.5535
C75A	C76A	2.0209
C76A	C77A	1.5177
C77A	C78A	1.5549
C80	C81	1.50(2)
Cl91	C91	1.722(16)
Cl92	C91	1.713(16)
Cl93	C91	1.739(17)

Table B.3 Bond angles in ° for **LPt-2**.

Atom	Atom	Atom	Angle/°
N1	Pt1	S1	100.6(4)
N2	Pt1	S1	99.1(4)
N2	Pt1	N1	160.3(5)
C6	Pt1	S1	179.1(4)
C6	Pt1	N1	80.1(5)
C6	Pt1	N2	80.2(5)
C29	S1	Pt1	106.4(5)
C30	S2	C29	86.9(8)
C2	O1	C17	114.9(11)
C13	O2	C23	117.9(13)
C1	N1	Pt1	125.0(11)
C1	N1	C5	120.1(13)
C5	N1	Pt1	114.8(9)
C12	N2	Pt1	124.8(11)
C12	N2	C16	119.5(12)
C16	N2	Pt1	115.6(11)
C29	N3	N4	112.7(14)
C30	N4	N3	112.2(14)
N1	C1	C2	120.4(15)
O1	C2	C1	125.3(14)
O1	C2	C3	114.8(14)
C1	C2	C3	119.9(14)
C2	C3	C4	118.0(15)
C5	C4	C3	119.3(16)
N1	C5	C7	114.4(12)
C4	C5	N1	122.3(14)
C4	C5	C7	123.2(14)
C7	C6	Pt1	119.2(10)
C11	C6	Pt1	117.6(10)
C11	C6	C7	123.1(13)
C6	C7	C5	111.4(13)
C8	C7	C5	129.7(13)
C8	C7	C6	118.9(13)
C7	C8	C9	119.0(14)
C8	C9	C10	122.1(15)
C11	C10	C9	118.4(14)
C6	C11	C10	118.4(14)
C6	C11	C16	113.1(13)
C10	C11	C16	128.5(14)
N2	C12	C13	121.9(15)
O2	C13	C12	114.6(15)
C14	C13	O2	125.3(15)
C14	C13	C12	120.1(16)
C13	C14	C15	119.0(14)
C16	C15	C14	118.1(15)
N2	C16	C11	113.4(13)
N2	C16	C15	121.4(15)
C15	C16	C11	125.2(15)
O1	C17	C18	108.8(11)
C19	C18	C17	111.8(11)
C18	C19	C20	112.2(12)
C21	C20	C19	112.0(12)
C20	C21	C22	112.9(14)
O2	C23	C24	106.9(15)
C25	C24	C23	117(2)
C24	C25	C26	111(3)
C27	C26	C25	110(2)
C26	C27	C28	109(3)
S2	C29	S1	119.9(9)
N3	C29	S1	126.8(12)
N3	C29	S2	113.2(12)
N4	C30	S2	115.0(13)
N4	C30	C31	123.9(17)
C31	C30	S2	121.1(15)
N51	Pt51	S51	97.7(4)
N52	Pt51	S51	101.9(4)
N52	Pt51	N51	160.3(5)
C56	Pt51	S51	176.6(5)
C56	Pt51	N51	80.2(6)
C56	Pt51	N52	80.2(6)
C79	S51	Pt51	111.7(6)
C80	S52	C79	89.0(8)
C73A	O51	C52	127.9(13)
C73	O51	C52	122.8(12)
C63	O52	C67	115.4(12)
C51	N51	Pt51	126.2(11)
C51	N51	C55	119.3(14)
C55	N51	Pt51	114.4(11)
C62	N52	Pt51	124.7(11)
C66	N52	Pt51	116.4(10)
C66	N52	C62	118.9(13)
C79	N53	N54	112.2(14)
C80	N54	N53	113.1(14)
N51	C51	C52	122.8(16)
O51	C52	C51	119.1(16)
O51	C52	C53	121.9(15)
C53	C52	C51	119.0(16)
C52	C53	C54	120.1(15)
C55	C54	C53	118.8(15)
N51	C55	C54	120.1(15)
N51	C55	C57	114.2(13)
C54	C55	C57	125.7(15)
C57	C56	Pt51	119.2(12)
C61	C56	Pt51	117.5(11)
C61	C56	C57	123.3(15)
C56	C57	C55	111.9(15)
C58	C57	C55	130.0(15)
C58	C57	C56	118.0(16)
C57	C58	C59	119.6(15)
C60	C59	C58	122.5(15)
C59	C60	C61	118.2(15)
C56	C61	C60	118.4(14)
C56	C61	C66	113.1(14)
C60	C61	C66	128.4(14)
N52	C62	C63	121.0(15)
O52	C63	C62	122.7(15)
C64	C63	O52	116.9(14)
C64	C63	C62	120.4(15)

Atom	Atom	Atom	Angle/°
C63	C64	C65	120.3(15)
C66	C65	C64	117.0(15)
N52	C66	C61	112.7(13)
N52	C66	C65	122.4(14)
C65	C66	C61	124.8(15)
O52	C67	C68	109.9(13)
C69	C68	C67	112.6(14)
C68	C69	C70	115.5(15)
C69	C70	C71	113.6(17)
C72	C71	C70	113(2)
O51	C73A	C74A	119.8(6)
O51	C73	C74	107.9(6)
C75	C74	C73	110.2
C74	C75	C76	108.9
C77	C76	C75	107.4
C78	C77	C76	113.8
C75A	C74A	C73A	103.1
C74A	C75A	C76A	98.5
C77A	C76A	C75A	95.7
C76A	C77A	C78A	111.2
S51	C79	S52	119.5(10)
N53	C79	S51	127.9(13)
N53	C79	S52	112.5(12)
N54	C80	S52	113.1(12)
N54	C80	C81	118.2(19)
C81	C80	S52	128.7(18)
Cl91	C91	Cl93	111.3(14)
Cl92	C91	Cl91	110.9(13)
Cl92	C91	Cl93	102.9(14)

Table B.4 Bond Lengths in Å for **LPd-2**.

Atom	Atom	Length/Å
Pd1	S1	2.4505(8)
Pd1	N1	2.054(3)
Pd1	N2	2.058(3)
Pd1	C11	1.931(3)
S1	C29	1.727(3)
S2	C29	1.738(3)
S2	C30	1.726(4)
O1	C2	1.359(4)
O1	C17	1.433(4)
O2	C13	1.350(5)
O2	C23	1.438(5)
N1	C1	1.338(4)
N1	C5	1.384(4)
N2	C12	1.338(5)
N2	C16	1.383(4)
N3	N4	1.383(4)
N3	C29	1.294(4)
N4	C30	1.273(5)
C1	C2	1.374(5)
C2	C3	1.386(5)
C3	C4	1.374(6)
C4	C5	1.375(6)
C5	C6	1.469(5)
C6	C7	1.402(4)
C6	C11	1.378(5)
C7	C8	1.396(7)
C8	C9	1.364(7)
C9	C10	1.403(5)
C10	C11	1.384(5)
C10	C16	1.453(6)
C12	C13	1.394(5)
C13	C14	1.386(6)
C14	C15	1.372(7)
C15	C16	1.386(6)
C17	C18	1.495(5)
C18	C19	1.518(5)
C19	C20	1.515(5)
C20	C21	1.501(5)
C21	C22	1.494(6)
C23	C24	1.517(7)
C24	C25	1.465(7)
C25	C26	1.649(10)
C26	C27	1.364(9)
C27	C28	1.587(11)
C30	C31	1.478(5)

Table B.5 Bond Angles in ° for **LPd-2**.

Atom	Atom	Atom	Angle/°
N1	Pd1	S1	98.93(7)
N1	Pd1	N2	159.96(11)
N2	Pd1	S1	101.10(8)
C11	Pd1	S1	176.53(9)
C11	Pd1	N1	79.98(14)
C11	Pd1	N2	80.02(15)
C29	S1	Pd1	99.18(10)
C30	S2	C29	88.06(17)
C2	O1	C17	119.0(3)
C13	O2	C23	117.5(4)
C1	N1	Pd1	126.3(2)
C1	N1	C5	118.5(3)
C5	N1	Pd1	115.2(2)
C12	N2	Pd1	125.7(2)
C12	N2	C16	120.1(3)
C16	N2	Pd1	114.2(3)
C29	N3	N4	113.6(3)
C30	N4	N3	113.5(3)
N1	C1	C2	123.2(3)
O1	C2	C1	114.8(3)
O1	C2	C3	126.5(4)
C1	C2	C3	118.7(4)
C4	C3	C2	118.7(4)
C3	C4	C5	121.1(3)
N1	C5	C6	112.0(3)
C4	C5	N1	119.8(3)
C4	C5	C6	128.2(3)
C7	C6	C5	127.2(4)
C11	C6	C5	114.6(3)
C11	C6	C7	118.2(4)
C8	C7	C6	118.5(4)
C9	C8	C7	122.6(4)

Atom	Atom	Atom	Angle/°
C8	C9	C10	119.4(4)
C9	C10	C16	128.3(4)
C11	C10	C9	117.8(4)
C11	C10	C16	113.9(3)
C6	C11	Pd1	118.2(3)
C6	C11	C10	123.5(3)
C10	C11	Pd1	118.3(3)
N2	C12	C13	122.6(3)
O2	C13	C12	115.4(3)
O2	C13	C14	126.4(4)
C14	C13	C12	118.2(4)
C15	C14	C13	118.8(4)
C14	C15	C16	122.3(4)
N2	C16	C10	113.6(3)
N2	C16	C15	118.1(4)
C15	C16	C10	128.3(3)
O1	C17	C18	107.0(3)
C17	C18	C19	113.4(3)
C20	C19	C18	113.0(3)
C21	C20	C19	114.4(3)
C22	C21	C20	113.8(4)
O2	C23	C24	107.2(4)
C25	C24	C23	113.6(4)
C24	C25	C26	114.3(5)
C27	C26	C25	111.7(8)
C26	C27	C28	111.2(8)
S1	C29	S2	121.54(18)
N3	C29	S1	126.7(2)
N3	C29	S2	111.8(3)
N4	C30	S2	113.1(3)
N4	C30	C31	123.0(4)
C31	C30	S2	123.9(3)

Table B.6 Bond Lengths in Å for **LNi-2**.

Atom	Atom	Length/Å
Ni1	N1	1.938(2)
Ni1	N4	1.959(2)
Ni1	N3	1.919(2)
Ni1	N2	1.827(3)
S2	C29	1.687(3)
S1	C28	1.738(3)
S1	C29	1.757(3)
O2	C22	1.440(3)
O2	C14	1.359(3)
O1	C2	1.364(3)
O1	C16	1.440(3)
N1	C5	1.381(3)
N1	C1	1.338(3)
N4	N5	1.384(3)
N4	C29	1.330(4)
N5	C28	1.293(3)
N3	C11	1.374(3)
N3	C15	1.332(3)
N2	C10	1.390(4)
N2	C6	1.391(4)
C12	C13	1.391(4)
C12	C11	1.386(4)
C10	C11	1.464(4)
C10	C9	1.395(4)
C5	C4	1.376(4)
C5	C6	1.460(4)
C28	C30	1.484(4)
C2	C1	1.389(4)
C2	C3	1.391(4)
C13	C14	1.381(4)
C17	C16	1.509(4)
C17	C18	1.530(4)
C19	C18	1.524(4)
C19	C20	1.524(4)
C4	C3	1.385(4)
C7	C6	1.395(4)
C7	C8	1.391(4)
C25	C26	1.520(4)
C25	C24	1.524(4)
C22	C23	1.515(4)
C23	C24	1.525(4)
C26	C27	1.524(4)
C9	C8	1.396(4)
C14	C15	1.395(4)
C20	C21	1.522(4)

Table B.7 Bond Angles in ° for **LNi-2**.

Atom	Atom	Atom	Angle/°
N1	Ni1	N4	99.51(9)
N3	Ni1	N1	163.66(9)
N3	Ni1	N4	96.73(9)
N2	Ni1	N1	82.51(11)
N2	Ni1	N4	167.33(11)
N2	Ni1	N3	82.02(11)
C28	S1	C29	89.09(14)
C14	O2	C22	118.1(2)
C2	O1	C16	116.4(2)
C5	N1	Ni1	115.17(17)
C1	N1	Ni1	126.07(18)
C1	N1	C5	118.6(2)
N5	N4	Ni1	115.87(17)
C29	N4	Ni1	129.0(2)
C29	N4	N5	115.1(2)
C28	N5	N4	112.9(2)
C11	N3	Ni1	116.22(17)
C15	N3	Ni1	124.58(19)
C15	N3	C11	119.2(2)
C10	N2	Ni1	119.20(19)
C10	N2	C6	121.9(2)
C6	N2	Ni1	118.6(2)
C11	C12	C13	120.5(3)
N2	C10	C11	110.7(2)
N2	C10	C9	119.2(2)
C9	C10	C11	130.1(2)
N1	C5	C6	111.8(2)
C4	C5	N1	120.6(2)
C4	C5	C6	127.6(2)
N5	C28	S1	113.2(2)
N5	C28	C30	123.3(3)
C30	C28	S1	123.5(2)
O1	C2	C1	115.9(2)
O1	C2	C3	125.0(2)
C1	C2	C3	119.1(2)
C14	C13	C12	118.3(2)
C16	C17	C18	111.0(2)
C18	C19	C20	112.6(2)
C5	C4	C3	120.8(2)
C8	C7	C6	119.2(2)
N1	C1	C2	122.6(2)
C4	C3	C2	118.2(2)
O1	C16	C17	108.0(2)
C26	C25	C24	113.7(2)
S2	C29	S1	124.14(17)
N4	C29	S2	126.2(2)
N4	C29	S1	109.6(2)
O2	C22	C23	106.2(2)
N3	C11	C12	120.3(2)
N3	C11	C10	111.5(2)
C12	C11	C10	128.2(3)
C22	C23	C24	113.8(2)
C25	C26	C27	113.0(2)
C25	C24	C23	112.9(2)
N2	C6	C5	111.5(2)
N2	C6	C7	119.1(3)
C7	C6	C5	129.5(2)
C10	C9	C8	118.9(2)
O2	C14	C13	126.3(2)
O2	C14	C15	114.4(2)
C13	C14	C15	119.3(2)
C7	C8	C9	121.7(3)
C19	C18	C17	113.6(2)
N3	C15	C14	122.3(3)
C21	C20	C19	113.5(3)

Table B.8 Bond Lengths in Å for **LPt-7**.

Atom	Atom	Length/Å
Pt1	S1	2.402(7)
Pt1	N1	2.00(2)
Pt1	N2	2.00(2)
Pt1	C11	1.963(12)
S1	C29	1.77(3)
O1	C2	1.35(3)
O1	C17	1.46(4)
O2	C15	1.39(4)
O2	C23	1.42(4)
N1	C1	1.38(4)
N1	C5	1.35(3)
N2	C12	1.42(3)
N2	C16	1.34(4)
C1	C2	1.42(4)
C2	C3	1.38(4)
C3	C4	1.42(4)
C4	C5	1.37(4)
C5	C6	1.52(3)
C6	C11	1.3900
C6	C7	1.3900
C11	C10	1.3900
C10	C9	1.3900
C10	C12	1.52(3)
C9	C8	1.3900
C8	C7	1.3900
C12	C13	1.38(4)
C13	C14	1.35(4)
C14	C15	1.45(4)
C15	C16	1.37(4)
C17	C18	1.54(4)
C18	C19	1.53(4)
C19	C20	1.56(4)
C20	C21	1.52(5)
C21	C22	1.54(4)
C23	C24	1.48(5)
C24	C25	1.61(5)
C25	C26	1.43(5)
C26	C27	1.52(7)
C27	C28	1.52(7)
C29	C30	1.39(4)
C29	C34	1.40(4)
C30	C31	1.46(4)
C31	C32	1.40(4)
C32	C33	1.37(4)
C33	C34	1.39(4)
Pt51	S51	2.412(6)
Pt51	N51	1.964(19)
Pt51	N52	1.99(2)
Pt51	C61	1.86(2)
S51	C79	1.77(3)
O51	C52	1.34(3)
O51	C67	1.41(3)
O52	C65	1.32(4)
O52	C73	1.45(4)
N51	C51	1.39(3)
N51	C55	1.39(3)
N52	C62	1.45(4)
N52	C66	1.33(4)
C51	C52	1.40(4)
C52	C53	1.38(4)
C53	C54	1.40(4)
C54	C55	1.37(4)
C55	C56	1.46(4)
C56	C57	1.43(4)
C56	C61	1.40(4)
C57	C58	1.40(5)
C58	C59	1.37(4)
C59	C60	1.34(4)
C60	C61	1.42(3)
C60	C62	1.45(4)
C62	C63	1.38(4)
C63	C64	1.41(5)
C64	C65	1.41(4)
C65	C66	1.44(4)
C67	C68	1.50(4)
C68	C69	1.53(4)
C69	C70	1.51(4)
C70	C71	1.53(4)
C71	C72	1.53(4)
C73	C74	1.51(5)
C74	C75	1.50(3)
C74	C75A	1.49(3)
C75	C76	1.49(3)
C76	C77	1.49(3)
C77	C78	1.49(3)
C75A	C76A	1.49(3)
C76A	C77A	1.49(3)
C77A	C78A	1.49(3)
C79	C80	1.38(4)
C79	C84	1.41(4)
C80	C81	1.38(4)
C81	C82	1.40(4)
C82	C83	1.38(4)
C83	C84	1.35(4)

Table B.9 Bond Angles in ° for **LPt-7**.

Atom	Atom	Atom	Angle/°
N1	Pt1	S1	99.9(6)
N1	Pt1	N2	160.5(9)
N2	Pt1	S1	99.5(7)
C11	Pt1	S1	173.8(6)
C11	Pt1	N1	80.5(8)
C11	Pt1	N2	80.1(8)
C29	S1	Pt1	110.0(8)
C2	O1	C17	116(2)
C15	O2	C23	120(3)
C1	N1	Pt1	124.0(17)
C5	N1	Pt1	116.9(18)
C5	N1	C1	119(2)
C12	N2	Pt1	115(2)
C16	N2	Pt1	129(2)
C16	N2	C12	116(3)
N1	C1	C2	121(2)
O1	C2	C1	114(2)
O1	C2	C3	127(3)
C3	C2	C1	119(3)
C2	C3	C4	119(3)
C5	C4	C3	120(3)
N1	C5	C4	122(3)
N1	C5	C6	113(2)
C4	C5	C6	125(2)
C11	C6	C5	110.8(14)
C11	C6	C7	120.0
C7	C6	C5	129.1(14)
C6	C11	Pt1	118.2(9)
C10	C11	Pt1	121.6(9)
C10	C11	C6	120.0
C11	C10	C9	120.0
C11	C10	C12	108.1(15)
C9	C10	C12	131.9(15)
C8	C9	C10	120.0
C9	C8	C7	120.0
C8	C7	C6	120.0
N2	C12	C10	115(2)
C13	C12	N2	121(3)
C13	C12	C10	124(2)
C14	C13	C12	124(3)
C13	C14	C15	114(3)
O2	C15	C14	117(3)
C16	C15	O2	121(3)
C16	C15	C14	121(3)
N2	C16	C15	124(3)
O1	C17	C18	105(2)
C19	C18	C17	110(2)
C18	C19	C20	110(2)
C21	C20	C19	110(3)
C20	C21	C22	111(3)
O2	C23	C24	107(3)
C23	C24	C25	110(3)
C26	C25	C24	113(4)
C25	C26	C27	112(4)
C26	C27	C28	111(5)
C30	C29	S1	120(2)
C30	C29	C34	121(3)
C34	C29	S1	119(2)
C29	C30	C31	119(3)
C32	C31	C30	119(3)
C33	C32	C31	119(3)
C32	C33	C34	124(3)
C33	C34	C29	119(3)
N51	Pt51	S51	99.4(6)
N51	Pt51	N52	160.5(8)
N52	Pt51	S51	99.6(6)
C61	Pt51	S51	175.7(8)
C61	Pt51	N51	79.7(9)
C61	Pt51	N52	81.1(10)
C79	S51	Pt51	109.5(10)
C52	O51	C67	117(2)
C65	O52	C73	117(2)
C51	N51	Pt51	128.3(17)
C55	N51	Pt51	118.4(19)
C55	N51	C51	113(2)
C62	N52	Pt51	113.6(17)
C66	N52	Pt51	128.3(18)
C66	N52	C62	118(2)
N51	C51	C52	126(2)
O51	C52	C51	117(2)
O51	C52	C53	126(3)
C53	C52	C51	117(3)
C52	C53	C54	119(3)
C55	C54	C53	121(3)
N51	C55	C56	110(3)
C54	C55	N51	124(3)
C54	C55	C56	126(3)
C57	C56	C55	129(3)
C61	C56	C55	112(2)
C61	C56	C57	119(3)
C58	C57	C56	121(3)
C59	C58	C57	119(3)
C60	C59	C58	121(3)
C59	C60	C61	122(2)
C59	C60	C62	128(2)
C61	C60	C62	110(2)
C56	C61	Pt51	120(2)
C56	C61	C60	118(2)
C60	C61	Pt51	121.8(18)
N52	C62	C60	114(2)
C63	C62	N52	120(3)
C63	C62	C60	126(3)
C62	C63	C64	120(3)
C65	C64	C63	122(3)
O52	C65	C64	119(3)
O52	C65	C66	126(3)
C64	C65	C66	115(3)
N52	C66	C65	125(3)
O51	C67	C68	107(2)

Atom	Atom	Atom	Angle/°
C67	C68	C69	111(2)
C70	C69	C68	113(2)
C69	C70	C71	115(3)
C70	C71	C72	113(3)
O52	C73	C74	105(3)
C75	C74	C73	108(4)
C75A	C74	C73	131(5)
C76	C75	C74	132(6)
C77	C76	C75	128(5)
C76	C77	C78	115(6)
C76A	C75A	C74	105(5)

Atom	Atom	Atom	Angle/°
C75A	C76A	C77A	111(5)
C78A	C77A	C76A	112(6)
C80	C79	S51	122(2)
C80	C79	C84	116(3)
C84	C79	S51	122(2)
C81	C80	C79	123(3)
C80	C81	C82	119(3)
C83	C82	C81	119(3)
C84	C83	C82	120(3)
C83	C84	C79	123(3)

Table B.10 Bond Lengths in Å for **LPt-1**.

Atom	Atom	Length/Å
Pt1	Cl1	2.4135(11)
Pt1	N1	2.033(4)
Pt1	N2	2.041(4)
Pt1	C11	1.915(4)
O1	C2	1.346(6)
O1	C17	1.446(5)
O2	C13	1.354(5)
O2	C23	1.444(5)
N1	C1	1.335(6)
N1	C5	1.392(6)
N2	C12	1.323(6)
N2	C16	1.388(6)
C1	C2	1.399(6)
C2	C3	1.383(7)
C3	C4	1.390(7)
C4	C5	1.380(6)
C5	C6	1.466(6)
C6	C7	1.396(6)
C6	C11	1.407(6)
C7	C8	1.407(7)

Atom	Atom	Length/Å
C8	C9	1.381(7)
C9	C10	1.450(7)
C10	C11	1.349(7)
C10	C16	1.448(6)
C12	C13	1.403(6)
C13	C14	1.379(7)
C14	C15	1.392(7)
C15	C16	1.381(6)
C17	C18	1.504(6)
C18	C19	1.528(6)
C19	C20	1.530(6)
C20	C21	1.524(6)
C21	C22	1.526(7)
C23	C24	1.498(6)
C24	C25	1.520(6)
C25	C26	1.521(6)
C26	C27	1.525(6)
C27	C28	1.525(7)

Table B.11 Bond Angles in ° for **LPt-1**.

Atom	Atom	Atom	Angle/°
N1	Pt1	Cl1	99.52(11)
N1	Pt1	N2	161.67(15)
N2	Pt1	Cl1	98.80(11)
C11	Pt1	Cl1	177.99(14)
C11	Pt1	N1	81.25(18)
C11	Pt1	N2	80.41(18)
C2	O1	C17	118.1(4)
C13	O2	C23	117.9(4)
C1	N1	Pt1	126.4(3)
C1	N1	C5	119.5(4)
C5	N1	Pt1	114.1(3)
C12	N2	Pt1	125.5(3)
C12	N2	C16	120.6(4)
C16	N2	Pt1	113.9(3)
N1	C1	C2	122.3(4)
O1	C2	C1	114.8(4)
O1	C2	C3	126.3(4)
C3	C2	C1	118.9(4)
C2	C3	C4	118.8(4)
C5	C4	C3	121.1(4)
N1	C5	C6	113.8(4)
C4	C5	N1	119.5(4)
C4	C5	C6	126.7(4)
C7	C6	C5	128.9(4)
C7	C6	C11	118.4(4)
C11	C6	C5	112.8(4)
C6	C7	C8	119.0(4)
C9	C8	C7	121.9(4)
C8	C9	C10	118.9(4)
C11	C10	C9	117.8(4)
C11	C10	C16	115.4(5)
C16	C10	C9	126.6(4)
C6	C11	Pt1	118.1(3)
C10	C11	Pt1	117.9(4)
C10	C11	C6	124.0(4)
N2	C12	C13	121.6(4)
O2	C13	C12	113.9(4)
O2	C13	C14	126.8(4)
C14	C13	C12	119.3(4)
C13	C14	C15	118.4(4)
C16	C15	C14	121.2(4)
N2	C16	C10	112.3(4)
C15	C16	N2	118.8(4)
C15	C16	C10	128.8(4)
O1	C17	C18	105.9(4)
C17	C18	C19	112.7(4)
C18	C19	C20	111.4(4)
C21	C20	C19	114.0(4)
C20	C21	C22	113.7(4)
O2	C23	C24	106.3(4)
C23	C24	C25	113.5(4)
C24	C25	C26	111.4(4)
C25	C26	C27	114.0(4)
C26	C27	C28	113.5(4)

B.2 EDA-NOCV results

Table B.12 EDA-NOCV results of complexes **L'M-X** calculated at ZORA-PBE-GD3BJ/TZ2P level of theory (in kJ mol^{-1}).

Complexes	ΔE_{int}	ΔE_{elstat}	ΔE_{disp}	ΔE_{orb}	ΔE_{Pauli}	1st NOCV	2nd NOCV
L'Ni-2	–113.1	–137.8 (40.0%)	–128.7 (37.3%)	–78.3 (22.7%)	231.7	–15.3	–14.1
L'Pd-2	–111.0	–156.0 (43.6%)	–131.8 (36.9%)	–69.7 (19.5%)	246.5	–14.1	–10.5
L'Pt-2	–111.0	–177.2 (45.8%)	–133.0 (34.4%)	–76.8 (19.8%)	276.1	–19.8	–12.1
L'Pt-3	–114.6	–185.5 (46.1%)	–135.8 (33.8%)	–80.7 (20.1%)	287.4	–20.1	–12.8
L'Pt-4	–119.6	–175.1 (45.9%)	–130.5 (34.2%)	–76.2 (20.0%)	262.2	–17.6	–12.5
L'Pt-5	–136.9	–215.1 (47.9%)	–143.9 (32.1%)	–89.9 (20.0%)	312.0	–19.5	–14.1
L'Pt-6	–136.0	–215.0 (47.2%)	–147.2 (32.3%)	–92.9 (20.4%)	319.1	–19.7	–11.8
L'Pt-7	–113.9	–182.6 (45.8%)	–135.8 (34.1%)	–80.3 (20.1%)	284.8	–19.7	–12.5
L'Pt-8	–109.3	–170.8 (45.1%)	–132.2 (34.9%)	–75.5 (19.9%)	269.2	–19.9	–11.2
L'Pt-9	–106.6	–180.1 (45.6%)	–132.4 (33.5%)	–82.9 (21.0%)	288.8	–21.1	–10.1

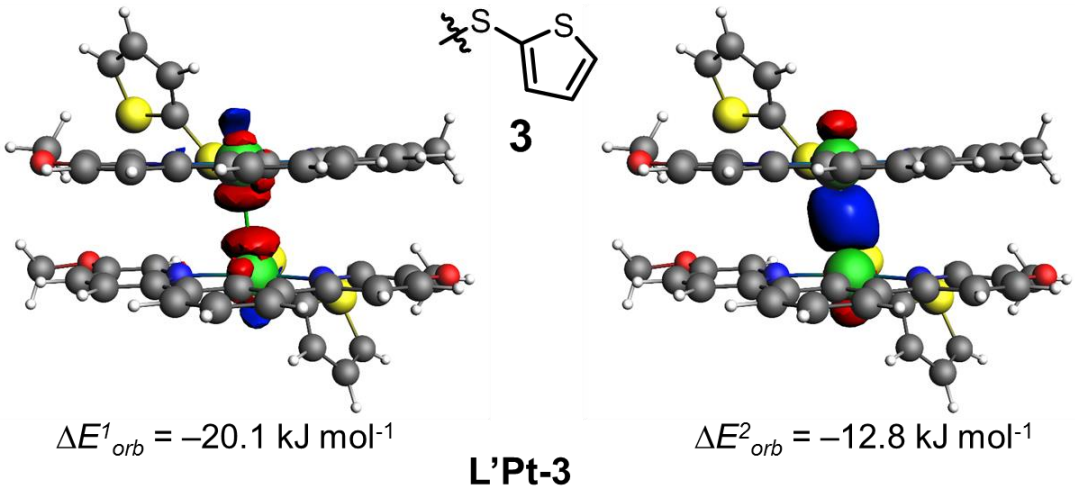

Figure B.11 NOCV orbitals of complex **L'Pt-3** with the corresponding density change and associated energies.

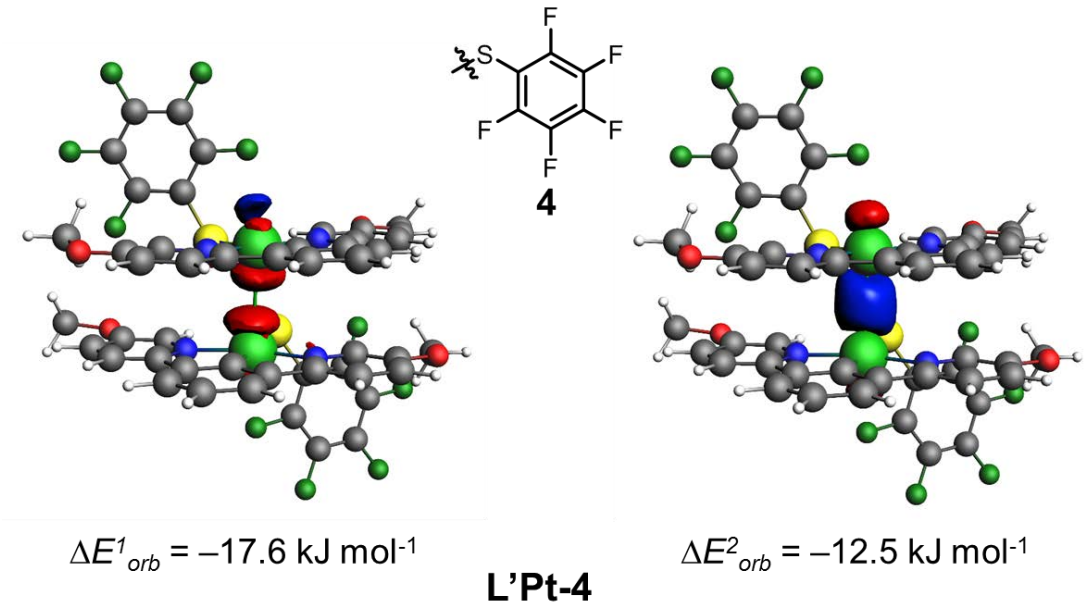

Figure B.12 EDA-NOCV deformation densities and corresponding contributions for complex **L'Pt-4**.

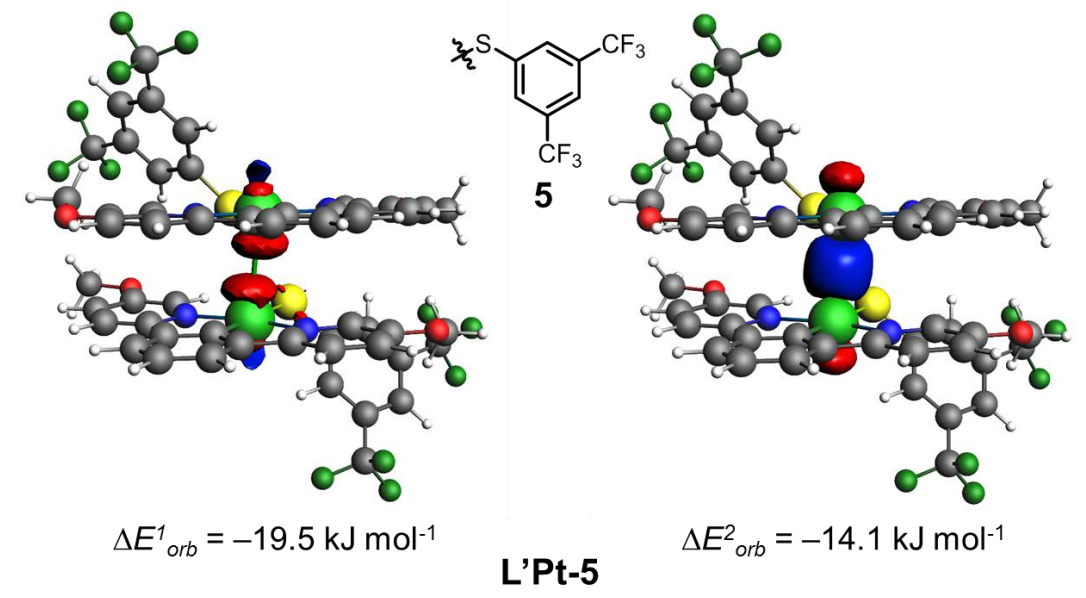

Figure B.13 EDA-NOCV deformation densities and corresponding contributions for complex **L'Pt-5**.

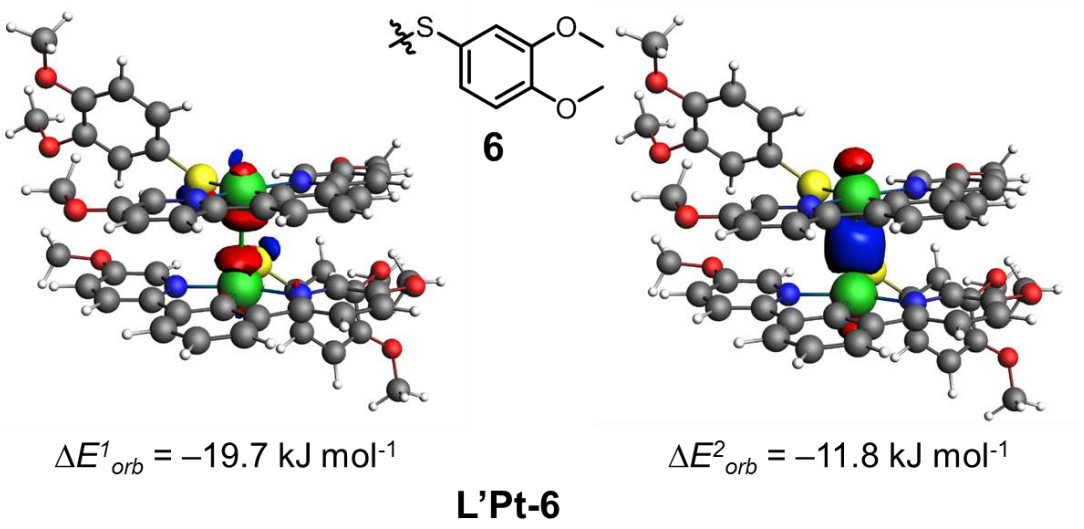

Figure B.14 EDA-NOCV deformation densities and corresponding contributions for complex **L'Pt-6**.

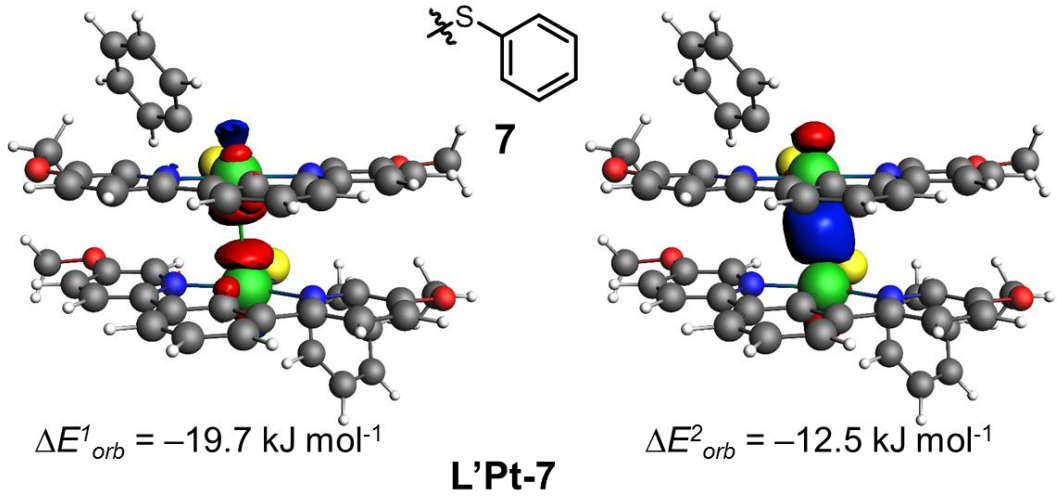

Figure B.15 EDA-NOCV deformation densities and corresponding contributions for complex **L'Pt-7**.

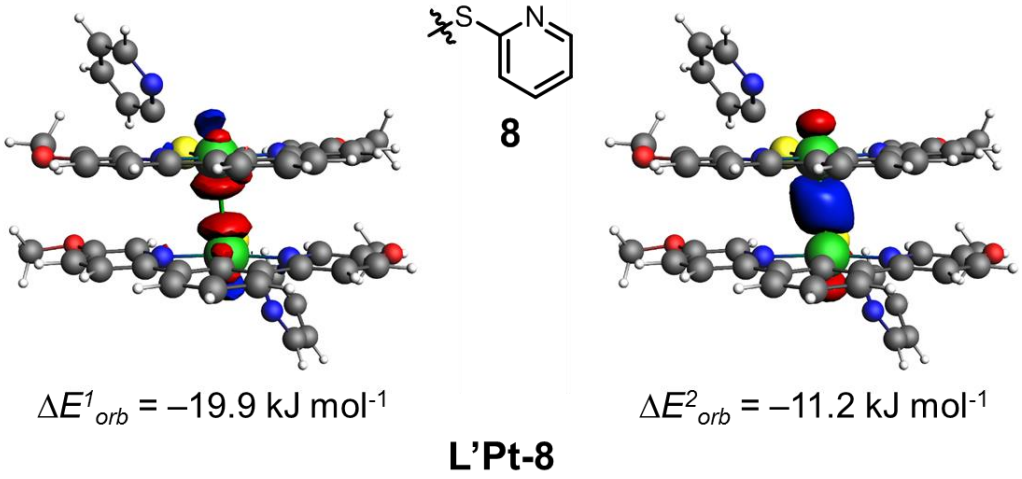

Figure B.16 EDA-NOCV deformation densities and corresponding contributions for complex **L'Pt-8**.

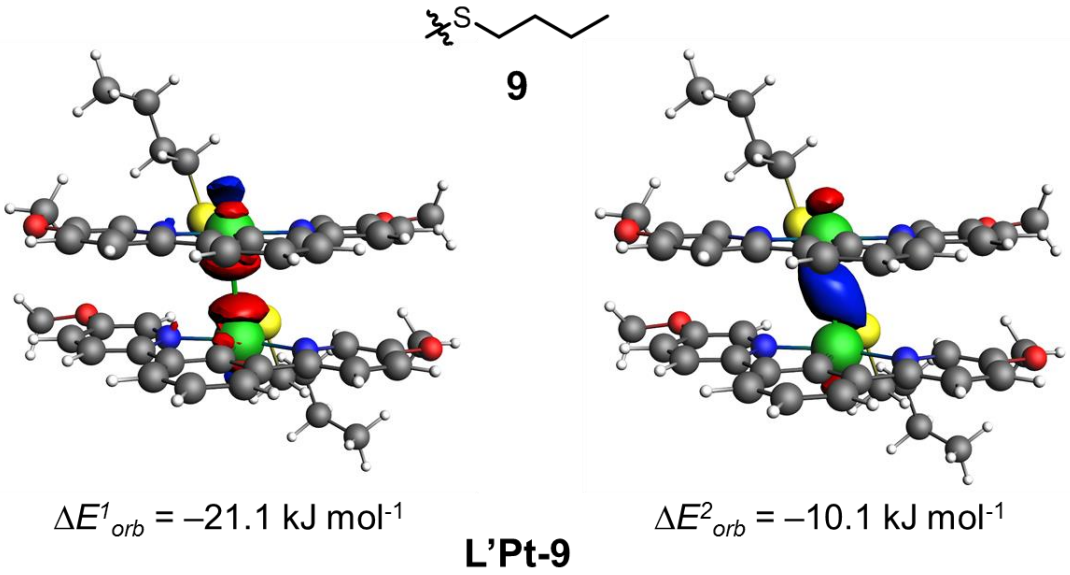

Figure B.17 EDA-NOCV deformation densities and corresponding contributions for complex **L'Pt-9**.